Étude multi-technique des minéraux terrestres et extraterrestres

Isabella Pignatelli

Synthèse d'activité scientifique

présentée en vue d'obtenir l'Habilitation à Diriger des Recherches

Université de Lorraine – École doctorale SIReNa

par

Isabella Pignatelli

Étude multi-technique des minéraux terrestres et extraterrestres

Membres du jury :

Rapporteurs :	Mme Martine Bautier	Professeur, Université Franche-Comté, Besançon
	M. Éric Ferrage	Directeur de recherche, CNRS, IC2MP, Poitiers
	M. Benjamin Rondeau	Maître de conférences, Université de Nantes, Nantes
Examinateurs :	Mme Judith Sausse	Professeur, Université de Lorraine, Nancy
	M. Gaston Giuliani	Directeur de recherche émérite, IRD, Université Paul Sabatier et de Lorraine
	M. Cristiano Ferraris	Maître de conférences, MNHN, Paris
	M. Jérôme Sterpenich	Professeur, Université de Lorraine, Nancy
	M. Massimo Nespolo	Professeur, Université de Lorraine, Nancy
Invités :	Mme Régine Mosser-Ruck	Maître de conférences, Université de Lorraine, Nancy
	M. Giovanni Ferraris	Professeur émérite, Università di Torino, Torino

Al mio adorato papà Mimmo

"Io di te ricorderò il sorriso
E mi dispiace dirlo
Ma il destino ci ha tradito

Ma non dirò mai
Mai a nessuno cosa penso
Ciò che è nostro resta nostro
E della guerra che ho già perso"
Tiziano Ferro

TABLE DES MATIERES

Annexes : les publications les plus représentatives de l'activité de recherche

I. Pignatelli I., Duseck M., De Titta G., Nespolo M. (2011) Structural modeling, refinement and possible formation mechanism of a $4M_3$ non-MDO ferriphlogopite (Ruiz Peak). European Journal of Mineralogy, 23, p. 73 - 84.

II. Pignatelli I., Bourdelle F., Bartier D., Mosser-Ruck R., Truche L., Mugnaioli E., Michau N. (2014) Iron-clay interactions: detailed study of the mineralogical transformation of claystone with emphasis on the formation of iron-rich T-O phyllosilicates in a step-by step cooling experiment from 90°C to 40°C. Chemical Geology, 387, p. 1-11.

III. Pignatelli I., Kumar A., Field K.G., Wang B., Yu Y., Le Pape Y., Bauchy M., Sant G. (2016) Direct Experimental Evidence for Differing Reactivity Alterations of Minerals following Irradiation: The Case of Calcite and Quartz. Scientific Report, 6, 20155. doi: 10.1038/srep20155.

IV. Pignatelli I., Marrocchi Y., Mugnaioli E., Bourdelle F., Gounelle M. (2017) Mineralogical, crystallographic and redox features of the earliest stages of fluid alteration in CM chondrites. Geochimica et Cosmochimica Acta, 209, 106-122.

V. Pignatelli I., Giuliani G., Morlot C., Pham L.V. (2019) The texture and chemical composition of trapiche ruby from Khoan Thong, Luc Yen mining district, northern Vietnam. Journal of Gemology, 36(8), 616-636.

VI. Pignatelli I., Mosser-Ruck R., Mugnaioli E., Sterpenich J., Gemmi M. (2020) The effect of the starting mineralogical mixture on the nature of Fe-serpentines obtained during hydrothermal synthesis at 90° C. Clays and Clay Minerals, 68(4), 394-412.

1. Curriculum Vitae

2017 – présent : Maître de Conférences au laboratoire GeoRessources, Université de Lorraine-CNRS, Faculté des Sciences et Technologies - Rue Jacques Callot, 54500 Vandoeuvre-lès-Nancy, France.

E-mail: isabella.pignatelli@univ-lorraine.fr

Numéro de téléphone : +33 372745546

Expériences professionnelles

2016 – 2017: Post-doc au laboratoire CRPG-CRNS. *L'altération aqueuse dans les météorites*.

2014 – 2016: Post-doc au laboratoire LC^2, University of California, Los Angeles (UCLA). *Dissolution des minéraux.*

2014: Post-doc au laboratoire CRPG-CRNS. *L'altération aqueuse dans les météorites*.

2011 – 2013: Post-doc au laboratoire GeoRessources, sur financement ANDRA (Agence nationale pour la gestion des déchets radioactifs). *Les interaction fer-argile dans le stockage des déchets radioactifs*.

Formation

2011: Doctorat en chimie, spécialisation en cristallographie au laboratoire CRM^2, Nancy. *Cristallographie et cristallochimie des polytypes à longue période des micas*.

2007: MsC degree in Geological Sciences; Università degli studi di Bari, Italie. *Stage de Master: Relations entre les défauts structuraux et l'activation de la couleur dans la topaze.*

Compétences expérimentales

- Diffraction X sur monocristal (Agilent SuperNOVA double microsource avec CCD, Brukex ApexII avec CCD, Mar345 avec image plate)
- Diffraction X sur poudre (Bruker D8)

- Résolution et affinement des structures cristallines (CrysalisPro, Apex2, SORTAV, Jana, SHELX)
- Microscopie optique et topographie X pour les études minéralogiques
- Microscopie électronique à balayage (MEB) et a transmission (MET)
- Vertical scanning interferometry (VSI)
- Analyse à la microsonde électronique (EMPA)
- Synthèse hydrothermale en autoclave

Formations spécifiques

2017: Les Houches Winter School – Chronology of the formation of the Solar System VI: The outer Solar System and its relationship with the InterStellar Medium.

2013: EMU School 2013: Minerals at the nanoscale. (Grenade, Spain).

2012: MinTEM School dedicated to Transmission Electron Microscopy and Mineralogy (Lille, France).

2010: Méthodes d'analyse des Matériaux et des Minéraux (Paris, France).

2010: Summer School on Mathematical Crystallography: Irreducible representations of space groups and Topological Crystal Chemistry: Theory and Practice (Nancy, France).

2009: The first ad hoc Workshop on Jana2006 (Prague, Czech Republic).

2009: École thématique «Analyse Structurale par Diffraction des Rayons X sur Monocristal et Applications à la Cristallographie sous Contraintes » (Pont à Mousson, France).

2009: Crystallography online: International School on the use and application of the Bilbao Crystallographic Server (Lekeitio, Spain).

2009: Structural Crystallography of Minerals (Copenhagen, Denmark).

2008: Summer School on Mathematical and Theoretical Crystallography (Gargnano, Italy).

2. Notice de titres et travaux

2.1 Articles

39 articles publiés dont 33 de Rang A et 21 en premier auteur

2.1.1 Articles de Rang A

2020 **Pignatelli I.**, Giuliani G., Morlot C., Cathelineau M., Liu S. Flower-shaped trapiche ruby from Mong Hsu, Myanmar: a revisited growth mechanism. Journal of Gemology, 37(4), 368-379.

2020 **Pignatelli I.**, Mosser-Ruck R., Mugnaioli E., Sterpenich J., Gemmi M. The effect of the starting mineralogical mixture on the nature of Fe-serpentines obtained during hydrothermal synthesis at 90° C. Clays and Clay Minerals, 68(4), 394-412.

2020 Ferraris C., **Pignatelli I.**, Cámara F., Parodi G., Pont S., Schreyer M., Wei F. Laurentthomasite, $Mg_2K(Be_2Al)Si_{12}O_{30}$: a new milarite-group-type member from the Ihorombe region, Fianarantsoa Province, Madagascar. European Journal of Mineralogy, 32, 355-365.

2020 Giuliani G., Groat L.A., Fallick A.E., **Pignatelli I.**, Pardieu V. Ruby deposits: a review and geological classification. Minerals, 10, 597, 1-83. doi:10.3390/min10070597.

2019 **Pignatelli I**., Giuliani G., Morlot C., Pham L.V. The texture and chemical composition of trapiche ruby from Khoan Thong, Luc Yen mining district, northern Vietnam. Journal of Gemology, 36(8), 616-636.

2019 Hsiao Y.H., Wang B., Callagon La Plante E., **Pignatelli** I., Krishnan A.N.M., Le Pape Y., Neithalath N., Bauchy M., Sant G. The effect of irradiation on the atomic structure and chemical durability of calcite and dolomite. Npj Materials Degradation-Nature, 3, 36, https://doi.org/10.1038/s41529-019-0098-x.

2019 Richard A., Morlot C., Creon L., Beaudoin N., Balistky V.S., Pentelei S., Dyja V., Giuliani G., **Pignatelli I.**, Legros H., Sterpenich J., Pironon J. Advances in 3D imaging

and volumetric reconstruction of fluid and melt inclusions by high resolution X-ray computed tomography. Chemical Geology, 508, 3-14.

2018 **Pignatelli I.**, Mugnaioli E., Marrocchi Y. Cronstedtite polytypes in the Paris meteorite. European Journal of Mineralogy, 30, 2, 349-354.

2018 Giuliani G., Dubessy J., **Pignatelli I.**, Schwarz D. Fluid inclusions study of trapiche and non-trapiche rubies from the Mong Hsu deposit, Myanmar. The Canadian Mineralogist, 56, 1, 1-13.

2018 Hybler J., Klementová M., Jarošová M., **Pignatelli I**., Mosser-Ruck R., Ďurovič S. Polytypes identification in trioctahedral 1:1 layer silicates by electron diffraction and application to cronstedtite mineral synthetized from iron-clay interaction. Clays and Clay Minerals, 66, 4, 379-402.

2017 **Pignatelli I.**, Marrocchi Y., Mugnaioli E., Bourdelle F., Gounelle M. Mineralogical, crystallographic and redox features of the earliest stages of fluid alteration in CM chondrites. Geochimica et Cosmochimica Acta, 209, 106-122.

2017 **Pignatelli I.**, Giuliani G., Morlot C., Rouer O., Claiser N., Chatagnier P.Y., Goubert D. Recent advances in understanding the similarities and differences of Colombian Euclases. The Canadian Mineralogist, 55, 1-22.

2017 Bourdelle F., Mosser-Ruck R., Truche L., Lorgeoux C., **Pignatelli I.**, Michau N. A new view on iron-claystone interactions under hydrothermal conditions (90 °C) by monitoring in-situ pH evolution and H_2 generation. Chemical Geology, 466, 600-607.

2017 Odey T., Kumar A., **Pignatelli I**., Yu Y., Neithalath N., Bullard J.W., Bauchy M., Sant G. Topological controls on the dissolution kinetics of glassy aluminosilicates. Journal of the American Ceramic Society, 100, 5521-5527.

2016 **Pignatelli I.**, Kumar A., Field K.G., Wang B., Yu Y., Le Pape Y., Bauchy M., Sant G. Direct Experimental Evidence for Differing Reactivity Alterations of Minerals following Irradiation: The Case of Calcite and Quartz. Scientific Report, 6, 20155. doi: 10.1038/srep20155

2016 **Pignatelli I.**, Marrocchi Y., Vacher L., Delon R., Gounelle M. Multiple precursors of secondary mineralogical assemblages in CM chondrites. Meteoritics & Planetary Science, 51(4), 785-805.

2016 **Pignatelli I.**, Kumar A., Bauchy M., Sant G. Topological control on silicates' dissolution kinetics. Langmuir, 32, 4434-4439.

2016 **Pignatelli I.,** Kumar A., Alizadeth R., Le Pape Y., Bauchy M., Sant G. A dissolution-precipitation mechanism is at the origin of concrete creep in moist environments. The Journal of Chemical Physics, 145, 054701.

2016 **Pignatelli I.**, Kumar A., Shah K., Balonis M., Bauchy M., Wu B., Sant G. Vertical Scanning Interferometry: a new method to quantify re-/de-mineralization dynamics of dental enamel. Dental Materials, 32, Issue 10, 251-261.

2016 Mosser-Ruck R., **Pignatelli I.**, Bourdelle F., Abdelmoula M., Barres O., Guillaume D., Charpentier D., Rousset D., Cathelineau M., Michau N. Contribution of long-term hydrothermal experiments for understanding the smectite-to-chlorite conversion in geological environments. Contribution to Mineralogy & Petrology, 171, 97, doi 10.1007/s00410-016-1307-z.

2016 **Pignatelli I.**, Faure F., Mosser-Ruck R. Self-mixing magma in the Ruiz Peak rhyodacite (New Mexico, USA): a mechanism explaining the formation of long period polytypes of mica. Lithos, 266-267, 332-347.

2015 Wang B., Yu Y., **Pignatelli I.**, Sant G., Bauchy M. Nature of Radiation-Induced Defects in Quartz. Journal of Chemical Physics, 143, 024505.

2015 Vance K., Falzone G., **Pignatelli I.**, Bauchy M., Balonis M., Sant G. Direct Carbonation of $Ca(OH)_2$ using Liquid and Supercritical CO_2: Implications for Carbon-Neutral Cementation. Industrial & Engineering Chemistry Research, 54 (36), 8908–8918.

2015 **Pignatelli I.,** Giuliani G., Ohnenstetter D., Agrosì G., Mathieu S., Morlot C., Branquet Y. Colombian Trapiche Emeralds: Recent Advances in Understanding Their Formation. Gems and Gemology, 51(3), 222-259.

2015 **Pignatelli I.,** Giuliani G. Trapiche nomenclature: Reply. Gems and Gemology, 51(4), p. 463.

2015 **Pignatelli I.**, Vacher L., Marrocchi Y. Comment on "Hydrothermal preparation of analogous matrix minerals of CM carbonaceous chondrites from metal alloy particles" by Y. Peng and Y. Jing [Earth Planet. Sci. Lett. 408 (2014) 252-262]. Earth and Planetary Science Letters, 428, 304-306.

2014 **Pignatelli I.,** Mugnaioli E., Mosser-Ruck R., Barre O., Kolb U., Michau N. A multi-technique micrometer- to atomic-scale description of a synthetic analogue of chukanovite $Fe_2(CO_3)(OH)_2$. European Journal of Mineralogy, 26, 221-229.

2014 Bourdelle F., Truche L., **Pignatelli I.**, Mosser-Ruck R., Lorgeoux C., Roszypal C., Michau N. Iron-clay interactions under hydrothermal conditions: impact of iron specific surface area on reaction pathway revealed by mineralogy and a continuous monitoring of pH, solution and gas compositions. Chemical Geology, 381, 194-205.

2014 **Pignatelli I.**, Bourdelle F., Bartier D., Mosser-Ruck R., Truche L., Mugnaioli E., Michau N. Iron-clay interactions: detailed study of the mineralogical transformation of claystone with emphasis on the formation of iron-rich T-O phyllosilicates in a step-by step cooling experiment from 90°C to 40°C. Chemical Geology, 387, 1-11.

2013 **Pignatelli I.**, Mugnaioli E., Hybler J., Mosser-Ruck R., Cathelineau M., Michau N. A multi-technique characterization of cronstedtite synthesized by iron-clay interaction in a step-by-step cooling procedure. Clays and Clay Minerals, 61, 277-289.

2011 **Pignatelli I.**, Nespolo M., Ferraris G. A survey of hybrid twins in silicate minerals. European Journal of Mineralogy, 23, 779 – 794.

2011 **Pignatelli I.**, Duseck M., De Titta G., Nespolo M. Structural modeling, refinement and possible formation mechanism of a 4M_3 non-MDO ferriphlogopite (Ruiz Peak). European Journal of Mineralogy, 23, 73 - 84.

2011 **Pignatelli I.**, Nespolo M. 5M_3 ferriphlogopite from Ruiz Peak (New Mexico, USA): First occurrence of a mica polytype with coexistence of M1- and M2-layers. European Journal of Mineralogy, 23, 703 – 715.

2.1.2 Articles de Rang B

2019 Giuliani G., **Pignatelli I.**, Lheur C., Feneyrol J., Claiser N., Tissandier L., Fallick A., Boyce A., Ohnenstetter D. La zoisite de Canari (France) et Merelani (Tanzanie): similitudes et differences. Le Régne Mineral, 149, 20-51.

2018 **Pignatelli I.**, Giuliani G. La texture trapiche de l'emeraude colombienne et du rubis birman. Le Régne Mineral, 144, 39-52.

2017 Giuliani G., **Pignatelli I.**, Fallick A. Gem Andradite garnet deposits – Demantoid variety. InColor, 36, 28-38.

2017 Odey T., Hsiao Y., Callagon La Plante E., Wang B., **Pignatelli I.**, Bauchy M., Sant G. Rate controls on silicate dissolution in cementitious environments. RILEM Technical Letters, 2, 67-73.

2016 Giuliani G., **Pignatelli I**. "Trapiche" *vs* "trapiche-like" textures in minerals. InColor, 31, 45-46.

2016 Morlot C., **Pignatelli** I., Giuliani G., Sterpenich J., Boiron M.C., Ohnenstetter D., Andriamamonjy A., Raoul J., Chatagnier P.Y. La tomographie à rayons X et ses applications en gemmologie : exemples de l'emeraude trapiche et du grenat démantoïde. Revue de gemmologie, 198, 13-18.

2.1.3 Articles en préparation ou soumis

Hsiao, Y.H., **Pignatelli**, I., Shah, K., Wu, B., Sant, G. Elucidating the effects of bleaching agents on the dissolution of dental enamel. Journal of the American Ceramic Society, under review.

2.2 Résumés ayant fait l'objet d'une présentation orale

2.2.1 Congres internationaux

• 27 - 31 Aout 2019 Nantes: 36th International Gemmological Conference (IGC) 2019

Trapiche texture in emeralds and rubies

• 13 - 17 Aout 2018 Melbourne: IMA2018

Trapiche rubies from Vietnam

• 13 - 17 Aout 2018 Melbourne: IMA2018

Minerals as markers of fluid alteration in Paris chondrite.

• 6 – 10 Novembre 2017 Prague: General Meeting of International Committee on Irradiated Concrete

TEM characterization of irradiated minerals.

• 23 – 28 Juliet 2017 Santa Fe (USA) 80th Annual Meeting of the Meteoritical Scociety

Minerals as markers of fluid alteration in Paris chondrite.

• 11st – 15th Septembre 2016 Rimini EMC2016

Colombian emerald and euclase: trapiche *versus* trapiche-like texture?

• 2nd – 5th Novembre 2015 Knoxville: First General Meeting (FGM) International Committee on Irradiated Concrete

Direct experimental evidence for differing reactivity alteration of minerals following irradiation.

• 1 – 5 Septembre 2014 Johannesburg: IMA2014

X-ray diffraction topography images of Colombian trapiche emeralds.

• 11 – 15 Septembre 2013 St. Petersburg: 2nd International Conference Clays, Clay Minerals and Layered Materials – CMLM2013

Polytype characterization of synthetic cronstedtite.

• 22 – 25 Octobre 2012 Montpellier: **International meeting "Clays in Natural and Engineered Barriers for Radioactive Waste Confinement"**

Experimental formation of cronstedtite from COx argillite-iron interaction at decreasing temperature in 90° - 40° C range.

• 2 - 6 Septembre 2012 Frankfort: EMC2012

Self-mixing magma: a natural origin for rare long period polytypes of micas.

• 21 - 27 Aout 2010 Budapest : IMA2010

Structural refinement and OD chracter of a 4-layer ferriphlogopite.

2.2.2 Congres nationaux

• 22nd – 23rd Janvier 2013 Nancy: Rencontres Scientifiques du groupe Pétrologie Endogène

L'auto-convection dans les chambres magmatiques: une explication possible pour la formation des polytypes à longue période des micas.

• 7 - 10 Juliet 2010 Strasbourg : AFC2010

Nouveaux polytypes dans les micas : polytypes à quatre et cinq feuillets dans la ferriphlogopite du volcan Ruiz Peak.

3. Présentation synthétique des activités d'enseignement et d'administration

Mes heures d'enseignement sont réparties entre **CM** (**44h**), **TD** (**52h**) et **TP** (**76h**).

Pour les niveaux L1 et L2 des parcours Sciences de la Terre (ST) et Sciences de la vie (SVE), j'interviens dans les UE suivantes :

Introductions aux Géosciences (UE 1.06), **Géologie générale** (UE 202), **Projet Professionnel Personnalisé** (UE 1.04C), **Outils et cultures numériques** (UE 401), **Minéralogie** (UE 3.35), et **UE libre « La beauté des pierres précieuses »**, que j'ai proposé et organisé pour montrer aux étudiants une double approche scientifique et historique dans l'étude des gemmes.

Pour les niveaux M1 STPE (Sciences de la Terre, planètes, environnement), et M2 du parcours Systèmes Métallogéniques, Géologie et Exploration et du parcours Sols, Eaux, Environnement (SEE), j'interviens dans :

- **Exploration Géochimique - Applications à la Prospection** (UE 906) pour illustrer les outils de terrain qui peuvent être utilisés pour l'analyse des gemmes exploitables.
- **Géochimie minérale** (UE 902) pour expliquer l'intérêt de la géochimie minérale dans les problématiques environnementales (processus physico-chimique aux interfaces solide-liquide, aérosols atmosphériques, zéolites, minéraux argileux, etc.).
- **Objets métallogéniques** (UE 805): pour expliquer les minéraux industriels (kaolinite, bentonites, barytine, etc.), ressources non métalliques de grand intérêt économique (lien entre les caractéristiques structurales de minéraux, leurs propriétés physico-chimiques et donc les utilisations dans l'industrie).
- **Processus Métallogéniques** (UE 902) pour montrer des exemples de processus géologiques qui portent à la formation des gisements d'intérêt gemmologique, (opale, corindon, grenats, etc.).

Pour les étudiants 1A de l'ENSG :

- **Techniques d'études des roches** : les étudiants doivent apprendre à préparer et caractériser les échantillons, pour ensuite pouvoir dialoguer avec des spécialistes de la caractérisation dans leur future vie professionnelle.

Depuis 2018 je suis **responsable administratif** de l'UE 1.06 Introductions aux Géosciences.

1. Encadrements thèses et stages

1.1 Thèses

J'ai co-encadré trois thèses, dont deux à l'UCLA et une à l'Université de Lorraine :

- la thèse de la **doctorante Linda Monfardini** , qui a fait moitié de sa thèse à l'UCLA et moitie en Italie, à la faculté d'ingénierie structurale de l'Université de Brescia (l'équivalent des écoles françaises). Elle a soutenu sa thèse en juillet 2017 sur le sujet de la réhabilitation structurale des bâtiments historiques et modernes. Avec elle, on a travaillé sur le risque des réactions alcali-granulat dans les bétons pour un projet en collaboration avec l'entreprise COMAX®. On a aussi participé à des expériences pour la réutilisation de la CO_2 dans le cadre de la réalisation de bêtons durables, comme montré par un reportage réalisé dans notre laboratoire :

https://luskin.ucla.edu/carbon-upcycling-turning-co2-into-a-new-sustainable-co2ncrete/

- J'ai aussi co-encadré le travail de la **doctorante Yi-Hsuan Hsiao** pendant mon séjour aux États-Unis et après mon retour en France pour finaliser le travail et rédiger les publications liées aux travaux de thèse. J'ai lui appris à utiliser la technique du VSI (Vertical Scanning Interferometry), à choisir et préparer les échantillons synthétiques et naturelles, mais surtout les bases de la minéralogie, compte tenu qu'elle provenait de la faculté des sciences des matériaux. Nous avons étudié la dissolution des minéraux dans deux contextes : le contexte de la durabilité des bétons dans les centrales nucléaires et le contexte médical pour la préservation de l'émail dentale. Mlle Yi-Hsuan Hsiao a soutenu sa thèse en juin 2019 et pour l'instant nous avons co-redigé trois publications:

Oey, T., Hsiao, Y.H., Callagon, E., Wang, B., Pignatelli, I., Bauchy, M. and Sant, G., 2017. Rate controls on silicate dissolution in cementitious environments. RILEM Technical Letters, 2, pp.67-73.

Hsiao, Y.H., Wang, B., Callagon La Plante, E., Pignatelli, I., Krishnan, A.N.M., Le Pape, Y., Neithalath, N., Bauchy, M., Sant G, 2019. The effect of irradiation on the atomic structure and chemical durability of calcite and dolomite. Npj Materials Degradation-Nature, 3, 36, https://doi.org/10.1038/s41529-019-0098-x

Hsiao, Y.H., Pignatelli, I., Shah, K., Wu, B., Sant, G., 2019. Elucidating the effects of bleaching agents on the dissolution of dental enamel. Journal of the American Ceramic Society, under review.

- J'ai enfin co-encadré **le doctorant Lionel Vacher** pendant sa thèse au laboratoire CRPG de Nancy (thèse soutenue en novembre 2018) sur la partie analytique et expérimentale concernant les minéraux formés pendant l'altération aqueuse des météorites de type CM. En particulier, j'ai aidé M. Lionel Vacher sur l'étude des minéraux ayant structures et compositions complexes, comme par exemples les serpentines et la tochilinite. Nous avons co-redigé deux publications :

Pignatelli, I., Marrocchi, Y., Vacher, L., Delon, R., Gounelle, M. (2016) Multiple precursors of secodnary mineralogical assemblages in CM chondrites. Metoeritics & Planetary Science, 51 (4), 785-805.

Pignatelli, I., Vacher, L., Marrocchi, Y. (2015) Comment on "Hydrothermal preparation of analogous matrix minerals of CM carbonaceous chondrites from metal alloy particles". Earth & Planetary Science Letters, 428, 304'306.

1.2 Stages

J'ai encadré trois **stagiaires 2A** de l'école de géologie de Nancy (ENSG) :

2017-2018 Fabrice de Quattro et Tugdual Kervierl. Leurs stages avaient pour objectif la synthèse des serpentines ferrifères dans les autoclaves @Parr pour mieux comprendre leurs conditions de formation et contraindre leurs champs de stabilité.

2018-2019 Romaine Pettinger, qui a étudié la cronstedtite de la mine d'or de Salsigne.

J'ai encadré les **élèves des lycées à l'UCLA** pendant le « High School Summer Research Program » en 2015, un programme pour initier les étudiants à la recherche et les aider à choisir la faculté la plus adaptée à leur capacités/intérêts. J'ai peu leur presenter les méthodes expérimentales et analytiques utilisées au laboratoire, ainsi que les techniques de communication pour clarifier la présentation des résultats (présentés lors de la session des posters scientifiques à UCLA à la fin de leur stage).

2. Participation à des jurys

- J'ai été membre du jury de stage 2A des élevés de l'ENSG (mai 2018).

- J'ai évalué les rapports de stage M2 des étudiants du Master Ressources Minérales, parcours Géologie Exploration (2018 et 2019).

- En juillet 2019, j'ai participé aux jury du Master de Physique en qualité de rapporteur pour les travaux en cristallographie.

3. Rayonnement scientifique

- Les résultats scientifiques et mes compétences en minéralogie et cristallographie m'ont permis d'être nommée :

en 2014, **consultante de la Commission on Inorganic and Mineral Structures** (CIMS) de l'Union International de Cristallographie (IUCr)

http://www.iucr.org/iucr/commissions/inorganic-and-mineral-structures

en 2015, **membre du International Committee on Irradiated Concrete** (ICIC)

http://web.ornl.gov/sci/psd/mst/ICICFGM/index.shtml

- J'étais/je serai **chairwoman** aux congres internationaux suivants :

2021, 25th Congress of the International Union of Crystallography (14-22 August 2021 – Prague, Czech Republic) session "Modular structure of inorganic and mineral compounds".

2021, 3rd European Mineralogical Conference (29 August - 2 September 2021 – Krakow, Poland) session "The Geology of Gem Deposits: A Session in Honour of Gaston Giuliani".

2018, XXII Meeting of the International Mineralogical Association (13-17 August 2018 – Melbourne, Australia) session "Modular aspects of mineral structures''.

2017, 24th Congress of the International Union of Crystallography (21-28 August 2017 – Hyderabad, India) microsymposium "Topology and symmetry of modular structures".

- J'ai été régulièrement sollicitée par des éditeurs de journaux scientifiques pour réaliser plusieurs **reviews d'articles** pour des revues internationales à comité de lecture (Physics and Chemistry of Minerals, American Mineralogist, European Journal of Mineralogy, The Canadian Mineralogist, Rendiconti dei Lincei).

- Actuellement, je fais partie du **comité de lecture d'un livre** sur les émeraudes, qui sera publié par Prof. Giuliani.

- Je suis **membre du comité de thèse** de Umayahara Akihiro, qui travaille sur l'investigation théorique des structures modulaires et de leurs clichés de diffraction.

4. Responsabilités scientifiques

2020 : j'ai soumis un projet ANR jeune chercheur sur les serpentines ferrifères. Il a été retenu pour la deuxième étape mais pas financé. Il est resoumis cette année.

2019-2022: participation à l'ANR CASSYS « Chronologie et origine des premiers solides du jeune Système Solaire » obtenu par le Dr. Villeneuve Johan. Les rôles des participants sont repartis comme indiqués dans le tableau ci-dessous :

Partner	Name	First name	Current position	Role & responsibilities in the project	Involvement (P.M)
CRPG (Nancy, UMR 7358)	VILLENEUVE	Johan	IR2 CNRS	Project coordination (all tasks)	40
CRPG	MARROCCHI	Yves	CR1 CNRS	Cosmochemistry (Task 2, 3, 4, 5)	18
CRPG	X	X	PhD student	Characterization and dating of earliest solids (Tasks 2 and 4)	36
CRPG	CARTIER	Camille	Lecturer	Experimental petrology, thermodynamical modelling (Task 2, 3, 5)	30
IMPMC-MNHN	JACQUET	Emmanuel	Lecturer	Cosmochemistry, astrophysical modelling (Tasks 2, 5)	18
CRPG	X	X	Master student	Trace elements diffusion experiments (Task 3)	5
GeoRessources	PIGNATELLI	Isabella	Lecturer	Mineralogy, petrology (Tasks 2, 3)	12
CRPG	TISSANDIER	Laurent	IE CNRS	Experimental petrology (Task 3)	Expert

2018: responsable du projet Jeunes Chercheurs financé par le pôle scientifique OTELo « Les interactions rayonnements-minéraux : caractérisation des conséquences structurales sur les minéraux et implications géologique et industrielle ».

2018 : responsable du projet DOE NSUF RTE (Nuclear Science User Facilities Rapid turnaround experiment). Titre du projet : « Investigation of the effects of ion implantation on mineral analogues of concrete aggregates" qui nous a permis d'utiliser les instruments analytiques de l'ORNL quand je suis allée en novembre 2018 pour une collaboration avec Thomas M. Roseel et Elena Tajuelo Rodriguez.

2014-2016 : responsable des expériences d'interférométrie verticale à balayage au laboratoire LC^2 de l'UCLA (USA).

5. Action de valorisation et transfert

- J'ai participé en qualité d'intervenant **à l'école thématique** "Ecole de microscopie électronique" organisée par J. Cauzid pour les doctorants et le personnel du pôle scientifique OTELO (à l'Université de Lorraine, du 3 au 7 février 2020). J'ai fait le cours sur la microscopie électronique expliquant le fonctionnement du microscope électronique ainsi que le type d'analyse et la préparation d'échantillons les plus adaptées aux recherches des participants.

- J'ai participé à **l'école thématique** "Analyse Structurale par diffraction des rayons X sur monocristal et applications" organisée en juillet 2019 par le laboratoire CRM2 à Pont à Mousson. Pendant la première journée, j'ai expliqué la théorie de la symétrie cristallographique (groupe ponctuels, réseaux de Bravais, mailles, symboles d'Hermann-Mauguin, etc.) avec des TP sur les groupes d'espace.

- J'ai participé en qualité de **tutor à l'école thématique** "Summer School on mathematical Crystallography" qui a eu lieu en juin 2019 à l'Université de Lorraine.

- J'ai fait de la vulgarisation scientifique pour expliquer mes résultats de recherche au grand publique, à :

- l'Association Français de Gemmologie (AFG), où j'ai animé un après-midi sur la formation de la texture trapiche dans les minéraux, texture issue d'interaction fluide-roche ;

- l'association Terrae Genesis, où j'ai tenu une conférence sur l'histoire et les applications de la cristallographie dans les géosciences ;

- la BU de l'Université de Lorraine, j'ai participé au projet « la fabrique des chercheurs » qui visait à mettre en contact le publique avec les chercheurs en science.

- l'école primaire de ma ville natale, où j'ai expliqué le métier de géologique aux enfants.

- J'étais aussi membre du jury d'évaluation du concours de croissance cristalline pour les élèves lorrains de l'école primaire jusqu'au collège, organisé par le laboratoire CRM2 en 2018 et 2019, qui a comme but de rapprocher les élèves aux principes de croissance cristalline et des méthodes de synthèse.

6. Collaborations internationales

2013: j'ai été accueillie dans le laboratoire de microscopie électronique à transmission dirigé par le Dr. Kolb à l'Institut für Physikalische Chemie (Johannes Gutenberg Universität, Mainz – Germany). J'ai collaboré sur un travail d'acquisition de données de diffraction électronique par ADT/PET (Automated Diffraction Tomography/Precession Electron Diffraction) pour caractériser la cronstedtite et la chukanovite (Pignatelli et al., 2013 ; Pignatelli et al., 2014).

2014 - 2016 : j'ai collaboré avec l'hôpital de l'UCLA, avec le Department of Bioengineering et la School of Dentistry pour une étude sur la dissolution/précipitation de l'hydroxyapatite des dents dans le cadre de traitements médicaux, tels que l'application des médicaments pour protéger les dents de l'attaque acide ou de gels blanchissants pour les soins esthétiques (Pignatelli et al., 2016 ; Hsiao et al., under review).

2013 – jusqu'au présent : je collabore avec le Dr. Jiří Hybler de l'université de Prague (Institute of Physics, Academy of Science of the Czech Republic) pour étudier les structures modulaires des phyllosilicates T-O, en particulier de la cronstedtite, afin de décrire leurs structures selon les principes de la théorie mathématique « Order-Disorder » (OD) (Pignatelli et al., 2013 ; Hybler et al., 2018).

2014 – jusqu'au présent : je collabore avec l'Oak Ridge National Laboratory (ORNL), en particulier avec les Drs. Thomas M. Rosseel et Yan Le Pape, sur des problématiques concernant l'irradiation des minéraux dans les bétons des centrales nucléaires (Pignatelli et al., 2016, 2016). J'ai eu aussi la possibilité de visiter le réacteur et j'essaye de me rendre une fois par an aux USA pour continuer cette collaboration. On a soumis ensemble la demandes de financement US DOE NSUF RTE (Nuclear Science User Facilities Rapid turnaround experiment).

2013 – jusqu'au présent : je collabore avec le Dr. Enrico Mugnaioli qui travaille à l'Istituto Italiano di Tecnologia (IIT) de Pise pour les analyses de diffraction électronique 3D grâce à un microscope électronique équipé d'un tomographe pour la précession (Automated Diffraction Tomography / Precession Electron Diffraction - ADT/PED) (Pignatelli et al., 2013, 2014, 2017, 2018, 2020). Cette année, une demande de financement ANR JCJC ont été soumise.

7. Bilan scientifique

Je suis géologue spécialisée en cristallographie et minéralogie. Pour réassumer ma démarche scientifique, je tiens à citer le commentaire du président de mon jury de thèse et rapporteur, le Prof. Denis Gratias: « les travaux de recherche se situent donc à la frontière entre ces trois sciences qui sont naturellement liées mais apparaissent aujourd'hui éloignées car la connexion entre elles a été malheureusement perdue au fil du temps ». Cette citation bien résume ma vie quotidienne de chercheuse et mon constant intérêt pour les minéraux et la symétrie qui me passionnent depuis le tendre âge, quand mon père m'avait offert le livre «M.C. Echer kaleidocycles » à une époque où je connaissais déjà les gemmes les plus connues.

Mes travaux de recherche sont basés sur une approche qui permet de relier les caractéristiques cristallochimiques/cristallographiques et les propriétés physiques des minéraux à leurs conditions de formation et/ou altération. Il s'agit d'une approche multi-échelle qui s'appuie sur la maîtrise des techniques analytiques de pointe et que j'ai utilisées pour étudier les minéraux extraterrestres et terrestres dans des contextes variés qui vont de la cosmologie à la biominéralogie.

Je vais détailler ces approches à travers la description des travaux effectués lors de ma thèse et de mes différents contrats postdoctoraux.

7.1 Les polytypes à longue période de micas

Ma thèse porte sur l'utilisation de la cristallographie mathématique et expérimentale pour comprendre le polytypisme dans les micas, dont j'ai étudié des polytypes à longue période (Fig. 1). Il s'agit de cristaux avec une séquence d'empilement variant de quelques dizaines à quelques centaines d'Angströms (justifiant l'utilisation de l'adjectif « long »). Le polytypisme dans les micas a été remarqué depuis longtemps par Pauling (1934) et confirmé par les premières études de diffraction de rayons X, mais le mécanisme et les conditions de formation des polytypes à longue période sont peu compris même si plusieurs modèles ont été proposés (Baronnet, 1975 ; Pandeley et al., 1982 ; Nespolo, 2001).

La maîtrise de la théorie géométrique appelée « Order-Disorder » (OD) m'a permis de résoudre les structures de 2 polytypes à longue période et obtenir les premiers affinements structuraux fiables pour ces polytypes (Pignatelli et al., 2011 ; Pignatelli et Nespolo, 2011), formés respectivement par 4 et 5 feuillets.

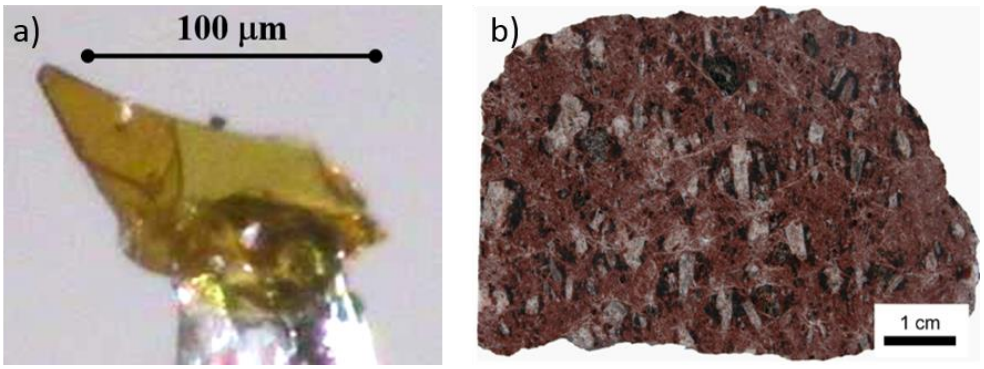

Figure 1. (a) Cristal d'un polytype à longue période de mica préparé pour l'étude de diffraction X sur monocristal ; (b) Rhyodacite dans laquelle les cristaux de micas ont été prelevès.

Pour le polytype à 4 feuillets $4M_3$, les paramètres de maille sont : a = 5.3166 (2) Å, b = 9.2080(2) Å, c = 39.814(1) Å, β = 92.550(3)°. Le groupe d'espace obtenu par la séquence d'empilement est *C*2/*c*. En sachant que la symétrie du polytype peut être plus basse que celle obtenue de la séquence d'empilement, l'affinement a été effectué aussi dans tous les sous-groupes possibles de *C*2/*c* (*Cc*, *C*2, $C\bar{1}$ et *C*1) afin de trouver la vraie symétrie de la structure (bien que l'analyse de la carte de densité électronique effectuée avec le logiciel Superflip, implémenté dans Jana2006, nous ait indiqué que la symétrie du polytype est *C*2/*c*). Selon la définition de Guinier et al., (1984) un polytype doit être formé par de feuillets du même type avec seulement une petite différence dans la distribution des cations. Pour cette raison, au début on a testé *Cc* et *C*1 : dans ces sous-groupes les atomes sont tous en position générale, ainsi les feuillets M sont du même type, au contraire de *C*2/*c*. Puis on a aussi testé *C*2 et $C\bar{1}$: dans ce cas les atomes occupent des positions de Wyckoff différentes et les feuillets ne sont pas du même type, comme en *C*2/*c*. Les résultats des affinements ne montrent aucune amélioration; au contraire de corrélations apparaissent. Le nombre des corrélations augmente avec la réduction de la symétrie ; ainsi, en *C*1 on observe le nombre maximal, qui s'annule en *C*2/*c*. Cela confirme que le groupe d'espace du polytype est bien *C*2/*c*.

Les résultats de l'affinement effectué en *C*2/*c* montrent que dans le polytype $4M_3$ le miroir translatoire *c* relie le premier feuillet au troisième et le deuxième au quatrième feuillet. Le polytype, ainsi, présente seulement deux feuillets M indépendants, qui ont des symétries différentes. Dans le premier feuillet le site *trans* est en position spéciale sur un centre d'inversion (position de Wyckoff 4*c*, symétrie du site $\bar{1}$) ; le site *cis M*2 (appelé *M*2a dans l'affinement) est équivalent à *M*3 et se trouve en position générale (position de Wyckoff 8*f*).

Les tétraèdres sont aussi en position générale 8*f*. Le premier feuillet est meso-octaédrique (*M*2

= *M*3) et sa symétrie est *C*12/*m*(1) ; en effet, la symétrie du feuillet inclut deux opérations locales[1] ρ (l'inversion et la rotation autour de $2_{[010]}$) et deux opérations locales τ (l'identité et la réflexion par le miroir $m_{(010)}$, qui relie les deux sites *cis M*2 et *M*3). Dans le deuxième feuillet les sites tétraédriques sont encore en position générale, mais les sites octaédriques sont tous indépendants et en position particulière sur l'axe 2 (position de Wyckoff 4*e*). La symétrie du feuillet se réduit à *C*12(1), car le miroir $m_{(010)}$ est perdu et, par conséquent, *M*2b n'est plus équivalent à *M*3b. En considérant que *M*1b ≠ *M*2b ≠ *M*3b, le feuillet pourrait être hétéro-octaédrique. Cependant, les pics de la carte de densité électronique correspondants aux sites *M*2b et *M*3b diffèrent pour moins d'un électron. Le feuillet peut être considéré à la limite entre les définitions de méso et hétéro-octaédrique, car les deux sites *cis* sont équivalents même si la symétrie du feuillet ne l'impose pas. L'équivalence est confirmée aussi par le fait que les longueurs de liaison des deux octaèdres *M*2b et *M*3b sont similaires.

En conclusion, les deux feuillets M sont méso-octaédriques et de type M1, parce que l'origine de la couche octaédrique est dans le site *trans* M1 dans les deux cas.

Pour expliquer la formation de ce polytype on peut utiliser le modèle « Faulted Matrix Model » de Pandey et al. (1982), car sa séquence d'empilement est relativement simple. Deux interprétations, qui prennent en considération la combinaison des deux sous-structures de base, sont possibles (Fig. 2). La première interprétation prend en considération le fait que la séquence peut résulter de la perturbation de la spirale de croissance d'une structure de base 3*T* par la formation d'un défaut d'empilement : la présence du défaut dans le pas de la spirale formée par 3 feuillets produit une nouvelle séquence constituée par 4 feuillets. Le polytype à 4 feuillets peut être, ainsi, considéré comme formé par la combinaison de deux sous-structures, 3*T* et 1*M*. Dans la deuxième interprétation, la séquence d'empilement est considérée comme formée par l'inter-croissance de deux sous-structures $2M_1$. Cela implique que le polytype peut être considéré comme un exemple de « *cell twin* ». Le concept de « cell twin » a été introduit par Ito (1950) pour indiquer des structures modulaires dans lesquelles les modules sont reliés par des opérations définies d'un groupoïde. Ce concept est similaire à celui de macle, où à la place des modules il y a les individus ; la différence fondamentale consiste dans le fait que les individus de la macle forment un édifice hétérogène, en revanche les modules du « cell twin » forment un édifice homogène (Nespolo et al., 2004).

[1] Dans les structures OD les feuillets géométriquement équivalents sont reliés par l'application de deux type d'opérations de symétrie: les opérations τ, qui ne changent pas le signe de la coordonnée dans la direction d'empilement, et les opérations ρ, qui au contraire changent le signe en renversant le feuillet. Le produit de deux opérations ρ équivaut à une opération τ. Les opérations τ et ρ peuvent être *locales* ou *globales* selon qu'elles opèrent seulement dans un sous-espace du cristal ou dans tout l'espace.

Il est important de remarquer que dans les deux interprétations la séquence d'empilement du polytype 4M_3 peut être décomposée en deux structures de base. Cela explique pourquoi dans ce polytype le deuxième et quatrième feuillet sont méso-octaédriques, (comme le premier et troisième feuillet) même si la symétrie du groupe d'espace n'impose pas aux sites *cis* d'être équivalents. Dans les structures de base, en fait, les feuillets sont tous du même type et cette caractéristique est préservée pendant la croissance par spirale par un effet de « mémoire » d'empilement.

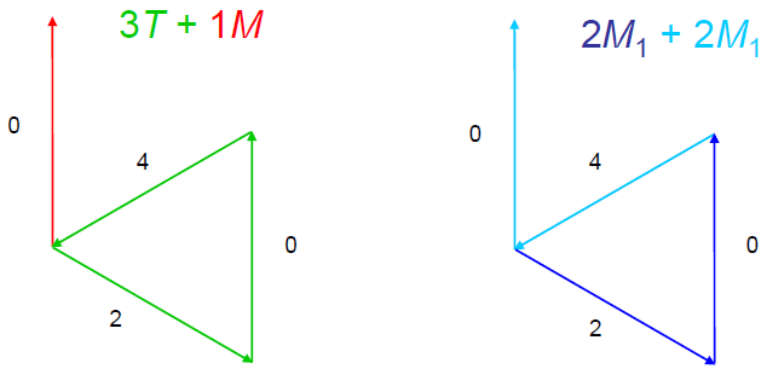

Figure 2. Le polytype à 4 feuillets peut être interprété comme formé par deux sous-structures 3*T* et 1*M* ou par deux sous-structures 2M_1.

Pour le polytype 5M_3, les paramètres de maille sont : a = 5.3146 (2) Å, b = 9.2063(3) Å, c = 49.730(2) Å, β = 92.031(4)°. Les résultats de l'affinement effectué en *C*2 montrent que tous les feuillets indépendants sont méso-octaédriques (le troisième feuillet est équivalent au quatrième et le deuxième au cinquième). Dans le premier feuillet les sites *M* sont en position particulière sur l'axe 2 (position de Wyckoff 2*a*), alors que dans les autres feuillets les sites *M* sont en position générale 4*c*, comme d'ailleurs les sites tétraédriques. Les trois feuillets sont de type différent : les deux premiers sont de type M2 et le troisième de type M1, car pour ce dernier l'origine de la couche octaédrique est dans le site *trans* et pour les autres dans un site *cis*.

Les résultats de l'affinement de ce polytype ont permis de prouver pour la première fois la coexistence des feuillets M1 et M2 dans un polytype des micas. Ce polytype est formé par deux feuillets de type M1 (le troisième et le quatrième) et les autres de type M2 (Pignatelli et Nespolo, 2011). On peut supposer que ces derniers se sont formés suite aux transformations des feuillets M1 en feuillets M2, à cause des ajustements structuraux comme décrit dans le modèle « perturbative theory » (Nespolo, 2001). Plusieurs combinaisons de deux sous-structures de

base sont possible pour expliquer la séquence d'empilement de ce polytype : 3*T*+1*M*, 3*T*+2M_1, 1*M*+2M_1 ou deux 1*M* tournés de 120°.

Les résultats de ma thèse ont permis de :

(i) prouver expérimentalement la coexistence des feuillets de type M1 et M2 dans les micas. Auparavant, on savait que la plupart des micas sont formées par des feuillets de type M1 mais aucun échantillon contenant les deux types de feuillets n'était connu (Zvyagin et al., 1985 ; Bloch et al., 1990 ; Zhukhlistov et Zvyagin, 1991 ; Zhukhlistov et al., 1996, Guggenheim et Bailey, 1977 ; Brown, 1978 ; Guggenheim, 1981, Mizota et al., 1986 ; Rieder et al., 1996 ; Brigatti et al., 2000).

Les données obtenues ont montré qu'il existe une relation entre la formation des polytypes et la distribution des cations dans les feuillets comme prédit par le modèle « perturbative theory » (Nespolo, 2001).

(ii) obtenir les premiers affinements des polytypes à longue période de micas, qui restent les seuls connus dans la littérature encore aujourd'hui, probablement à cause de la complexité structurale et des difficultés expérimentales à affronter.

Ma thèse a aussi montré que les polytypes des micas n'ont pas seulement un intérêt minéralogique ou cristallographique, mais jouent aussi un rôle fondamental pour la compréhension des phénomènes pétrogénétiques qui sont à la base de la formation des roches. En fait, pour mieux comprendre la formation des polytypes étudiés, l'histoire pré et post éruptive de la roche (rhyodacite de Ruiz Peak) qui les contient a été reconstruite sur la base de l'étude des textures de déséquilibre de plusieurs minéraux. C'est très probablement un phénomène d'auto-convection dans la chambre magmatique favorisant les interactions du type spirale-spirale, spirale-cristal et cristal-cristal qui est à l'origine de la formation des polytypes analysés (Pignatelli et al., 2016). Le développement de cellules convectives augmente le nombre des spirales actives et, par conséquent, la possibilité d'interaction spirale-spirale. Les cellules convectives sont également responsables d'une plus grande mobilité des cristallites durant leur croissance. Cela favorise les interactions de type spirale-cristal et/ou cristal-cristal. En conclusion, ma thèse relie une étude cristallographique/cristallochimique à l'échelle atomique à une étude pétrographique à plus grande échelle, celle de la chambre magmatique.

7.2 Évolution du système Fer-Argilite dans le cadre du stockage des déchets radioactifs

Pendant cette étude financée par l'ANDRA, j'ai étudié le comportement des barrières argileuses après introduction des containers de déchets nucléaires dans les sites de stockage profond. Les travaux de recherche effectués portent plus précisément sur les perturbations aux interfaces container-argilite. Des études expérimentales du système fer-argilite ont été réalisées pour : (1) simuler le gradient de température dans l'espace entre 90° et 40 °C (éloignement du colis de déchets) et dans le temps (décroissance radioactive) ; (2) tester les rôles de paramètres tels que la température ou la surface spécifique du fer sur la nature des phases minérales de l'argilite du Callovo-Oxfordien du bassin de Paris et (3) connaître les modifications chimiques que subira le fluide interstitiel naturel lors des différentes phases de la vie du stockage. L'objectif majeur était de comprendre l'évolution chimique globale de la zone perturbée autour des colis de déchets (mécanismes, cinétiques, nature des phases altérées et néoformées) et les effets de la corrosion du fer. Pour atteindre cet objectif, j'ai eu la possibilité d'effectuer des expériences de synthèse hydrothermale en utilisant différents types d'autoclaves et de suivre une formation pour utiliser le logiciel de calculs géochimiques Phreeqc pour mieux comprendre les réactions géochimiques complexes du système de stockage. J'ai aussi utilisé plusieurs techniques analytiques pour caractériser les produits expérimentaux (e.g. diffraction sur poudre, microscopie électronique à transmission (MET) et à balayage (MEB), spectroscopie infrarouge (IR)).

La baisse de température (de 90° à 40°C) a montré que l'argilite, déjà réactive à 90°C, continue de réagir à plus basse température. En fait, on observe une disparition progressive des phases silicatées de type illite, smectite et interstratifiés I/S et du quartz. Cela entraîne une disponibilité de silicium en solution qui permet la néoformation des phyllosilicates ferrifères de type T-O, en particulier la cronstedtite (Fig. 3) jamais vue auparavant dans les expériences similaires avec du fer en poudre (Pignatelli et al., 2013, 2014).

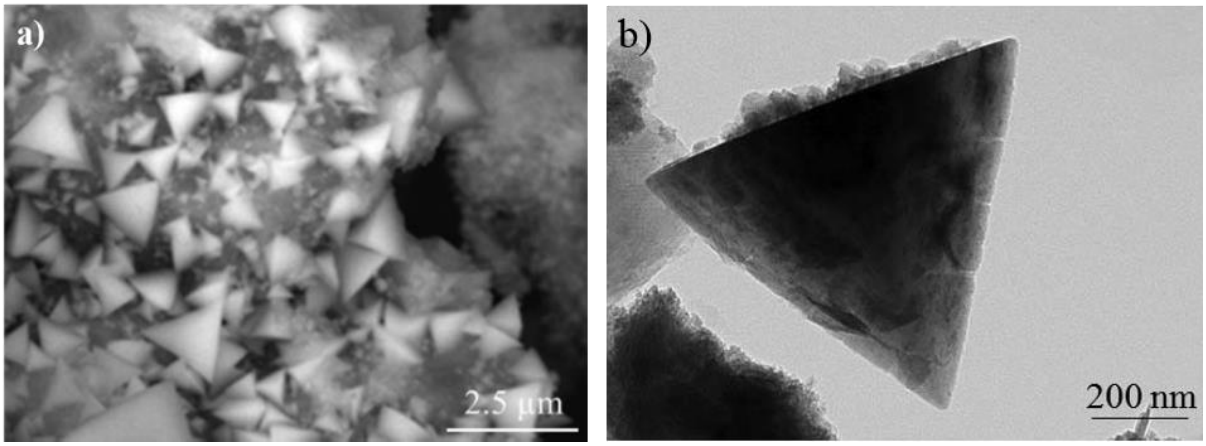

Figure 3. Images MEB (a) et MET (b) d'un cristal pyramidal de cronstedtite synthétisé dans les expériences d'interaction fer-argilite (Pignatelli et al., 2013).

L'évolution des phyllosilicates a été mieux comprise grâce à la décomposition des pics principaux à 10 et 7 Å sur les diffractogrammes X sur poudre comme montré dans la Fig. 4. La dissolution des minéraux de l'argilite libère aussi du magnésium en solution, de façon croissante avec la baisse de température, mais ceci n'est apparemment pas repris dans la cristallisation de nouvelles phases minérales.

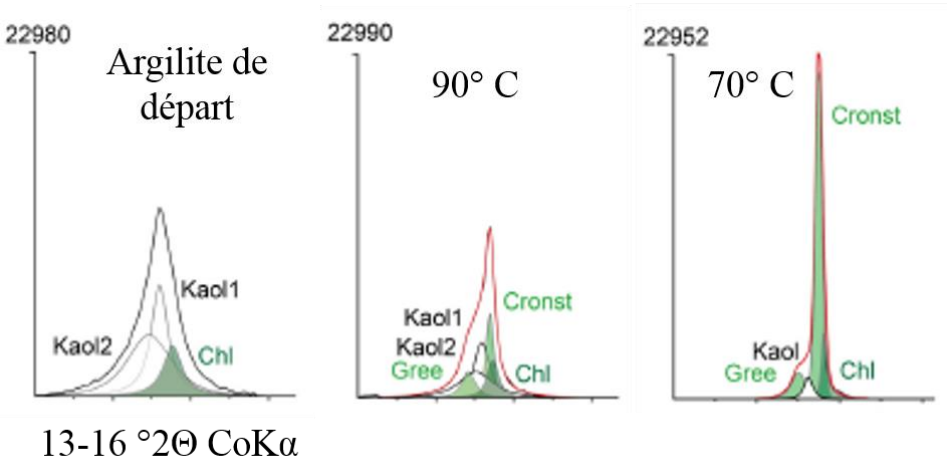

Figure 4. Décomposition du pic à 7Å sur les diffractogrammes des produits expérimentaux dans l'expérience simulant le refroidissement. A 90°C on distingue les pics de la cronstedtite et de la greenalite ; à 70°C le pic de la cronstedtite devient plus fin et intense témoignant d'une présence plus importante de cette phase et aussi d'une augmentation de son degré de cristallinité.

Le baisse de température a un effet sur le polytypisme des cronstedtites néoformées : le polytype le plus abondant est 1*M*. Il se forme entre 90° et 60° C, mais aux températures les plus élevées il est mélangé au polytype 1*T* (« mixed crystals 1*M*+1*T*). Entre 90°C et 80°C on trouve aussi le polytype 3*A* et dans l'intervalle 70°-60° C le polytype $2M_1$ (Hybler et al., 2018).

Parmi les minéraux secondaires à l'interaction fer-argilite, la chukanovite - un carbonate de fer hydraté - a été observée mais seulement au contact du fer (Fig. 5). Elle a été décrite pour la première fois par Pekov et al. (2007) comme minéral d'origine météoritique mais elle est également un produit de la corrosion du fer souvent observé sur les objets archéologiques, où elle forme des couches très fines seulement décelables avec des techniques de microanalyse (Schlegel et al., 2010, 2012). Dans notre étude, une acquisition de données de diffraction électronique par ADT/PED (Automated Diffraction Tomography/Precession Electron Diffraction) a été réalisée grâce à une collaboration avec le Dr. Mugnaioli pour étudier la structure de cette phase néoformée (Pignatelli et al., 2014).

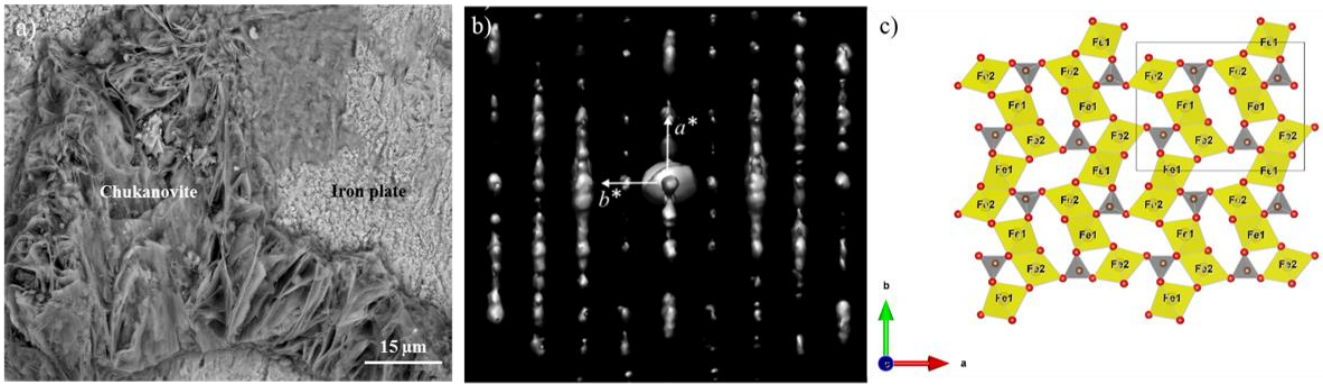

Figure 5. (a) Image MEB de la chukanovite formée sur une plaque de fer ; (b) Données obtenues par ADT/PED d'un cristal de chukanovite - projection le long de l'axe *c**; (c) structure de la chukanovite obtenue à partir des données ADT/PED.

Les études sur impact de la surface spécifique du fer (le fer était sous forme de poudre, grains ou cyclindres) sur la réactivité du système fer-argilite ont montré que la réactivité est toujours plus important lorsque la surface spécifique est plus élevée. Les transformations minéralogiques de l'argilite sont identiques mais la cinétique change : les réactions sont plus lentes en présence de grains de fer que de poudre. A part la dissolution partielle de l'illite des interstratifiés I/S et du quartz, les autres minéraux semblent rester en quantités stables et comparables à celle de l'argilite de départ. Dans les produits de réaction, il n'y a pas de magnétite, mais on forme des smectites sodico-calciques enrichies sous forme de « flocons », ainsi que des phases intermédiaires entre I/S et Fe-serpentines (Bourdelle et al., 2014).

Enfin, une étude a été réalisée pour mettre en évidence l'effet d'une disponibilité rapide du fer en solution. Ceci a été réalisé en replaçant la poudre de fer par du sel de Mohr (publication en préparation). L'utilisation du sel de Mohr conduit à des produits expérimentaux très différents de ceux observés dans les précédentes expériences fer-argilite. De changements minéralogiques

profonds sont observés avec la formation de gypse et d'alunite liés à la présence d'une grande quantité de sulfates en solution apportés par le sel de Mohr. La cristallisation d'alunite est possible grâce à la présence d'une teneur élevée de potassium mis en solution lors de la dissolution importante des I/S. Les I/S encore présents dans le produit de réaction sont également appauvris en potassium. Le milieu réactionnel étant très acide (pH < 4), les carbonates sont complètement dissous et le quartz présente des signes d'altération. Parmi les nouvelles phases minérales, la goethite apparaît en assez grande quantité. Des argiles à 7 Å de type Fe-serpentine n'ont pas été observées.

En conlusion, les études sur les interactions fer-argilite ont permit de prévoir les évolutions du système fer-argilite pour réduire les risques environnementaux. Dans le conteste du stockage, il faut s'assurer que les modifications minéralogiques (structurales et chimiques) ne compromettent pas les propriétés du système de stockage et que le confinement des déchets est assuré. À ce propos, on a mis en évidence que la néoformation de phyllosilicates de type T-O aux dépens de tous phyllosilicates de type T-O-T au cours de l'interaction du système argilite-fer avec un fluide naturel interstitiel semble être problématique pour le stockage. En fait, les phyllosilicates T-O réduisent la capacité d'échange cationique et le degré de gonflement des barrières argileuses et peuvent obstruer les pores de l'argilite au contact des containers en modifiant les propretés mécaniques des barrières (Bildstein et al., 2006).

7.3 La formation de minéraux secondaires par altération aqueuse dans les météorites

Je me suis intéressée à l'étude des interactions fluide-roche dans le cadre d'échantillons extraterrestres, c.à.d. des météorites de type CM, parce qu'on retrouve les serpentines ferrifères qui se sont formées à partir de silicates anhydres qui ne contiennent pas de fer dans leurs structures. Le but était de reconstruire les conditions physico-chimiques pendant les interactions fluide-roche grâce aux caractéristiques des minéraux secondaires. Une première étude a été effectuée sur Paris, qui est considérée l'une des météorites les moins altérées par les fluides (Leroux et al., 2014 ; Hewins et al., 2014). Cette météorite est caractérisée par la présence de portions non altérées et bien préservées et par des portions altérées qui contiennent des assemblages minéralogiques complexes appelés 'PCPs' (Poorly Characterised Phases) ou plus communément 'tochilinite/cronstedtite intergrowths' (TCIs). Des observations MEB montrent que les TCIs présentent souvent une morphologie héritée des minéraux anhydres préexistants, qui peuvent être identifiés par l'analyse des angles entre les faces morphologiques des TCIs. L'étude morphologique a ensuite été mise en relation avec la composition chimique des TCIs (EMPA, MEB), qui s'avère n'être pas homogène. En fait, les cartographies EDX (Fig. 6) ont mis en évidence un zonage caractérisé par une partie externe plus riche en S et Fe, une partie intermédiaire contenant Fe, S et Si, et une partie interne où seulement le fer a été détecté. Ce zonage est vraisemblablement lié à la formation des minéraux secondaires (tochilinite, cronstedtite et goethite), donc il indique que les conditions d'altération ont changé dans le temps.

L'approche minéralogique et cristallographique a permis de : (1) identifier les minéraux primaires et secondaires ; (2) montrer que les minéraux secondaires remplacent ceux primaires par pseudomorphose; (3) proposer trois étapes d'interaction fluide-roche qui se distinguent par la présence de fluides avec différentes compositions (Pignatelli et al., 2016).

La première étape est caractérisée par un fluide riche en soufre, comme montré par la formation de la tochilinite. La source du soufre ne peut pas être identifiée par cette étude, mais plusieurs hypothèses ont été prises en considération (par exemple gaz riches en soufre présents dans la nébuleuse solaire ou altération de la troilite). La seconde étape prévoit un fluide enrichi en silicium, nécessaire pour la formation de la cronstedtite et libéré par la dissolution des silicates précurseurs pendant la pseudomorphose ou par la mésostase vitreuse de chondres. Enfin, dans la troisième étape le fluide est appauvri en Si et S, mais enrichi en Fe, permettant la précipitation d'un hydroxyde de fer.

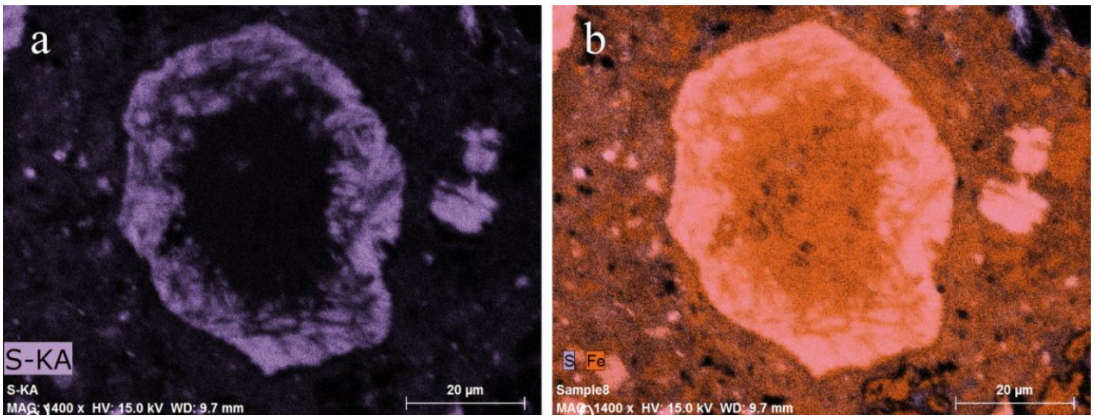

Figure 6. Cartographies EDX qui montrent le zonage minéralogique/chimique des TCIs dans la météorite Paris (Pignatelli et al., 2016).

Ensuite, les minéraux secondaires ont été étudiés par microscopie électronique à transmission et le rapport $Fe^{3+}/\Sigma Fe$ a été mesuré par STXM-XANES au synchrotron suisse (PSI). Les résultats ont montré que le rapport $Fe^{3+}/\Sigma Fe$ dans les serpentines des météorites de type CM peut être considéré un témoin du dégrée d'interaction fluide-roche (Pignatelli et al., 2017). Ce rapport a été aussi utilisé pour quantifier la production de H_2 dans la serpentinisation comme montré dans la réaction suivante :

$$5/2Mg_2SiO_4\ [Forsterite] + Fe^{2+} + Fe^{3+} + 2H_2O$$
$$\rightarrow (Fe^{2+}{}_2Fe^{3+})(SiFe^{3+})O_5(OH)_4\ [Cronstedtite] + 5Mg^{2+} + 3/2SiO_{2(aq)} + H_2$$

La production de H_2 contribue à reconstituer l'évolution des conditions redox au fil du temps: H_2 peut soit être perdu par le système, générant des conditions plus oxydantes (Le Guillou et al, 2015), soit être conservé et réagir localement avec le carbone et jouer un rôle dans la synthèse de composés aliphatiques (Guo et Eiler, 2007; Elmaleh et al, 2015; DeSanctis et al, 2017). Pour le météorite Paris on pense que la première hypothèse est la plus probable, car les derniers minéraux secondaires qui se forment sont des hydroxydes de Fe^{3+}, ce qui requiert des conditions de plus en plus oxydantes au cours des interactions fluide-roche.

7.4 Les minéraux d'intérêt gemmologique

Mon intérêt pour les gemmes a commencé pendant mes études de licence et master en Italie où je me suis intéressée à l'étude des défauts structuraux par topographie X d'un cristal de topaze (Fig. 7) et d'un cristal de quartz naturel à partir desquels des gemmes ont été découpées. Les objectifs de ces études étaient : identifier les défauts présents (dislocations, macles, bandes de croissance, etc.) et établir si on pouvait reconnaître des « growth marks », c'est-à-dire des défauts typiques d'un environnement ou d'un milieu de croissance (Graziani et al., 1990), ou des défauts post-croissance dus à d'éventuels traitements.

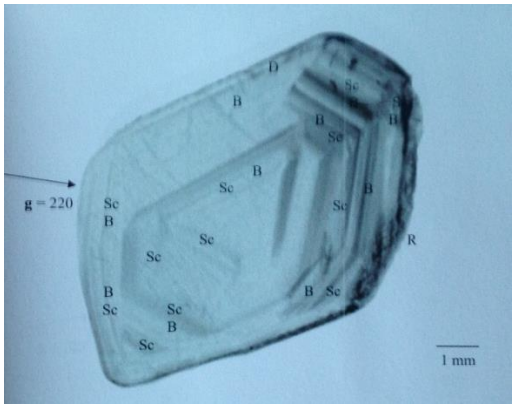

Figure 7. Topographie X d'un cristal de topaze, qui montre la présence de dislocations (D), secteurs de croissance (Sc), bande de croissance (B) et le bord externe du cristal (R).

Puis, à Nancy, j'ai collaboré avec le Prof. Giuliani pour étudier plusieurs minéraux (l'émeraude, l'euclase, la zoisite, le rubis et le demantoïde) afin de combiner les données minéralogiques et cristallographiques avec celles géologiques acquises sur le terrain précédemment (Cheillez et al., 1994 ; Branquet et al., 1999 ; Garnier et al., 2008).

Plusieurs publications portent sur la formation d'une texture particulière, dite "trapiche". A l'origine, le mot "trapiche" fut utilisé en Colombie pour décrire des échantillons d'émeraude dont la texture ressemblait au système de roues dentées entraînant une meule qui écrase la canne à sucre en vue de sa distillation (McKague, 1964). Cette analogie texturale est particulièrement évidente sur des sections orientées perpendiculairement à l'axe cristallographique *c* des cristaux (Fig. 8) avec au centre un cœur hexagonal (qui correspond aux secteurs de croissance pinacoïdaux) entouré par six secteurs de croissance prismatiques. Les limites entre les secteurs équivalents ou non par symétrie sont séparés par des inclusions en forme de chevrons (« boundaries of inclusions » en anglais). Parfois une zone de surcroissance est visible à la périphérie du cristal.

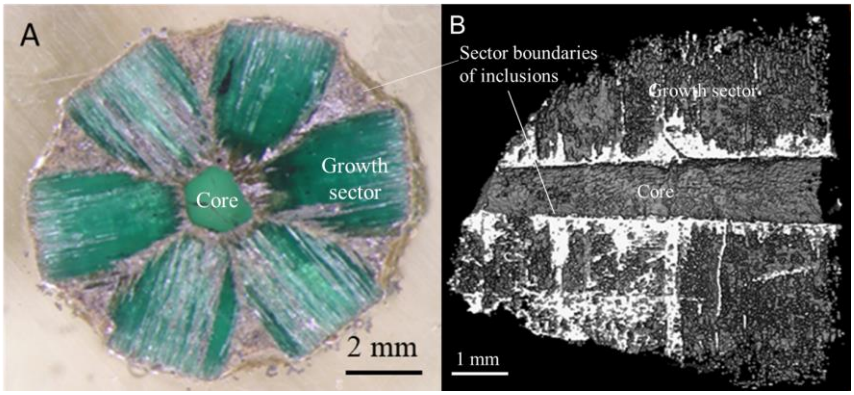

Figure 8. (a) Texture typique d'un émeraude trapiche avec le cœur, les secteurs de croissance et les inclusions qui marquent les limites entre les secteurs ; (b) image de tomographie X qui montre les différentes parties de la texture à l'intérieur de l'émeraude.

Trente ans plus tard, le terme "trapiche" a également été utilisé pour caractériser la texture du rubis de Mong Hsu au Myanmar, ex-Birmanie (*e.g.* Müllenmeister et Zang, 1995; Schmetzer et al., 1996), à cause de ses similitudes texturales avec les émeraudes colombiennes. Ces ressemblances s'expliquent par la cristallographie de l'émeraude (groupe d'espace de type $P6/mcc$) et du rubis (groupe de type d'espace $R\bar{3}c$) qui appartiennent tous les deux à la famille cristalline hexagonale. Ainsi, les deux minéraux ont le même référentiel axial ($a = b$, $\alpha = \beta =$ 90° et γ = 120°). Dans les années 2000, l'augmentation de la demande sur le marché des minéraux gemmes à texture trapiche a conduit à une généralisation systématique et erronée de l'utilisation de la nomenclature propre à la texture trapiche. Des mises au point sur la définition furent réalisées dans diverses publications (Win, 2005; Schmetzer et al., 2011) qui redéfinirent la texture par la présence de secteurs de croissance équivalents par symétrie et séparés par des inclusions solides. Ces différents auteurs introduisirent une nouvelle nomenclature "trapiche-type" ou "trapiche-like" c'est-à-dire "comme le trapiche" pour distinguer les vraies texture trapiche des non trapiche, mais qui est désormais utilisée de façon systématique pour tous les minéraux (Bergman, 2016). Contrairement à la texture trapiche, la texture des minéraux "trapiche-like" est due à la présence d'inclusions ou d'impuretés chimiques présentes dans des zones distinctes du cristal. A cette catégorie appartiennent le saphir (Koivula et al., 1994) ainsi que des cristaux d'aigue-marine trouvés en Namibie (Befi, 2012) ou des émeraudes au Brésil (DelRe, 1994). Le débat sur cette distinction et l'utilisation des deux nomenclatures est toujours en cours et loin d'être terminé (Giuliani et Pignatelli, 2016a). Cependant, de nouveaux minéraux avec une appellation trapiche-like apparaissent sur le marché, comme par exemple des cristaux de quartz trapiche qui furent exposés dans l'édition de MINERAL & GEM 2017 à Sainte-

Marie-aux-Mines (Chabrol et Michelou, 2017). Cela prouve que l'intérêt pour les minéraux trapiche n'a pas diminué au fil du temps mais que bien au contraire il s'est amplifié.

Les donnes publiées en 2015 ont montré que l'acquisition de la texture trapiche de l'émeraude colombienne est reliée évidemment à la genèse du gisement. Les conditions géologiques sont le fruit de circulations fluides, d'interactions fluide-roches complexes et de la variation des paramètres physico-chimiques (pression, température, composition des fluides). Dans le cas de l'émeraude trapiche colombienne, la genèse est assez bien contrôlée par la tectonique compressive responsable de la formation des gisements situés dans la ceinture à émeraude occidentale du bassin sédimentaire de la Cordillère. Une déformation marquée par la circulation de fluides dans les plans de failles et de chevauchements. Les phénomènes de surpressions fluides ont engendré des variations de pression responsables de la sursaturation des fluides et d'une augmentation de la force motrice conduisant à une croissance dendritique. Cette complexe histoire de croissance a été réassumée en trois étapes de formation de la texture trapiche (Pignatelli et al., 2015).

Au contrôle géologique sur la genèse des émeraudes, il faut ajouter le contrôle cristallographique pour l'acquisition de la texture trapiche. La symétrie cristalline, qui établit le nombre des secteurs de croissance équivalents et les directions de piégeage des inclusions, joue un rôle qui ne peut être négligé. En effet, la texture trapiche a été observée seulement dans des minéraux à symétrie élevée (cubique, hexagonal, trigonal), e.g. le grenat, le béryl et la tourmaline, avec la seule exception de la chiastolite qui est orthorhombique mais pseudotétragonale ($a \approx b$). Jusqu'à présent on ne connaît pas de minéraux à faible symétrie qui présenteraient une texture trapiche. En fait, si la symétrie diminue on réduit le nombre des secteurs de croissance équivalents par symétrie, en perdant la ressemblance caractéristique avec le système de roues dentées à laquelle la texture trapiche doit son nom.

L'absence de la texture trapiche dans les minéraux à faible symétrie est confirmée par l'étude de l'euclase colombien, minéral monoclinique, qui est vendu sur le marché comme étant un minéral à texture trapiche. L'utilisation de plusieurs techniques expérimentales, et notamment de la tomographie X, a permis de comprendre qu'il ne s'agit pas d'une texture trapiche mais simplement d'une incorporation de phases minéralogiques syngénétiques le long des axes cristallographiques, comme on peut observer aussi dans d'autres minéraux tels que la fluorine (Pignatelli et al., 2017).

La dernière étude sur les rubis trapiche dits « fleurs » de Mong Hsu (Myanmar) montrent l'importance du développement des secteurs de croissance dans l'aspect de la texture (Fig. 9).

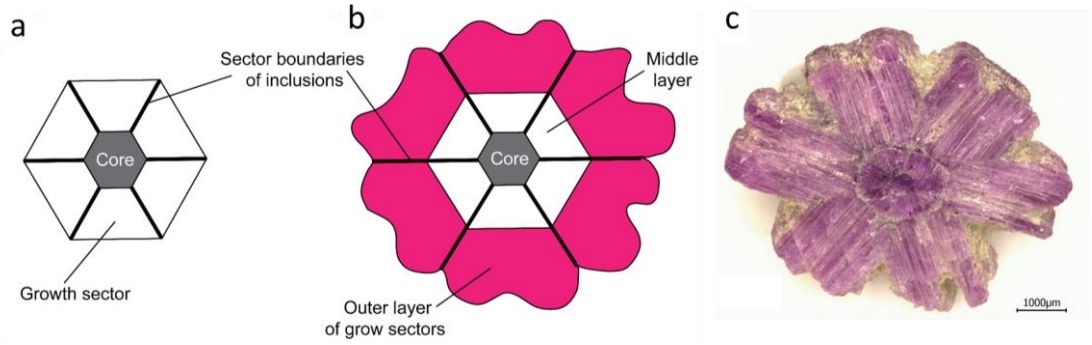

Figure 9. (a) Schéma de la texture trapiche « classique » dans un rubis. Schéma (b) et photo (c) d'un trapiche « fleur » du Myanmar, qui se différentie par la présence d'une couche de rubis interne et externe autour du cœur.

Les rubis de Mong Hsu présentent des habitus différents (Perretti et al., 1995; Smith et Surdez, 1994), délimités par des faces pinacoïdales {0001}, des faces bipyramidales hexagonales $\{hh\bar{2}h1\}$ parfois associées à de petites faces du rhomboèdre $\{10\bar{1}1\}$. Des faces du prisme de deuxième espèce $\{11\bar{2}0\}$ sont également observées sur certains rubis. Les faces bipyramidales les plus petites sont $\{22\bar{4}3\}$, alors que les faces bipyramidales les plus développées sont souvent $\{44\bar{8}1\}$ ou $\{14\ 14\ \bar{2}\bar{8}\ 3\}$, moins souvent $\{22\bar{4}1\}$ ou $\{11\bar{2}1\}$. Les indices $\{14\ 14\ \bar{2}\bar{8}\ 3\}$ sont trop élevés pour des faces morphologiques (faces F) et il est possible qu'ils consistent en une alternance de microsteps entre les faces $\{11\bar{2}0\}$ et {0001} (Sunagawa et al., 1999; Sunagawa, 1995). A chaque face est associé un secteur de croissance qui est indiqué par les mêmes indices de Miller.

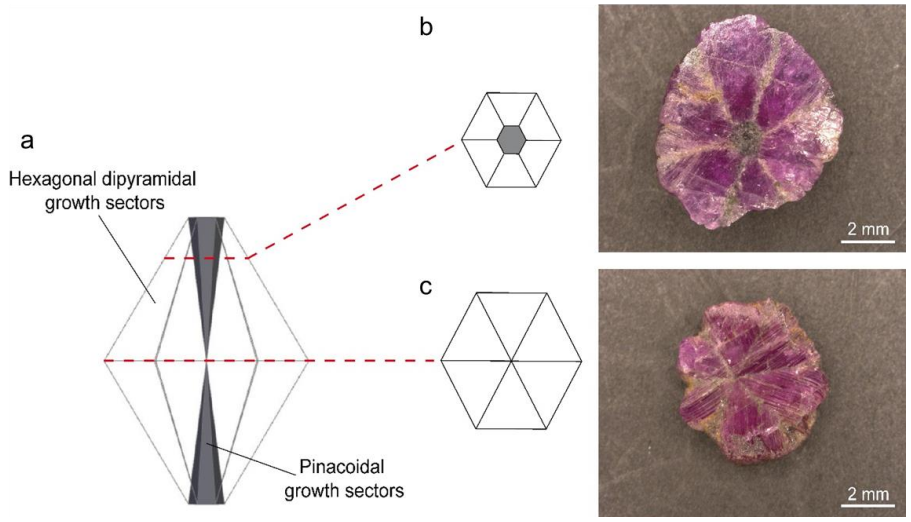

Figure 10. (a) Aspect du cœur en 3D, qui corresponds aux secteurs de croissance pinacoïdaux représentés en gris. Ces secteurs ont une forme pyramidale. La taille du cœur sur une section perpendiculaire à l'axe *c* varie en fonction de la coupe: plus grande si la section est coupée près de la base de la pyramide (b), plus petite près du sommet de la pyramide. Si la section est coupée exactement entre les deux secteurs pinacoïdaux, les bandes d'inclusions se croisent en un point central (c). Les deux sections de rubis trapiche avec et sans cœur proviennent de Mong Hsu au Myanmar.

Sur des sections perpendiculaires à l'axe *c* on observe généralement le cœur de la texture trapiche qui corresponds aux secteurs pinacoïdaux, entouré par des portions de qualité gemme qui sont les secteurs bipyramidaux (Fig. 10a, c). Si la section est coupée exactement entre les deux secteurs pinacoïdaux, alors le cœur n'est plus visible et la texture trapiche et les bandes d'inclusions se croisent au milieu de la section (Fig. 10c).

Il faut remarquer que la texture trapiche en pétrographie a été trouvée dans d'autre minéraux et appelée « textural secteur zoning » (e.g. pour l'andalousite, la staurolite et les grenats - Rice et Mitchell, 1991; Wilbur et Ague, 2006; Rice; et al., 2006). La caractéristique de ce type de zonage est la présence d'inclusions qui définissent les limites entre les secteurs de croissance adjacents (Andersen, 1984). Ce zonage textural peut être mis en évidence par au zonage chimique par secteur (chemical sector zoning, en anglais), lorsque les secteurs de croissance non équivalents par symétrie ont des compositions différentes. C'est le cas dans les rubis trapiche «fleurs » où la fluorescence X et la tomographie X ont permis d'expliquer la morphologie caractéristique de ces minéraux. La morphologie est due simplement à un effet de coupe : les rubis ont été coupes de façon à voir la projection des plusieurs secteurs de croissance sur le cabochon. On reconnaît le cœur, secteur pinacoidale, deux groupes de secteurs bipyramidaux avec inclination différente par rapport à l'axe *c*, qui forment respectivement la couche interne (c.à.d. l'hexagone qui entoure le cœur) et la couche externe (Fig. 9b, c). Ces secteurs sont probablement $\{22\bar{4}3\}$ et $\{22\bar{4}1\}$. L'existence des deux groupes de secteurs bipyramidaux a été mise en évidence par la fluorescence X (XRF), qui a montré une différence de composition marquée par la distribution du Ti et du Cr. La présence des secteurs bipyramidaux est confirmée par des mesures angulaires effectuées sur de cavités tubulaires, qui résultent de la dissolution partielle des dislocations. Étant donné que les dislocations sont perpendiculaires au front de croissance et donc aux faces qui délimitent les secteurs de croissance, si on parvient à mesurer l'angle qu'elles forment avec l'axe *c*, on peut indexer les faces et leurs secteurs (Fig. 11). Cet angle, mesuré grâce aux images de tomographie X, est très poche de celui théorique, calculé en utilisant le tenseur métrique **G*** :

$$\cos(h_1\ k_1\ l_1)\wedge(h_2\ k_2\ l_2)=\frac{\langle h_1\ k_1\ l_1|\mathbf{G}^*|h_2\ k_2\ l_2\rangle}{\sqrt{\langle h_1\ k_1\ l_1|\mathbf{G}^*|h_1\ k_1\ l_1\rangle}\sqrt{\langle h_2\ k_2\ l_2|\mathbf{G}^*|h_2\ k_2\ l_2\rangle}}$$

Pour les calculs, on a pris en compte l'angle entre la face (0001) et celles inclinées, par exemple $(22\bar{4}1)$ comme montré en Fig. 11.

On en déduit, ainsi, que la texture des trapiche fleurs est la même que celle des autres rubis trapiche, mais le nombre des secteurs de croissance est différent (secteurs pinacoïdaux + deux

groupes de secteurs bipyramidaux {22$\bar{4}$3} et {22$\bar{4}$1}). Cette analyse morphologique contredit le modèle de formation proposé auparavant pour ces rubis à l'aspect si particulier. On pensait, en fait, que la forme en fleur était due à plusieurs épisodes de croissance qui auraient formé une première couche interne de rubis (celle qui entoure le cœur) ; la croissance se serait ensuite arrêtée pour reprendre en un deuxième temps et former la couche externe. L'effet de la dégradation météoritique sur cette dernière aurait porté à sa dissolution partielle et à l'acquisition d'un aspect proche à celle des pétales d'une fleur.

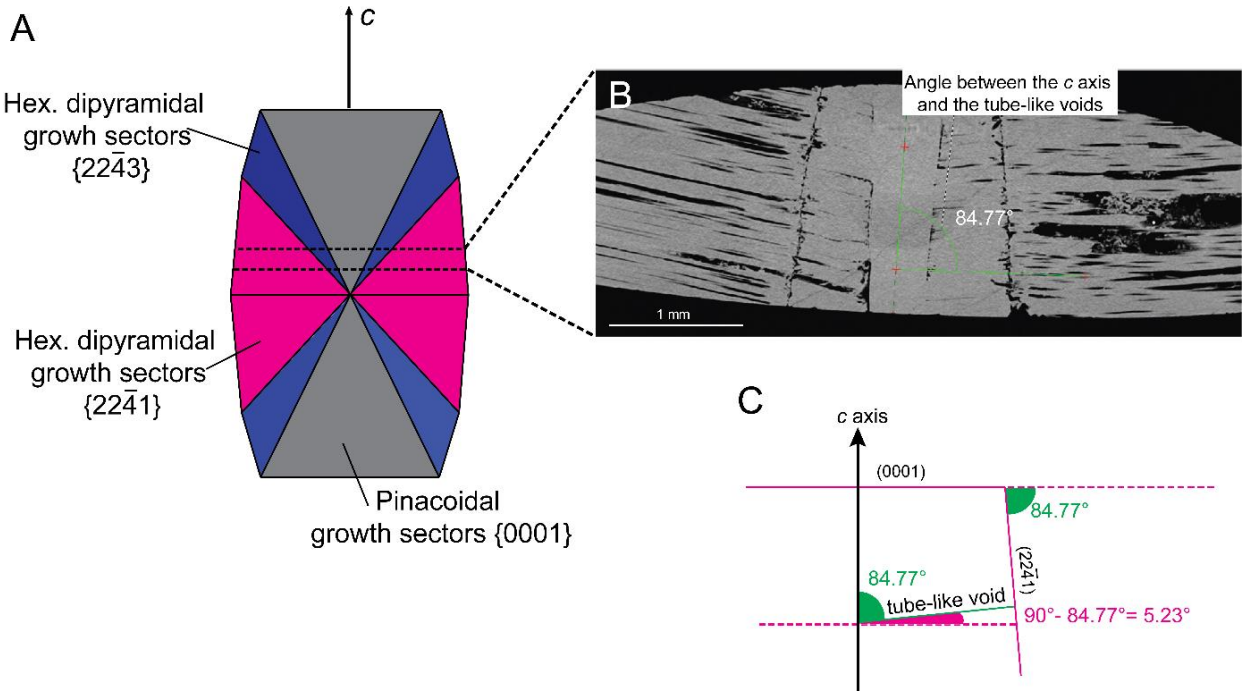

Figure 11. (a) Schéma d'une section parallèle à l'axe *c* qui montre le développement des secteurs pinacoïdaux (en gris) et des deux groupes de secteurs bipyramidaux {22$\bar{4}$3} (en rose) et {22$\bar{4}$1} (en bleu). (b) Image tomographique où on reconnaît les secteurs cités et sur laquelle on a effectué les mesures angulaires. (c) Schéma représentant l'angle entre la face (0001) et une face inclinée. La même valeur angulaire on la retrouve entre les dislocations et l'axe *c*.

7.5 Les minéraux dans les problématiques d'ingénierie civile et environnementale

J'ai effectué un post-doc à l'Université de Claifornie Los Angeles (UCLA) où j'ai étudié la dissolution/précipitation de différents échantillons avec une nouvelle technique appelée 'Vertical Scanning Interferometry' (VSI) qui permet de mesurer les variations topographiques d'un échantillon avec une résolution verticale de ~0.1 nm et latérale de ~500 nm. Mon projet principal était relié aux minéraux utilisés dans le béton des centrales nucléaires, ce qui m'a permis de devenir membre de l'International Committee on Irradiated Concrete. La dissolution des minéraux dans le béton se vérifie quand ils sont en contact avec les alcalins de la solution interstitielle (qui a un pH basique, supérieur à 12). La dissolution, qui est suivie par la précipitation d'autres phases, provoque la détérioration du béton et donc le changement des propriétés physico/chimiques, compromettant sa durabilité. La durabilité est un problème non négligeable pour les centrales nucléaires, car elle est accrue par l'exposition aux différents rayonnements produits par les matériaux nucléaires. Cette exposition endommage la structure cristalline des minéraux, qui deviennent progressivement amorphes, provoquant des changements de densité et des propriétés physico-chimiques. Cela se traduit par une détérioration plus rapide, qui compromet la fonctionnalité et la sécurité des centrales nucléaires. Une étude a été conduite en collaboration avec Oak Ridge National Laboratory pour comprendre comment la radiation peut modifier la structure des minéraux en affectant leur réactivité chimique, quantifiée en termes de vitesse de dissolution (Pignatelli et al., 2016 ; Wang et al., 2015). Les minéraux analysés (quartz, calcite, mica, etc.) sont irradiés avec un faisceau d'ions Ar^+ (400 keV) et puis dissous à 25°C en utilisant différentes solutions. Par exemple, des solutions à pH ≥ 12 ont été utilisées pour le quartz, des solutions à pH 10, 12 et 13 pour la calcite. Les résultats ont montré qu'après l'exposition à la radiation, la vitesse de dissolution du quartz augmente significativement (3 ordres de grandeur) et devient proche de celle de la silice amorphe (Pignatelli et al., 2016). En revanche, les vitesses de dissolution de la calcite avant et après l'exposition à la radiation sont comparables si on considère l'erreur expérimentale (Fig. 12). Ces résultats sont confirmés par les données MET : les clichés électroniques du quartz irradié sont caractérisés par l'absence de taches de diffraction, qui sont remplacées par une bande de diffusion, indicative d'une amorphisation complète. Par contre, aucune différence n'a été observée sur les clichés de diffraction de la calcite, ce que signifie que ce minéral est plus résistant à la radiation. Les simulations de dynamique moléculaire effectuées pour modéliser les expositions du quartz et de la calcite à une radiation incidente avec une énergie entre 300

eV et 1000 eV reproduisent avec les résultats expérimentaux (Wang et al., 2015). La simulation montre que la structure du quartz devient complètement désordonnée après irradiation mais la structure de la calcite est très peu affectée car la radiation provoque seulement la distorsion/rotation du groupe CO_3^{2-} par rapport à la position du calcium. Les résultats de cette étude montrent que pour une meilleure durabilité des centrales nucléaires, le choix de granulats contenant principalement de la calcite serait plus approprié.

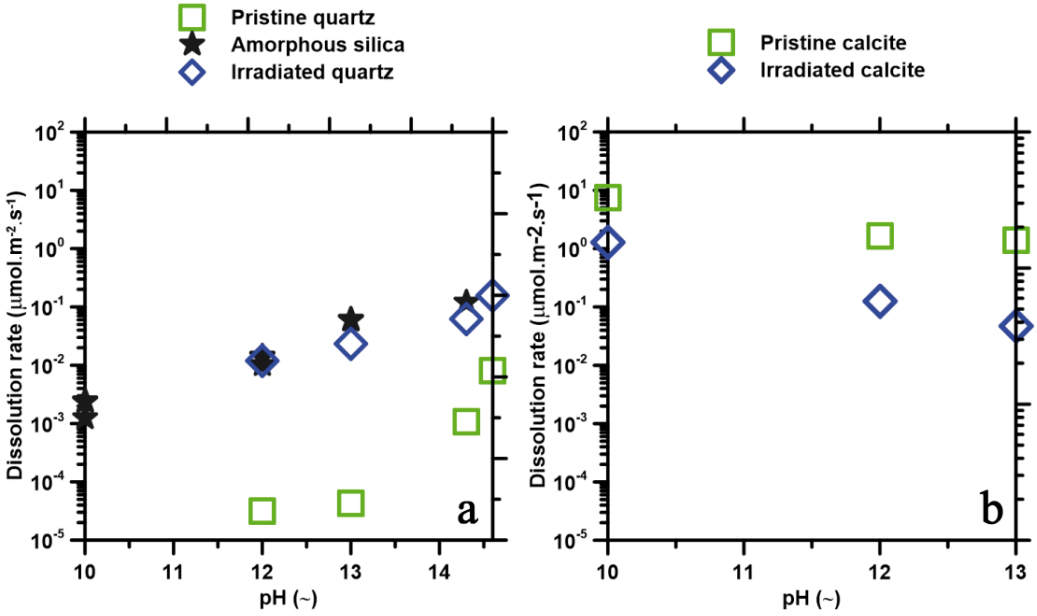

Figure 12. Vitesses de dissolution du quartz (a) et de la calcite (b) à différents pHs (Pignatelli et al., 2016).

A l'UCLA j'ai aussi travaillé sur la dissolution des CSHs ('calcium silicate hydrates'), phases nanocristallines qui se forment par hydratation dans le ciment pour mieux comprendre le fluage dans le béton, dont les origines sont peu connues. Plusieurs modèles ont été proposés ; l'un d'entre eux concerne le mécanisme de dissolution-précipitation des CSHs dans un environnement humide (RH > 50%). Le mécanisme se base sur les étapes suivantes : un stress externe provoque des changements dans le potentiel chimique et l'équilibre entre solide et liquide est modifié pour favoriser la dissolution et réduire le stress. Les éléments en solution se déplacent vers les régions à basse concentration où ils précipitent. Sur la base de ce modèle, le fluage serait le résultat de la dissolution des CSHs dans l'eau inter-granulaire dans les régions où le stress est élevé. L'étude de dissolution des CSHs et la simulation des dynamiques moléculaires confirment ce modèle. Les résultats montrent que la vitesse de dissolution des CSHs avec un rapport Ca/Si compris entre 0.8 et 1.8 diminue quand le pH augmente. Par ailleurs, à pH constant, l'évolution de la vitesse de dissolution n'est pas linéaire par rapport au

rapport Ca/Si: en fait, à pH 12, le minimum est observé pour Ca/Si = 1.5, mais, à pH 10, le minimum correspond à un rapport Ca/Si plus faible. Cela est bien en accord avec la simulation qui a permis de reproduire le développement du fluage après l'application d'un stress constant sur le long terme pour comprendre la relation entre le fluage et la composition des CSHs. Les calculs mettent également en évidence que, de la même manière que pour le fluage, l'évolution est non linéaire et que la valeur minimale du fluage correspond à un rapport Ca/Si = 1.5. La présence d'un minimum à Ca/Si = 1.5 pour la dissolution et le fluage est expliqué par la théorie de la contrainte topologique (Topological constraint theory) qui montre que la structure atomique est isostatique (nombre des contraintes topologiques par atome n_c = 3) seulement lorsque Ca/Si = 1.5. Le couplage entre expérimentation et calcul indique ainsi que la dissolution et le fluage sont corrélés et que pour augmenter la résistance au fluage du béton il serait convenable d'utiliser des CSHs avec une faible rapport Ca/Si (Fig. 13 - Pignatelli et al., 2016).

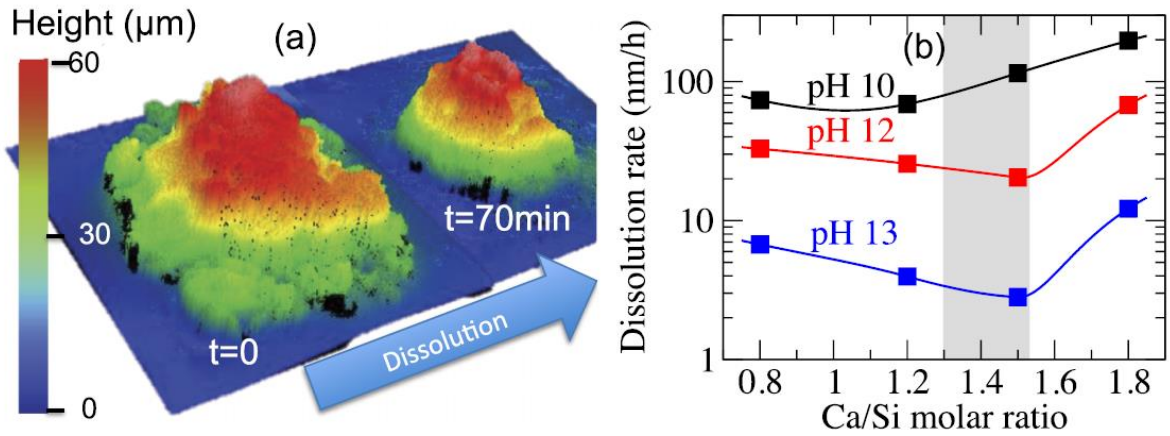

Figure 13. (a) Images de la dissolution du CSH avec Ca/Si = 0.8 à pH 10 obtenues avec le VSI avant et après 70 minutes d'interaction avec la solution. (b) Vitesses de dissolution à 25ºC des CSHs en fonction du rapport Ca/Si (Pignatelli et al., 2016).

Actuellement on essaie de développer une étude sur les minéraux irradiés par neutrons avec la résonance paramagnétique électronique (RPE) sur monocristal. Les premiers échantillons (calcite, dolomite, quartz) ont été déjà mis à notre disposition par le laboratoire ORNL, après avoir vérifié qu'ils ne sont plus radioactifs. Dans un deuxième temps et en fonction des résultats obtenus, d'autres silicates seront envoyés par la suite (e.g. micas et grenats). Une irradiation aux neutrons des échantillons a été privilégiée par rapport à celle utilisant un faisceau d'Ar^+, car plus pénétrante et permettant ainsi de caractériser la perturbation structurale sur une épaisseur plus importante (les ions Ar^+ ne pénètrent que jusqu'à ~500 nm). La RPE permettra

de dénombrer et d'identifier les défauts structuraux formés lors de l'irradiation, et de les localiser précisément dans la structure du minéral. Les résultats permettront aussi de vérifier la stabilité structurale de certains minéraux vis-à-vis de l'exposition aux rayonnements (e.g. la calcite – Wong, 1974). Par exemple, les calcites exposées aux ions Ar^+ restent incolores, aux contraire celles exposées aux neutrons présentent un changement de couleur (Fig. 14): à quelle modification structurale est dû ce changement ?

Figure 14. Photo d'un cristal de calcite contenant des traces de Mn avant (incolore – à droite) et après (brun – à gauche) exposition aux neutrons.

7.6 Les biominéraux : l'hydroxyapatite, le minéral qui constitue les dents

J'ai étudié les phénomènes de déminéralisation et reminéralisation des dents en utilisant le Vertical Scanning Interferometry (VSI) dans le cadre d'une collaboration avec le Department of Bioengineering et la School of Dentistry de l'UCLA. La déminéralisation correspond à la dissolution de l'hydroxyapatite de l'émail suite à une attaque qui peut entraîner la formation d'une carie ou l'érosion dentaire (e.g., acides contenus dans les aliments/boissons ou produit par les bactéries de la plaque dentaire). Pour combattre ce phénomène, des traitements avec des gels reminéralisants sont proposés par les dentistes mais leur efficacité peut varier en fonction de leur composition. Les échantillons d'émail ont été d'abord dissous à pH 4 et puis traités avec deux gels pour déterminer les vitesses de dissolution et de reminéralisation. Les gels testés dans cette étude sont: 'PreviDent5000' et 'MI paste' qui contiennent respectivement NaF et CPP-ACP (CPP : casein phosphopeptide; ACP : amorphous calcium phosphate). Successivement, les échantillons traités avec les gels sont eux aussi dissous à pH 4 pour évaluer la stabilité du précipitât et donc choisir le traitement le plus efficace. Les résultats ont montré que la capacité de reminéralisation de 'PreviDent5000' est environ 6 fois supérieure de celle de 'MI paste', mais le précipitât de ce dernier gel semble être plus résistant à l'attaque acide, car il se dissous environ 3 fois plus lentement en comparaison du précipitât de 'PreviDent5000' (Fig. 15 - Pignatelli et al., 2016).

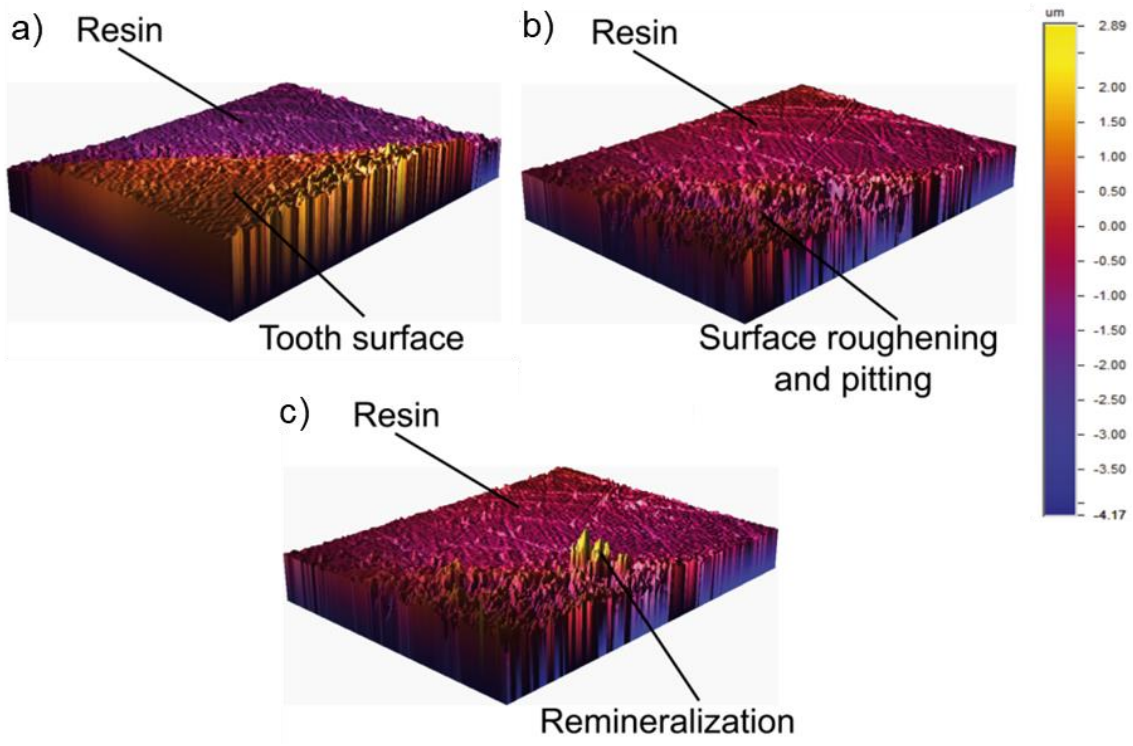

Figure 15. Images VSI qui montrent (a) l'échantillon d'émail avant l'expérience, (b) la dissolution de l'émail, et (c) la reminéralisation après l'utilisation du gel 'PreviDent5000'.

On a ensuite effectué une autre étude sur la déminéralisation pour comprendre l'effet des traitements blanchissants sur l'hydroxyapatite de l'émail. Ces traitements sont à base de peroxyde d'hydrogene (HP) ou peroxyde carbamide (CP), qui va se transformer en HP et urée au contact avec l'eau. Ainsi, le principal agent blanchissant est le HP qui semble avoir des effets adverses sur les patients lors du traitement (déminéralisation de l'émail, irritation de la gencive et même de la muqueuse gastrique – Lima et al., 2018 ; Markowits, 2010). Même si dans la littérature il n'y a pas de consensus sur les effets adverses, la quantité de HP contenue dans les traitements dentaires varie en fonction des pays : par exemple les traitements qui contiennent plus de 6% de HP sont interdits en Europe mais autorisés ailleurs (Polydorou et al., 2018).

On a comparé les effets déminéralisant de 2 traitements en gel utilisés par les dentistes (Zoom Nite White 22% CP and LumiSmile 16% CP) à ceux des solutions avec différentes concentrations de peroxyde d'hydrogène. Les taux de déminéralisation de l'émail induits par les deux traitements sont similaires. Ils sont comparables aux taux induits par de solutions d'HP avec concentrations de 23.7% et 24.7% respectivement. Les résultats ont montré que les solutions de peroxyde d'hydrogène moins concentrées endommagent plus l'émail (taux de dissolution plus élevé) comme montré en Fig. 16.

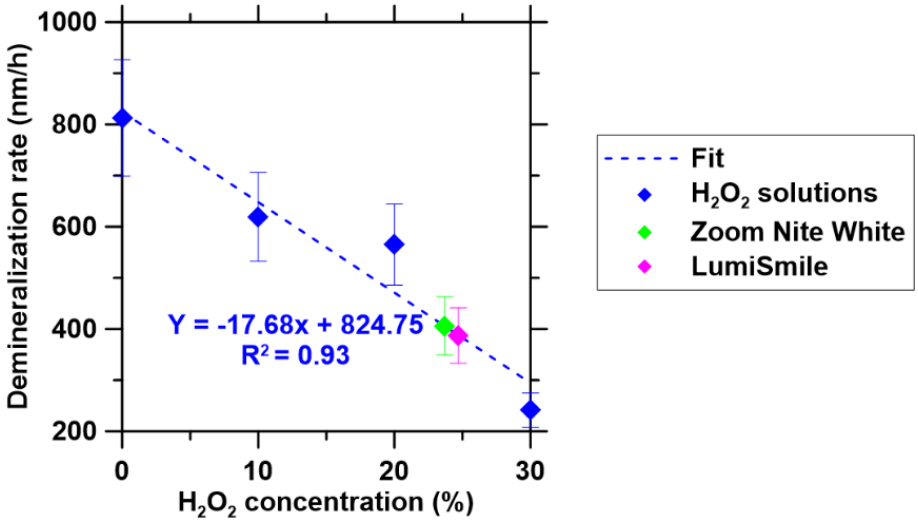

Figure 16. Les taux de déminéralisation de l'émail après exposition aux solutions avec différentes concentrations de H_2O_2 (0%, 10%, 20% et 30%) et à deux gels de blanchiment disponibles dans le commerce avec respectivement 22% (Zoom Nite White; diamant vert) et 16% (LumiSmile, diamant rose) de peroxyde de carbamide. En utilisant H_2O_2 comme référence, on peut comparer quantitativement les taux de déminéralisation d'autres agents de blanchiment.

8. Projet de recherche

Les serpentines sont des phyllosilicates dont le feuillet est constitué d'une couche tétraédrique et d'une couche octaédrique (feuillet T-O ou 1: 1). Elles se caractérisent par une composition chimique et une structure cristalline complexes.

Du point de vue de la structure, l'absence de cations interfoliaires rend le polytypisme des serpentines plus complexe que dans les micas car les feuillets T-O adjacents peuvent être empilés avec un déplacement et/ou une rotation (Bailey, 1969), donnant lieu à plusieurs structures avec différentes symétries.

Leur formule générale est $(M, \square)_3T_2O_5(OH)_4$, où T et M sont les sites tétraédrique et octaédrique, respectivement. Les sites T sont généralement occupés par Si^{4+}, Al^{3+} et Fe^{3+}, alors que les sites M contiennent Mg^{2+}, Al^{3+}, Mn^{2+}, Fe^{3+} et Fe^{2+}. Lorsque les sites M sont partiellement vides, le symbole □ - représentant les lacunes - apparaît dans la formule (Guggenheim et al., 1982; Bailey, 1988).

Bien que le Fe puisse remplacer partiellement le Mg dans les serpentines de Mg (lizardite, antigorite et chysotile) plus couramment étudiées, les teneurs en Fe les plus élevées sont rapportées dans la berthierine, la cronstedtite (Fig. 17), la greenalite, l'odinite et la guidottiite récemment découverte (Wahle et al., 2010).

La cronstedtite se distingue des autres serpentines ferrifères par: (i) la teneur en Fe la plus élevée (ii) l'absence de lacunes dans la couche octaédrique, (iii) Fe^{3+} en coordination tétraédrique, et (iv) de très faibles quantités de cations autres que Fe et Si (Bailey , 1969, Geiger et al., 1983; Hybler et al., 2000, 2002; Kogure et al., 2002).

Les serpentines ferrifères se forment lors des interactions fluide-roche à basse température (T <150 ° C) dans des environnements extraterrestres et terrestres (i.e. serpentinisation), où le fer est disponible ainsi que le silicium provenant d'autres minéraux dits 'précurseurs'. Cependant, les conditions de formation sont mal comprises, de même que la répartition du fer et les possibles substitutions Fe-Mg (Evans et al., 2012).

Dans le milieu terrestre, les serpentines ferrifères peuvent se former dans des contextes naturels et anthropiques. La greenalite se trouve dans des formations archéennes métamorphisées et riches en fer (Gole 1980a, b), où elle a pu précipiter dans des conditions marines anoxiques et ferrugineuses (Tosca et al., 2016). On pense que l'odinite se forme à 25° C dans des milieux marins et lagunaires à l'interface sédiment-eau (Bailey, 1988). La berthierine peut se former par transformation diagénétique de la kaolinite dans des conditions légèrement alcalines, ou par des processus hydrothermaux et diagénétiques dans un environnement sédimentaire marin (Iijima

et Matsumoto, 1982; Bhattacharyya, 1983; Rivas-Sanchez et al., 2006). La cronstedtite se trouve dans des gisements de sulfures métamorphosés à basse température ou des veines hydrothermales (Frondel, 1962; López-García et al., 1992; Hybler et al., 2016, 2017). Dans le contexte anthropique, la modélisation thermodynamique et les données expérimentales ont prédit la formation des serpentines ferrifères au cours des interactions fer-argile simulant les conditions du stockage de déchets radioactifs dans des systèmes à barrières multiples (par exemple, Wilson et al., 2006; de Combarieu et al., 2011; Mosser-Ruck et al., 2010; Rivard et al., 2013; Pignatelli et al., 2014, etc.). Malgré les progrès accomplis au cours des 20 dernières années, la formation des serpentines ferrifères dans ce contexte n'est toujours pas élucidée, parce que la comparaison des données est compliquée par les différentes conditions expérimentales testées au cours des études, ainsi que les matières premières, les températures, la composition de la solution, le timing, etc. Cependant, la compréhension de leur formation et stabilité dans ce type de milieu est importante parce que les serpentines pourraient modifier les propriétés chimiques, physiques et mécaniques de la barrière argileuse avec le temps (Bildstein et al., 2006).

Les serpentines ferrifères se trouvent également dans d'autres corps du système solaire. Des interstratifications de berthierine et greenalite ont été reportées dans la météorite martienne Nakhla, en tant que produit d'altération des verres inclus dans les phénocristaux d'olivine (Lee et Chatzitheodoris, 2016). Une serpentine ne contenant que du fer ferrique et avec une composition similaire à celle de l'odinite a été observée dans les fractures de la mésostase de la météorite martienne Lafayette (Hicks et al., 2014). De plus, les données spectroscopiques dans le visible et proche infrarouge suggèrent la présence de: (i) la cronstedtite et la greenalite dans certaines régions de Mars (Calvin, 1998); (ii) la cronstedtite sur la planète naine Cérès (Zolotov, 2014); (iii) la berthierine dans les météorites CI et CM telles qu'Orgueil, Murchison et Murray (Calvin et King, 1997). D'autres travaux ont confirmé la présence des serpentines ferrifères, en particulier de la cronstedtite et la greenalite, dans les météorites CM où elles peuvent être mélangées à des serpentines riches en Mg (Barber 1981, Browning et al., 1996; Lauretta et al., 2000, Elmaleh et al, 2012, 2015.). Des cristaux de cronstedtite peuvent se former par pseudomorphose d'olivines et de pyroxènes dans ces météorites (Fig. 17 - Pignatelli et al., 2016 ; 2017 ; 2018).

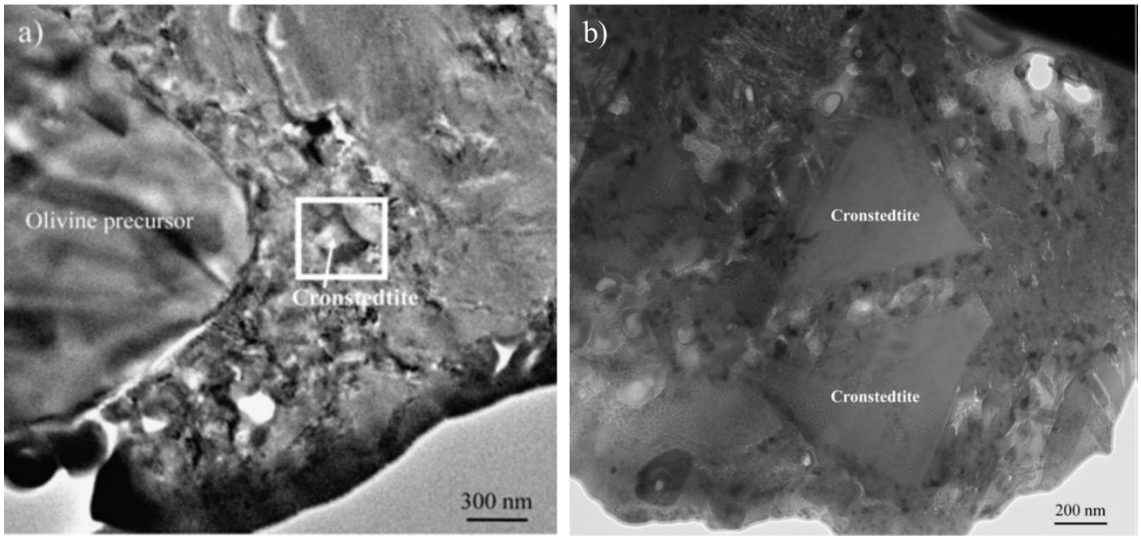

Figure 17. Cristaux de cronstedtite formés par pseudomorphose d'une olivine et d'un pyroxène dans la météorite Paris (Pignatelli et al., 2018).

Pourquoi est-il important d'étudier les serpentines ferrifères?

• Les conditions de formation et les champs de stabilité des serpentines ferrifères sont encore peu connues, car peu de données sont disponibles dans la littérature. Ces données sont issues des synthèses effectuées en laboratoire et sont donc limitées aux conditions utilisées lors de ces expériences. Les études pétrographiques/minéralogiques des roches terrestres contenant des serpentines sont rares ou incomplètes : l'une d'entre elles a été récemment publiée par Hybler et al. (2017), mais seule la paragenèse a été rapportée et le contexte géologique de formation n'a pas été établie. Pour les échantillons extraterrestres, les conditions de formation dans l'espace sont inconnues, les observations analytiques sont donc interprétées sur la base d'analogies avec des échantillons terrestres et ceux obtenus par synthèse. Une autre limitation peut être l'altérabilité de certaines serpentines ferrifères au fil du temps: l'odinite et la berthierine sont connues pour se transformer en chlorite par une série d'interstratifiés chlorite-serpentine (Beaufort et al., 2015; Šegvić et al., 2020). Cela peut expliquer pourquoi on ne les trouve pas dans des échantillons géologiques plus anciens que le quaternaire (Bailey, 1988).

Les codes géochimiques, tels que ceux du logiciel Phreeqc, ne peuvent pas être utilisés pour décrire correctement les conditions et les champs de stabilité des serpentines ferrifères en raison de la pénurie de données thermodynamiques disponibles pour ces minéraux. En fait, les données ne font référence qu'à un seul polytype (par exemple, polytype 1*T* pour la cronstedtite), ce qui entraîne une incohérence entre les résultats de la modélisation et les observations expérimentales, (Seyfried et al., 2007; Pignatelli et al., 2014).

• Les caractérisations cristallographiques/cristallochimiques des serpentines ferrifères font défaut. Ce manque pourrait être dû au fait que ces serpentines sont mélangées à d'autres phases ou qu'elles sont souvent de taille micrométrique, limitant leur identification et conduisant à des confusions avec d'autres minéraux (par exemple, elles sont confondues avec les chlorites dans les météorites - Lauretta et al., 2000).

L'étude structurale des serpentines ferrifères donne des informations sur la séquence polytypique qui semble être liée aux paramètres physico-chimiques lors de leur formation. Un travail récent a montré que les cristaux de cronstedtite formés à différentes températures sont caractérisés par différentes séquences polytypiques (Hybler et al., 2018), soulignant que le lien entre la structure et les conditions de formation nécessite des recherches plus approfondies. Les quelques données sur le polytypisme de la cronstedtite dans les météorites semblent étayer ce lien. En fait, l'absence de gravité, la fugacité d'oxygène ou la température pourraient expliquer pourquoi certains polytypes trouvés dans les météorites sont très rares sur Terre (Müller et al., 1979; Zega et Buseck, 2003; Pignatelli et al., 2018; Hybler et al., 2008).

La caractérisation cristallochimique, en particulier la partition Fe-Mg, est très importante pour élucider la formation des serpentines ferrifères. Les précurseurs sources de Fe et Si et leurs effets sur la nature des serpentines sont mal connus. Sur Terre, la présence des serpentines ferrifères est souvent expliquée par des apports de fer dans la lizardite et l'antigorite. Trois mécanismes de substitution Mg-Fe sont proposés (Evans et al., 2012; Streit et al., 2012):

- les substitutions couplées du Mg et Si par Fe^{3+} respectivement dans les sites M et T produisent une cronstedtite riche en Mg $(Mg_2Fe^{3+})(SiFe^{3+})O_5(OH)_4$;
- Mg est remplacé par Fe^{3+}, donnant une serpentine ferrifère de formule $Fe_2Si_2O_5(OH)_4$;
- Mg est remplacé par Fe^{2+}, formant une lizardite ferreuse. Ensuite, Fe^{2+} est oxydé par déprotonation.

Les mécanismes ci-dessus semblent improbables parce que : (i) ils suggèrent qu'un précurseur de lizardite ou d'antigorite est nécessaire pour former des serpentines ferrifères, mais il n'y a aucune preuve de cela dans la nature; (ii) ils prennent en compte la formation d'une cronstedtite riche en Mg, mais ce minéral contient généralement de faibles quantités de Mg (la valeur la plus élevée rapportée est de 0,71 a.p.f.u. - Geiger et al., 1983); (iii) une serpentine dioctaédrique de formule $Fe_2Si_2O_5(OH)_4$ n'a jamais été trouvée. En effet, son existence est douteuse car la formule viole la définition propre des serpentines comme phyllosilicates trioctaédriques (Bailey, 1969).

Dans la littérature, des précurseurs possibles autres que les serpentines manganésifères sont proposés. Dans les oolithes, la berthierine peut se former par interaction de la kaolinite avec un

minéral riche en fer comme la sidérite (Bhattacharyya, 1983; Brindley, 1951; Iijima et Matsumoto, 1982); tandis que dans les météorites, les serpentines ferrifères se forment à partir de minéraux riches en Mg tels que l'olivine et le pyroxène ainsi que le fer qui est libéré par les grains d'alliage Fe-Ni ou par la sidérite/ankérite (Zolensky et al.1997; Brearley 2006; Rubin et al.2007; Changela et Bridges, 2011 ; Pignatelli et al., 2016).

Dans les échantillons extraterrestres, non seulement les précurseurs sont différents mais aussi les substitutions cationiques sont supposées être inverses par rapport à ce que l'on observe sur Terre: c'est-à-dire que d'abord se forment des serpentines ferrifères qui par la suite s'enrichissent progressivement en Mg lorsque le degré d'altération aqueuse augmente (Tomeoka et Buseck, 1985; Browning et al., 1996; Hanowski et Brearley, 2001; Palmer et Lauretta, 2011). Ceci est confirmé par des observations expérimentales montrant le remplacement pseudomorphique de la forstérite et de l'enstatite par la cronstedtite dans les météorites CM (Pignatelli et al., 2017). Cela signifie que les serpentines ferrifères pauvres en Mg peuvent se former directement à partir d'un précurseur riche en Mg, mais il y a un paramètre qui régule la distribution Mg-Fe, par exemple un gradient chimique qui éloigne le Mg.

• La partition du fer dans la structure des serpentines et la production de H_2

Dans les environnements terrestres et extraterrestres, la quantité de fer et son état d'oxydation dans les serpentines ferrifères sont des facteurs importants pour la génération de H_2. Comme de nombreux micro-organismes peuvent extraire l'énergie métabolique de l'H_2, on peut supposer que la serpentinisation a favorisé la vie chimioautotrophique avant l'évolution de la photosynthèse (McCollom et Seewald, 2013). Ce type de vie pourrait exister sur d'autres corps du système solaire (par exemple, Mars, Europe, etc.), où se trouvent des serpentines ferrifères et les conditions sont trop hostiles pour des organismes photosynthétiques. Le H_2 produit lors de la formation des serpentines ferrifères peut également contribuer aux flux de méthane abiotique et d'autres hydrocarbures plus complexes dans la croûte terrestre à partir de la réduction du CO_2, selon la réaction de Fischer-Tropsch (McCollom et Seewald, 2007; McCollom et Bach, 2009) :

$$n\mathrm{CO_2} + (2n+1)\mathrm{H_2} \rightarrow \mathrm{C}_n\mathrm{H}_{2n+2} + n\mathrm{H_2O}$$

Ce type de réaction nécessite de temps longs, la catalyse par des minéraux et/ou l'intervention de communautés microbiennes, comme ceux organismes à métabolisme méthanogène (Chapelle et al., 2002; McCollom et Seewald, 2013). Afin de mieux étudier la relation potentielle entre la formation des serpentines et l'origine de la vie, les taux et la quantité de H_2

produit devraient être mieux élucidés. Ceci est possible en couplant la quantification $Fe^{3+}/\Sigma Fe$ dans les serpentines ferrifères et une détection précise du H_2 libéré lors de leur formation.

Malgré les progrès substantiels accomplis au cours des dernières décennies, les questions fondamentales concernant le mécanisme et les conditions de formation des serpentines pour contraindre leur champ de stabilité sont toujours posées :

- Quelles sont les gammes de P, T, pH, rapport eau/roche, conditions d'oxydoréduction et compositions de fluide nécessaires pour former les serpentines ferrifères?
- Quels sont les effets des conditions de formation sur leurs caractéristiques chimiques/structurelles ?
- Quelle est la teneur en fer et son état d'oxydation dans ces minéraux ?
- Quels sont les effets des précurseurs sur la nature des serpentines ?
- Est-il possible d'obtenir une serpentine ferrifère à partir d'une serpentine magnésienne ?
- Quelle est la cinétique des réactions lors de l'interaction fluide-roche ?
- Quelle est la quantité de H_2 générée lors de la serpentinisation ?

Pour répondre à ces questions, je propose une approche en 5 étapes : (1) l'expérimentation hydrothermale en autoclave ; (2) la caractérisation multi-échelle ; (3) la comparaison des données expérimentales avec celles obtenues par modélisation ; (4) le développement expérimental pour déterminer les cinétiques de réaction ; (5) l'étude des serpentines trouvées dans les échantillons naturels.

(1) Expérimentation hydrothermale en autoclave

Les synthèses des serpentines sont rares, assez difficiles et chronophages. (Lanthenois et al., 2005; de Combarieu et al., 2007; Mosser-Ruck et al., 2010; Lanson et al., 2012; Pignatelli et al., 2013, 2014). La plupart de ces synthèses sont réalisées dans des autoclaves Parr® (Fig. 18a) sans surveillance pH, P, T, à partir d'un matériau de départ constitué d'une argile ou smectite mélangée à du fer métallique afin d'étudier les interactions argile-fer dans les sites de stockage des déchets nucléaires. Aucun autre silicate n'a été considéré comme un possible précurseur. En utilisant ce matériau, les serpentines ferrifères peuvent être synthétisées dans les conditions suivantes : températures inférieures à 150 ° C, fO_2 élevée, rapport liquide/argile > 10 et rapport fer métal/argile ~ 0,5 (Fig. 19 - Mosser- Ruck et al., 2010).

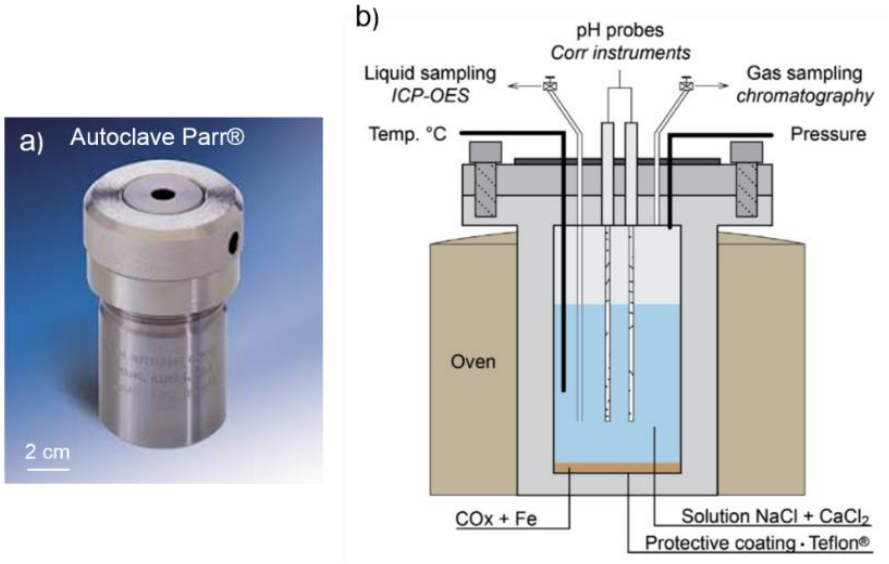

Figure 18. a) Autoclave Parr® chemisé en téflon ; b) schéma d'un autoclave pour le monitorage *in situ* de pH, *P* et *T* (Bourdelle et al., 2014).

Dans ce projet, les synthèses seront réalisées dans des autoclaves en acier inoxydable (volume de 150 cm^3) revêtus de Téflon® équipés de sondes pH et P-T pour des mesures *in situ* (Fig. 18b). La pression est estimée avec une précision de 0,1 bar, tandis que la température est obtenue avec une précision de 0,1 °C. La sonde pH peut fonctionner à des températures de 60°-200° C et à pressions < 140 bars. Les autoclaves permettent aussi de prélever des fluides et des gaz en cours d'expérience et de les analyser ensuite. La production d'H_2 typique des réactions de serpentinisation, peut être monitorée grâce à la chromatographie en phase gazeuse (Bourdelle et al., 2014; 2017). Le chromatographe sera préalablement calibré à l'aide de plusieurs mélanges gazeux de concentrations différentes comme le décrit Bourdelle et al. (2014). La sensibilité du détecteur pour H_2 est de quelques mmol dans l'appareil expérimental actuel (Bourdelle et al., 2017).

Un assemblage minéralogique de départ (par exemple des silicates et du fer métallique) mélangé à de l'eau sera utilisé. Dans un premier temps, les expériences seront réalisées à T < 150 °C, dans des conditions de pH neutre et avec une durée d'au moins six mois afin d'obtenir des serpentines ferrifères bien cristallisées (Rivard et al., 2013 ; Pignatelli et al., 2013, 2014). Ensuite, la composition de l'assemblage de départ, le fluide, la température et la durée expérimentale seront modifiées pour vérifier l'effet de ces paramètres sur la cristallisation des serpentines ferrifères. Par exemple, au lieu d'utiliser le fer métallique, un minéral tel que la pyrite peut être utilisé comme source du fer. Avant d'exécuter chaque synthèse, l'autoclave sera rincé et barboté avec un flux d'argon (2-5 bars) pendant 30 minutes pour assurer des conditions anoxiques et sera scellé avec une pression de départ de 1,1-1,3 bars d'argon (mesurée à 25° C).

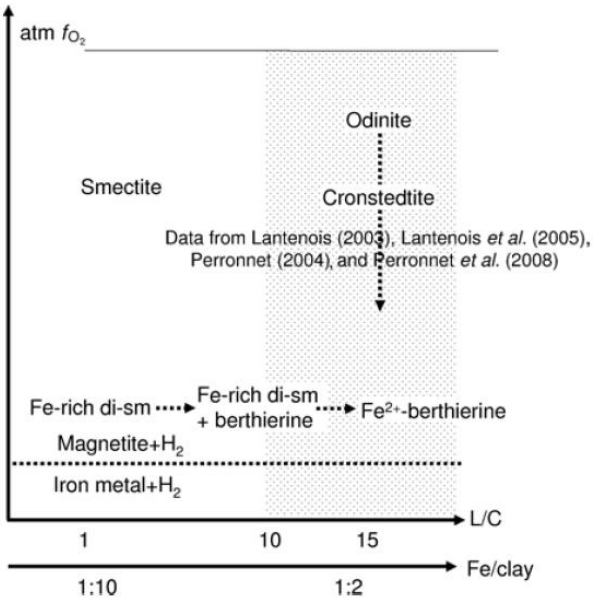

Figure 19. Schéma des conditions favorables à la formation des serpentines ferrifères à partir d'une smectite (Mosser-Ruck et al., 2010).

L'objectif de ces synthèses est d'acquérir une compréhension globale des conditions de formation des serpentines ferrifères. En particulier, elles permettront :

(I) de quantifier le H_2 produit, qui peut être utilisé comme sonde pour la mesure du taux d'oxydation du fer en fonction de la réaction:

$$Fe^0 + 2H_2O = Fe^{2+} + 2OH^- + H_2$$

(II) de relier l'effet des paramètres physico-chimiques (P, T, composition du fluide, etc.) ainsi que des précurseurs (e.g. olivine, pyroxène, kaolinite, quartz, etc.) sur la nature des serpentines. Les tests préliminaires indiquent que : (i) l'effet des précurseurs n'est pas négligeable, parce que la kaolinite conduit à la formation de la berthierine, tandis que le quartz à la formation de la cronstedtite (Pignatelli et al., 2020). Le mécanisme de croissance de ces serpentines semble être aussi affecté : la conversion kaolinite-berthierine pourrait se produire via une phase intermédiaire appelée « protoberthierine » ou par croissance épitaxiale (Bhattacharyya, 1983; Rivard et al., 2013), alors que la cronstedtite se forme probablement par précipitation à partir d'une solution sursaturée (Pignatelli et al., 2013).
(III) Un effet de la température sur la structure de la cronstedite cristallisée lors d'un refroidissement entre 90° et 40° C (Pignatelli et al., 2013; 2014) a été mis en évidence. Les résultats ont montré qu'entre 70° - 60° C, le polytype le plus abondant était 1*M* (Fig. 20), suivi

en abondance par les polytypes $2M_1$ et 3*A*, qui se formaient moins fréquemment. À des températures plus élevées, des cristaux de cronstedtite caractérisés par l'intercroissance de deux séquences polytypiques sont observés (appelés «mixed crystals») (Hybler et al., 2018). Il faut néanmoins remarquer que ces résultats ont été obtenus grâce aux expériences réalisées dans des autoclaves Parr® et, donc, il faudra les répéter dans un autoclave équipé pour suivre l'évolution du pH, P et T pendant de la formation des serpentines.

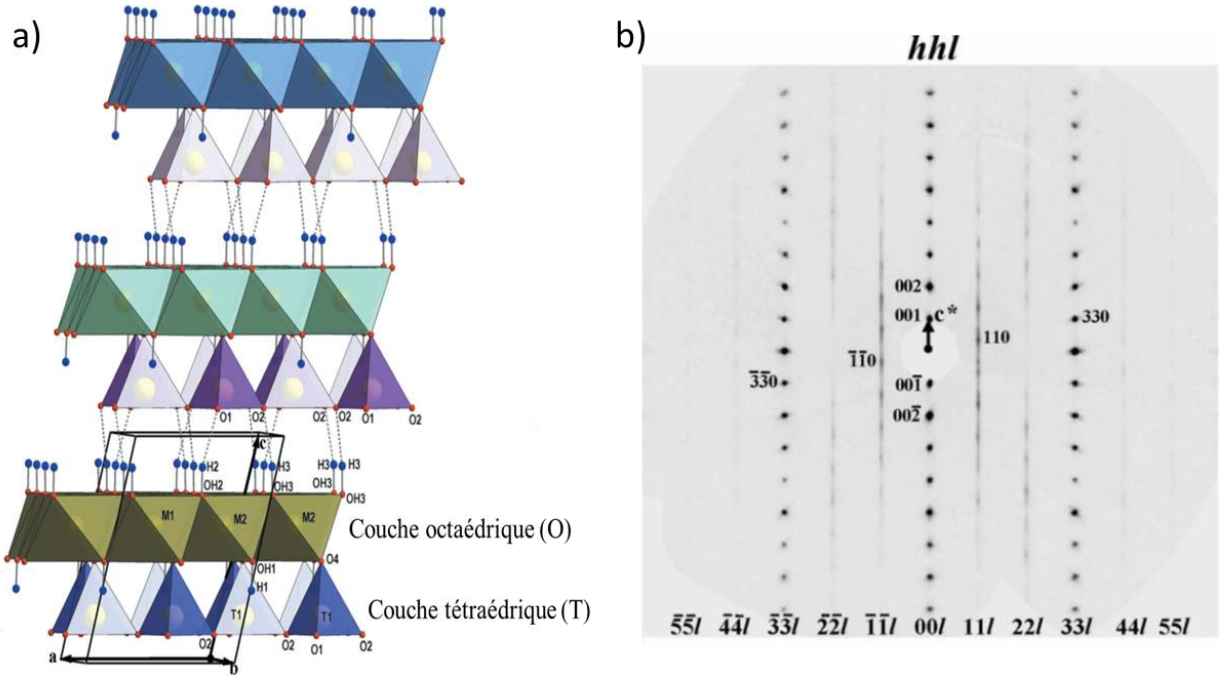

Figure 20. Structure du polytype 1*M* de la cronstedtite (a) et son cliché de diffraction (b) correspondant au plan réciproque (*hhl*)* (Hybler, 2014).

La principale difficulté de ces synthèses est d'obtenir une quantité de Fe-serpentines suffisante pour effectuer toutes les caractérisations prévues. En fait, la teneur en fer métallique utilisé est limitée par la pression H_2 qui sera générée au cours de l'expérience. Cette pression ne doit pas dépasser les limites autorisées par le système de sécurité (100 bars), obligatoire pour ce type d'expérimentation. Pour des pressions plus élevées, une solution possible est d'effectuer des prélèvements de gaz dès que la pression atteint 10 bars. Les prélèvements peuvent perturber le système et les équilibres des réactions, en affectant la formation de serpentines, mais ils présentent l'avantage de booster l'oxydation du fer et d'accélérer la cinétique de réaction. Afin de vérifier si le système est perturbé, chaque synthèse pourra être répétée dans des autoclaves Parr® chemisés en téflon ou en or (volume respectivement de 24 cm^3 et 18 cm^3).

(2) Caractérisation multi-échelle

Les produits expérimentaux seront analysés avec différentes techniques analytiques en fonction de leur nature : gazeuse (chromatographie en phase gazeuse), liquide (chromatographie ionique, ICP-OES) ou solide. Pour ces derniers, des techniques analytiques de pointe seront utilisées afin de relier les effets des conditions utilisées lors de la synthèse aux caractéristiques structurales et chimiques des serpentines néoformées (e.g., la microscopie électronique à balayage (MEB) et la diffraction des rayons X sur poudre (DRXP) en association avec la microscopie électronique à transmission (MET)). Le MET est probablement le moyen technique le plus approprié pour obtenir une caractérisation détaillée des serpentines, parce qu'il permet:

(i) d'obtenir des données chimiques (Energy Dispersive X-ray) sur des cristaux très petits et de voir des éventuelles zonations compositionnelles ;

(ii) d'avoir des images à haute résolution (HRTEM) qui permettent d'étudier les interstratifications (Fig. 21) ;

(iii) d'avoir des clichés de diffraction électronique (SAED patterns) dont l'interprétation n'est pas triviale à cause du polytypisme (voir par exemple Ďurovič, 1997). Une connaissance cristallographique et, en particulier, de la théorie Ordre-Désordre (OD) (Dornberger-Schiff, 1956 ; 1964 ; 1966 ; 1975 ; 1979) apparaît nécessaire pour l'étude structurale fine des serpentines ainsi que tous les phyllosilicates (voir par exemple, Ďurovič, 1997 ou Hybler et al., 2008 ; Pignatelli et al., 2011 ; Pignatelli et Nespolo, 2011 ; Pignatelli et al., 2013).

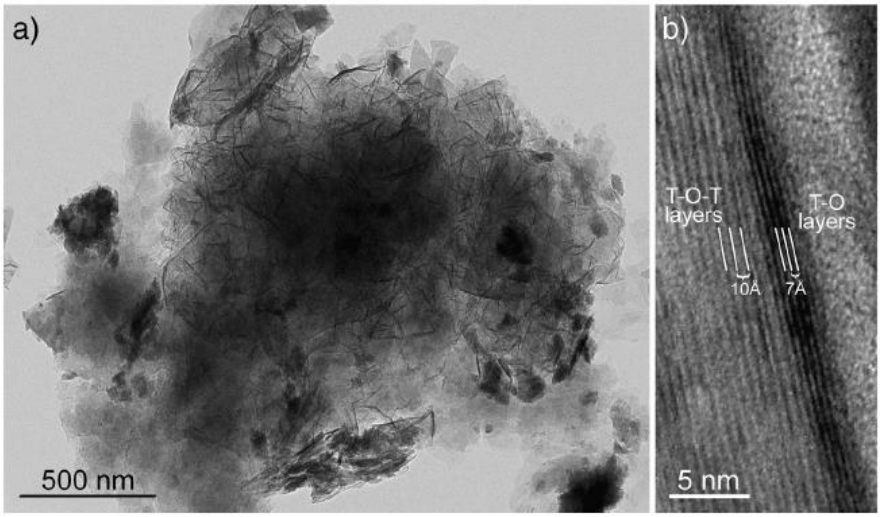

Figure 21. Images MET (a) et HRTEM (b) qui montrent les interstratifications complexes entre phyllosilicates de type T-O-T et T-O (Pignatelli et al., 2014).

(iv) d'obtenir des informations structurales si le microscope est équipé d'un tomographe pour la précession (Automated Diffraction Tomography/Precession Electron Diffraction - ADT/PED).

Cet équipement permet d'effectuer la diffraction électronique 3D (ED) utilisée pour résoudre et affiner les structures cristallines comme cela se fait habituellement avec la diffraction des rayons X (Fig. 22a). Le principal avantage est d'étudier des cristaux de quelques dizaines de nanomètres, c'est-à-dire des cristaux de 2 à 3 ordres de grandeur plus petits que ceux accessibles par diffraction des rayons X sur monocristal, indépendamment des éventuelles phases environnantes (Pignatelli et al., 2014; Mugnaioli et Gemmi, 2018). Cela n'est pas négligeable parce que la taille des serpentines ferrifères synthétisées est généralement inférieure à 1 µm (Fig. 22b). L'acquisition des données consiste en un échantillonnage de l'espace réciproque collecté grâce à la large rotation du goniomètre du microscope (± 60°), en utilisant un pas fixe de 1° et en négligeant toute orientation cristalline le long d'un axe cristallographique spécifique (Kolb et al., 2007, 2008; Mugnaioli et al., 2009). Pour éviter les dommages causés par le faisceau - ce qui est possible pour les minéraux hydratés comme les serpentines - les données seront acquises avec une faible irradiation et un temps d'exposition court (par exemple, une série complète de tilt sera collectée en 2 minutes - Pignatelli et al., 2014).

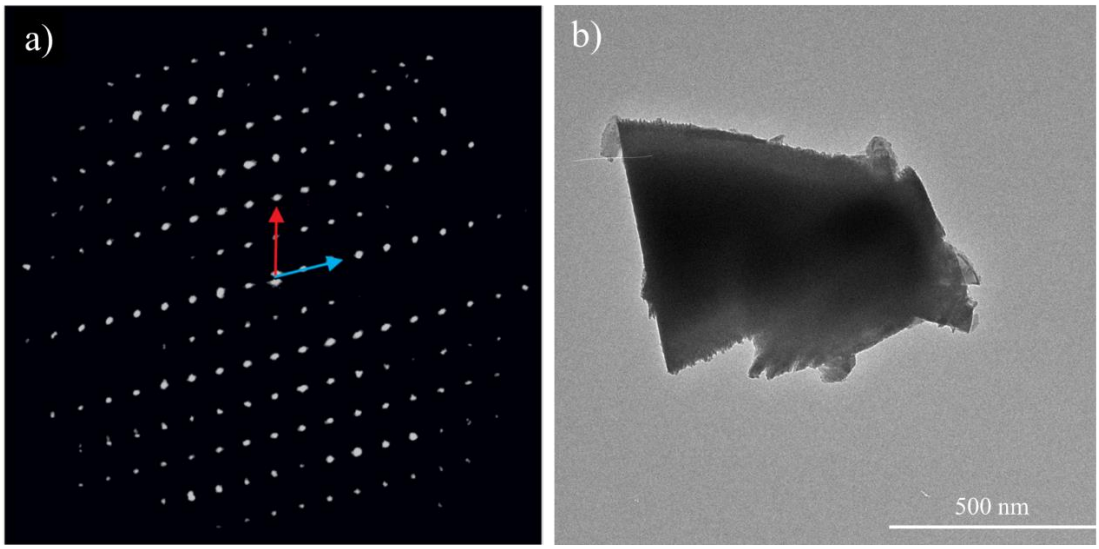

Figure 22. Projection le long de l'axe *b** du volume de diffraction (a) reconstruit en 3D à partir des données ED d'une cronstedtite synthétisée (b) (Pignatelli et al., 2020).

L'échantillon pour les analyses au MET peut être utilisé pour quantifier le rapport $Fe^{3+}/\Sigma Fe$ par spectroscopie XANES réalisée avec un microscope à transmission de type STXM (Scanning Transmission X-ray Microscope) (Bourdelle et al., 2013; Elmaleh et al., 2015; Pignatelli et al., 2017). Le rapport $Fe^{3+}/ \Sigma Fe$ sera quantifié avec une incertitude de l'ordre de ± 5% et une

résolution spatiale d'environ 50 nm selon la procédure détaillée par Bourdelle et al. (2013). Ceci sera très utile pour définir si les conditions redox étaient constantes pendant la serpentinisation ou si des fluctuations ont eu lieu.

La STEM-XANES permet de maintenir les échantillons dans des conditions anoxiques avant et pendant les mesures (Miot et al., 2009). Par rapport à la spectroscopie par perte d'énergie électronique (EELS), la STEM-XANES ne nécessite pas d'étalonnage et il n'y pas de dommages dus au faisceau, tels que l'oxydation induite du fer (Lauterbach et al., 2000; Garvie et al., 2004).

La caractérisation sera complétée par l'acquisition des données thermodynamiques des serpentines ferrifères à l'aide de la calorimétrie différentielle à balayage (DSC) pour les capacités thermiques, et de la calorimétrie isotherme pour les enthalpies de dissolution (Ganteaume et al., 1991). Les enthalpies et entropies de formation, ainsi que les énergies de Gibbs seront calculées grâce à des équations thermodynamiques de façon similaire aux travaux réalisés par Gailhanou et ses collaborateurs (Gailhanou et al., 2012 ; Gailhanou et al., 2017 ; Roosz et al., 2018). L'acquisition de paramètres thermodynamiques pour les serpentines ferrifères avec une structure et une composition bien connues sera particulièrement utile pour améliorer les bases de données géochimiques existantes comme Thermochimie et Thermoddem, qui ont des données scares pour ces minéraux. Il faut plusieurs dizaines de milligrammes de serpentines pour mesurer les propriétés thermodynamiques. Ainsi, l'acquisition de ces données dépend strictement de la quantité des serpentines que nous obtiendrons par synthèse. Cette quantité ne devra pas contenir d'autres phases comme par exemple les minéraux coprécipités ou les restes de l'assemblage de départ. Pour cette raison, une séparation par densité et/ou magnétique est à prévoir au préalable.

Les caractérisations des serpentines extraterrestres ont mis en évidence l'efficacité des méthodes analytiques décrites ci-dessus. Les résultats ont souligné que la plupart des cristaux de cronstedtite dans la météorite Paris sont des polytypes désordonnés ou 1*T* (Fig.3), bien que nous ayons remarqué la coexistence contemporaine de $3T + 2M_1$, décrite pour la première fois, (Pignatelli et al., 2018). Cette association n'a jamais été observé dans les échantillons terrestres, où le polytype 3*T* est couramment décrit en association avec le 1*M* (Ďurovič, 1997; Hybler et al., 2016, 2017). La quantification du rapport $Fe^{3+}/\Sigma Fe$ par STXM-XANES (Fig. 23) indique que la teneur en Fe^{3+} peut être considérée comme un indicateur du degré d'altération aqueuse dans les météorites CM : les cronstedtites des météorites les plus altérées contiennent plus de Fe^{3+} (Pignatelli et al., 2017). Le rapport $Fe^{3+}/\Sigma Fe$ a également été utilisé pour estimer la production d'H_2 lors de la formation des cronstedtites dans la météorite Paris. Cette production

est importante parce qu'elle ouvre des perspectives intéressantes : l'hydrogène peut avoir réagi avec des espèces carbonées et joué un rôle dans la synthèse organique prébiotique, ou s'échapper et produire des conditions de plus en plus oxydantes lors de l'altération (Guo et Eiler, 2007 ; Elmaleh et al., 2015).

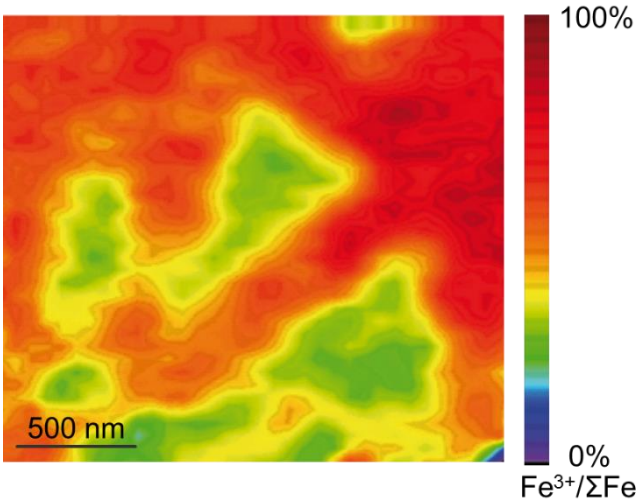

Figure 23. Cartographie obtenues par XANES-STXM sur une coupe FIB (Pignatelli et al., 2017) où on voit en vert la cronstedtite et en rouge/orange des oxydes/hydroxydes de fer. Les données ont été collectées sur la ligne PolLux du synchrotron suisse PSI (Paul Scherrer Institute) et ont été utilisées pour déterminer le rapport $Fe^{3+}/\Sigma Fe$.

(3) Comparaison des données expérimentales avec celles obtenues par modélisation

Pour prédire l'évolution géochimique et minéralogique pendant la formation des serpentines, il est envisageable d'effectuer des *allers-retours* entre expérimentation et modélisation thermodynamique pour comparer les résultats.

Actuellement, les données géochimiques des serpentines dans les bases de données (e.g. PHREEQC_Thermoddem – Blanc et al., 2012) sont très limitées. Par exemple, seules les données thermodynamiques du polytype 1*T* de la cronstedtite sont disponibles. Son champ de stabilité a été déterminé à plusieurs températures en fonction de la fugacité d'oxygène et de la quantité de Si en solution (Fig. 24a - Pignatelli et al., 2014). Pour cette serpentine, les calculs indiquent que, d'une part, son champ de stabilité se réduit si la température augmente, jusqu'à devenir négligeable au-dessus de 150° C. Cela est en accord avec les résultats de Zolotov (2014) et Schulte et Shock (2004) qui prédisent que la cronstedtite ne peut pas se former respectivement à des T > 120° C et > 100° C.

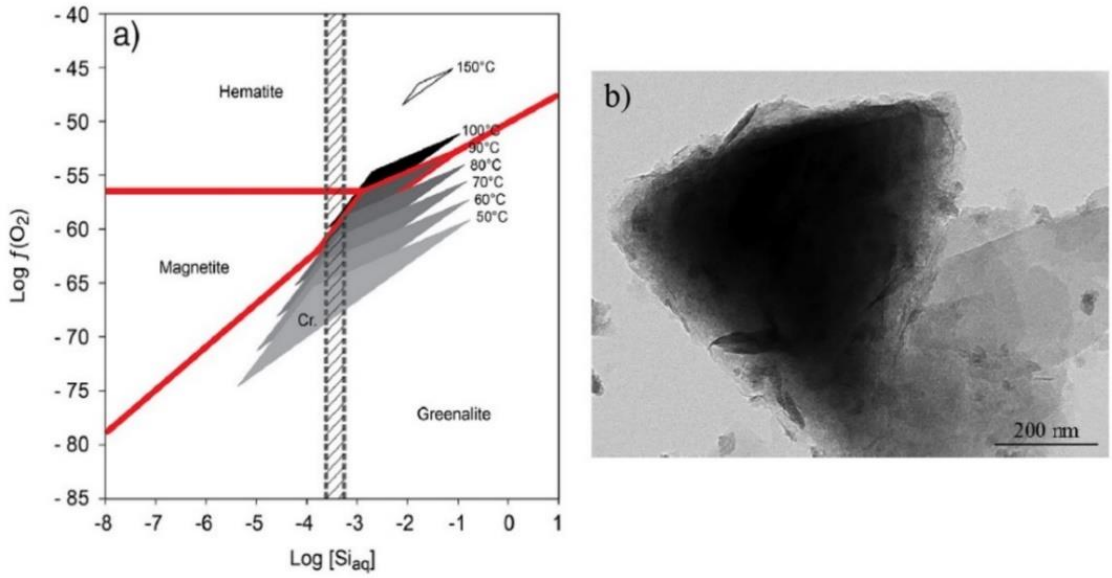

Figure 24. a) Champ de stabilité de la cronstedtite; b) image MET d'un cristal de cronstedtite qui devient instable à 50° C (Pignatelli et al., 2013 ; 2014).

Le problème concerne la limite inférieure de température du champ de stabilité de ce minéral : en effet, les expériences indiquent clairement que la cronstedtite n'est plus stable à T ≤ 50°C (Fig. 24b - Pignatelli et al., 2013), mais les calculs thermodynamiques prédisent qu'à 50° C le champ de stabilité s'élargit (Fig. 24a). Cette divergence est due au fait que les bases de données thermodynamiques ne prennent pas en compte le polytpisme, l'état d'hydratation et la présence à la fois de Fe^{2+} et de Fe^{3+} (Seyfried et al., 2007 ; Pignatelli et al., 2014). Hormis le polytypisme, toutes caractéristiques structurales, telles que les paramètres de la maille, le groupe d'espace et la symétrie du site cationique, sont négligées. Cela signifie que les mêmes données thermodynamiques, et donc les mêmes champs de stabilité, sont obtenus pour différents polytypes ayant période d'un seul feuillet T-O, c'est-à-dire les polytypes 1*T* et 1*M*. De plus, ces données thermodynamiques font l'hypothèse que la distribution des cations dans la couche octaédrique est très simple, en ne considérant qu'une distribution toujours méso-octaédrique, ce qui n'est pas tout à fait vrai pour ces minéraux. Par conséquent, les calculs d'enthalpie et d'entropie ne sont qu'approximatifs.

J'ai également remarqué un autre problème majeur lors de simulations thermodynamiques: la formule des serpentines prise en compte par les bases de données est souvent erronée. Par exemple, la base de données Thermoddem (Blanc et al., 2012) utilise la formule suivante pour la cronstedtite $Fe^{2+}_3(SiAl)O_5(OH)_4$ qui diffère nettement de la formule $(Fe^{2+}_{3-x}Fe^{3+}_x)(Si_{2-x}Fe^{3+}_x)O_5(OH)_4$ avec $0 < x < 0{,}8$ (Geiger et al., 1983; Smrčok et al., 1994; Hybler et al., 2000, 2002; Kogure et al., 2002). Une quantité d'Al trop élevée, l'absence de fer dans les sites

tétraédriques, ainsi que la présence du seul Fe^{2+} conduisent à une prédiction erronée du champ de stabilité. Cette observation est également valable pour plusieurs autres serpentines et les bases de données, e.g. la greenalite et la berthierine. La greenalite est souvent considérée comme une phase qui contient exclusivement du Fe^{2+}, en désaccord avec les données minéralogiques (Guggenheim et al., 1982). La composition de la berthierine est approximée et décrite par deux formules, l'une contenant uniquement du Fe^{2+} et l'autre que du Fe^{3+}. De plus, dans ce dernier cas, la formule de la berthierine $(Fe^{3+}_{2,67}Al_{0,33})(Si_{1,34}Al_{0,66})O_5(OH)_4$ est même irréaliste, n'étant pas électroniquement neutre, et par conséquent ne respectant pas les règles de Pauling pour les structures cristallines. Pourtant la partition du fer et son état d'oxydation dans les serpentines ferrifères sont des points cruciaux: par exemple, la cronstedtite a une composition très proche de celle de la greenalite, dont elle diffère par la présence de Fe^{3+} dans les sites tétraédriques. Cette différence modifie considérablement la limite supérieure de leurs champs de stabilité, rendant la greenalite stable à des températures plus élevées (c'est-à-dire jusqu'à 150 °C) que la cronstedtite (Schulte et Shock, 2004).

Par ailleurs, la coexistence de plusieurs polytypes, qui se vérifie inévitablement dans tous les échantillons naturels ou synthétiques, ne peut pas être prise en compte par les calculs thermodynamiques et se traduit par une description imprécise voire inexacte de leur champ de stabilité.

(4) Développement expérimental pour déterminer les cinétiques de réaction

Pour compléter les bases de données géochimiques et mieux comprendre les environnements favorables à la formation des serpentines ferrifères, il faut connaître les cinétiques des réactions, c.à.d. leurs vitesses de dissolution et de précipitation. A partir des cinétiques, il sera possible d'améliorer les simulations thermodynamiques et de réduire les écarts avec les résultats expérimentaux.

Grâce à l'interférométrie à balayage vertical (VSI en anglais) on peut mesurer les vitesses de dissolution/précipitation avec une résolution nanométrique (résolution verticale de ≈ 0,1 nm; résolution latérale de 500 nm) qui permet d'une part, une réduction significative de la durée expérimentale et d'autre part, l'utilisation de très peu de matière (de Groot, 2011). Par exemple, pour une résolution donnée, une microscopie à force atomique prendra 60 minutes pour scanner une zone de ~ 0,5x0,5 mm^2 contre 10 minutes pour un VSI (Barbour et Ress, 2004). Raccourcir la durée expérimentale, donc le temps de contact entre la solution et l'échantillon, est extrêmement important pour les réactions cinétiquement lentes qui nécessiteraient des

expériences d'une durée de plusieurs jours/mois (par exemple, dissolution du quartz à basse température - Pignatelli et al., 2016).

Ainsi, les autres méthodes expérimentales couramment utilisées (par exemple synthèse dans les autoclaves) pour la compréhension des cinétiques nécessitent non seulement une longue durée mais elles fournissent une « vitesse moyenne » de dissolution/précipitation (Fischer et Luttge, 2017). Cette « vitesse moyenne » est insuffisante pour comprendre les mécanismes de réaction qui sont la signature cinétique des processus à l'échelle atomique dans les minéraux (e.g. type et densité des défauts structuraux, formation d'une couche de passivation - Daval et al., 2011 ; Luttge et al., 2013). Si on ne tient pas compte de ces mécanismes, le risque est de surestimer les vitesses de dissolution/précipitation et cela peut conduire à des prévisions erronées de l'évolution des systèmes naturels ou anthropiques (Daval et al., 2013 ; Friscer et Luttge, 2017).

Au contraire, le VSI permet de prendre en compte l'hétérogénéité de la réactivité de surface grâce à sa haute résolution et de décrire les variations de la vitesse de dissolution/précipitation dans l'espace et dans le temps, sans perdre la fiabilité statistique des résultats (en multipliant les expériences sur le même échantillon ou sur des échantillons différents).

Le protocole expérimental permet d'acquérir des images 2D ou 3D de la surface d'un échantillon en trois étapes (Kumar et al. 2013), comme le montre la figure 25 :

- Étape 1 : l'image de l'échantillon est acquise avant de le faire interagir avec une solution (image de référence au « temps zéro ») ;

- Étape 2 : l'échantillon interagit avec une solution pendant un intervalle de temps (Δt) prédéfini pour permettre la dissolution/précipitation.

- Étape 3 : la solution est retirée en exposant la surface de l'échantillon à un flux de N_2 et une autre image de l'échantillon est acquise.

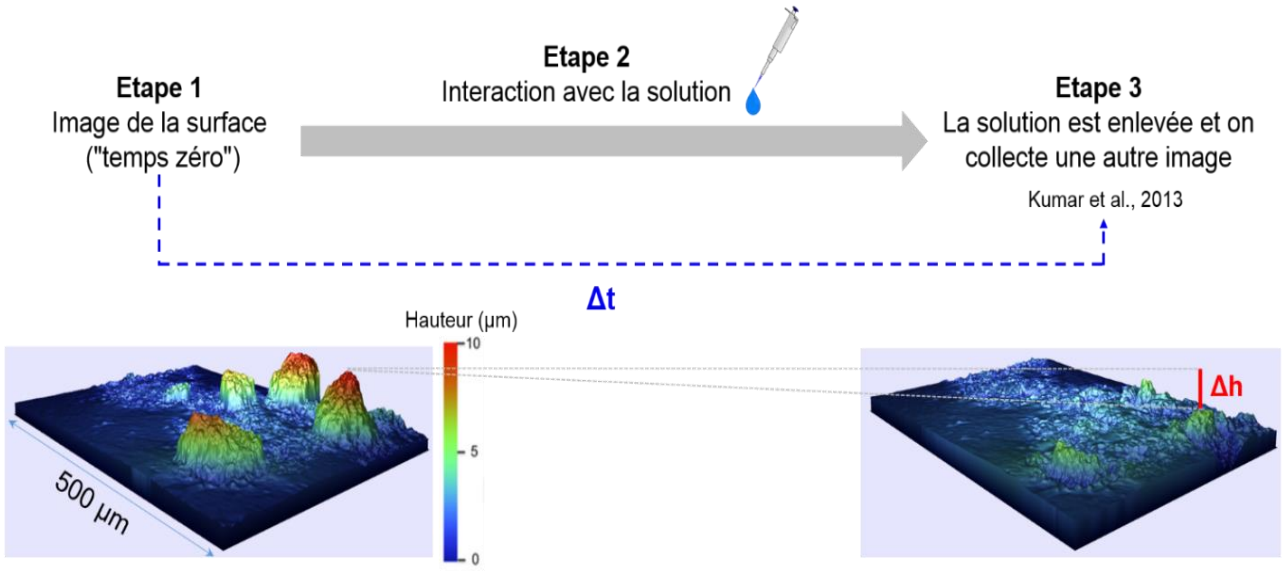

Figure 25. Schéma du protocole expérimental.

Après un traitement des données acquises, il est possible de calculer la vitesse de dissolution/précipitation selon la relation suivante :

$$R\ (\mathrm{nm/h}) = {}^{\Delta h}/_{\Delta t}$$

où Δh est le changement de hauteur de la surface de l'échantillon (en nm) et Δt le temps (heures) durant lequel la solution est en contact avec l'échantillon. Δh est négatif lorsque la surface de l'échantillon s'éloigne de l'objectif et cela signifie que la dissolution se produit, tandis que Δh est positif lorsque la surface de l'échantillon avance vers l'objectif (i.e. précipitation). La vitesse peut être aussi exprimée en $mol \cdot m^{-2} \cdot s^{-1}$ si on divise ${}^{\Delta h}/_{\Delta t}$ par le volume molaire ($m^3 \cdot mol^{-1}$) de l'échantillon.

Pour étudier les cinétiques de dissolution des serpentines ferrifères, on utilisera des solutions ayant différents pH (d'acide à alcalin), dont les compositions seront modifiées pas-à-pas sur la base des résultats obtenus. Par exemple, chaque expérience pourra être répétée en ajoutant des composés organiques dans les solutions, car ils peuvent être présents dans le milieu de formation des serpentines, e.g. dans les météorites. Le rôle des composés organiques dans la dissolution/précipitation des minéraux n'est pas négligeable d'après certains auteurs (Harrison et Thyne, 1992 ; Franklin et al., 1994 ; Welch et Ullman, 1996) bien qu'il soit encore débattu (Brantley et Chen, 1995 ; Hanowksi et Brearley, 2001).

Etant donné que le VSI est conçu pour collecter des images à température ambiante, les mesures seront d'abord effectuées à 25° C. Puis elles pourront être répétées à d'autres températures pour

reproduire le plus fidèlement possible les conditions réelles de formation des serpentines dans les différents milieux. Par exemple, en milieu anthropique, la température dans le site de stockage varie dans l'espace (éloignement du colis de déchets) et dans le temps (décroissance radioactive) (Fig. 26 - ANDRA, 2005). Des variations de température peuvent se vérifier aussi en milieu extraterrestre lors de la formation des serpentines pendant l'altération aqueuse des météorites à cause de la fusion de la glace provoquée par désintégration de l'^{26}Al.

Pour tester les effets de la température, il est possible de retirer l'échantillon du VSI, de le chauffer/refroidir ailleurs et de le repositionner exactement au même endroit pour poursuivre les expériences. Cette procédure a été testée pour des températures comprises entre 3 et 45 °C (Pignatelli et al., 2016). Ainsi, au moins trois expériences à différentes températures ont été réalisées et on peut extrapoler les taux de dissolution/précipitation pour d'autres températures par régression linéaire.

Dans un second temps, je souhaite utiliser une nouvelle cellule expérimentale brevetée à l'Université de l'UCLA en collaboration avec l'entreprise Zygo pour monitorer les changements de la composition de la solution pendant l'interaction avec l'échantillon, car cette cellule peut être connectée à la chromatographie ionique (des tests sont en cours) et permet d'acquérir les images sans enlever la solution. Cela permet de comprendre l'évolution du fluide.

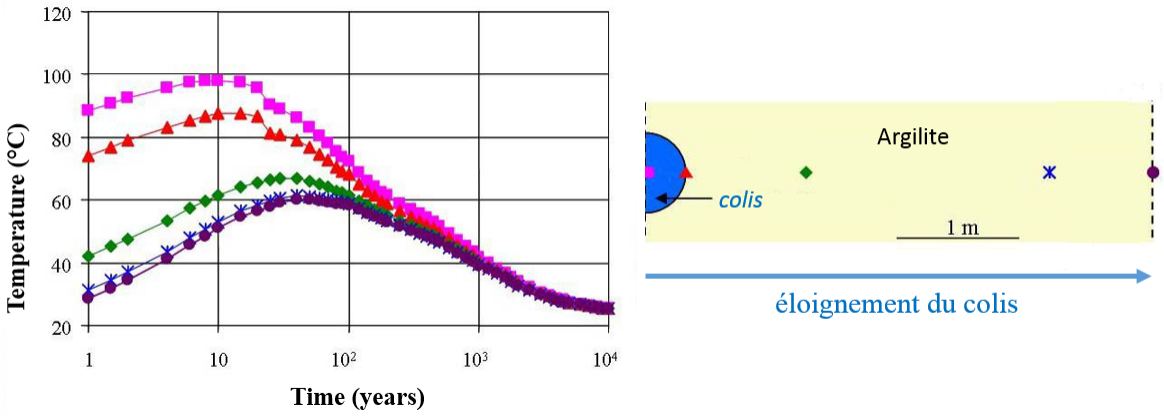

Figure 26. Variation de la température dans le site de stockage en fonction du temps (suite à la décroissance radioactive) et de l'espace (éloignement du colis de déchets) – ANDRA, 2005.

(5) Etude des serpentines trouvées dans les échantillons naturels.

Les informations sur la formation des serpentines ferrifères sont incomplètes et/ou très difficiles à reconstituer à travers l'étude d'échantillons naturels. Souvent, ils ne sont pas collectés *in situ* et la plupart proviennent de collections privées ou publiques, perdant toute information sur le contexte géologique de formation. Néanmoins, des cristaux de cronstedtite provenant de la mine d'or de Salsigne donnés par un collectionneur privé et des cristaux prêtés par l'Université de

Prague sont actuellement disponibles. D'autres échantillons terrestres et extraterrestres pourront être demandés au Muséum National d'Histoire Naturelle de Paris ou au Musée de Minéralogie de MINES ParisTech.

Par analogie entre les serpentines ferrifères et les serpentines naturelles, on pourra reconstruire l'environnement de formation de ces dernières, sur la base des informations acquises dans les étapes 1-4 du projet.

Pour étudier les serpentines dans des échantillons terrestres et extraterrestres, on prévoit une approche multi-technologique organisée comme suit: (i) caractérisations pétrographiques et chimiques par microscopie électronique à balayage (MEB) et analyse par microsonde électronique (EPMA) afin d'analyser à la fois les serpentines et leur paragenèse. (ii) Caractérisation structurale par diffraction des rayons X sur monocristal ou diffraction électronique 3D en fonction de la taille des cristaux (par exemple les plus grosses serpentines terrestres peuvent avoir une taille de 100 μm (Fig. 27), alors que celles trouvées dans les météorites sont < 1 μm, comme montré dans la figure 17. (iii) Quantification du rapport $Fe^{3}+/\Sigma Fe$ par STXM-XANES.

Figure 27. Image sous la binoculaire de cristaux naturels de cronstedtite (noirs) provenant de la mine de Salsigne, mélangés à des sulfures et des carbonates.

Conclusions

Ce projet qui se situe dans le domaine de la recherche fondamentale, présente des nouvelles perspectives et des implications en minéralogie, géochimie et cosmochimie. Le projet permet d'aborder des questions importantes concernant les conditions de formation et le champ de stabilité des serpentines ferrifères dans les environnements terrestres et extraterrestres. Ces conditions sont vraisemblablement favorables à l'évolution de la matière organique dans le système solaire, qui a rendu la vie possible sur Terre. Les serpentines auraient pu servir de centre actif pour les molécules organiques, facilitant la polymérisation des monomères prébiotiques sur leurs surfaces (Bishop et al., 2013 ; Erastova et al., 2017). Ces minéraux auraient pu aussi agir de catalyseurs pour la synthèse de protéines, RNA et ADN (Brack, 2006 ; Pedreira-Segade et al., 2015). La formation des molécules organiques serait liée à la production de H_2 pendant la serpentinisation, selon la réaction de Fischer-Tropsch :

$$n\mathrm{CO_2} + (2n+1)\mathrm{H_2} \rightarrow \mathrm{C}_n\mathrm{H}_{2n+2} + n\mathrm{H_2O}$$

Puis en présence d'ammoniac NH_3 ou de cyanure d'hydrogène HCN, on pourrait obtenir des acides aminés par la synthèse de Strecker (Nuth et al., 2008), qui est catalysée par la présence de Fe^{2+} in solution, comme c'est le cas au cours de la formation des serpentines ferrifères. Le lien entre ces minéraux et les composés organiques semble être étayé par leur présence simultanée dans la matrice des météorites de type CM et CI e.g. Murchison (Pearson et al., 2002 ; Sephton, 2004). Dans ces météorites, on trouve des acides carboxyliques, hydrocarbures aromatiques et surtout des acides aminés (Sephton et al., 2004). Bien que ce soient les mêmes composés organiques sur Terre, le problème de la chiralité surligne encore l'absence de clarté quant aux conditions de formation qui affectent leur structure. En fait, dans le milieu terrestre seulement l'énantiomère gauche de ces composés organiques existe (L-form, en anglais) (Fitz et al., 2007). En revanche, dans le milieu extraterrestre, les deux énantiomères sont présents bien que l'énantiomère gauche soit le plus abondant (Sephton, 2004). Ainsi, comprendre les conditions dans lesquelles les serpentines et les composés organiques se forment pourrait permettre d'élucider cette différence et de mieux comprendre l'évolution de la matière organique.

Par ailleurs, H_2 et Fe^{2+} produits pendant la formation des serpentines ferrifères peuvent être utilisés pour la synthèse de biomasse par de micro-organismes chimiosynthétiques. Ceux-ci peuvent extraire l'énergie métabolique dont ils ont besoin grâce à des réactions d'oxydoréduction réalisées par leurs cellules (McCollom et Seewald, 2013). Si H_2 est le

donneur d'électron, plusieurs accepteurs sont possibles et différents types de micro-organismes chimiosynthétiques existent: e.g. les organismes qui utilisent la réaction d'oxydation de l'hydrogène suivant la réaction $H_2 + 1/2O_2 \rightarrow H_2O$ ou ceux méthanogènes qui sont anaérobiques et produisent du méthane selon la réaction $4H_2 + CO_2 \rightarrow CH_4 + 2H_2O$ (Jannasch, 1985).

Finalement, les données issues de ce projet seront utiles non seulement pour une meilleure compréhension du passé, mais aussi pour prédire l'évolution minéralogique et chimique des serpentines ferrifères au fil du temps dans les systèmes géologiques et anthropiques.

Références

Andra (2005) Dossier 2005 Argile - Référentiel du site de Meuse/Haute- Marne, Rapport Andra n°C.RP.ADS.04.0022

Bailey (1969) Clays Clay Miner., 17, 355-371.

Bailey (1988) Clay Minerals, 23, 237-247.

Barber (1981) Geochim. Cosmochim. Acta, 45, 945-970.

Barbour, Ress (2004) J. Dent., 32, 591-602.

Beaufort, Rigault, Billon, Billault, Inoue (2015) Clay Minerals, 50, 497-523.

Bhattacharyya (1983) Clays Clay Miner., 31, 173-182.

Bildstein, Trotignon, Perronnet, Jullien (2006) Phys. Chem. Earth 31, 618–625.

Bishop, Loizeau, McKeown, Saper, Dyar, Marais, Parente, Murchie (2013) Planet. Space. Sci., 86, 130-149.

Blanc, Lassin, Piantone, Azaroual, Jacquemet, Fabbri, Gaucher, (2012) Appl. Geochem. 27 (10), 2107–2116.

Bourdelle, Benzerara, Beyssac, Cosmidis, et al. (2013) Contrib. Mineral. Petr., 166, 423-434.

Bourdelle, Mosser-Ruck, Truche, Lorgeoux, Pignatelli, Michau (2017) Chem. Geol. 466, 600-607.

Bourdelle, Truche, Pignatelli, Mosser-Ruck, Lorgeaux, Roszypal, Michau (2014) Chem. Geol., 381, 194-205.

Brack (2006) Handbook of Clay Science. Chapter 7.4, 379-391.

Brantley, Chen (1995) Chemical weatherinf rates of silicates. Rev. Mineral., Mineralogical Society of America, 31, 119-172.

Brearley (2006) The action of water. In Meteorites and the Early Solar System II, 584–624.

Brindley (1951) Mineral. Mag., 29, 502–525.

Browning, McSween, Zolensky (1996) Geochim. Cosmochim. Acta, 60, 2621–2633.

Calvin (1998) Geophys. Res. Lett., 25, 1597-1600.

Calvin, King (1997) Meteorit. Planet. Sci., 32, 693–701.

Changela & Bridges (2011) Meteorit. Planet. Sci., 45, 1847-1867.

Chapelle, O'Neill, Bradley, Methé, Ciufo, Knobel, Lovley (2002) Nature, 415, 312-315.

Daval, Hellmann, Saldi, Wirth, Knauss (2013) Geochim. Cosmochim. Acta, 107, 121-134.

Daval, Sissmann, Menguy, Saldi, Guyot, Martinez, et al. (2011) Chem. Geol., 284, 193-209.

de Combarieu, Barboux, Minet (2007) Phys. Chem. Earth, 32, 346-358.

de Combarieu, Schlegel, Neff, Foy, Vantelon, Barboux, Gin (2011) Appl. Geochem., 26, 65-79.

de Groot P. (2011) Phase Shifting Interferometry. In: Leach R. (eds) Optical Measurement of Surface Topography. Springer, Berlin, Heidelberg.

Dornberger-Schiff, Ďurovič (1975) Clays Clay Miner., 23, 219–229.

Ďurovič (1997) Ceram. Silik., 41, 98–104.

Elmaleh, Bourdelle, Caste, Benzerara, Leroux, Devouard (2015) Geochim. Cosmochim. Acta, 158, 162-178.

Elmaleh, Tarantino, Zema, Devouard, Fialin (2012) Geochem. Geophy. Geosy., 13, Q05Z42.

Erastova, Degiacomi, Fraser, Greenwell (2017) Nature Communications, 8, 2033.

Evans, Dyar, Kuehner (2012) Am. Mineral., 97, 184-197.

Fischer, Luttge (2017) Earth Planet. Sci. Lett., 457, 100-105.

Fitz, Reiner, Rode (2007) Pure Appl. Chem., 79(12), 2101-2117.

Franklin, Hajash, Dewers, Tieh (1994) Geochim. Cosmochim. Acta, 58, 4259-4279.

Frondel (1962) Am. Mineral., 47, 781-783.

Gailhanou, Blanc, Rogez, Mikaelian,Kawaji, et al. (2012) Geochim. Cosmochim. Acta, 89, 279-301.

Gailhanou, Vieillard, Blanc, Lassin, Denoyel, Bloch, De Weireld, Gaboreau, Fialips, Madé, Giffaut (2017) Appl. Geochem., 82, 146–163.

Ganteaume, Coten, Decressac (1991) Thermochim. Acta, 178, 81-98.

Garvie, Zega, Rez, Buseck (2004) Am. Mineral., 89(11–12), 1610–1616

Geiger, Henry, Bailey, Maj (1983) Clays Clay Miner., 31, 97-108.

Gemmi, Mugnaioli, Gorelik, Kolb, Palatinus, et al. (2019) ACS Central Science, 5, 1315-1329

Gole (1980a) Can. Mineral., 18, 205-214.

Gole (1980b) Am. Mineral., 65, 8-25.

Guggenheim, Bailey, Eggleton, Wilkes (1982) Can. Mineral., 20, 1-18.

Guo, Eiler (2007) Geochim. Cosmochim. Acta, 71, 5565-5575.

Hanowski, Brearley (2001) Geochim. Cosmochim. Acta, 65, 495–518.

Harrison, Thyne (1992) Geochim. Cosmochim. Acta, 56, 565-586.

Hicks, Bridges, Gurman (2014) Geochim. Cosmochim. Acta, 136, 194-210.

Hybler, Ďurovič, Kogure (2008) Acta Crystallogr., A64, 498–499.

Hybler, Klementová, Jarošová, Pignatelli, Mosser-Ruck, Ďurovič (2018) Clays Clay Miner., 66, 4, 209-232.

Hybler, Petříček, Ďurovič, Smrčok (2000) Clays Clay Miner., 48, 331-338.

Hybler, Petřiček, Fábry, Ďurovič (2002) Clays Clay Miner., 50, 601-613.

Hybler, Sejkora, Venclík (2016) Eur. J. Mineral., 28, 765–775.

Hybler, Števko, Sejkora (2017) Eur. J. Mineral., 29, 91–99.

Iijima, Matsumoto (1982) Clays Clay Miner., 30, 264-274

Jannasch (1985) Proc. R. Soc. Lond., 225, 277-297.

Kogure, Hybler, Yoshida (2002) Clays Clay Miner., 50, 504-513.

Kolb, Gorelik, Kübel, Otten, Hubert (2007) Ultramicroscopy, 107, 507–513.

Kolb, Gorelik, Otten (2008) Ultramicroscopy, 108, 763–772.

Kumar, Reed, Sant (2013) J. Am. Ceram. Soc., 96, 2766–2778.

Lanson, Lantenois, Aken, Bauer, Plançon (2012) Am. Mineral. 97, 864–871.

Lantenois, Lanson, Muller, Bauer, Jullien, Plançon (2005) Clays Clay Miner., 53, 597–612.

Lauretta, Hua, Buseck (2000) Geochim. Cosmochim. Acta, 64, 3263-3273.

Lauterbach, McCammon, van Aken, Langenhorst, Seifert (2000) Contrib. Mineral. Petr., 138(1), 17–26

Lee, Chatzitheodoris (2016) Meteorit. Planet Sci., 51, 1643-1653.

López-García, Manteca, Prieto, Calvo (1992) Bol. Soc. Esp. Mineral., 15, 21-25.

Luttge, Arvidson, Fischer (2013) Elements, 9, 183-188.

McCollom, Bach (2009) Geochim. Cosmochim. Acta, 73, 856-875.

McCollom, Seewald (2007) Chemical Reviews, 107, 382-401.

McCollom, Seewald (2013) Elements, 9, 129-134.

Miot, Benzerara, Morin, Kappler, Bernard, et al. (2009) Geochim. Cosmochim. Acta, 73(3), 696–71.

Mosser-Ruck, Cathelineau, Guillaume, Charpentier (2010) Clays Clay Miner., 58, 280-291.

Mugnaioli, Gemmi (2018). Zeitschrift für Kristallographie, 233, 163-178.

Mugnaioli, Gorelik, Kolb (2009) Ultramicroscopy, 109, 758–765.

Müller, Kurat, Kracher (1979) Tschermaks Mineral. Petrogr. Mitteilungen, 26, 293–304.

Nuth, Johnson, Manning (2008) Astrophys. J. Lett, 673, L225.

Palmer, Lauretta (2011) Meteorit. Planet. Sci., 46, 1587–1607.

Pearson, Sephton, Kearsley, Bland, Franchi, Gilmour (2002) MAPS, 37, 1829-1833.

Pedreira-Segade, feuille, Pelletier, Michot, Daniel (2015) Geochim. Cosmochim. Acta, 176, 81-95.

Pignatelli, Bourdelle, Bartier, Mosser-Ruck, Truche, Mugnaioli, Michau (2014) Chem. Geol., 387, 1–11.

Pignatelli, Duseck, De Titta, Nespolo (2011) Eur. J. Mineral., 23, 73-84.

Pignatelli, Kumar, Bauchy, Sant (2016) Langmuir, 32, 4434-4439.

Pignatelli, Kumar, Field, Wang, Yu, Le Pape, Bauchy, Sant (2016) Scientific Report, 6, 20155.

Pignatelli, Marrocchi, Mugnaioli, Bourdelle, Gounelle (2017) Geochim. Cosmochim. Acta, 209, 106-122.

Pignatelli, Marrocchi, Vacher, Delon, Gounelle (2016) Meteorit. Planet. Sci., 51, 785-805.

Pignatelli, Mosser-Ruck, Mugnaioli, Sterpenich, Gemmi (2020) Clays and Clay Miner., 68, 394-412.

Pignatelli, Mugnaioli, Hybler, Mosser-Ruck, Cathelineau, Michau (2013) Clays Clay Miner., 61,277–289.

Pignatelli, Mugnaioli, Marrocchi (2018) Eur. J. Mineral., 30, 349-354.

Pignatelli, Mugnaioli, Mosser-Ruck, Barres, Kolb, Michau (2014) Eur. J. Mineral., 26, 221–229.

Pignatelli, Nespolo (2011) Eur. J. Mineral., 23, 703-715.

Rivard, Pelletier, Michau, Razafitianamaharavo, Bihannic, Abdelmoula, Ghanbaja, Villiéras (2013) Am. Mineral., 98, 163-180.

Rivas-Sanchez, Alva-Valdivia, Arenas-Alatorre, Urrutia-Fucugauchi, Ruiz-Sandoval, Ramos-Molina (2006) Earth Planets Space, 58, 1389-1400.

Roosz, Vieillard, Blanc, Gaboreau, Gaihanou, Braithwaite, Montouillout, Denoyel, Henocq, Madé (2018) Appl. Geochem., 92, 140-156.

Rubin, Trigo-Rodríguez, Huber, Wasson (2007) Geochim. Cosmochim. Acta, 71, 2361–2382.

Schulte, Shock (2004) Meteorit. Planet. Sci., 39, 1577-1590.

Šegvić, Zanoni, Moscariello (2020) Mar. Petrol. Geol., 112, 104064

Sephton (2004) Astronony & Geophysics, 45(2), 2.08-2.14.

Seyfried, Foustoukos, Fu (2007) Geochim. Cosmochim. Acta, 71, 3872–3886.

Smrčok, Ďurovič, Petříček, Weiss (1994) Clays Clay Miner., 42, 544-551.

Streit, Kelemen, Eiler (2012) Contrib. Mineral. Petrol., 164, 821-837.

Tomeoka, Buseck (1985) Geochim. Cosmochim. Acta, 49, 2149–2163.

Tosca, Guggenheim, Pufahl (2016) GSA Bulletin, 128, 511-530.

Wahle, Bujnowski, Guggenheim, Kogure (2010) Clays Clay. Miner., 58, 364-376.

Welch, Ullman (1996), Geochim. Cosmochi. Acta, 60, 2939-2948.

Wilson, Cressey, Cressey, Cuadros, Ragnarsdottir, Savage, Shibata (2006) Geochim. Cosmochim. Acta, 70, 323-336.

Zega, Buseck (2003) Geochim. Cosmochim. Acta, 67, 1711–1721.

Zolensky, Mittlefehldt, Lipschutz, Wang, Clayton, Mayeda, Grady, Pillinger, David (1997) Geochim. Cosmochim. Acta 61, 5099–5115.

Zolotov (2014) Icarus, 228, 13–26.

ANNEXES :

les publications les plus représentatives de l'activité de recherche

Eur. J. Mineral.
2011, **23**, 73–84
Published online December 2010

Structural modelling, refinement and possible formation mechanism of a $4M_3$ non-MDO ferriphlogopite (Ruiz Peak volcano)

ISABELLA PIGNATELLI[1], MICHAL DUSEK[2], GEORGE DE TITTA[3] and MASSIMO NESPOLO[1,*]

[1] CRM[2], UMR-CNRS 7036, Institut Jean Barriol, Faculté des Sciences et Technologies, Nancy-Université, BP 70239, Boulevard des Aiguillettes, 54506 Vandœuvre-lès-Nancy, France
*Corresponding author, e-mail: Massimo.Nespolo@crm2.uhp-nancy.fr
[2] Institute of Physics, Academy of Science of the Czech Republic, Cukrovarnicka 10, 16253 Praha 6, Czech Republic
[3] Hauptman-Woodward Medical Research Institute, 700 Ellicott Street, Buffalo, NY 14203-1102, USA

Abstract: The first reliable structural refinement of a non-MDO mica polytype from single-crystal X-ray diffraction data is presented. The sample is a 4-layer ferriphlogopite from the Ruiz Peak volcano, New Mexico, with cell parameters $a = 5.3166(2)$ Å, $b = 9.2080(2)$ Å, $c = 39.814(1)$ Å, $\beta = 92.550(3)^\circ$. Its stacking sequence, determined by the periodic-intensity-distribution (PID) analysis, is expressed by the RTW symbols $22\bar{2}\bar{2}$: it corresponds to $4M_3$ in Ramsdell notation. Structural refinement in the space group $C2/c$ converges to $R_{(obs)} = 6.3$ %. This is the highest-symmetry space group compatible with the observed stacking sequence and means that no desymmetrisation occurs in this polytype. The peaks of electron density in the Fourier map show that the polytype is meso-octahedral and contains two independent layers in the asymmetric unit, one with symmetry $C12/m(1)$, the other $C12(1)$, which however are both of type M1. The meso-octahedral nature of the layers is confirmed by the Charge Distribution analysis. The OD symbol for the polytype is |1.1 3.3 5.5 3.3|. The formation of this polytype by spiral growth can be interpreted either as the result of the occurrence of a stacking fault in the exposed ledge of a $3T$ polytype or as a cell-twin formed by two $2M_1$ substructures. In both interpretations the $4M_3$ structure is decomposed in two basic structures ($3T$ and $1M$ or two $2M_1$); the formation of a non-MDO polytype from two substructures corresponding to MDO polytypes explains why the second and fourth layers of the polytype are meso-octahedral even if the space-group symmetry does not force the *cis* sites to be equivalent.

Key-words: mica polytypism, ferriphlogopite, non-MDO polytype, PID analysis, OD character, structural refinement, Charge Distribution.

1. Introduction

Micas are common layer silicates whose layer consists of one octahedral sheet between two tetrahedral sheets of opposite polarity (T-O-T or 2:1 layer, also known as the M layer). The general formula of micas is $I_1M_{2-3}\square_{1-0}Z_4O_{10}A_2$ (Rieder *et al.*, 1998), where I represents the interlayer cation, M and Z respectively the octahedrally and tetrahedrally coordinated cations, $\square$ a vacancy and A is commonly OH, F, Cl. In the octahedral sheet, the cation sites are termed $M1$, $M2$ or $M3$ on the basis of their position with respect to the OH group ($M1$ is in *trans* position, the others in *cis* position). If these three sites are all occupied the sheet is said *trioctahedral*, otherwise *dioctahedral* (one site is vacant). Such a dichotomy is often a poor description of the nature of the octahedral sheet, because the coexistence of cations with different oxidation numbers frequently leads to a global site occupancy in the sheet intermediate between 2 and 3. A more precise and rigorous classification is that in *families*, on the basis of the cation and vacancy distribution in the M sites. Micas then belong to the *homo-octahedral* family, when the sites have the same occupation and size; the *meso-octahedral* family, when two sites have equal occupation and size; and the *hetero-octahedral* family, when all sites are differently occupied (see *e.g.*, Nespolo & Ďurovič, 2002). Interlayer cations find place between successive layers and their coordination depends on the relative orientation of layers. Because of the pseudo-hexagonal symmetry of the basal oxygen atoms in the tetrahedral sheets, the M layer can take six possible orientations, rotated by $n60^\circ$ ($0 \leq n \leq 5$). For $2n \times 60^\circ$ rotations, the interlayer coordination is trigonal antiprismatic and the polytype belongs to the *subfamily A*; $(2n + 1) \times 60^\circ$ rotations are characteristic of *subfamily B* polytypes, where the interlayer cations have trigonal prismatic coordination (Backhaus & Ďurovič, 1984). Polytypes with both kinds of rotations also exist: they are called *mixed-rotation* polytypes (Nespolo, 1999).

The orientation of the M layers can be expressed by different orientational or rotational symbols: Z symbols

DOI: 10.1127/0935-1221/2011/0023-2078
0935-1221/11/0023-2078 $ 5.40

(Zvyagin, 1962), OD symbols (Ďurovič, 2004), TS symbols (Takeda & Sadanaga, 1969) – orientational – and RTW symbols (Ross *et al.*, 1966) – rotational – are the most used. Hereafter the OD symbols are used as orientational symbols because they are the richest in information.

Polytypes are classified in *MDO* (Maximum Degree Order) or *non-MDO* polytypes (Dornberger-Schiff *et al.*, 1982). Polytypes in which all layer triples, quadruples, *etc.* are geometrically equivalent or, at least, which contain the smallest possible number of kinds of *n*-tuples of layers are called MDO polytypes. By using the Ramsdell notation (1947), MDO polytypes in micas are $1M$, $2M_1$, $2M_2$, $2O$, $3T$ and $6H$; all the others are non-MDO.

The study of non-MDO mica polytypes is important to understand their formation mechanism. In fact, they are commonly formed far from equilibrium conditions; their occurrence frequency is not simply a function of the number of layers in the period but depends on the structural control related to the crystal chemistry and to the geometrical distortions of the structure (Baronnet, 1980); they are often unique (the occurrence of a non-MDO polytype in different samples being a rather exceptional event), while MDO polytypes are more frequent and widely spread in different environments. In micas, the crystallization of non-MDO polytypes occurs, in fact, in the final differentiation stage of magma, characterized by the presence of super-critical vapour phase (Tomisaka, 1958, 1962; Ross *et al.*, 1966). In these conditions heterogeneous nucleation takes place and the spiral growth mechanism becomes active with the decreasing of the supersaturation, determining the final stacking sequence. The experimental observations show that statistically the frequency of occurrence of non-MDO polytypes increases when the structural control decreases, provided that this control is nevertheless enough to preserve a ''stacking memory'' during the growth (Güven, 1971; Baronnet, 1980); otherwise, a disordered polytype is obtained instead.

The occurrence of non-MDO polytypes is also related to the possibility of lamellar crystals to move in the crystallization medium during their growth, like ''flying magic carpets'' (Sunagawa & Tomura, 1976). This movement can determine the deposition of a small crystal from the fluid on the surface of another growing crystal. If the small platelet is deposited far from the core of spiral growth, a new polytype can form from the interaction of the two stacking sequences (platelet mechanism, Takeda & Ross, 1995). The knowledge of the structural details of the polytypes is necessary to understand their formation mechanism, in particular for the likely relation between the cation distribution in the octahedral sheets and the formation mechanism (Nespolo, 2001).

In the past, several stacking sequences of non-MDO polytypes have been identified by means of X-ray diffraction, oblique-texture electron diffraction (Zvyagin, 1967; Zvyagin *et al.*, 1979) and high-resolution transmission electron microscopy (*e.g.*, Kogure & Nespolo, 1999), but no reliable structural refinement of non-MDO mica polytypes has been performed. The only examples reported so far are those of $6M_1$ and $3M_2$ polytypes of a lepidolite sample from Tørdal, Norway (Rule *et al.*, 1987), which however converged only at $R_1 = 23$ and 12 % respectively. In this work, the study of non-MDO $4M_3$ polytype is essentially divided in two parts: in the first one the stacking sequence has been determined by means of the Periodic Intensity Distribution (PID) function, introduced by Takeda (1967) and expressed by OD symbols in the homo-octahedral approximation. The maximal space-group type compatible with stacking sequence has been derived by exploiting the symmetry properties of the OD symbols. In the second part the OD theory has been used to obtain a structural model for the refinement, applying the stacking vectors to the atomic coordinates of the $1M$ polytype.

2. Specimen description

A crystal of ferriphlogopite from rhyodacite ash flow at Ruiz Peak (New Mexico) was analysed in this study. It belongs to the same rock hand specimen previously investigated, among others, by Ross *et al.* (1966).

The crystal is a very thin plate, flattened on {001}, with dimensions 0.20 × 0.16 × 0.01 mm. Its colour, dark reddish brown, is due to the oxidation process which occurred during and after the lava eruption. The oxidation of Fe^{+2} to Fe^{+3}, useful to re-equilibrate the ferriphlogopite crystals with respect to the oxygen fugacity, causes the change of colour from dark to reddish brown (Takeda & Ross, 1975). Furthermore, Robbins & Strens (1972) emphasise the influence of octahedral Ti on the particular colour of the ferriphlogopite crystals.

The chemical composition, obtained by electron microprobe analysis on 21 points (Table 1), is $(K_{0.848}\,Na_{0.163}Ba_{0.04})(Mg_{1.822}Al_{0.146}Fe_{0.643}Ti_{0.39})(Si_{2.908}\ Al_{1.092})\ O_{11.455}F_{0.117}\ OH_{0.428}$. The microprobe analysis was performed on the basis of ferrous iron, while the sample under investigation is highly oxidised and contains mainly ferric iron. This explains the slight difference between the iron content in the formula and the average in Table 1. The formula is in reasonably good agreement with the wet chemical analysis previously reported by Takeda & Ross (1975) for a different crystal from the same sample. The content of OH has been derived by the difference between the total positive and negative charges to assure the electrostatic neutrality.

3. Experimental procedure

Single-crystal X-ray diffraction of a fragment of the sample was obtained with an Oxford SuperNOVA microsource at room temperature, using mirror-monochromatized Mo$K\alpha$ radiation ($\lambda = 0.7107$ Å) at the CRM^2 laboratory of Nancy-Université. The Oxford Diffraction package CrysAlisPro (2009) was used for cell determination, data collection and data reduction. The unit-cell parameters, refined from 7678 reflections using the least-squares method, are $a = 5.3166(2)$, $b = 9.2080(2)$, $c = 39.814(1)$, $\beta = 92.550(3)^\circ$, $V = 1947.15(6)$ Å^3.

Table 1. Details of electron microprobe analysis.

Atomic %	Na	Si	Al	Fe	O	Mg	K	F	Ti	Ba
1	0.778	14.568	5.783	4.258	58.007	8.875	4.722	0.772	2.084	0.102
2	0.989	15.503	6.265	3.607	58.806	8.434	3.837	0.397	1.789	0.220
3	0.870	14.618	6.417	3.843	58.449	9.427	3.794	0.450	1.854	0.211
4	0.916	14.625	6.318	3.697	58.423	9.621	4.013	0.308	1.833	0.191
5	0.725	14.692	6.007	4.200	58.201	8.887	4.338	0.726	1.976	0.205
6	0.767	14.421	6.194	4.013	58.125	9.218	4.268	0.728	1.966	0.212
7	0.792	14.519	6.164	4.110	58.247	9.275	4.028	0.533	1.922	0.177
8	0.804	14.510	6.116	4.138	58.140	9.163	4.374	0.605	1.913	0.198
9	0.836	14.517	6.183	4.129	58.252	9.179	4.145	0.582	1.974	0.189
10	0.746	14.526	6.206	4.064	58.312	9.173	4.271	0.461	1.968	0.207
11	0.827	14.421	6.256	4.063	58.125	9.273	4.242	0.608	1.906	0.223
12	0.796	14.597	6.193	4.008	58.327	9.077	4.216	0.556	2.032	0.195
13	0.835	14.414	6.109	4.083	58.254	9.237	4.237	0.509	2.083	0.166
14	0.874	14.384	6.081	4.128	58.173	9.272	4.250	0.561	2.028	0.161
15	0.723	14.244	5.994	4.458	58.001	8.652	4.562	0.834	2.223	0.238
16	0.824	14.499	6.119	4.228	58.146	9.038	4.493	0.495	1.893	0.198
17	0.749	14.461	6.216	4.295	58.097	9.006	4.477	0.605	1.847	0.178
18	0.859	14.328	6.092	4.312	58.038	9.202	4.354	0.630	1.951	0.193
19	0.854	14.556	6.263	3.955	58.384	9.210	4.212	0.309	1.925	0.178
20	0.750	14.535	6.312	4.095	58.392	9.135	4.163	0.423	2.001	0.212
21	0.797	14.399	6.668	3.982	57.966	8.928	4.004	1.214	1.808	0.184
Average	0.815	14.540	6.188	4.079	58.232	9.109	4.238	0.586	1.951	0.192
Normalized	0.163	2.908	1.238	0.816	11.646	1.822	0.848	0.117	0.390	0.038

Another fragment of the same crystal was measured at the Academy of Sciences of the Czech Republic, Prague, with larger exposure time. The data were collected at room temperature with ω-scan, on an Oxford Gemini diffractometer and graphite-monochromated Mo$K\alpha$ radiation ($\theta_{min} \sim 4.61$ and $\theta_{max} \sim 27.58°$) with Enhanced(Mo) collimator. The crystal-detector distance was fixed at 120 mm, the width scan was 0.5°/frame and the exposure time 120 s/frame. The Oxford package CrysAlisPro was used again to determine the cell and also for the data collection and reduction. For the primitive cell, the parameters refined from 4234 reflections are: $a = 5.3207(2)$ Å, $b = 5.3195(3)$ Å, $c = 39.842(2)$ Å, $\alpha = 88.695(4)°$, $\beta = 87.445(4)°$ and $\gamma = 60.040(5)°$, which give slightly different values, and not rigorously monoclinic, with respect to the Nancy data set, for the *mC* cell [$a = 5.3207(2)$ Å, $b = 9.2173(4)$ Å, $c = 39.8413(18)$ Å, $\alpha = 89.969(4)°$, $\beta = 92.556(3)°$ $\gamma = 89.953(3)°$, V = 1951.96(15) Å^3]. This small discrepancy is most likely due to the different beams used in the data collections: the mirror-collimated Mo beam in Nancy, in fact, is much sharper than the corresponding one in Prague, which uses optic fibres.

After correcting the data from Lorentz-polarization the analytical absorption correction was not applied. This correction, in fact, gives a diverging Wilson curve and, consequently, a negative overall parameter, because of the very anisotropic morphology of the crystal. Finally the scaling and the empirical absorption correction were, instead, performed using spherical harmonics (Blessing, 1995). The R_{int} of the data reduced in *P*1 is 3.1 % on 12065 reflections.

The merging of equivalent reflections was performed with Sortav program (Blessing, 1997), after the cell transformation from *P*1 to *C*1.

As shown by the cell parameters, the polytype is metrically monoclinic, but its structure can present a lower symmetry. As we cannot know *a priori* the true structural symmetry, we preferred to reduce the data using the lowest space group. The non-conventional *C*1 space group was used instead of *P*1, because all mica polytypes are characterized by a *C*-centred orthorhombic two-dimensional cell, with parameters close to satisfying the pseudo-orthohexagonal relation $b = a3^{1/2}$.

Of the two data sets, the one collected in Prague shows a better overall quality. The Nancy data set, in fact, presents fewer unique reflections and a worse R_{int} value (Table 2). The Prague data set is characterized, moreover, by a better intensity/sigma ratio, because of the longer exposure time used during the measurement.

4. Geometry of diffraction pattern

The geometry of the diffraction pattern is the clue to identify the stacking sequence of mica polytypes. There are, in fact, three types of lattice rows in the diffraction pattern of a mica polytype (Nespolo *et al*., 1997):

- S rows [$h = 0(\mathrm{mod}3)$, $k = 0(\mathrm{mod}3)$]: these reflections are called ''family reflections'' because they are common to all polytypes of the same family and cannot be used for the identification of polytype;
- D rows [$h \neq 0(\mathrm{mod}3)$, $k = 0(\mathrm{mod}3)$]: these reflections are also called ''family reflections'' but they actually determine the subfamily;
- X rows [$k \neq 0(\mathrm{mod}3)$]: ''non-family reflections'' typical of each polytype. An *N*-layer polytype presents *N* reflections in the 1*M* period (1/10 Å^{-1}) along these rows.

Table 2. Experimental details of data collections.

	Nancy	Prague
X-ray power	50 mV 30 mA	55 kV 40 mA
Wavelength of radiation	Mo$K\alpha$	Mo$K\alpha$
Temperature	296 K	297 K
Detector to sample distance	75 mm	120 mm
Number of frames	3683	2040
Rotation width per frame	0.5°	0.5°
Measuring time	25 s	120 s
θ_{min}	3.58°	4.61°
θ_{max}	30.80°	27.58°
Total reflections	29651	12065
Unique reflections	9100	8131
Range of h, k, l	$-7 < h < 7$	$-6 < h < 6$
	$-13 < k < 12$	$0 < k < 11$
	$-56 < l < 51$	$-51 < l < 51$
R_{int}	7.9	3.1

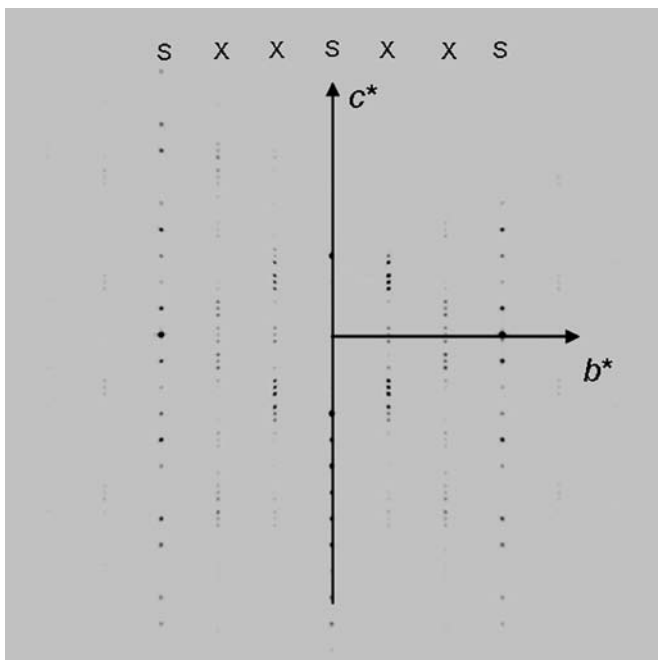

Fig. 1. Diffraction pattern from (0kl)* plane of 4-layer polytype (S = S row and X = X row).

Figures 1 and 2 are the diffraction patterns corresponding to two reciprocal planes obtained by reconstruction of the reciprocal space.

Figure 1 is the diffraction pattern corresponding to the (0kl)* plane; one clearly sees four reflections in the 1/10 $Å^{-1}$ period along the X rows, indicating that the sample is a 4-layer polytype. The number of layers is not a multiple of 3, thus the presence of twinning simulating a longer polytype (apparent polytypism, Takano & Takano, 1958) can be excluded.

Figure 2 is the diffraction pattern corresponding to the (h0l)* plane: the presence of only one reflection in the 1M period (1/10 $Å^{-1}$) along the D rows shows that this polytype belongs to the subfamily A (Nespolo *et al*., 1999).

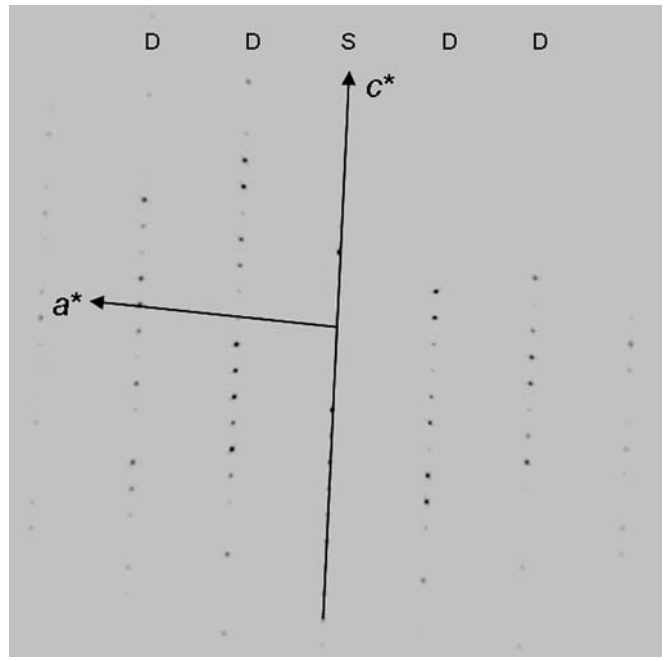

Fig. 2. Diffraction pattern from (h0l)* plane of 4-layer polytype (S = S row and D = D row).

5. Determination of stacking sequence by means of the periodic intensity distribution (PID) function

The stacking sequence of a mica polytype can be determined by means of the periodic intensity distribution (PID) function. This is the Fourier transform of the stacking sequence obtained by removing the modulating effect of the single-layer transform in the structure factor (Takeda, 1967):

$$S^N(\mathrm{hkl}) \approx \frac{G^N(\mathrm{hkl})}{G_o(\mathrm{hkl})}$$

where G^N is the Fourier transform of an N-layer polytype and G_o is the Fourier transform of the single layer (Fig. 3). The periods where G_o is weak are not taken into account, because of the larger relative error on weaker intensities leading to less reliable PID values (Nespolo *et al.*, 1999). Finally, the PID function is normalized as follows, to facilitate the comparison, because the measured intensities on the different periods vary with G_0:

$$\sum_{j=1}^{N} \left[S_j^N \left(hk\hat{l} \right) \right]^2 = N^2$$

where $\hat{l} = l(\bmod N)$. The comparison of the calculated and observed values of the PID allows us to unambiguously identify the stacking sequence of the polytype. However, the only information one gets from the PID analysis is the sequence of stacking vectors, which does not allow differentiating the family and corresponds to assuming that all the M sites are equally occupied. This assumption is called *the homo-octahedral approximation* (Nespolo *et al*., 1999). To distinguish the family (homo, meso or hetero-octahedral) of the polytype one needs to know the electron density in the octahedral sheets: this

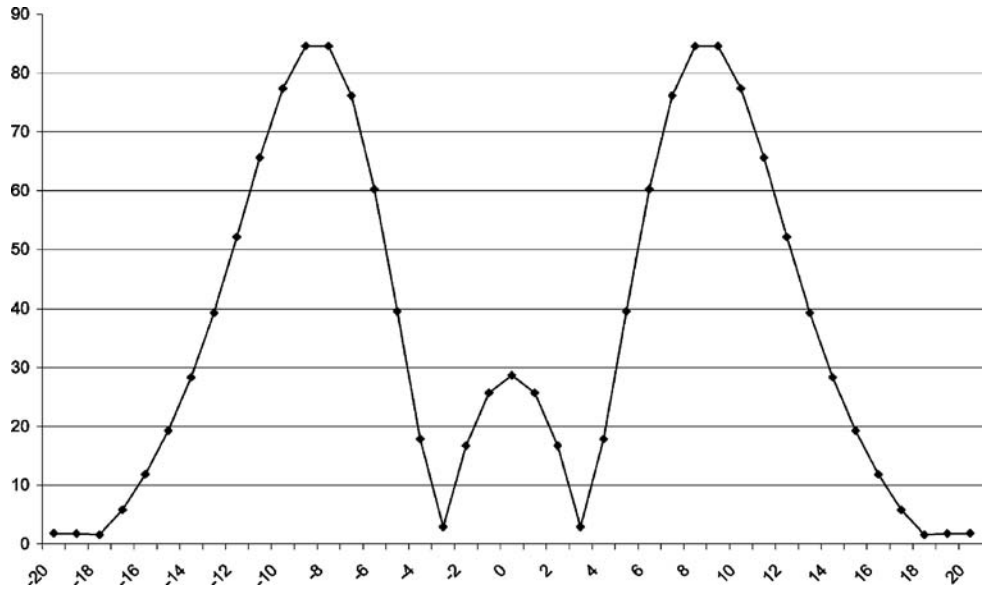

Fig. 3. The single-layer Fourier transform G_O (the l values are reported along the abscissa, whereas the Fourier transform along vertical axis); F is in the absolute value of the transform.

information can be obtained from the analysis of the peaks in the Fourier map.

The total number of possible 4-layer polytypes, found by Ross *et al*. (1966) considering the combination of layer rotations, is 26. However, only four of them belong to the subfamily A. The homo-octahedral OD stacking sequences of these four polytypes are 2220, 4422, 0042 and 2040. These sequences are well known (see, for example, Takeda & Ross, 1995) and can be obtained with the PTGR program (Takeda, 1971). The corresponding PID functions were calculated with PTST98 program (Nespolo *et al*., 1999).

Because of the symmetry of the PID function for subfamily A polytype:

$$S^N\left(0, 2k, \hat{l}\right) = S^N\left(k\bar{k}\hat{l}\right) = S^N\left(kk, N-\hat{l}\right)$$

the PID calculated from intensities of only one reciprocal lattice plane containing non-family reflections is enough to identify the polytype (Nespolo *et al*., 1999).

The PID has been calculated from the Prague data set for eight periods along the [02l]* row and is reported in Table 3. The comparison of the observed and calculated PID values for the [02l]* row is listed in Table 4, where the possible stacking sequences are expressed by RTW and OD symbols in the homo-octahedral approximation.

The agreement between experimental and calculated PID is expressed by the R_{PID} factor, defined as follows:

$$R_{PID} = \frac{\sum_{j=1}^{N} \left| S_j^N(hkl)_O - S_j^N(hkl)_C \right|}{\sum_{j=1}^{N} S_j^N(hkl)_O}$$

where $S^N_j(hkl)_O$ and $S^N_j(hkl)_C$ are the observed and computed PID values of jth layer respectively.

The best R_{PID} value of 0.14 indicates that the stacking sequence corresponds without ambiguity to the RTW symbols $22\bar{2}\bar{2}$, *i.e*. a homo-octahedral OD sequence 2040.

Table 3. Derivation of PID from measured intensities of 4-layer polytype. F_O are the structure factors observed along 02l reciprocal lattice rows. SLFT is the single-layer Fourier transform.

Period	l	$\hat{l}$	F_o	SLFT	PID
1	−28	1	10.65	16.72	0.64
	−27	2	14.14	19.08	0.74
	−26	3	1.70	19.89	0.09
	−25	0	11.15	18.75	0.59
2	−16	1	5.20	11.83	0.44
	−15	2	8.66	19.28	0.45
	−14	3	1.22	28.33	0.04
	−13	0	18.26	39.33	0.46
3	−12	1	18.42	52.14	0.35
	−11	2	101.19	65.59	1.54
	−10	3	2.93	77.38	0.04
	−9	0	39.33	84.55	0.45
4	−8	1	32.76	84.53	0.39
	−7	2	31.20	76.14	0.41
	−6	3	2.72	60.25	0.05
	−5	0	12.49	39.59	0.32
5	8	1	33.08	84.53	0.39
	9	2	39.03	84.55	0.46
	10	3	2.90	77.38	0.04
	11	0	31.51	65.59	0.48
6	12	1	18.37	52.14	0.35
	13	2	18.07	39.33	0.46
	14	3	1.90	28.33	0.07
	15	0	9.02	19.28	0.47
7	24	1	6.77	15.63	0.43
	25	2	11.29	18.75	0.60
	26	3	0	19.89	0
	27	0	13.81	19.08	0.72
8	28	1	10.48	16.72	0.63
	29	2	12.68	13.37	0.95
	30	3	2.57	9.64	0.27
	31	0	6.70	6.09	1.10

Table 4. Comparison between measured and computed PID of 4-layer polytype. RTW symbols and homo-octahedral OD symbols (in parentheses) are given.

$\hat{l}$	Average	Normalized	$002\bar{2}$ (2220)	$0\bar{2}02$ (4422)	0222 (0042)	$22\bar{2}\bar{2}$ (2040)
1	0.45	1.77	1.00	1.00	2.65	2.00
2	0.70	2.75	0.90	1.73	1.73	2.45
3	0.07	0.28	1.73	3.00	1.73	0.00
0	0.58	2.28	3.35	1.73	1.73	2.45
R_{PID}			0.73	0.72	0.55	0.14

6. OD character

In the OD interpretation a polytype can be considered as formed by parts periodic in two dimensions, called the OD layers, which do not necessarily coincide with chemically identified layers like the M layer. Mica polytypes are composed by two types of OD layers: the octahedral layer (Oc), consisting of a plane of octahedral cations and halves of coordinating oxygen atoms on both sides of this plane, and the tetrahedral layer (Tet), corresponding to the plane of the interlayer cations and the two tetrahedral sheets (Dornberger-Schiff *et al*., 1982).

Another unit commonly used in the OD theory is the OD packet. The M layer, in fact, can be considered formed by two parts called the OD packets, identical in their composition (one half of the plane of interlayer cations, one tetrahedral sheet and one half of octahedral plane) and differing for the orientation. The two OD packets have opposite polarity with respect to the stacking direction (***c*** axis), thus they are indicated with letters p_{2j} and q_{2j+1} ($p_{2j} = Tet_{2j}/2 + Oc_{2j+1}$ and $q_{2j+1} = Oc_{2j-1}/2 + Tet_{2j}/2$). Because adjacent OD layers are equivalent in all types of mica families, also the OD packets are equivalent (Dornberger-Schiff *et al*., 1982). Consequently the derivation of the polytype symbols is simplified, because it is possible to use only one type of OD packet, instead of two kinds of OD layers.

The OD symbols for layers silicates are formed by a sequence of characters distributed on two lines and contained in two vertical bars that delimitate the period. The first line is composed by $2N$ digits T_j ($j = 0, 2N-1$) representing the packet orientations ($T_j = 0$–5), while the second line is composed by N digits $v_{2j,2j+1}$ representing the displacements between the packets. The value of $v_{2j,2j+1}$ corresponds to the sum $T_{2j}+T_{2j+1}$ mod(6) and gives the orientation of the layer formed by the two packets. The vector sum can correspond to the characters $0 \sim 5$ ($|a|/3$ in six directions), * (null), $-$ and $+$ ($-b/3$ and $+b/3$ respectively). In micas, however, the packet-to-packet displacement vector is null, because the presence of the interlayer cations do not allow any shift between the packets, therefore only the * symbol is used. Finally between two packets a dot is placed to indicate the position of octahedral layer. The full OD symbol is:

$$\left| \begin{matrix} T_0 \cdot T_1 \cdot T_2 \cdot T_3 \ldots \\ v_{0,1} * v_{2,3} \ldots \end{matrix} \right|$$

The OD symbol of a mica polytype depends on the family (Dornberger-Schiff *et al.*, 1982):

- ***homo-octahedral family***: in this case there are only two possible orientations, differing by a 180° rotation, for each packet. Because of the hexagonal symmetry of the homo-octahedral layer, the three origins can be reached by the three even or odd T vector respectively. For this reason these orientations are described with the letters e (''even'' for 0, 2 and 4 vectors) and u (''uneven'' for 1, 3, 5 vectors). The first line thus becomes redundant and a simplified symbol formed only by the displacement vectors is used instead.
- ***meso-octahedral family***: the orientation of the packet is indicated by the displacement vector. Because this is the sum of the orientation vectors T_{2j} and T_{2j+1} of the respective packets, only the first line of the OD symbol is necessary to describe the polytype.
- ***hetero-octahedral family***: the dot in the symbols is substituted by a prime or double prime to indicate the handedness of the OD packet.

The symmetry analysis of a polytype is possible from its OD symbol, considering the ρ- and τ-operations (Backhaus & Ďurovič, 1984). The τ-operations are symmetry or coincidence operations which do not change the sign of coordinates in the layer stacking direction. The ρ-operations, instead, change the sign of coordinates and thus they turn a layer or a sequence of layers upside down. Consequently a ρ-operation inverts the order of the sequence of characters in the symbol, whereas a τ-operation leaves it unchanged.

For the polytype under investigation the space-group type has been derived by exploiting the symmetry properties of the homo-octahedral OD symbols (Table 5) obtained by the PID analysis, *i.e*. 2040.

The stacking sequence of the polytype is characterized by two ρ-operations: the OD symbol sequence ⟨i⟩,⟨j⟩,⟨k⟩,⟨l⟩ is converted into ⟨–l⟩,⟨–k⟩,⟨–j⟩,⟨–i⟩ by the twofold rotation along the [010] direction (*i.e*., 2040 → 0204) and into ⟨l⟩,⟨k⟩,⟨j⟩,⟨i⟩ by the inversion centre (2040 → 0402). The τ-operation, instead, is a glide reflexion perpendicular to [010] converting ⟨i⟩,⟨j⟩,⟨k⟩,⟨l⟩ into

Table 5. Transformation rules for OD symbols (after Nespolo & Ďurovič, 2002).

τ-Point operation				ρ-point operation			
H–M	ORT	Effect on OD symbol sequence	Effect on Z-symbol sequence	H-M	ORT	Effect on OD symbol sequence	Effect on Z-symbol sequence
		$\langle$i'$\rangle$,$\langle$j'$\rangle$,. . .,$\langle$p'$\rangle$	$\langle$i$\rangle$,$\langle$j$\rangle$,. . .$\langle$p$\rangle$	$\bar{1}$	$\bar{1}$	$\langle$p''$\rangle$,. . .,$\langle$j''$\rangle$,$\langle$i''$\rangle$	$\langle$p$\rangle$. . .,$\langle$j$\rangle$,$\langle$i$\rangle$
$(6)^{-1}$	$(6)^{-1}$	$\langle$1+i'$\rangle$,$\langle$1+j'$\rangle$,. . .,$\langle$1+p'$\rangle$	$\langle$5+i$\rangle$,$\langle$5+j$\rangle$,. . .,$\langle$5+p$\rangle$	$(\bar{6})^{-1}$	$(\bar{6})^{-1}$	$\langle$1+p''$\rangle$,. . .,$\langle$1+j''$\rangle$,$\langle$1+i''$\rangle$	$\langle$5+p$\rangle$,. . .,$\langle$5+j$\rangle$,$\langle$5+i$\rangle$
$(3)^{-1}$	$(3)^{-1}$	$\langle$2+i'$\rangle$,$\langle$2+j'$\rangle$,. . .,$\langle$2+p'$\rangle$	$\langle$4+i$\rangle$,$\langle$4+j$\rangle$,. . .,$\langle$4+p$\rangle$	$(\bar{3})^{-1}$	$(\bar{3})^{-1}$	$\langle$2+p''$\rangle$,. . .,$\langle$2+j''$\rangle$,$\langle$2+i''$\rangle$	$\langle$4+p$\rangle$,. . .,$\langle$4+j$\rangle$,$\langle$4+i$\rangle$
$(2)^1$	$(2)^1$	$\langle$3+i'$\rangle$,$\langle$3+j'$\rangle$,. . .,$\langle$3+p'$\rangle$	$\langle$3+i$\rangle$,$\langle$3+j$\rangle$,. . .,$\langle$3+p$\rangle$	$(\bar{2})^1 = m_{(001)}$	$(\bar{2})^1 = m_{(001)}$	$\langle$3+p''$\rangle$,. . .,$\langle$3+j''$\rangle$,$\langle$3+i''$\rangle$	$\langle$3+p$\rangle$,. . .,$\langle$3+j$\rangle$,$\langle$3+i$\rangle$
$(3)^1$	$(3)^1$	$\langle$4+i'$\rangle$,$\langle$4+j'$\rangle$,. . .,$\langle$4+p'$\rangle$	$\langle$2+i$\rangle$,$\langle$2+j$\rangle$,. . .,$\langle$2+p$\rangle$	$(\bar{3})^1$	$(\bar{3})^1$	$\langle$4+p''$\rangle$,. . .,$\langle$4+j''$\rangle$,$\langle$4+i''$\rangle$	$\langle$2+p$\rangle$,. . .,$\langle$2+j$\rangle$,$\langle$2+i$\rangle$
$(6)^1$	$(6)^1$	$\langle$5+i'$\rangle$,$\langle$5+j'$\rangle$,. . .,$\langle$5+p'$\rangle$	$\langle$1+i$\rangle$,$\langle$1+j$\rangle$,. . .,$\langle$1+p$\rangle$	$(\bar{6})^1$	$(\bar{6})^1$	$\langle$5+p''$\rangle$,. . .,$\langle$5+j''$\rangle$,$\langle$5+i''$\rangle$	$\langle$1+p$\rangle$,. . .,$\langle$1+j$\rangle$,$\langle$1+i$\rangle$
$[m\ .\ .\ (.)\ .\ .\ .]$	$m_{(1\bar{3}0)}$	$\langle$5–i''$\rangle$,$\langle$5–j''$\rangle$,. . .,$\langle$5–p''$\rangle$	$\langle$1–i$\rangle$,$\langle$1–j$\rangle$,. . .,$\langle$1–p$\rangle$	$[2\ .\ .\ (.)\ .\ .\ .]$	$2_{[1\bar{1}0]}$	$\langle$5–p'$\rangle$,. . .,$\langle$5–j'$\rangle$,$\langle$5–i'$\rangle$	$\langle$1–p$\rangle$,. . .,$\langle$1–j$\rangle$,$\langle$1–i$\rangle$
$[.\ .\ .\ (.)\ .\ m\ .]$	$m_{(1\bar{1}0)}$	$\langle$4–i''$\rangle$,$\langle$4–j''$\rangle$,. . .,$\langle$4–p''$\rangle$	$\langle$2–i$\rangle$,$\langle$2–j$\rangle$,. . .,$\langle$2–p$\rangle$	$[.\ .\ .\ (.)\ .\ 2\ .]$	$2_{[3\bar{1}0]}$	$\langle$4–p'$\rangle$,. . .,$\langle$4–j'$\rangle$,$\langle$4–i'$\rangle$	$\langle$2–p$\rangle$,. . .,$\langle$2–j$\rangle$,$\langle$2–i$\rangle$
$[.\ .\ m\ (.)\ .\ .\ .]$	$m_{(100)}$	$\langle$3–i''$\rangle$,$\langle$3–j''$\rangle$,. . .,$\langle$3–p''$\rangle$	$\langle$3–i$\rangle$,$\langle$3–j$\rangle$,. . .,$\langle$3–p$\rangle$	$[.\ .\ 2\ (.)\ .\ .\ .]$	$2_{[100]}$	$\langle$3–p'$\rangle$,...,$\langle$3–j'$\rangle$,$\langle$3–i'$\rangle$	$\langle$3–p$\rangle$,. . .,$\langle$3–j$\rangle$,$\langle$3–i$\rangle$
$[.\ .\ .\ (.)\ m\ .\ .]$	$m_{(110)}$	$\langle$2–i''$\rangle$,$\langle$2–j''$\rangle$,. . .,$\langle$2–p''$\rangle$	$\langle$4–i$\rangle$,$\langle$4–j$\rangle$,. . .,$\langle$4–p$\rangle$	$[.\ .\ .\ (.)\ 2\ .\ .]$	$2_{[310]}$	$\langle$2–p'$\rangle$,...,$\langle$2–j'$\rangle$,$\langle$2–i'$\rangle$	$\langle$4–p$\rangle$,. . .,$\langle$4–j$\rangle$,$\langle$4–i$\rangle$
$[.\ m\ .\ (.)\ .\ .\ .]$	$m_{(130)}$	$\langle$1–i''$\rangle$,$\langle$1–j''$\rangle$,. . .,$\langle$1–p''$\rangle$	$\langle$5–i$\rangle$,$\langle$5–j$\rangle$,. . .,$\langle$5–p$\rangle$	$[.\ 2\ .\ (.)\ .\ .\ .]$	$2_{[110]}$	$\langle$1–p'$\rangle$,. . .,$\langle$1–j'$\rangle$,$\langle$1–i'$\rangle$	$\langle$5–p$\rangle$,. . .,$\langle$5–j$\rangle$,$\langle$5–i$\rangle$
$[.\ .\ (.)\ .\ .\ m]$	$m_{(010)}$	$\langle$–i''$\rangle$,$\langle$–j''$\rangle$,. . .,$\langle$–p''$\rangle$	$\langle$–i$\rangle$,$\langle$–j$\rangle$,. . .,$\langle$–p$\rangle$	$[.\ .\ .\ (.)\ .\ .\ 2]$	$2_{[010]}$	$\langle$–p'$\rangle$,. . .,$\langle$–j'$\rangle$,$\langle$–i'$\rangle$	$\langle$–p$\rangle$,. . .,$\langle$–j$\rangle$,$\langle$–i$\rangle$

$\langle$–i$\rangle$,$\langle$–j$\rangle$,$\langle$–k$\rangle$,$\langle$–l$\rangle$ (2040 $\rightarrow$ 4020). Finally, taking into account the *C*-centring common to all mica polytypes, the maximal space-group type compatible with the homo-octahedral stacking sequence is *C*2/c. The space group of the structure can indeed be of this type or correspond to a subgroup, depending on the family and on the degree of desymmetrisation.

7. Structure refinement

The application of the OD theory plays a fundamental role in establishing the initial model for the structural refinement. This model, in fact, is obtained from the atomic positions of the 1*M* polytype, by applying the stacking vectors corresponding to the OD packets. The refinement was first attempted in *C*2/*c* with Jana2006 (Petricek *et al.*, 2006). The occupancies of the octahedra and tetrahedra were at first supposed to be the same in all respective sites, fixed by the stoichiometry. In the refinement, both the Nancy and Prague data sets have been at first tested, but the second data set has been chosen to continue the structural refinement, because of the lower value of R_{int} and of the higher intensity/sigma ratio. At the beginning, the atomic coordinates and the isotropic thermal parameters were refined. The refinement converged to 9.6 %. In the next step, the thermal parameters have been refined anisotropically, leading to $R_{(obs)} = 6.5$ %. The cation distribution could not be refined. In fact, in the tetrahedra Si and Al substitute isomorphically but these two atoms cannot be differentiated by a conventional X-ray diffraction experiment, differing by only one electron. The occupancies of the tetrahedral sites have therefore been adjusted on the basis of the bond lengths in the coordination polyhedra (Table 6). The fractional content of Si and Al, in fact, can be obtained as a function of the average tetrahedral bond lengths $\langle$T-O$\rangle$ by the equation: $\langle \text{T-O} \rangle = 0.163[x_{Al}/(x_{Al} + x_{Si})] + 0.168$ (Hazen & Burnham, 1973). Finally, the Si/Al content computed in this way has been normalized with respect to the chemical formula.

In the octahedral sites, up to four cations (Mg, Al, Fe, Ti) can substitute, of which two (Mg, Al) are again not distinguishable because they differ by only one electron. Even considering Mg + Al together, we are left with three cations that can distribute over up to three sites in each layer. It is unfortunately not possible to restrain the fractional occupancy by each cation a non-zero value and the total occupation of the site to 1, the refinement algorithm giving instead non-physical values of negative occupation for some cations. However, a clear indication of the occupation of each site can be obtained by the heights of the peaks in the Fourier map (Table 7).

After adjusting the occupancies of the cation sites on the basis of bond lengths for the tetrahedral sites and of the height of the peaks in the Fourier map for the octahedral sites, as described above, the R_{obs} and R_{all} values are 6.4 and 12.9 % respectively. The relatively high value of R_{all} comes from the high number (1096) of non-observed ($I < 3\sigma$) reflections (nearly 50 %).

Table 6. T-O and M-O bond distances.

Bond	Lengths	Bond	Lengths
T1a-O11	1.669(6)	M2a-O21	2.082(6)
T1a-O12	1.639(6)	M2a-O21	2.135(6)
T1a-O13	1.649(6)	M2a-O22	2.143(5)
T1a-O21	1.696(7)	M2a-O22	2.081(6)
		M2a-O23	1.935(6)
T2a-O11	1.653(6)	M2a-O23	1.943(6)
T2a-O12	1.647(5)		
T2a-O13	1.639(6)	M1b-O61	2.114(6)
T2a-O22	1.669(6)	M1b-O61	2.114(6)
		M1b-O62	2.108(7)
T1b-O51	1.665(6)	M1b-O62	2.108(7)
T1b-O52	1.656(6)	M1b-O63	2.036(5)
T1b-O53	1.645(5)	M1b-O63	2.036(5)
T1b-O61	1.663(6)		
		M2b-O61	2.089(5)
T2b-O51	1.651(6)	M2b-O61	2.089(5)
T2b-O52	1.654(6)	M2b-O62	2.159(7)
T2b-O53	1.636(6)	M2b-O62	2.159(7)
T2b-O62	1.623(9)	M2b-O63	1.952(7)
		M2b-O63	1.952(7)
M1a-O21	2.080(6)		
M1a-O21	2.080(6)	M3b-O61	2.129(6)
M1a-O22	2.096(6)	M3b-O61	2.129(6)
M1a-O22	2.096(6)	M3b-O62	2.110(6)
M1a-O23	2.047(7)	M3b-O62	2.110(6)
M1a-O23	2.047(7)	M3b-O63	1.952(7)
		M3b-O63	1.952(7)

Table 7. List of first ten positive peaks of the experimental Fourier map (Prague data set).

Peak	Charge	Peak	Charge
M3b	16.34	M1a	15.14
M2b	16.17	T2b	12.65
I	15.79	T2a	12.34
M1b	15.46	T1b	12.33
M2a	15.22	T1a	11.88

The result in *C*2/*c* indicates the presence of two kinds of M layer differing in their layer symmetry. In fact, the glide plane *c* relates the first and third layer, as well as the second and the fourth. In the first layer the *trans M*1 site is in special position (site-symmetry $\bar{1}$, Wyckoff position 4*c*), instead the *cis M*2 site, symmetrically equivalent to *M*3, is in general position 8*f*, and it is the case also for the tetrahedral sites. The layer is thus meso-octahedral with symmetry *C*12/*m*(1). In the second layer the two tetrahedral sites are again in general position 8*f*, while the three octahedral sites are all independent and in special position on a twofold axis (Wyckoff position 4*e*). The layer symmetry is only *C*12(1) and the layer could therefore be hetero-octahedral. The Fourier map, however, shows that the peak in the *M*1 site is different from the others, whereas the *M*2 and *M*3 peaks are close within the precision of the experiment (the difference between the *M*2 and *M*3 charges is less than one electron). The layer can be, therefore, considered borderline between the hetero and meso-octahedral definition: the layer symmetry does not impose *M*2 and *M*3 to be equivalent but they actually are, so that the layer can be considered meso-octahedral. The similar bond lengths of the *M*2 and *M*3 octahedra (in the range of 3σ) also confirm that these two sites are equal within the experimental precision. For the meso-octahedral family, the origin of the octahedral sheet is chosen on the site with different occupancy, according to Dornberger-Schiff *et al*. (1982), that here is the *trans M*1 site in both cases. This type of layer is called the M1-layer to distinguish it from that whose origin is on a *cis* site, called the M2-layer (Nespolo *et al*., 1999).

On the basis of the refinement results, the final OD symbol of the 4-layer polytype is thus:

|1.1 3.3 5.5 3.3|

The atomic coordinates and the thermal parameters obtained in the refinement performed in *C*2/*c* are listed in Table 8.

Actually, the structural symmetry of the polytype could be lower than that obtained simply by the stacking sequence, due to the desymmetrisation of the OD layers (Ďurovič, 1979). For this reason the refinement was also attempted in all the *translationengleiche* subgroups of *C*2/*c* (*C*2, *Cc*, $C\bar{1}$, *C*1) to find the true structural symmetry. No improvement was observed when the refinement was performed in all these subgroups, whereas several correlations appeared. The maximum number of correlations was observed in *C*1. Moving from *C*1 to *C*2/*c*, the number of correlations reduced and finally disappeared. This confirms that the correct space group for this polytype is indeed *C*2/*c*. The result is corroborated by the analysis of the electron density map from charge flipping (program Superflip included in Jana package: Petricek *et al*., 2006), which strongly confirms *C*2/*c*. The $R_{(obs)} = 6.4$ % can be considered a satisfactory value, given that in a natural layer material like micas stacking faults are always present and, even if they are not so abundant to produce streaking along the non-family rows, they nevertheless affect to some degree the intensity of the non-family reflections.

8. A model for the cation distribution based on the Charge Distribution analysis

Charge Distribution (CD or Chardi) is an empirical method of structural analysis which represents the ultimate extension of Pauling's concept of bond strength (for details, see Nespolo *et al*., 2001). In a case with several cations of different charge distributing in various sites, the CD analysis can help getting a model of the cation distribution: the distribution that minimises the discrepancy of charges over the cation sites represents a most likely model. In our case, we have to distribute two divalent cations (Mg and Fe), two trivalent cations (Fe and Al) and one tetravalent cation (Ti) over five sites, keeping the chemical formula and the electroneutrality. The position of the hydrogen atoms has not been determined; however, in the mica structure they do not form hydrogen bonds but only

Table 8. Atom coordinates and anisotropic displacement parameters for 4-layer polytype.

		s.o.f.	*x*	*y*	*z*	U^{11}	U^{22}	U^{33}	U^{12}	U^{13}	U^{23}	U_{iso}
I	K	0.848	0.3746(3)	0.4165(2)	−0.12498(5)	0.0301(7)	0.0297(7)	0.0470(9)	0.0042(9)	0.0022(6)	−0.0012(1)	0.0356(5)
	Na	0.163										
	Ba	0.040										
M1a	Mg	0.305	0.25	0.25	0	0.010(1)	0.006(1)	0.017(2)	0.0066(9)	0	−0.0029(9)	0.0111(8)
	Ti	0.195										
M2a	Mg	0.606	0.2684(2)	0.5765(2)	0	0.0131(5)	0.0129(7)	0.0141(6)	0.0041(5)	0	−0.0008(5)	0.0134(3)
	Fe^{+3}	0.321										
	Al	0.073										
M1b	Mg	0.305	0.5	0.0794(3)	0.25	0.0070(9)	0	0.021(1)	0	0.0034(9)	0	0.0092(6)
	Ti	0.195										
M2b	Mg	0.303	0.5	0.4229(3)	0.25	0.0010(8)	0.012(1)	0.014(1)	0	0.0009(7)	0	0.0087(6)
	Fe^{+2}	0.058										
	Fe^{+3}	0.104										
	Al	0.035										
M3b	Mg	0.303	0.5	0.7339(3)	0.25	0.0018(9)	0.004(1)	0.019(1)	0	0.0001(9)	0	0.0080(6)
	Fe^{+2}	0.058										
	Fe^{+3}	0.104										
	Al	0.035										
T1a	Si	0.661	0.3894(5)	0.7505(2)	−0.06934(8)	0.012(1)	0.011(1)	0.014(1)	0.0047(6)	0.0018(9)	−0.0005(6)	0.0121(7)
	Al	0.339										
T2a	Si	0.738	0.3950(3)	0.0824(2)	−0.06927(4)	0.0090(7)	0.0089(7)	0.0151(8)	0.0093(8)	0.0011(6)	−0.0018(9)	0.0110(4)
	Al	0.262										
T1b	Si	0.702	0.1424(3)	0.4139(2)	0.18076(4)	0.0070(7)	0.0064(7)	0.0164(8)	0.0079(8)	0.0004(6)	−0.0017(8)	0.0099(4)
	Al	0.298										
T2b	Si	0.807	0.1455(4)	0.7496(2)	0.18083(7)	0.0002(8)	0.0028(9)	0.021(1)	0.0032(5)	−0.0008(8)	−0.0004(6)	0.0079(6)
	Al	0.193										
	O11	1	0.159(1)	0.1858(6)	−0.0833(2)	0.017(2)	0.023(3)	0.028(3)	0.010(2)	0.004(2)	0.001(2)	0.022(2)
	O12	1	0.157(1)	0.6479(6)	−0.0838(1)	0.013(2)	0.025(3)	0.017(3)	−0.002(2)	−0.001(2)	−0.002(2)	0.018(1)
	O13	1	0.3513(9)	0.9173(6)	−0.0838(1)	0.023(2)	0.011(2)	0.021(2)	0.002(2)	0	−0.002(2)	0.018(1)
	O21	1	0.405(1)	0.7520(6)	−0.0267(2)	0.024(3)	0.008(3)	−0.006(2)	0.013(2)	0.001(2)	0.002(1)	0.009(1)
	O22	1	0.4119(9)	0.0822(7)	−0.0273(2)	0.012(2)	0.002(2)	0.014(2)	0.009(2)	0.003(2)	0.004(2)	0.009(1)
	O23	1	0.410(1)	0.4183(7)	−0.0250(2)	0.020(2)	0.004(2)	0.016(2)	0.014(2)	0.003(2)	0.004(2)	0.013(1)
	O51	1	0.1000(9)	0.5827(6)	0.1666(1)	0.025(2)	0.014(2)	0.022(2)	0.001(2)	0.001(3)	−0.001(2)	0.020(1)
	O52	1	0.408(1)	0.3509(6)	0.1662(1)	0.014(2)	0.020(2)	0.025(3)	0.009(2)	0.004(2)	0.001(2)	0.020(2)
	O53	1	0.4056(9)	0.8139(6)	0.1662(1)	0.012(2)	0.020(2)	0.017(3)	0.002(2)	−0.001(2)	−0.001(2)	0.016(1)
	O61	1	0.1569(8)	0.4077(7)	0.2226(2)	0.002(2)	0.010(2)	0.017(2)	0.005(2)	−0.001(2)	−0.001(2)	0.010(1)
	O62	1	0.1562(9)	0.7474(6)	0.2216(2)	−0.010(2)	0.006(3)	0.044(4)	0.005(2)	0.002(2)	−0.001(2)	0.014(2)
	O63	1	0.157(1)	0.0784(8)	0.2251(2)	0.008(2)	0.022(3)	0.018(2)	0.008(2)	−0.003(2)	0.003(3)	0.016(1)

Table 9. Charge Distribution analysis of the $4M_3$ ferriphlogopite.

Cation	ECoN	Input charge	Output charge	ratio	Anion	Input charge	Output charge	ratio
K1	10.9	1.00	0.98	1.02	O11	−2.00	−1.99	1.01
M1a	6.0	2.78	2.89	0.96	O12	−2.00	−2.11	0.95
M2a	5.6	2.39	2.50	0.96	O13	−2.00	−2.11	0.95
M1b	5.9	2.78	2.85	0.98	O21	−2.00	−1.93	1.04
M2b	5.6	2.28	2.35	0.97	O22	−2.00	−1.96	1.02
M3b	5.7	2.28	2.35	0.97	O23	−1.68	−1.59	1.06
T1a	4.0	3.66	3.59	1.02	O51	−2.00	−1.99	1.01
T2a	4.0	3.74	3.66	1.02	O52	−2.00	−2.08	0.96
T1b	4.0	3.70	3.67	1.01	O53	−2.00	−2.02	0.99
T2b	4.0	3.81	3.74	1.02	O61	−2.00	−1.99	1.01
					O62	−2.00	−2.05	0.98
					O63	−1.68	−1.56	1.08
Data dispersion: 0.08					Data dispersion: 0.08			

covalent bonds with one oxygen atom, and thus hydrogen atoms can be implicitly treated by using O^{-1} to represent the OH group, as well as F^{-1} anion. In our ferriphlogopite, hydrogen atoms are bonded to oxygen labelled O23 and O63 but because of the oxidising conditions in which the sample was formed, only part of the hydrogen atoms are left. The computed anion charge may thus vary between −1 (no oxidation) and −2 (complete oxidation and depletion of fluorine). Results in Table 9 indicate a computed charge of −1.6, suggesting partial oxidation. The most probable distribution of the cations has been fixed by minimizing the divergence between the input and output charges of the cations. The *trans* sites (M1a and M1b, in the two independent layers) have a computed charge close to 3, the *cis* sites a lower charge, with M2a and M2b value very close to the 2.0, confirming the meso-octahedral nature of this layer. The computed charges follow closely the order of the peaks in the Fourier map and correspond to the cation distribution model in Table 10.

As discussed in Section 2, the iron content of the sample was overestimated in the EPMA analysis by the use of a ferrous standard and had to be adjusted from 0.816 (Table 1) to 0.643 to comply with a site occupancy of 3 for the three octahedral sites. This indicates that iron is highly oxidised in our sample, in agreement with the results of Takeda & Ross (1975). The CD analysis has been performed starting from a Fe^{+3}/Fe^{+2} ratio similar to that reported by these authors and adjusting the ferric-to-ferrous ratio to minimise the divergence between the input and output charges. The results of the CD analysis suggest a ratio of 82 %, which is somewhat lower than that reported by Takeda & Ross (1975) but nevertheless confirms the predominance of ferric iron in this sample.

Table 10. Distribution of cations in the octahedral sheet giving the best agreement with the computed charges according to the Charge Distribution analysis.

	M1a	M2a	M1b	M2b	M3b
Mg^{2+}	0.61	0.61	0.61	0.61	0.61
Fe^{2+}	–	–	–	0.11	0.11
Fe^{3+}	–	0.32	–	0.21	0.21
Al^{3+}	–	0.07	–	0.07	0.07
Ti^{4+}	0.39	–	0.39	–	–

Table 11. Experimental details of refinement for the Prague data set.

Crystal data	
Chemical formula	$(K_{0.848}Na_{0.163}Ba_{0.04})(Mg_{1.822}Al_{0.146}Fe^{+3}_{0.528}Fe^{+2}_{0.115}Ti_{0.39})Si_{2.908}Al_{1.092})O_{11.455}F_{0.117}OH_{0.428}$
Space–group type	*C2/c*
Cell parameters	$a = 5.3166(2)$ Å $b = 9.2080(2)$ Å $c = 39.814(1)$ Å $\beta = 92.550(3)^\circ$
Volume	1947.51(6) Å^3
Z	8
μ	2.5 mm^{-1}
dimensions	0.20 × 0.16 × 0.01 mm
Refinement data	
Unique reflection	2135
Range of h, k, l	$-6 < h < 6$ $0 < k < 11$ $0 < l < 51$
R(obs)	6.28
R(all)	12.79
Rw(obs)	13.42
Rw(all)	15.27
GooF(obs)	2.07
GooF(all)	1.57
Reflections with $I > 3\sigma$	1039
Number of least-squares parameters	184
Weighting scheme	$w = 1/(\sigma^2(I_o)+0.0004\cdot I_o^2)$
$\Delta\rho_{max}$	1.12 eÅ^{-3}
$\Delta\rho_{min}$	−0.56 eÅ^{-3}

When putting this cation distribution in the refinement cycle, the agreement factors improve slightly ($R_{obs} = 6.3$ %, $R_{all} = 12.79$ %), and the same is true also for the values of the maximal and minimal difference Fourier peak (from 1.13 to 1.12 eÅ^{-3} and from −0.57 to −0.56 eÅ^{-3}) (Table 11).

9. Discussion

Four 4-layer mica polytypes have been reported so far in the literature. Takeda (1967) found a rare example of

mixed-rotation polytype, $4A_5$ (OD symbols = 3325) and Ross *et al.* (1966) discovered the $4M_2$ polytype (OD symbols = 0042). Takeda & Ross (1995) reported that also the $4M_1$ polytype (OD symbols = 4422) has been found in a synthetic fluorophlogopite coexisting with $1M$ mica (T. Nishida, 1969, personal communication to the authors). The $4M_3$ polytype presented in this study was already found by Zhukhlistov *et al.* (1988, 1990) in a Ti-biotite by means of oblique texture electron diffraction. No reliable structural refinement was however ever obtained before for a non-MDO mica polytype.

The stacking sequences of non-MDO polytypes are based on $1M$, $2M_1$ or $3T$ polytypes, called the *basic structures* (Baronnet, 1975); from them, three structural series arise. The presence of these series suggests that the formation mechanism of non-MDO polytypes can be explained by the development of a stacking fault perturbing the normal spiral growth of one of the basic structures. This causes a change in the number of layers present in the exposed ledge of the spiral growth, modifying the sequence of the basic structure. When the stacking fault is formed, the layer generated after the faulted one will be influenced by the previous layers, so that the stacking direction will return as closely as possible to the original direction (Takeda & Ross, 1995). Several models have been proposed to explain the formation of non-MDO polytypes with the occurrence of basic structures. Baronnet (1975) proposed the Perfect Matrix Model (**PMM**), in which the formation of non-MDO polytypes could result from the occurrence of an exposed ledge corresponding to a number of layers that is not an integral multiple of the period. This model allows an explanation of the formation of few polytypes; Pandey *et al.* (1982) extended this idea and introduced the Fault Matrix Model (**FMM**). In the FMM, contrary to the PMM, the presence of a stacking fault in the matrix is taken into account. During the spiral growth, a stacking fault can appear in the exposed ledge and can be incorporated in the new stacking sequence, which becomes longer than the one of the matrix. The application of the Fault Matrix Model has its limitations too, because it cannot explain the occurrence of more complex sequences, which would require the presence of two or more stacking faults in the exposed ledge. For this reason the *perturbative theory* was proposed by Nespolo (2001) to explain the formation of all non-MDO polytypes.

In our case, however, the Fault Matrix Model is sufficient to explain the formation of the $4M_3$ non-MDO polytype, because its stacking sequence is quite simple and is closely related to the basic structures. Analysing the stacking sequence of this polytype two interpretations for its formation are possible. The polytype, in fact, can be considered as formed by a $3T$ basic structure perturbed during the growth by the formation of one stacking fault. If an exposed ledge consisting of three layers of the $3T$ basic structure and a single stacking fault is produced, the spiral growth mechanism generates a 4-layer polytype that appears as a combination of $3T$ and $1M$ substructures. The observed stacking sequence of the $4M_3$ polytype can, however, be also considered as composed by two substructures of $2M_1$ in mirror-image relation. The occurrence of these two $2M_1$ substructures suggests that this polytype can be considered as a case of cell-twin. The concept of cell-twin was introduced by Ito (1950) to indicate a modular structure in which the modules are related by point-space operations. This concept is analogous to that of a twin, where the modules (individual crystals) are instead related by vector-space operations, but here the modules give rise to a homogeneous edifice, whereas the individuals in the twin form a heterogeneous edifice (Nespolo *et al.*, 2004). In this case, the $4M_3$ polytype would be the second example of non-MDO polytype belonging to the $2M_1$ series found in the Ruiz Peak sample, after the $8A_2$ polytype discovered by Nespolo & Takeda (1999). The other non-MDO polytypes of Ruiz Peak sample belong, instead, to the $1M$ and $3T$ series (Ross *et al.*, 1966).

Whatever of the two cases correspond to the actual formation of the $4M_3$ structure, the stacking sequence of this polytype can be decomposed in two parts, both formed by the basic structures and this explains why in this polytype the second and fourth layers are meso-octahedral even if the space-group symmetry does not impose the *cis* sites to be equivalent. In each basic structure, in fact, the layers are of the same type and the ''stacking memory'' effect preserves this characteristic during the spiral growth of the polytype.

Acknowledgements: The data collections have been performed at the X-ray diffraction facility of the Institute Jean Barriol of Nancy-Université and at the Academy of Science of the Czech Republic in Prague (within the framework of the institutional research plan No. AVOZ10 100521 of the Institute of Physics and the project Praemium Academiae of the Academy of Sciences of the Czech Republic). We thank Mr. Emmanuel Wenger and Dr. Slimane Dahaoui for their help in the data collection in Nancy, Drs. Nicolas Claiser and Sébastien Pillet for several profitable discussions. Dr. Malcom Ross, US Geological Survey, kindly provided the sample. The critical remarks by two anonymous referees are gratefully acknowledged.

References

Backhaus, K.O. & Ďurovič, S. (1984): Polytypism of micas. I. MDO polytypes and their derivation. *Clays Clay Miner.*, **32**, 453–463.

Baronnet, A. (1975): Growth spiral and complex polytypism in micas. I. Polytypic structure generation. *Acta Crystallogr. A*, **31**, 345–355.

— (1980): Polytypism in micas: a survey with emphasis on the crystal growth aspects. *in* ''Current Topics in Material Science'', E. Kaldis, ed. **5**, North-Holland Publishing Company, Amsterdam, 446–548.

Blessing, R.H. (1995): An empirical correction for absorption anisotropy. *Acta Crystallogr. A*, **51**, 33–38.

— (1997): Outlier treatment in data merging. *J. Appl. Crystallogr.*, **30**, 421–426.

Dornberger-Schiff, K., Backhaus, K.O., Ďurovič, S. (1982): Polytypism of micas: OD interpretation, stacking symbols, symmetry relations. *Clays Clay Miner.*, **30**, 364–374.

Ďurovič, S. (1979): Desymmetrization of OD structure. *Krist. Tech.*, **14**, 1047–1053.

— (2004): Jayes stadeing in general polytypic structures. *In* ''J International Table for Crystallography'', **C**, section 9.2.2 E. Prince, (ed.). Wiley & sons, 760–773.

Güven, N. (1971): Structural factors controlling stacking sequence in dioctahedral micas. *Clays Clay Miner.*, **19**, 159–165.

Hazen, R.M. & Burnham, C.W. (1973): The crystal structure of one layer phlogopite and annite. *Am. Mineral.*, **58**, 889–900.

Ito, T. (1950): X-ray studies on polymorphism. Maruzen, Tokyo.

Kogure, T. & Nespolo, M. (1999): A TEM study of long-period polytypes: determination of the stacking sequence of oxybiotite by means of atomic resolution images and Periodic Intensity Distribution (PID). *Acta Crystallogr. B*, **55**, 507–516.

Nespolo, M. (1999): Analysis of family reflections of OD-mica polytype, and its application to twin identification. *Mineral. J.*, **21**, 53–85.

— (2001): Perturbative theory of mica polytypism. Role of the M2 layer in the formation of inhomogeneous polytypes. *Clays Clay Miner.*, **49**, 1–23.

Nespolo, M. & Ďurovič, S. (2002): Crystallographic basis of polytypism and twinning in micas. *in* ''Micas: Crystal Chemistry & Metamorphic Petrology''. A. Mottana, F.P. Sassi, J.B. Thompson, Jr., S. Guggenheim, eds. *Rev. Mineral. Geochem.*, **46**, Mineralogy Society of America, Washington, 155–279.

Nespolo, M. & Takeda, H. (1999): Inhomogeneous mica polytypes: 8-layer polytype of the $2M_1$ structural series determinated by the Periodic Intensity Distribution (PID) analysis of the X-ray diffraction pattern. *Mineral. J.*, **21**, 103–118.

Nespolo, M., Takeda, H., Ferraris, G., Kogure, T. (1997): Composite twins of 1M mica: derivation and identification. *Mineral. J.*, **19**, 173–186.

Nespolo, M., Takeda, H., Kogure, T., Ferraris, G. (1999): Periodic intensity distribution (PID) of mica polytypes: symbolism, structural model orientation and axial settings. *Acta Crystallogr. A*, **55**, 659–676.

Nespolo, M., Ferraris, G., Ivaldi, G., Hoppe, R. (2001): Charge Distribution as a tool to investigate structural details. II. Extension to hydrogen bonds, distorted and hetero-ligand polyhedra. *Acta Crystallogr. B*, **57**, 652–664.

Nespolo, M., Ferraris, G., Ďurovič, S., Takéuchi, Y. (2004): Twins *vs.* modular structures. *Z. Kristallogr.*, **219**, 773–778.

Oxford Diffraction (2009): CrysAlisPro CCD and CrisAlisPro RED. Oxford Diffraction Ltd, Yarnton, Oxfordshire, England.

Pandey, D., Baronnet, A., Krishna, P. (1982): Influence of stacking faults on the spiral growth of polytype structures in mica. *Phys. Chem. Miner.*, **8**, 268–278.

Petricek,V., Dusek, M., Palatinus, L.(2006): Jana2006. The crystallographic computing system. Institute of Physics, Praha, Czech Republic.

Ramsdell, L.S. (1947): Studies on silicon carbide. *Am. Mineral.*, **32**, 64–82.

Rieder, M., Cavazzini, G., D'yakonov, Y., Frank-Kamenetskii, V.A., Gottardi, G., Guggenheim, S., Koval, P.V., Müller, G., Neiva, A.M.R., Radoslowich, E.W., Robert, J.L., Sassi, F.P., Takeda, H., Weiss, Z., Wones, D.R. (1998): Nomenclature of the micas. *Can. Mineral.*, **36**, 905–912.

Robbins, D.W. & Strens, R.G.J. (1972): Charge transfer in ferromagnesian silicates: The polarized electronic spectra of trioctahedral micas. *Mineral. Mag.*, **38**, 551–563.

Ross, W., Takeda, H., Wones, D.R. (1966): Mica polytypes: systematic description and identification. *Science*, **151**, 191–193.

Rule, A.C., Bailey, S.W., Livi, K.J.T., Veblen, D.R. (1987): Complex stacking sequence in a lepidotite from Tørdal, Norway. *Am. Mineral.*, **72**, 1163–1169.

Sunagawa, I. & Tomura, S. (1976): Twinning in phlogopite. *Am. Mineral.*, **61**, 939–943.

Takano, Y. & Takano, K. (1958): Apparent polytypism and apparent cleavage of micas. *J. Mineral. Soc. Japan*, **3**, 674–692 (in Japanese).

Takeda, H. (1967): Determination of the layer stacking sequence of a new complex mica polytype: a 4-layer lithium fluorophlogopite. *Acta Crystallogr.*, **22**, 845–853.

— (1971): Distribution of mica polytypes among space groups. *Am. Mineral.*, **56**, 1042–1056.

Takeda, H. & Ross, M. (1975): Mica polytypism: dissimilarities in the crystal structure of coexisting $1M$ and $2M_1$ biotite. *Am. Mineral.*, **60**, 1030–1040.

—, — (1995): Mica polytypism: identification and origin. *Am. Mineral.*, **80**, 715–724.

Takeda, H. & Sadanaga, R. (1969): New unit layer for micas. *Mineral. J.*, **5**, 434–449.

Tomisaka, T. (1958): On the chemical properties, optical properties and structural types of some muscovites and phlogopites (studies in the mica group, report 1). *J. Mineral. Soc. Japan.*, **3**, 710–721 (in Japanese).

— (1962): Polytypes of the phlogopite-biotite series and their mutual relations. *J. Jpn. Assoc. Mineral. Petrol. Econ. Geol.*, **47**, 134–143.

Zhukhlistov, A.P., Zvyagin, B.B., Pavlishin, V.I. (1988): Biotite 4M with an inhomogeneous layer alteration. *Z. Kristallogr.*, **185**, 624.

—, —, — (1990): Polytypic 4M modification of Ti-biotite with nonuniform alteration of layers, and its appearance in electron-diffraction patterns from textures. *Kristallografiya*, **35**, 406–413.

Zvyagin, B.B. (1962): A theory of polymorphism of micas. *Sov. Phys. Crystallogr.*, **6**, 571–580.

— (1967): Electron Diffraction Analysis of Clay Mineral Structures, XVI. Plenum Press, New York, 364 p.

Zvyagin, B.B., Vrublevskaya, Z.V., Zhukhlistov, A.P., Sidorenko, O.V., Soboleva, S.V., Fedotov, A.F. (1979): High-Voltage Electron Diffraction in the Study of Layeres Minerals. Nauka press, Moscow, 223 p. (in Russian).

Received 23 June 2010
Modified version received 17 September 2010
Accepted 26 October 2010

Chemical Geology 387 (2014) 1–11

Contents lists available at ScienceDirect

Chemical Geology

journal homepage: www.elsevier.com/locate/chemgeo

Iron–clay interactions: Detailed study of the mineralogical transformation of claystone with emphasis on the formation of iron-rich T–O phyllosilicates in a step-by-step cooling experiment from 90 °C to 40 °C

Isabella Pignatelli [a,*], Franck Bourdelle [a], Danièle Bartier [a], Régine Mosser-Ruck [a], Laurent Truche [a], Enrico Mugnaioli [b], Nicolas Michau [c]

[a] GeoRessources, UMR 7359, CNRS-INSU-Université de Lorraine-CREGU, Faculté des Sciences, Campus Aiguillettes, BP 70239, 54506 Vandœuvre-lès-Nancy, France
[b] Institut für Physikalische Chemie, Johannes Gutenberg-Universität Mainz, Welderweg 11, 55099 Mainz, Germany
[c] Agence nationale pour la gestion des déchets radioactifs (Andra), Direction Recherche et Développement/Service Colis et Matériaux, Parc de la Croix Blanche, 1/7 rue Jean Monnet, 92298 Châtenay-Malabry Cedex, France

ARTICLE INFO

Article history:
Received 2 May 2014
Received in revised form 1 August 2014
Accepted 5 August 2014
Available online 15 August 2014

Editor: J. Fein

Keywords:
Iron–claystone interaction
Cronstedtite
Greenalite
Magnetite
Cooling experiment

ABSTRACT

Iron–minerals–water interactions are of primary importance in the contexts of underground structure engineering (*e.g.* reactive barriers or deep geological storage) and for the understanding of secondary alteration processes in primitive meteorites. To improve our understanding of these systems, we determine the mineralogical transformations induced by the association of iron and silicates during a cooling through an experimental simulation of iron–clay interactions with a step-by-step procedure in the range of 90 °C to 40 °C. The run products and solutions are well characterised, by means of different techniques (X-ray diffraction, scanning and transmission electron microscopy, manocalcimetry, inductively coupled plasma optical emission spectrometry and ion chromatography), and the thermodynamic data concerning Fe-bearing phyllosilicates are well-tested comparing the modelling and experimental results. Therefore, the main mineralogical modifications observed include the remarkable formation of cronstedtite and greenalite, as well as the formation of magnetite at all temperatures, along with a significant dissolution of quartz, mixed-layer illite–smectite clays, illite (affecting more than 70% of each mineralogical phase) and a partial alteration of chlorite, kaolinite and dolomite. The experimental results confirm the reaction path predicted by thermodynamic modelling, *i.e.* the formation of iron-rich T–O phyllosilicates (cronstedtite and greenalite) and magnetite at the expense of metal iron and silicates. Both the experimental and thermodynamic results presented in this study provide important constraints to well predict the impact of nuclear waste canister corrosion in a claystone media and to better understand secondary alteration processes, which could also affect the mineralogical and chemical composition of primitive meteorites.

1. Introduction

Zero-valent iron does not occur naturally on Earth. However, metallic iron–minerals–water interactions are of primary importance in the context of underground structure engineering (*e.g.* reactive barriers or deep geological storage) and for the understanding of secondary alteration processes in primitive meteorites.

For example, the prediction of the long-term evolution of minerals in contact with iron is a key process in the frame of deep geological repository construction for high-level nuclear waste (HLW) involving multi-barrier systems. Several industrialised countries envisage a combination of natural (claystone, granite or salt formations) and engineered (glass, steel canisters, bentonite, reinforced concrete structures) barriers for radioactive waste containment. Among these different concepts, one of the considered technical options involves the disposal of vitrified waste emplaced in metal canisters and surrounded by a deep clayey rock formation. In this context, iron–clay interactions will take place as soon as the storage conditions become water-saturated and anoxic (*e.g.* de Combarieu et al., 2011), which will lead to major mineralogical and geochemical transformations of the host rocks.

Iron–mineral interactions are also important processes affecting the evolution of primitive meteorites (Brearley, 2006) and in particular CM chondrites. The link between secondary alteration of CM meteorites and the storage of radioactive waste is not immediately evident. However, the common feature is the presence of metallic iron (widespread

* Corresponding author at: GeoRessources, UMR 7359 CNRS, Faculté des Sciences et Techniques, Entrée 3B - Campus des Aiguillettes, Université de Lorraine, 54506 Vandœuvre-lès-Nancy, France. Tel.: +33 3 83 68 47 28; fax: +33 3 83 68 47 01.
E-mail address: isabella.pignatelli@univ-lorraine.fr (I. Pignatelli).

http://dx.doi.org/10.1016/j.chemgeo.2014.08.010
0009-2541/

in chondrites but non-existent on Earth), which is massively present in the engineered barriers envisaged for the underground storage of radioactive waste. Others similarities include the reducing conditions, the presence of neutral-alkaline fluids (Zolensky et al., 1989) and silicates, as well as the formation of magnetite and cronstedtite as secondary minerals (Pignatelli et al., 2013; Zolotov, 2014), and the expected low-temperature hydrothermal conditions (~0–100 °C; Zolensky et al., 1997).

In these contexts, it becomes essential to understand the long-term evolution of minerals in contact with metallic iron. Although the processes affecting the alteration of primary minerals and the precipitation of secondary phases in these environments are still a matter of debate, these aspects are essential for assessing the safety of an eventual underground nuclear waste repository in claystone formations, and can also provide important keys to better understand the physico-chemical conditions that have affected the evolution of primitive meteorites in the solar system. Therefore, studies from both fields of investigation can be compared to obtain better constraints on the reaction kinetics, the reaction paths and the stability of secondary minerals.

Up to the present, the large majority of studies have focused on iron–smectite systems (Guillaume et al., 2003, 2004; Lantenois et al., 2005; Perronnet et al., 2007, 2008; Mosser-Ruck et al., 2010; Jodin-Caumon et al., 2010; Lanson et al., 2012) and only a few deal with interactions between claystone and iron at constant temperature (de Combarieu et al., 2007, 2011; Martin et al., 2008; Schlegel et al., 2008, 2010; Pierron, 2011; Rivard, 2011; Bourdelle et al., 2014) or under thermal gradients of between 80°–150 °C and 150°–300 °C (Jodin-Caumon et al., 2012). These studies demonstrate that, even at moderate temperature (T < 100 °C), metallic iron can react with the surrounding materials, under certain conditions, to form new Fe-bearing phases, such as magnetite, siderite, Fe–smectites, Fe–serpentines, chukanovite or chlorite.

In comparison with previous studies on iron–clay or iron–silicate interactions, the originality of the present approach is that the effect of a cooling is taken into account for the first time. Indeed, an experiment is carried out at temperatures from 90 °C down to 40 °C to determine the mineralogical evolution of a claystone in contact with iron during the cooling of nuclear waste (ANDRA, 2005). The Callovo-Oxfordian claystone (abbreviated as COx) of Bure (France), designed by Andra (French national radioactive waste management agency) as a possible host rock for nuclear waste, was chosen as the starting claystone. The run products and solutions are characterised by means of different techniques (X-ray diffraction, scanning and transmission electron microscopy, manocalcimetry, inductively coupled plasma optical emission spectrometry and ion chromatography). This paper reports the reaction path leading to mineralogical changes of the claystone mineralogy (clays, calcite, quartz, pyrite and other accessories minerals), with a particular attention to the formation of iron-rich T–O phyllosilicates (cronstedtite and greenalite). The reaction path is compared with thermodynamic modelling of the experiment, and these modifications are discussed to evaluate their impact on the physical and chemical properties of the claystone. Although nuclear waste storage issues have initially motivated this study, some observations and conclusions may be relevant for the study of secondary alteration processes in primitive meteorites given the experimental conditions used. Indeed, the obtained results can be used to constrain the cronstedtite stability field and the mineralogical, textural and chemical evolutions of iron–silicate systems.

2. Materials and methods

2.1. Materials and cooling experiment

The claystone starting material used in the experiment comes from the Callovo-Oxfordian formation (COx) of the Paris Basin (Bure, Meuse/Haute-Marne, France). On average, this material contains 40% clay minerals (15% illite and micas, 20 to 25% illite–smectite mixed-layered minerals (MLMs), kaolinite + chlorite < 5%), 25% quartz and 30% carbonates (calcite and dolomite, with minor amounts of ankerite). The remaining 5% consists of pyrite, feldspar and organic matter (Rousset, 2002; Gaucher et al., 2004). A starting solution was prepared in a glove box under inert argon atmosphere, adding Na and Ca chlorides to ultrapure water to simulate the salinity of natural porewater in sediments. The solution contains 0.0207 mol/kg_{water} NaCl and 0.0038 mol/kg_{water} $CaCl_2$ and its pH is 6.4 at 25 °C (Guillaume et al., 2003, 2004; Jodin-Caumon et al., 2010, 2012; Rivard, 2011). The ground COx (1 g) and the solution (10 ml) were mixed in six Parr® non-stirred pressure vessels made of Teflon® with a capacity of ~20 ml, together with 2 plates of metallic iron (dimension 3 × 6 × 1 mm) and iron powder (500 mg, mean grain size ~ 40 μm). The iron powder/COx mass ratio is 0.5. All the Parr® vessels were heated in a furnace at 90 (±2) °C for 6 months, and the temperature was then reduced in monthly steps of 10 °C down to 40 °C (Fig. 1). At each temperature step, a vessel was removed from the furnace, quenched at room temperature and opened in a glove box. The run products were dried under an argon flux and prepared for analysis by different techniques.

2.2. Manocalcimetry (MCM)

The carbonate content of the samples was measured using a manocalcimeter (MCM, Museum National d'Histoire Naturelle, Paris) on 200 mg of powdered material (Ledésert et al., 2009). The MCM consists of a "Karbonat-Bombe", which is a simple apparatus composed of a glass flask and a high-precision manometer (Dunn, 1980). Calibration is performed using pure calcite crystals; uncertainty precision is around 0.5 wt.%.

2.3. X-ray diffraction (XRD)

The data were collected at room temperature with a D8 Bruker diffractometer, using CoKα radiation, 35 kV accelerating voltage and 45 mA current (LIEC Laboratory, Université de Lorraine). X-ray patterns were recorded on bulk-rock samples, using a scan step of 0.035° 2θ, exposure time of 3 s, $2\theta_{min} = 3°$ to $2\theta_{max} = 75°$. Semi-quantitative mineral contents were estimated using the EVA© software coupled with the PDF2 database of the ICDD comparing principal reflection amplitudes of minerals with that of calcite. The calcite content was accurately determined by MCM analysis and was used as an internal standard. The following conditions used to record air-dried XRD patterns for <2 μm fractions of the run products: scan step of 0.02° 2θ, exposure time of 4 s, $2\theta_{min} = 2°$ to $2\theta_{max} = 40°$.

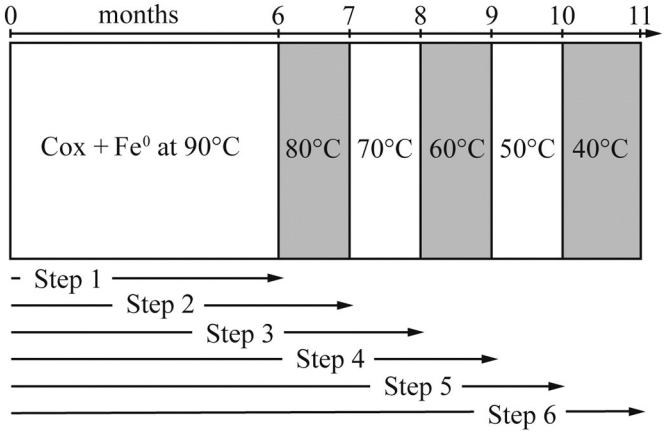

Fig. 1. Experimental design.

2.4. Scanning electron microscopy (SEM)

Secondary electron (SE) and backscattered electron (BSE) images of run products were obtained with an accelerating voltage of 15 kV and a beam current of 10 nA using a Hitachi S-4800 cold field emission gun (SCMEM laboratory, Université de Lorraine). Qualitative chemical compositions were determined by energy dispersive X-ray (EDX) spectroscopy.

2.5. Transmission electron microscopy (TEM)

TEM and high resolution TEM (HRTEM) analyses were carried out with two electron microscopes: a Philips CM200 operating at 200 kV (Institut Jean Lamour, Université de Lorraine, France), and a Tecnai F30 S-Twin scanning instrument operating at 300 kV (Institut für Physikalische Chemie, Johannes Gutenberg-Universität Mainz, Germany), both equipped with an energy dispersive X-ray (EDX) spectrometer. TEM specimens were prepared by dispersing the <2 μm fraction powders in ethanol under ultrasonication and then evaporating a drop of suspension on a carbon film placed on a 200 mesh copper grid.

2.6. Analysis of solutions

Run solutions were filtered (∅ 0.025 μm) and split into three aliquots. A first aliquot was used solely for the measurement of pH at room temperature in a glove box. No cation or anion concentrations were measured in this aliquot to avoid any contamination of the samples with the KCl electrolyte solution of the reference probe. The second aliquot was diluted ten times in HNO_3 2% to analyse Al, Ca, Fe, K, Mg, Na, Si, Mn, S and P by inductively coupled plasma optical emission spectrometry (LIMOS laboratory, Université de Lorraine). The final aliquot was diluted three times in H_2O to determine CO_3^{2-}, SO_4^{2-} and Cl^- concentration by ion chromatography.

2.7. Modelling approach

The modelling of thermodynamic equilibria as well as the reaction path was calculated with the Phreeqc geochemical code (Parkhurst and Appelo, 1999) using the Thermodem database (http://thermoddem.brgm.fr; Blanc et al., 2012). To simulate the experiments, iron (as Fe^0) was added step by step (until 0.89 $mol.l^{-1}$) to saline solution and reacted with a simplified mineralogy representative of the COx claystone (0.3 mol of calcite, 0.5 mol of quartz, 0.5 mol of clays (Illite_IMt-2) in 1 kg of solution), while solid solutions were not considered.

3. Results

3.1. Time–temperature evolution of COx

In the experimental conditions of this study, the iron–COx system is very reactive and many changes occur during the first heating step at 90 °C for 6 months.

XRD pattern of 90 °C experiment (step 1) indicates that the peak intensity of Fe^0 (52.3° 2θ) is strongly decreased compared to that observed on the X-ray pattern of the starting sample (Fig. 2a). Peak intensities of quartz (24.3 and 31° 2θ) and T–O–T phyllosilicates (~10.3° 2θ) are also significantly reduced. The formation of magnetite is shown by the appearance of peaks at 35° and 41.5° 2θ. The increase of the peak intensity at ~14.7° 2θ on XRD pattern of the 90 °C experiment is related to the formation of T–O phyllosilicates. The dolomite peak (36.2° 2θ) nearly disappears after heating at 90 °C, whereas the calcite peaks (34.4° 2θ and 27° 2θ) appear unchanged on X-ray patterns of run products from the 90 °C-experiment and from experiments at lower temperatures. The stability of calcite is confirmed by the MCM results, showing that calcite content remains constant, with percentages of 11.5% in the starting claystone and 10% in all run samples. As calcite seems unaffected by the temperature decrease, the peak at 34.4° 2θ is used in Fig. 2 to normalize all XRD patterns and facilitate their comparison. From 90 °C to 40 °C, a similar mineralogical change is observed characterised by a decrease in the intensities of the Fe^0, quartz, T–O–T phyllosilicates and dolomite peaks. Using the normalization of X-ray patterns, we can calculate the extent of dissolution of quartz and iron (Fig. 2b). At 90 °C, the dissolved amounts are 70% (±5%) and 85% (±5%) for quartz and iron, respectively. During the cooling (step 2 to step 6), the percentage dissolution of quartz continues to increase and reaches 90% (±5%), whereas it ranges between 75 and 85% in the case of iron. The pyrite peak at 38.6° 2θ is observed on X-ray patterns of all run samples, as well as the peaks of newly formed magnetite and T–O phyllosilicates (described in detail below).

SEM observations support the mineralogical trends shown by XRD. Very rare particles of iron are observed after heating at 90 °C. Their dimensions are greatly reduced (~20 μm) compared to the initial grain size (~40 μm), and they appear highly corroded (Fig. 3a). Quartz crystals show rectangular etches pits of different sizes due to the dissolution (Fig. 3b). The formation of automorphic octahedral crystals of magnetite (Fig. 3c) and pyramidal crystals of T–O phyllosilicates (Fig. 3d), identified as cronstedtite by Pignatelli et al. (2013), are also observed. SEM results confirm that calcite crystals are not altered, whereas dolomite is affected by the dissolution. Rhombohedral crystals of ankerite also show signs of dissolution at the corners or on the edges.

3.2. Time–temperature evolution of clay minerals

Clay minerals appear very reactive in this experiment, and they are affected by cooling in two main ways: transformation and disappearance of T–O–T minerals and formation of T–O minerals (Fig. 2). To obtain an accurate characterisation of the evolution of clays minerals, a decomposition routine was performed using DECOMPXR software (Lanson, 1997). The XRD patterns of air-dried <2 μm fractions of the starting sample and run products were decomposed using the methods outlined by Lanson and Besson (1992) and Lanson (1997). This method involves the subtraction of background and the decomposition of the superimposed peaks into elementary peaks with Gaussian and Lorentzian shapes.

3.2.1. T–O–T minerals

The decomposition of the 5–12° 2θ region in the XRD pattern of the starting sample requires the combination of five elementary peaks to obtain a good fit (Fig. 4). These peaks are assigned to a well-crystallized illite (WCI) at 10.4° 2θ, a poorly crystallized illite (PCI) at 10.2° 2θ, chlorite at 7.3° 2θ and two illite–smectite mixed-layered minerals (noted MLM_1 and MLM_2). These two MLMs are characterised by different proportions of illite: MLM_1 contains about 40 to 50% illite and MLM_2 about 70% illite.

For the 90 °C experiment (step 1 in Fig. 1), the decomposition shows that the intensity of all peaks is more than halved compared to the decomposition of the starting sample. The peaks of mixed layer minerals appear weaker and broader, and their positions do not correspond to those of MLM_1 and MLM_2 in the starting sample. These differences are probably due to the formation of more complex mixed-layered clays involving non-swelling T–O layers, and also to a reduction of the crystallite size. These new phases are denoted MLM_3 and MLM_4 in Fig. 4 to distinguish them from MLM_1 and MLM_2 in the COx. This hypothesis is supported by the HRTEM and TEM images showing the presence of clay particles with both T–O–T and T–O layers, which are characterised by a foil-like morphology (Fig. 5). For step 3 (70 °C), the sample requires the combination of only three peaks attributed to WCI, PCI and chlorite. These phases remain present during the course of cooling, but their intensities are even more reduced (less than a quarter of the intensities in the starting sample).

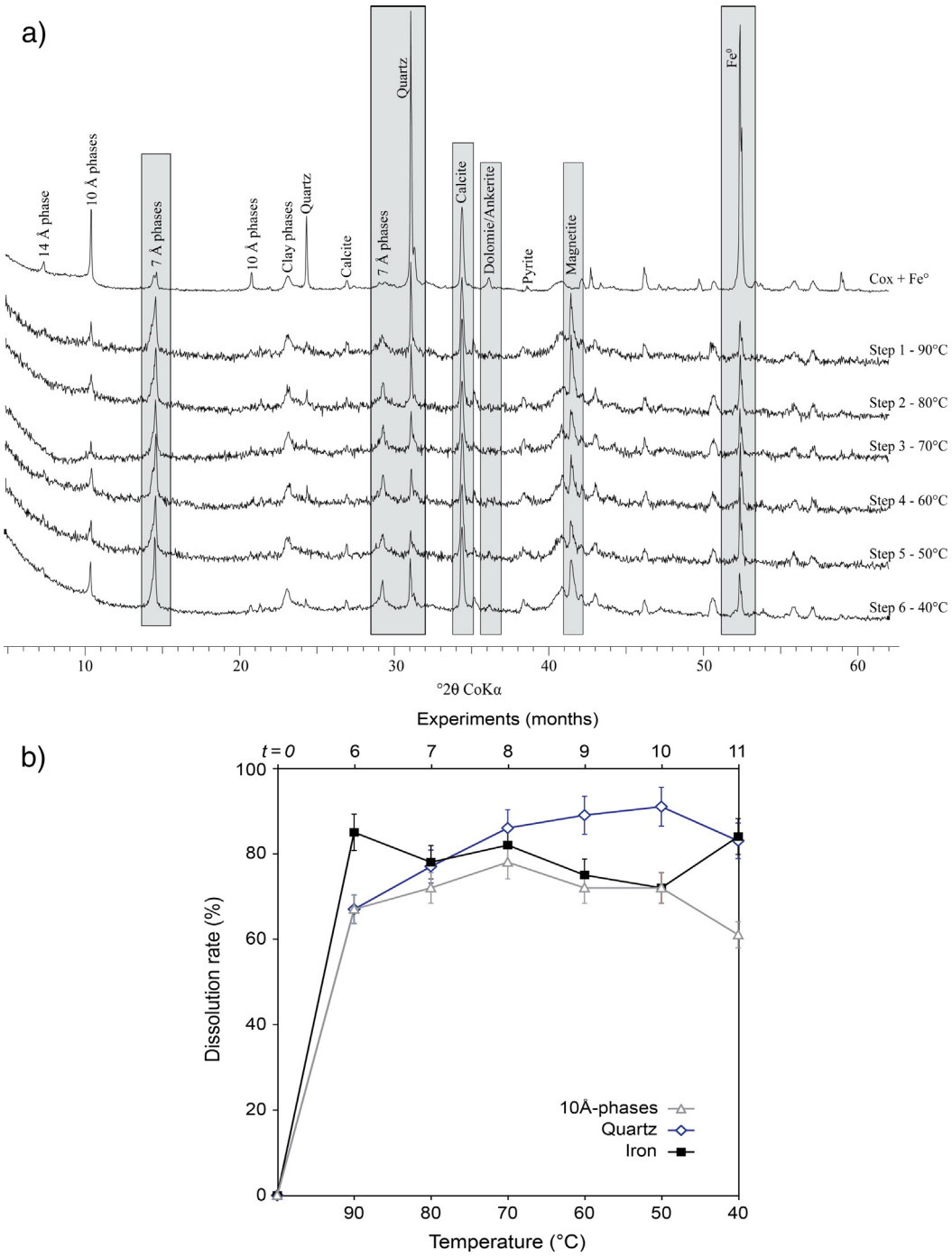

Fig. 2. (a) Bulk-rock XRD patterns of iron–COx starting mixture with Fe/COx mass ratio of 0.5 and run samples at different steps of the experiment. (b) Percentage dissolution of quartz, iron and 10 Å-phases as a function of experiment temperature, calculated from XRD patterns of bulk rock. The uncertainty is estimated from the diffractogram background.

3.2.2. T–O minerals

The width and intensity variations of peak at ~14° 2θ (7 Å) on XRD patterns of the 90° to 40 °C run samples (Fig. 2) are related to the formation of T–O minerals. The decomposition of the 12–16° 2θ region on the XRD pattern of the starting sample (Fig. 4) shows that three peaks are needed to obtain a good fit; these peaks are attributed to chlorite and two kaolinites with different degrees of crystallinity ($Kaol_1$ and $Kaol_2$ in Fig. 4). However, the decomposition of the X-ray pattern of the 90 °C sample (step 1) requires more peaks: the three peaks previously mentioned (Chl, $Kaol_1$ and $Kaol_2$) and two additional peaks attributed to newly formed T–O phyllosilicates. In agreement with SEM and TEM observations, the first peak, which is thinner and more intense, would correspond to cronstedtite. This latter phase is an iron-rich T–O phyllosilicate characterised by the presence of Fe^{2+} and Fe^{3+} in the octahedral sites and a partial replacement of Si^{4+} by Fe^{3+} in the tetrahedral sites. Cronstedtite crystals observed in the 90°–70 °C experiments (steps 1 to 3) are well crystallized and show pyramidal and conic morphologies (Pignatelli et al., 2013), but the pyramidal shape become predominant at lower temperatures (Fig. 6a, b). No significant differences can be noted in the chemical composition of conic and pyramidal crystals, and their mean formula is $(Fe^{2+}_{2.2}Fe^{3+}_{0.8})(Si_{1.2}Al_{0.1}Fe^{3+}_{0.7})O_5(OH)_4$.

The other peak is broader and weaker and could be attributed to rosette-like morphology minerals in SEM (Fig. 6c). SEM-EDX analyses

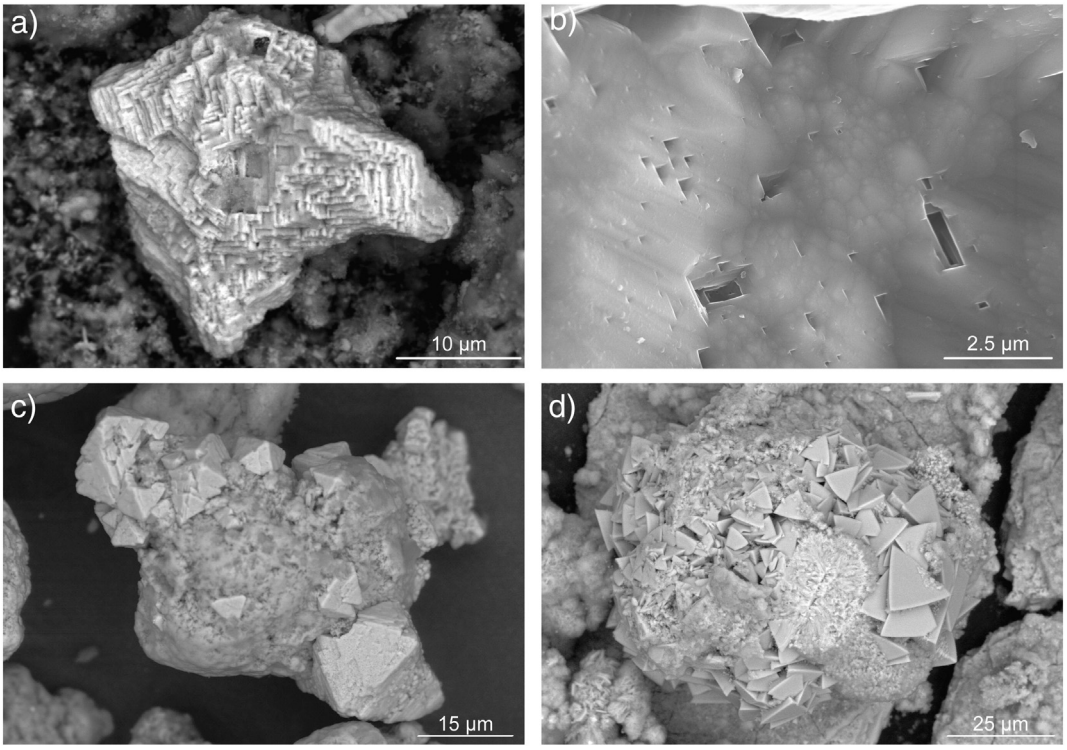

Fig. 3. Main mineralogical modifications observed by SEM: dissolution of (a) iron powder and (b) quartz; (c) formation of magnetite on iron powder and (d) cronstedtite.

show that these particles contain mainly Si and Fe (with a Si/Fe ratio higher than cronstedtite), with a small amount of Al (Fig. 6d). Considering the peak position on the XRD patterns (14.25° 2θ → 7.21 Å) and the chemical composition, we suggest that this rosette-like phase is greenalite. Decomposition of the XRD pattern of the 70 °C sample (step 3) shows that one of the kaolinite peaks disappears and that the cronstedtite peak is strongly intensified, underlining the abundance of this mineral at this step. At temperatures ≤60 °C, the peak at ~14° 2θ (7 Å) on XRD patterns is still present, but its intensity progressively declines. This can be due to the destabilization of cronstedtite below 50 °C, as already shown by Pignatelli et al. (2013).

3.2.3. Crystal-chemistry of clay minerals

The changes in crystal-chemistry of the clay minerals with decreasing experimental temperature are shown in the diagrams of Fig. 7. Here, we compare the composition of clay particles in the 90 °C and 50 °C run product samples (step 1 and step 5 in Fig. 1) with particles in the starting claystone (COx). The 50 °C sample is chosen rather than the 40 °C sample (step 6) because the reliability of compositional data for the latter is compromised by the formation of a Na-rich gel and/or by NaCl contamination. It is necessary to bear in mind that the EDX-TEM data of Fig. 7 are not representative of the abundance of each phase, but only give information about the chemical variations as a function of decreasing temperature. Three groups of particles are differentiated in Fig. 7:

(i) Less altered particles with compositions close to the MLMs of the starting claystone, which are characterised by a high Si content (>45 at.%) but which are not enriched in Fe. At 90 °C, as well as at 70 °C, no significant variations are observed in the interlayer cations, which still show high contents (Na + Ca + K > 7–8 at.%), and no K loss is noted (Fig. 7a–c). Nevertheless, at 50 °C, the range of Na + Ca + K at. % is wider (~3–12%) and the K content seems to be slightly lowered compared with the starting claystone (Fig. 7c).

(ii) The most altered particles, highly enriched in Fe, which show compositions close to cronstedtite (Fig. 7d).

(iii) Foil-like particles with a chemical composition between MLMs of the starting COx and iron-rich T–O phyllosilicates. They show Na + Ca + K contents varying from 1 to 6 at.%, along with depletion of K, Mg and Al and Fe-enrichment. These particles probably correspond to the complex mixed-layered clays involving non-swelling layers T–O layers whose occurrence is indicated by the results of XRD decomposition and HRTEM (see the evolution in the section of T–O–T minerals, Figs. 4 and 5).

3.3. Composition of solutions

The pH of each run solution, measured at room temperature, is plotted *versus* temperature in Fig. 8. It varies slightly from 7.23 to 7.62. Cation and anion concentrations of the run solutions are also reported *versus* experimental temperature, in cases where the values are above the detection limit. Si concentrations vary between 0.27 and 0.40 mM, falling below or close to the quartz solubility curve in run solutions of experiments carried out between 90° and 50 °C. This result explains the dissolution of some silicates (quartz, illite and MLMs) and the formation of cronstedtite and greenalite. At 50 °C, Si concentration in solution is in equilibrium with quartz. At this temperature, cronstedtite can no longer be formed and starts to dissolve (Pignatelli et al., 2013). Finally, Si concentration increases slightly in the last run solution (40 °C), and is above the quartz solubility curve. Concentrations of Al and Fe in the experimental solutions are not plotted because the values are very low (<0.02 mM) or below the detection limit. On the contrary, Mg concentration increases with falling temperature (from 0.2 mM to 1.2 mM), suggesting a partial dissolution of chlorite, dolomite and smectite layers of MLMs. K contents (between 4.90 and 7.25 mM) in solution are probably due to the partial dissolution of illite and/or illite layers in MLMs. The Na concentration remains of the same order as in the starting solution (20.14 mM) during the cooling; considering the analytical error of 10%, the impact of smectite layer dissolution and/or interlayer Na–Ca substitutions is probably undetectable. In the same way, the Ca concentration at each temperature is close to the initial Ca concentration (except for 40 °C) and is probably controlled by the calcite equilibrium.

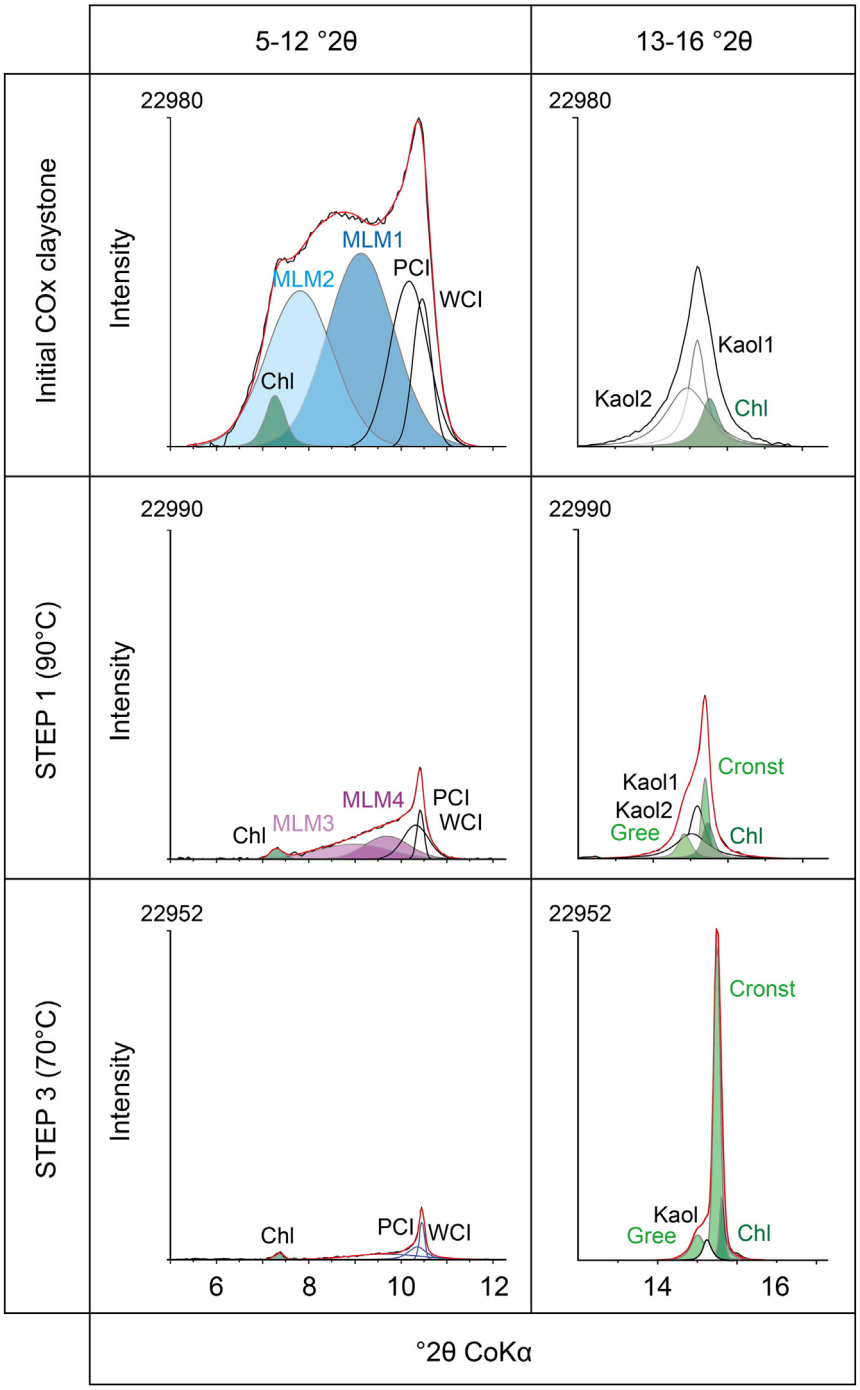

Fig. 4. Decomposition of air-dried XRD patterns in the 5 to 13 and 12 to 16° 2θ CoKα regions for starting mixture of COx + Fe and for run samples (<2 μm fraction) of steps 1 and 3. Chl: chlorite, Kaol: kaolinite, MLM: mixed-layered mineral, WCI: well crystallized illite, PCI: poorly crystallized illite, Cronst: cronstedtite, Gree: greenalite.

The presence of Ca in run solutions can be also related to the dissolution of smectite layers in MLMs. The trend of carbonate content shows slight fluctuations that are probably related to heterogeneity of the starting claystone (COx) in the sampled fractions. CO_3^{2-} in solutions can be explained by the dissolution of a small amount of calcite (less than 2% according to MCM results), dolomite and a minor ankerite. Sulfates concentration increases from 5 to 9 mM with the cooling, in agreement with the gypsum equilibrium. Cl^- concentrations measured in the experimental solutions increase slightly compared to the concentration of the starting solution. This slight increase (~7%) is probably due to the salts present in the COx, which vary in amount according to the porosity of the claystone and the consumption of water due to iron oxidation. Assuming the complete oxidation of the initial powdered iron (0.5 g) into magnetite, the consumption of water amounts to 0.2 ml (according to $3\ Fe + 4\ H_2O = Fe_3O_4 + 4\ H_2$) corresponding to 2% of the initial volume of solution. Thus, the effect on dissolved species concentrations is minor and included in the error bars (Fig. 8).

4. Discussion

The TEM, SEM and XRD data in this study are in agreement with previous experimental results and thermodynamic/kinetic simulations highlighting the high reactivity of the iron–COx system. Iron corrosion in the presence of Callovo-Oxfordian claystone at 90 °C is associated

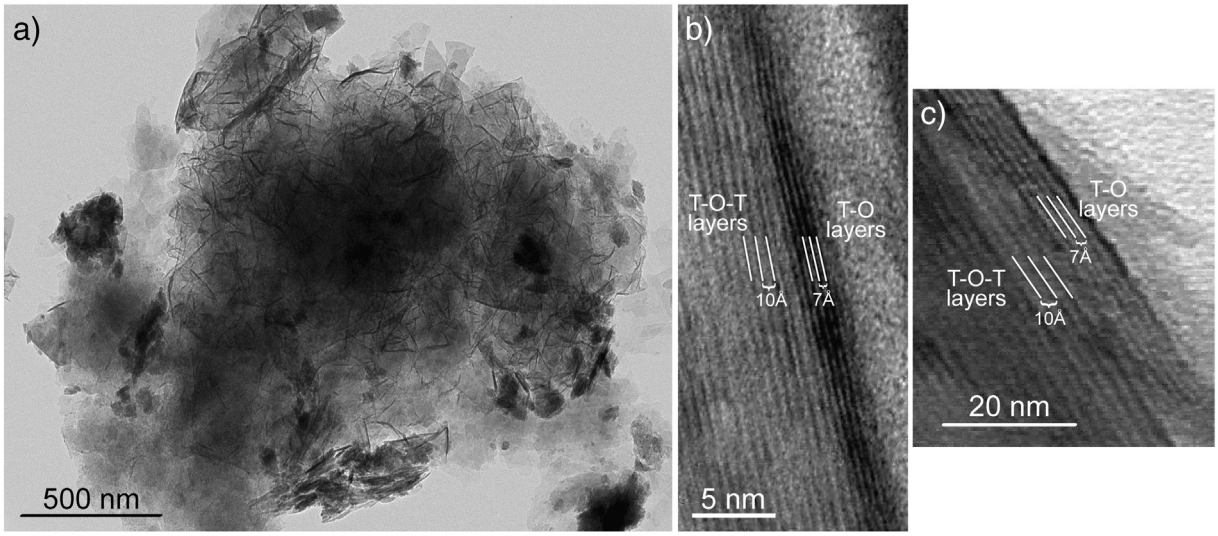

Fig. 5. (a) TEM and (b) HRETM images of complex mixed layered minerals at 90 °C. These MLMs are characterised by (a) foil-like morphology and (b, c) the presence of both T–O–T and T–O layers.

with a marked destabilization of clay minerals (MLMs, chlorite, kaolinite and illite) and the dissolution of quartz, along with the formation of magnetite and new iron-rich phyllosilicates (de Combarieu et al., 2007; Schlegel et al., 2008, 2010; Pierron, 2011; Rivard, 2011).

In our experiment, the 90 °C-run sample (step 1) contains clay particles inherited from the starting COx, newly formed iron-rich T–O phyllosilicates (above all cronstedtite) and complex mixed-layered minerals. The composition of these MLMs is characterised by a loss of Al and Mg correlated with Fe enrichment, and also by the loss of interlayer cations, especially K, compared to the composition of the starting clays. The structural complexity of the MLMs is due to the presence of both T–O–T layers and non-swelling T–O layers, as shown by HRTEM images and by the XRD decomposition results (Figs. 4 and 5). The formation of these new MLMs with foil morphology could be explained by a progressive transformation of T–O–T into T–O layers *via* a cannibalization process. It should be noted that, at this step, 65% or more of the quartz, iron and T–O–T phyllosilicates are already dissolved (Fig. 2b).

The progressive cooling from 90 °C (step 1) to 40 °C (step 6) leads to a dissolution of quartz (90%) and dolomite, as well as the alteration of chlorite, kaolinite and illite, whereas calcite is almost unaffected by the temperature variations (<2% dissolution). Magnetite is always observed down to 40 °C, while the complex T–O–T/T–O mixed layers disappear at temperatures ≤70 °C. Cooling also favours the precipitation of cronstedtite. The formation of cronstedtite together with magnetite

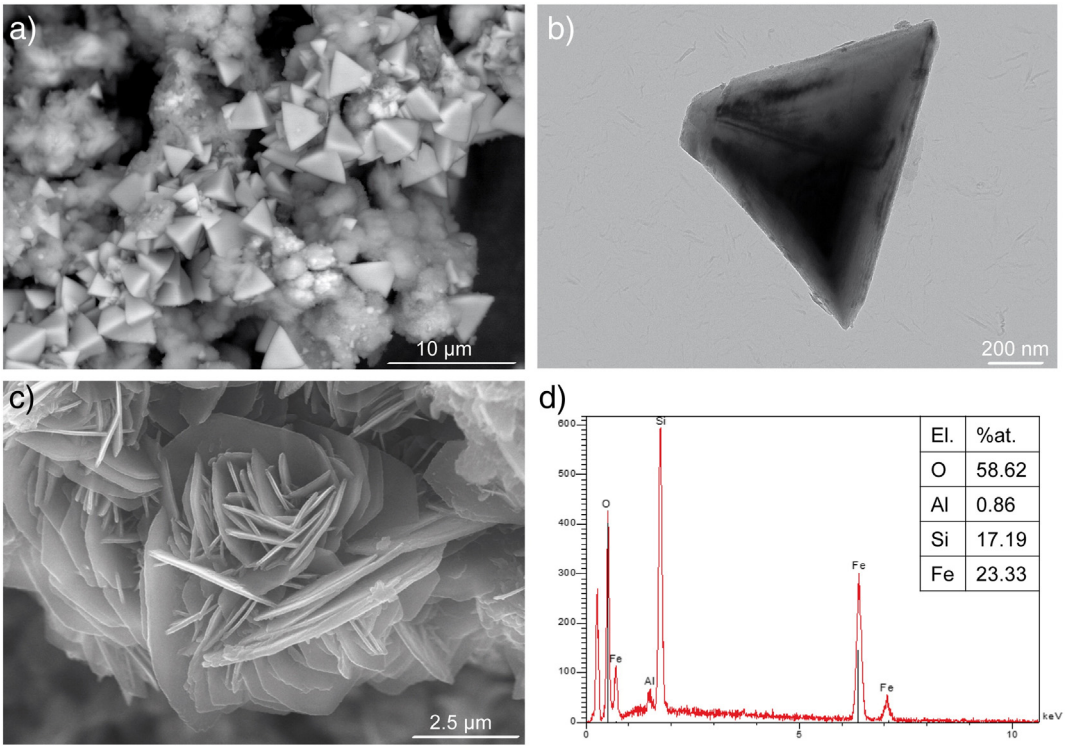

Fig. 6. (a) SEM and (b) TEM images of newly formed cronstedtite; (c) SEM image and (d) EDX spectrum of particles with a rosette-like morphology (70 °C experiment), identified as greenalite.

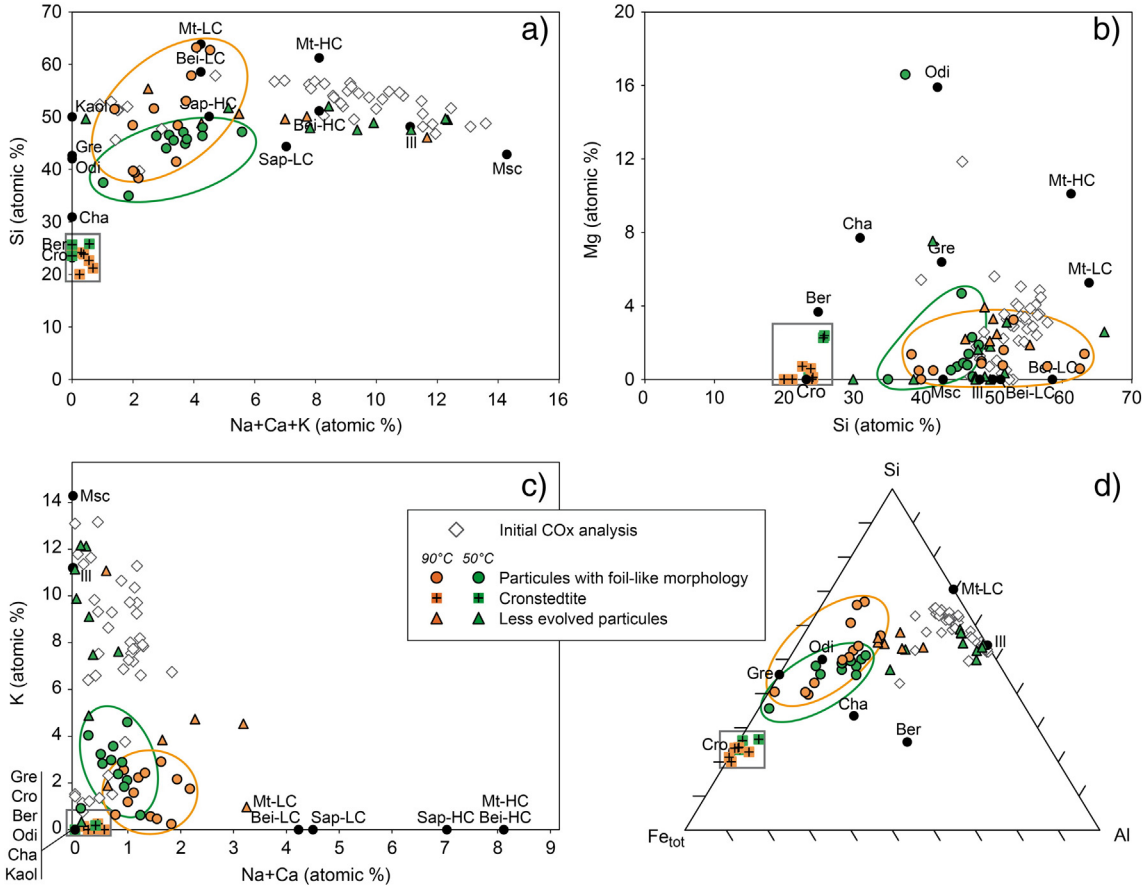

Fig. 7. Crystal-chemistry of clay minerals in the starting claystone, in the run products of 90 °C and 50 °C experiments, plotted in binary diagrams (a) Si at.% *vs.* Na + Ca + K at.%; (b) Mg at.% *vs.* Si at.%; (c) K at.% *vs.* Na + Ca at.%; and in a (d) Si–Al–Fe_{tot} ternary diagram. Reference clays, indicated by black circles, are (Kostov, 1968; Caillère et al., 1982): Kaol: kaolinite $Al_2Si_2O_5(OH)_4$; Cha: chamosite $(Fe^{2+}{}_{3.87}Mg_{0.76}Al_{1.23})(Si_{3.05}Al_{0.95})O_{10}(OH)_8$; Mt-LC: low-charge montmorillonite $(Na_{0.2}Ca_{0.065})(Al_{1.67}Mg_{0.33})Si_4O_{10}(OH)_2$; Mt-HC: high-charge montmorillonite $(Na_{0.4}Ca_{0.13})(Al_{1.34}Mg_{0.66})Si_4O_{10}(OH)_2$; Bei-LC: low-charge beidellite $(Na_{0.2}Ca_{0.065})Al_2(Si_{3.67}Al_{0.33})O_{10}(OH)_2$; Bei-HC: high-charge beidellite $(Na_{0.4}Ca_{0.13})Al_2(Si_{3.34}Al_{0.66})O_{10}(OH)_2$; Sap-LC: low-charge saponite $Na_{0.33}Mg_3(Si_{3.67}Al_{0.33})O_{10}(OH)_2$; Sap-HC: high-charge saponite $(Na_{0.4}Ca_{0.13})Mg_3(Si_{3.34}Al_{0.66})O_{10}(OH)_2$; Ill: illite $K_{0.75}Al_2(Si_{3.25}Al_{0.75})O_{10}(OH)_2$; Msc: muscovite $KAl_2(Si_3Al)O_{10}(OH)_2$; Gre: greenalite $(Fe^{3+}{}_{0.45}Fe^{2+}{}_{1.9}Mg_{0.3}\square_{0.35})Si_2O_5(OH)_4$ (Guggenheim et al., 1982); Odi: odinite $(Al_{0.15}Fe^{3+}{}_{1.2}Fe^{2+}{}_{0.35}Mg_{0.7}\square_{0.6})(Si_{1.85}Al_{0.15})O_5(OH)_4$ (Bailey, 1988); Ber: berthierine $(Al_{0.96}Fe^{3+}{}_{0.22}Fe^{2+}{}_{1.49}Mg_{0.17}\square_{0.17})(Si_{1.15}Al_{0.85})O_5(OH)_4$ (Brindley, 1982); Cro: cronstedtite $(Fe^{3+}{}_{0.84}Fe^{2+}{}_{2.16})(Si_{1.16}Fe_{0.84})O_5(OH)_4$ (Kogure et al., 2002).

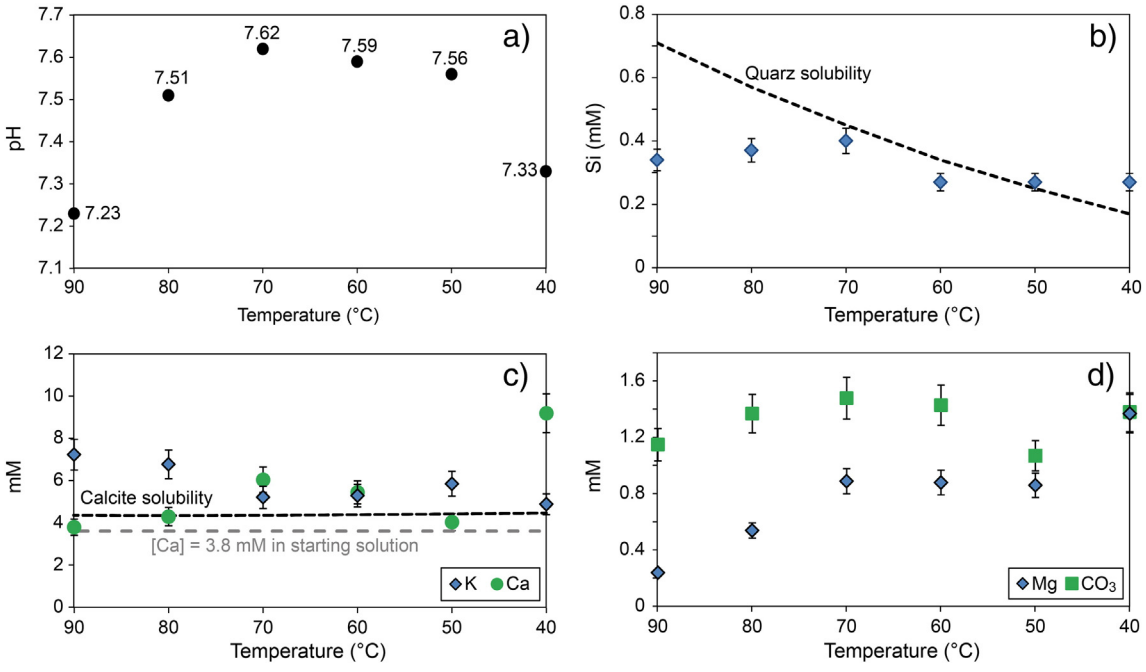

Fig. 8. (a) pH measured at 25 °C and (b–d) compositional variations of run solutions for different cations and anions as a function of temperature.

was already predicted by the modelling of Bildstein et al. (2006) performed at 50 °C in the iron–COx system, but the present experimental investigation is the first study which clearly demonstrates the occurrence of cronstedtite. In previous studies on iron–COx interactions, the newly formed iron-rich phyllosilicates were not accurately characterised and were generically described as "chlorite or serpentine-like minerals" (de Combarieu et al., 2007; Jodin-Caumon et al., 2012), "Fe–serpentine as berthierine" (Pierron, 2011), "Fe–serpentine as odinite–berthierine" (Rivard, 2011), while Schlegel et al. (2010), using different experimental conditions (undiluted medium), described Fe-silicate solids formed by replacing iron metal as "Fe-rich 7 Å phyllosilicates". The experiments of Rivard (2011) and Pierron (2011) were carried out under conditions comparable with the first step of our experiment at 90 °C, but the compositions of the most highly altered clays in this previous study are characterised by a higher Si/Fe ratio and are not close to that of cronstedtite. Cronstedtite formation at temperatures lower than 80 °C has only been observed by Lantenois (2003), Lantenois et al. (2005) and Lanson et al. (2012) in other systems, where dioctahedral smectites were used instead of a claystone.

The present experimental results also suggest that cronstedtite occurs together with another T–O phyllosilicates interpreted as greenalite, which display a regular rosette-like morphology (Fig. 6c). Two hypotheses can be proposed to explain the occurrence of greenalite in the run products:

(i) The crystallization of greenalite may be related to the dissolution of kaolinite. Recent results show, in fact, that iron-rich T–O phyllosilicates can form at the expense of pristine kaolinite, with a thickening of these minerals on the basal surface of the kaolinite by epitaxial growth (Rivard et al., 2013).

(ii) The neoformation of greenalite, as cronstedtite, probably depends on local variations of the Si/Fe ratio and of pH in the solution.

To improve our understanding of the formation of cronstedtite and greenalite as products of iron corrosion and the destabilization of silicates in the cooling experiment, we used the Phreeqc software to perform thermodynamic simulations of cronstedtite precipitation and reaction paths. Fig. 9 shows the calculated stability fields of hematite, cronstedtite, magnetite and greenalite in a $f(O_2)$ *vs.* log $[Si_{(aq)}]$ phase diagram ($[Si_{(aq)}]$ refers to total Si content in solution). According to this projection, the stability field of cronstedtite is located in-between those of magnetite, hematite and greenalite (in accordance with Dyl et al., 2006), and decreases in size with increasing temperature, until becoming negligible above 150 °C (Fig. 9a). This evolution of the cronstedtite stability field is in general agreement with the results of Zolotov (2014), which predict that cronstedtite may not form at T > 120 °C. This explains why cronstedtite was not observed in iron–COx experiments carried out at 150 °C, even if more iron was added to the system than in our experiment (Fe^0/clay ratio = 1 in Pierron, 2011). Both the $f(O_2)$ (determined (i) assuming that the system evolves along the H_2O/H_2 equilibrium line and (ii) recalculating the *in situ* pH at 90 °C) and the aqueous silicon concentrations measured after each run are consistent with the observed precipitation of cronstedtite and its expected stability field at each temperature (*i.e.*, 90 to 60 °C). At low temperature (T = 50 °C), we can note an apparent inconsistency between observed dissolution of cronstedtite and thermodynamic predictions (larger stability field). This can be explained by (i) the system is out of the stability field of cronstedtite (*e.g.* $f(O_2)$ slightly higher), (ii) the structural and kinetic constraints may influence the reaction pathway

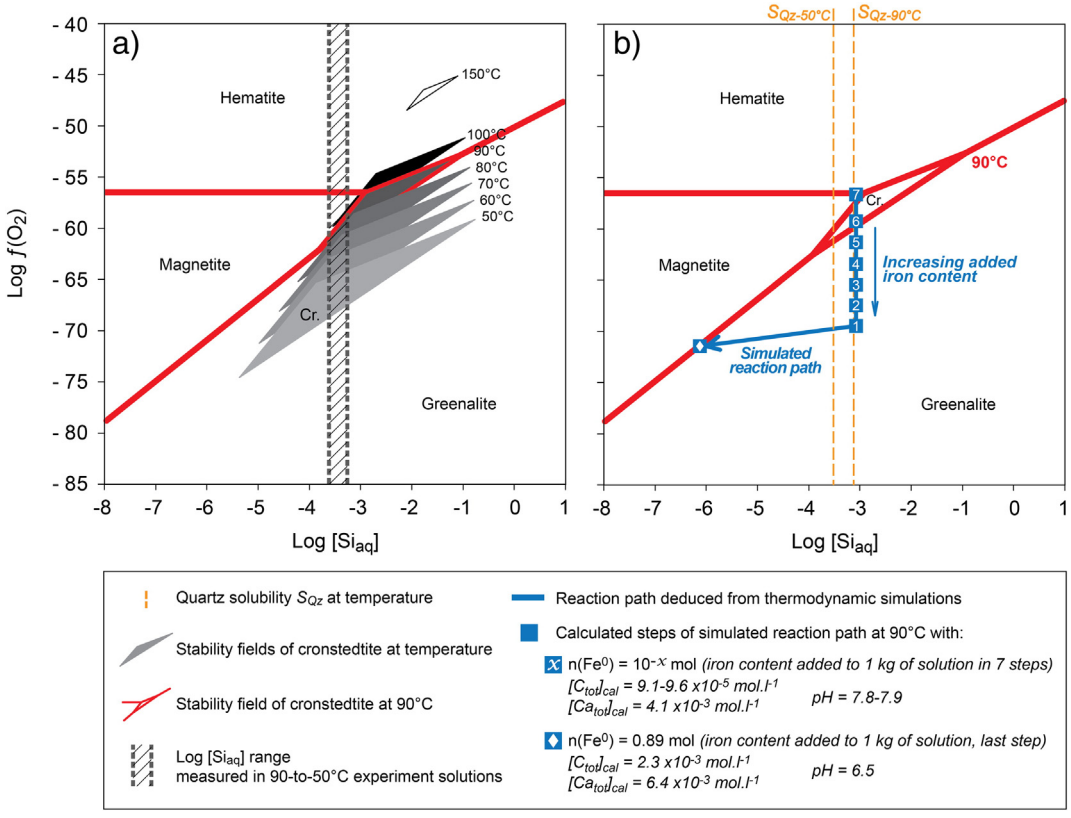

Fig. 9. Calculated stability fields of hematite, cronstedtite (denoted Cr.), magnetite and greenalite in $f(O_2)$ *vs.* log $[Si_{(aq)}]$ phase diagrams (a) at each temperature increment and (b) at 90 °C, superimposed onto a possible reaction path for iron/claystone interactions under hydrothermal conditions (90 °C) simulated by a step-by-step addition of iron in a simplified COx + solution system (8 steps with increasing iron content: 10^{-7}, 10^{-6}, 10^{-5}, 10^{-4}, 10^{-3}, 10^{-2}, 10^{-1} and 0.89 mol for 1 kg of solution). Diagrams also indicate the solubility of quartz at 50 and 90 °C, and range of Si concentration in solution (measured after the run).

and the nature of the end-products, and/or (iii) the lack of accurate thermodynamic data. As described by Pignatelli et al. (2013), several cronstedtite polytypes coexist in our experiments, while the available thermodynamic database does not permit to take into account more than one polytype.

To check the convergence between the modelling and observed mineralogical transformations, we calculate here a possible reaction path for iron–claystone interactions under hydrothermal conditions at 90 °C. In Fig. 9b, we superimpose this reaction path onto the stability fields of the selected iron-bearing phases. This calculation reveals that the system rapidly becomes reducing with the addition of small amounts of Fe^0. With decreasing $f(O_2)$, the system is in the stability field of cronstedtite during the early stages of the iron–claystone interaction (addition of 10^{-7} and 10^{-6} mol of Fe^0 per kg_{water}). Silicon concentration remains buffered by quartz, and greenalite should precipitate during the subsequent stages of the reaction path (addition of 10^{-5} to 10^{-1} mol of iron). In our experiments, greenalite, magnetite and cronstedtite are simultaneously observed, implying that the precipitation of these secondary minerals is probably kinetically controlled or that the Si/Fe ratio varies locally in the system. In fact, it is apparent from the silicon concentration measurements (Fig. 8) that the solution is undersaturated with respect to quartz until step 4 (from 90 to 60 °C) and that 85% of the iron is consumed after the first 6 months at 90 °C. At the last step of iron addition, when the added iron concentration is 0.89 $mol.l^{-1}$, quartz is fully consumed, magnetite and siderite start to precipitate and the recalculated pH decreases from 7.79 to 6.52. However, this last calculated step is not representative of the experimental results (outside the measured range of Si concentrations, considering total dissolution of iron, *etc.*) and the reaction path probably lies on or close to the greenalite/cronstedtite equilibrium.

In any case, the mineralogical evolution of a claystone in contact with metallic iron, as observed in our experiments, is consistent from a thermodynamic point of view, although simple thermodynamic considerations do not allow us to predict cronstedtite destabilization below 50 °C, raising the question of the validity of thermodynamic data for cronstedtite at very low T.

5. Conclusion

This study represents the first experimental simulation of the cooling from 90 °C to 40 °C of an iron–claystone–water system. The results clearly demonstrate that cronstedtite together with greenalite are the main run products. Since these newly formed iron-rich T–O phyllosilicates develop at the expense of mixed-layered illite–smectite clays, chlorite and kaolinite, there will only be a slight reduction in the cation exchange capacity and the degree of swelling of the clay barrier. Modifications of the clogging taking place in the porosity at the canister/clay interface will be also expected after a significant dissolution of quartz and illite associated with the precipitation of magnetite and T–O minerals (Bildstein et al., 2006). Thus, the formation of cronstedtite and minor amounts of greenalite has to be taken into account to predict the modifications of the chemical, physical and mechanical properties of the clay barrier with time for the safety assessment of an underground nuclear waste repository. Finally, the formation of cronstedtite and iron-rich secondary minerals due to the interaction between metallic iron and silicates can have wider implications in the geological sciences. Indeed, cronstedtite occurs rarely in terrestrial samples but is the dominant Fe-phyllosilicate phase in CM meteorites (Dyl et al., 2006), where it has been observed both in fine-grained rims around chondrules and within the matrix (Müller et al., 1979; Barber, 1981; Zolensky et al., 1993; Burbine and Burns, 1994; Browning et al., 1996; Lauretta et al., 2000; Zega and Buseck, 2003; Miyahara et al., 2008). A parallelism can thus be drawn between the conditions of formation of cronstedtite in nuclear waste multi-barrier systems and in many CM meteorites. The formation conditions of this mineral in meteorites are similar to those in the experiment described here: presence of metallic iron, reducing conditions, presence of fluids, low temperatures and neutral-alkaline solutions. As cronstedtite formation in CM meteorites is not yet well understood and is still a matter of debate, the present experimental and thermodynamic results can provide some keys to improve our understanding of the occurrence of this mineral in iron-rich contexts that are different from iron–clay/claystone interactions.

Acknowledgements

This research was financially supported by ANDRA — Agence nationale pour la gestion des déchets radioactifs (I11ABC3ANDRA) (French national agency for radioactive waste management). We are grateful to U. Kolb for providing access to the TEM laboratory at the Institut für Physikalische Chemie, Johannes Gutenberg Universität. S. Migot is thanked for the TEM images (Institut Jean Lamour, Université de Lorraine, France). The authors also wish to thank Michael Carpenter for his professional English language review.

References

ANDRA, 2005. Phenomenological evolution of a geological repository. http://www.andra.fr/international/download/andra-international-en/document/editions/269va.pdf.
Bailey, S.W., 1988. Odinite, a new dioctahedral-trioctahedral Fe^{3+}-rich 1:1 clay mineral. Clay Miner. 23, 237–247.
Barber, D.J., 1981. Matrix phyllosilicates and associated minerals in CM2 carbonaceous chondrites. Geochim. Cosmochim. Acta 45, 945–970.
Bildstein, O., Trotignon, L., Perronnet, M., Jullien, M., 2006. Modelling iron–clay interactions in deep geological disposal conditions. Phys. Chem. Earth 31, 618–625.
Blanc, P., Lassin, A., Piantone, P., Azaroual, M., Jacquemet, N., Fabbri, A., Gaucher, E.C., 2012. Thermoddem: a geochemical database focused on low temperature water/rock interactions and waste materials. Appl. Geochem. 27, 2107–2116.
Bourdelle, F., Truche, L., Pignatelli, I., Mosser-Ruck, R., Lorgeoux, C., Roszypal, C., Michau, N., 2014. Iron–clay interactions under hydrothermal conditions: impact of specific surface area of metallic iron on reaction pathway. Chem. Geol. 381, 194–205.
Brearley, A.J., 2006. The action of water. Meteorites and Early Solar System II,pp. 587–624.
Brindley, G.W., 1982. Chemical composition of berthierines — a review. Clays Clay Minerals 30, 153–155.
Browning, L.B., McSween Jr., H.Y., Zolensky, M.E., 1996. Correlated alteration effects in CM carbonaceous chondrites. Geochim. Cosmochim. Acta 60, 2621–2633.
Burbine, T.H., Burns, R.G., 1994. Questions concerning the oxidation of the ferrous iron in carbonaceous chondrites. Lunar Planetary Science XXV, pp. 199–200.
Caillère, S., Hénin, S., Rautureau, M., 1982. Minéralogie des Argiles. Structure et Propriétés Physico-Chimiques. Masson, Paris, (184 pp.).
de Combarieu, G., Barboux, P., Minet, Y., 2007. Iron corrosion in Callovo-Oxfordian argilite: from experiments to thermodynamic/kinetic modelling. Phys. Chem. Earth 32, 346–358.
de Combarieu, G., Schlegel, M.L., Neff, D., Foy, E., Vantelon, D., Barboux, P., Gin, S., 2011. Glass–iron–clay interactions in a radioactive waste geological disposal: an integrated laboratory-scale experiment. Appl. Geochem. 26, 65–79.
Dunn, D.A., 1980. Revised techniques for quantitative calcium carbonate analysis using the "Karbonat-Bombe", and comparisons to other quantitative carbonate analysis methods. J. Sediment. Res. 50, 631–636.
Dyl, K.A., Manning, C.E., Young, E.D., 2006. Modelling aqueous alteration of CM carbonaceous chondrites: implications for cronstedtite formation by water–rock reaction. Lunar and Planetrary Science, XXXVII.
Gaucher, E., Robelin, C., Matray, J.M., Négrel, G., Gros, Y., Heitz, J.F., Vinsot, A., Rebours, H., Cassagnabère, A., Bouchet, A., 2004. ANDRA underground research laboratory: interpretation of the mineralogical and geochemical data acquired in the Callovian–Oxfordian formation by investigative drilling. Phys. Chem. Earth 29, 55–77.
Guggenheim, S., Bailey, S.W., Eggleton, R.A., Wilkes, P., 1982. Structural aspects of greenalite and related minerals. Can. Mineral. 20, 1–18.
Guillaume, D., Neaman, A., Cathelineau, M., Mosser-Ruck, R., Peiffert, C., Abdelmoula, M., Dubessy, J., Villiéras, F., Baronnet, A., Michau, N., 2003. Experimental synthesis of chlorite from smectite at 300 °C in the presence of metallic Fe. Clay Miner. 38, 281–302.
Guillaume, D., Neaman, A., Cathelineau, M., Mosser-Ruck, R., Peiffert, C., Abdelmoula, M., Dubessy, J., Villiéras, F., Baronnet, A., Michau, N., 2004. Experimental study of the transformation of smectite at 80 and 300 °C in the presence of Fe oxides. Clay Miner. 39, 17–34.
Jodin-Caumon, M.C., Mosser-Ruck, R., Rousset, D., Randi, A., Cathelineau, M., Michau, N., 2010. Effect of a thermal gradient on iron–clay interactions. Clays Clay Minerals 58, 667–681.
Jodin-Caumon, M.-C., Mosser-Ruck, R., Randi, A., Pierron, O., Cathelineau, M., Michau, N., 2012. Mineralogical evolution of a claystone after reaction with iron under thermal gradient. Clays Clay Minerals 60, 443–455.
Kogure, T., Hybler, J., Yoshiba, H., 2002. Coexistence of two polytypic groups in cronstedtite from Lostwithiel England. Clays Clay Minerals 50, 504–513.
Kostov, I., 1968. Mineralogy. Oliver and Boyd, Edinburgh and London, (587 pp.).
Lanson, B., 1997. Decomposition of experimental X-ray diffraction patterns (profile fitting): a convenient way to study clay minerals. Clays Clay Minerals 45, 132–146.

Lanson, B., Besson, G., 1992. Characterisation of the end of smectite-to-illite transformation: decomposition of X-ray patterns. Clays Clay Minerals 40, 40–52.
Lanson, B., Lantenois, S. Van, Aken, P.A., Bauer, A., Plançon, A., 2012. Experimental investigation of smectite interaction with metal iron at 80 °C: structural characterization of newly formed Fe-rich phyllosilicates. Am. Mineral. 97, 864–871.
Lantenois, S., 2003. Réactivié fer metal/smectites en milieu hydraté à 80 °C. (Thesis) Orléans University, Orléans, France.
Lantenois, S., Lanson, B., Muller, F., Bauer, A., Jullien, M., Plançon, A., 2005. Experimental study of smectite interaction with metal Fe at low temperature: 1. Smectite destabilization. Clays Clay Minerals 53, 597–612.
Lauretta, D.S., Hua, X., Buseck, P.R., 2000. Mineralogy of fine-grained rims in the ALH 81002 CM chondrite. Geochim. Cosmochim. Acta 64, 3263–3273.
Ledésert, B., Hébert, R., Grall, C., Genter, A., Dezayes, C., Bartier, D., Gérard, A., 2009. Calcimetry as a useful tool for a better knowledge of flow pathways in the Soultz-sous-Forêts Enhanced Geothermal System. J. Volcanol. Geotherm. Res. 181, 106–114.
Martin, F.A., Bataillon, C., Sclegel, M.L., 2008. Corrosion of iron and low alloyed steel within a water saturated brick of clay under anaerobic deep geological disposal conditions: an integrated experiment. J. Nucl. Mater. 379, 80–90.
Miyahara, M., Uehara, S., Ohtani, E., Nagase, T., Nishijima, M., Vashaei, Z., Kitagawa, R., 2008. The anatomy of altered chondrules and FGRs covering them in a CM chondrite by FIB-STEM. Lunar Planetary Science, XXXIV, pp. 199–200.
Mosser-Ruck, R., Cathelineau, M., Guillaume, D., Charpentier, D., 2010. Effects of temperature, pH, and iron/clay and liquid/clay ratios on experimental conversion of dioctahedral smectite to berthierine, chlorite, vermiculite, or saponite. Clays Clay Minerals 58, 280–291.
Müller, W.F., Kurat, G., Kracher, A., 1979. Chemical and crystallographic study of cronstedtite in the matrix of the Cochabamba (CM2) carbonaceous chondrite. Tschermaks Mineral. Petrogr. Mitt. 26, 293–304.
Parkhurst, D.L., Appelo, C.A.J., 1999. User's Guide to PHREEQC (Version 2). A Computer Program for Speciation, Batch-reaction, One-dimensional Transport, and Inverse Geochemical Calculations. US Geol. Surv. Water Resour. Inv. Rep. 99-4259, p. 312.
Perronnet, M., Villiéras, F., Jullien, M., Razafitianamaharavo, A., Raynal, J., Bonnin, D., 2007. Towards a link between the energetic heterogeneities of the edge faces of smectites and their stability in the context of metallic corrosion. Geochim. Cosmochim. Acta 71, 1463–1479.
Perronnet, M., Jullien, M., Villiéras, F., Raynal, J., Bonnin, D., Bruno, G., 2008. Evidence of a critical content in Fe(0) on FoCa7 bentonite reactivity at 80 °C. Appl. Clay Sci. 38, 187–202.
Pierron, O., 2011. Interactions eau-fer-argilite: Rôle des paramètres Liquide/Roche, Fer/Argilite, Température sur la nature des phases minérales. (Thesis) Henri Poincaré University, Nancy, France.
Pignatelli, I., Mugnaioli, E., Hybler, J., Mosser-Ruck, R., Cathelineau, M., Michau, N., 2013. A multi-technique characterisation of cronstedtite synthesized by iron–clay interaction in a step-by-step cooling procedure. Clays Clay Minerals 61, 277–289.
Rivard, C., 2011. Contribution à l'étude de la stabilité des minéraux constitutifs de l'argilite du Callovo-Oxfordien en présence de fer à 90 °C. (Thesis) Henri Poincaré University, Nancy, France.
Rivard, C., Pelletier, M., Michau, N., Razafitianamahavaro, A., Bihannic, I., Abdelmoula, M., Ghanbaja, J., Villiéras, F., 2013. Berthierine-like mineral formation and stability during the interaction of kaolinite with metallic iron at 90 °C under anoxic and oxic conditions. Am. Mineral. 98, 163–180.
Rousset, D., 2002. Etude de la fraction argileuse de séquences sédimentaires de la Meuse et du Gard. Reconstruction de l'histoire diagénetique et des caractéristiques physico-chimiques des cibles. (Thesis) Louis Pasteur University, Strasbourg, France.
Schlegel, M.L., Bataillon, C., Benhamida, K., Blanc, C., Menut, D., Lacour, J.-L., 2008. Metal corrosion and argillite transformation at the water-saturated, high-temperature iron–clay interface: a microscopic-scale study. Appl. Geochem. 23, 2619–2633.
Schlegel, M.L., Bataillon, C., Blanc, C., Prêt, D., Eddy, F., 2010. Anodic activation of iron in clay media under water-saturated conditions at 90 °C: characterisation of the corrosion interface. Environ. Sci. Technol. 44, 1503–1508.
Zega, T.J., Buseck, P.R., 2003. Fine-grained-rim mineralogy of the Cold Bokkeveld CM chondrite. Geochim. Cosmochim. Acta 67, 1711–1721.
Zolensky, M.E., Bourcier, W.L., Gooding, J.L., 1989. Aqueous alteration on the hydrous asteroids: results of EQ3/6 computer simulations. Icarus 78, 411–425.
Zolensky, M.E., Barrett, R., Browning, L.B., 1993. Mineralogy and composition of matrix and chondrule rims in carbonaceous chondrites. Geochim. Cosmochim. Acta 57, 3123–3148.
Zolensky, M.E., Mittlefehldt, D.W., Lipschutz, M.E., Wang, M.S., Clayton, R.N., Mayeda, T.K., Grady, M.M., Pillinger, C., Barber, D., 1997. CM chondrites exhibit the complete petrologic range from type 2 to 1. Geochim. Cosmochim. Acta 61, 5099–5115.
Zolotov, M.Y., 2014. Formation of brucite and cronstedtite-bearing mineral assemblages on Ceres. Icarus 228, 13–26.

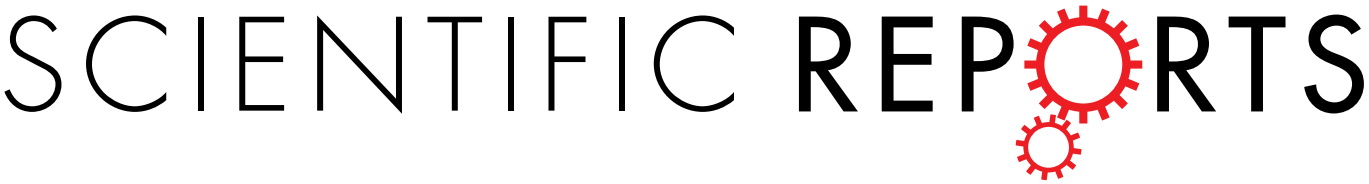

OPEN

Direct Experimental Evidence for Differing Reactivity Alterations of Minerals following Irradiation: The Case of Calcite and Quartz

Received: 27 August 2015
Accepted: 30 December 2015
Published: 29 January 2016

Isabella Pignatelli[1], Aditya Kumar[1], Kevin G. Field[2], Bu Wang[3], Yingtian Yu[3], Yann Le Pape[2], Mathieu Bauchy[3] & Gaurav Sant[1,4]

Concrete, used in the construction of nuclear power plants (NPPs), may be exposed to radiation emanating from the reactor core. Until recently, concrete has been assumed immune to radiation exposure. Direct evidence acquired on Ar^{+}-ion irradiated calcite and quartz indicates, on the contrary, that, such minerals, which constitute aggregates in concrete, may be significantly altered by irradiation. More specifically, while quartz undergoes disordering of its atomic structure resulting in a near complete lack of periodicity, calcite only experiences random rotations, and distortions of its carbonate groups. As a result, irradiated quartz shows a reduction in density of around 15%, and an increase in chemical reactivity, described by its dissolution rate, similar to a glassy silica. Calcite however, shows little change in dissolution rate - although its density noted to reduce by ≈9%. These differences are correlated with the nature of bonds in these minerals, i.e., being dominantly ionic or covalent, and the rigidity of the mineral's atomic network that is characterized by the number of topological constraints (n_c) that are imposed on the atoms in the network. The outcomes have major implications on the durability of concrete structural elements formed with calcite or quartz bearing aggregates in nuclear power plants.

Concrete is used for the construction of class-I safety structures of nuclear power plants (NPPs), e.g., the containment building, biological shield and spent-fuel handling buildings, in particular. The long-term operation (LTO) of NPPs, i.e., 40 years and beyond, is expected to be affected by concrete degradation that may modify its functionality and durability[1–3]. A recent report of the U.S. Nuclear Regulatory Commission/Department of Energy has identified irradiation effects and alkali-silica reaction [ASR: Alkali-silica reaction is caused due to the progressive dissolution of reactive silica bearing aggregates into the concrete's caustic pore-fluid (pH > 13). Following aggregate dissolution, a precipitate rich in alkaline elements, water and silica, i.e., an alkaline-silica hydrate ($Ca_x/Na_y/K_z$-S_a-H_b, where x, y, z, a, b are coefficients) of variable composition forms. This hydrate upon formation within the concrete's or aggregates porosity, can saturate it, resulting in deleterious cracking, and loss of mechanical properties due to internal volume expansion.] as key degradation mechanisms that require priority research in the context of license renewals and LTO of the U.S. commercial nuclear fleet[4]. In spite of several past and ongoing studies[5–14], comprehension of the effects of irradiation on the mechanical and physical properties of concrete remains very limited. This is because the evolution of irradiation effects depends on several factors:

(1) Damage can vary as a function of the neutron fluence and the γ-ray dosage, and also as a function of the concrete composition, i.e., the type of aggregates, and cement used and relative proportions of aggregates, water and cement in the mixture[6,13],

[1]Laboratory for the Chemistry of Construction Materials (LC[2]), Department of Civil and Environmental Engineering, University of California, Los Angeles, CA 90095. [2]Materials Science and Technology Division, Oak Ridge National Laboratory, Oak Ridge, TN 37861. [3]Physics of Amorphous and Inorganic Solids Laboratory (PARISlab), Department of Civil and Environmental Engineering, University of California, Los Angeles, CA 90095. [4]California Nanosystems Institute (CNSI), University of California, Los Angeles, CA 90095. Correspondence and requests for materials should be addressed to G.S. (email: gsant@ucla.edu)

(2) Irradiation damage cannot be clearly distinguished from thermal damage caused due to absorption of radiation energy[6,9], and,
(3) The potential impacts of irradiation, which may render the concrete vulnerable to the other physical and/or chemical degradation processes, and vice-versa.

Mineral aggregates used in concrete are often composed of fragments of rocks including: granite and limestone, whose constituents include quartz and calcite, respectively. As per the Streckeisen diagram[15], granites can contain between 20–60% of quartz (i.e., in terms of mineral content). Quartz is also found in other rocks such as sandstones. On the other hand, limestone is composed of calcite and minor amounts of clay and/or dolomite. Radiation damage caused to minerals such as quartz, by neutrons or, analogously, heavy-ions has been noted to be similar, suggesting similar damage mechanisms[16,17]. Such damage has been described by the so-called "direct impact" or "cascade" models[18] wherein interactions between radiation and minerals causes the displacement of the primary knock-on atoms (PKAs). When these atoms have sufficient kinetic energy (K.E.), they produce subsequent "displacements cascades"[19] within the remainder of the atomic network. This causes the formation of point defects that can return to their original lattice positions or recombine to form other defects, e.g., defect clusters, voids, dislocations, etc. When the degree of damage or amount of energy imparted into the system reaches a threshold value, amorphization localizes and then accumulates following a homogenous or heterogeneous process. This causes the disordering ["disordering" implies all actions which result in an increase in the entropy of a solid, at fixed composition. This includes the formation of defects and imperfections in initially crystalline mineral structures including the random movement of atoms to positions far removed from their original positions, due to ballistic (collision) effects. When ballistic effects dominate, a previously a previously crystalline structure, such as quartz undergoes progressive disordering until an aperiodic end-state is achieved] of the mineral's crystal structure, resulting in a progressive loss of its structural periodicity[20–22]. Bylov *et al.* compiled data obtained from Russian and U.S. test reactors of the effects of irradiation temperature (from 25 °C to greater than 210 °C) on neutron radiation induced volumetric expansion of quartz for a range of amorphization levels, and for fluence levels up to about 6×10^{20} n/cm^2 (E > 10 keV)[23]. An increase in the irradiation temperature was noted to shift the expansion offset to higher doses due to the annealing of point defects. Such annealing was however noted only for temperatures >200 °C. Since the operations temperature of light water reactors is limited by design to 65 °C with localized hot zones that achieve 93 °C – the annealing of defects under irradiation is expected to have little if any impact for typical nuclear power plant environments.

There is evidence in the literature that suggests that radiation-induced volumetric expansion of concrete aggregate is a major source of mechanical damage in the surrounding hardened cement paste[24–27]. Such mechanical damage resulting from expansion of the aggregates affects the structural properties of the concrete far more dramatically than direct irradiation effects on the cement paste itself. The effects of radiation damage on quartz and calcite (i.e., common minerals in aggregates in concrete) have been described in terms of changes in physical properties, such as density, optical properties, hardness, conductivity, etc[28–30]. Of these, volume change is thought to be prominent in quartz, but less significant for calcite even for neutron fluence reaching 1.0×10^{20} n/cm^2 (E > 0.1 MeV)[31,32]. Broadly, the disordering or the amorphization of mineral aggregates is expected to result in two main effects[33–36]:

(1) Volume changes of mineral aggregates[37–39] as at fixed composition, loss of crystallinity may alter the solid density, and/or,
(2) Increases in the chemical reactivity of the mineral aggregates[8,10], as disordered materials are typically less chemically stable than their crystalline counterparts.

These effects would be problematic in the context of concrete durability as:

(1) Increases in volume of the aggregates can cause mechanical degradation of concrete due to microcracking of the binding cement paste matrix, e.g., when the aggregate density reduces (i.e., the aggregates expand), due to a radiation induced volumetric expansion (RIVE)[13,14,39], and,
(2) Increases in aggregate reactivity could cause chemical degradation of the concrete due to the onset of irradiation-assisted alkali-silica reaction (IA-ASR); caused by the dissolution of siliceous aggregates into the caustic liquid-phase (pH > 13) contained in the concrete's porosity[8,10].

Given that the aggregates form around 70% of a concrete's volume, their degradation would weaken the concrete, perhaps compromising the integrity of concrete elements that fulfill structural, shielding, and/or containment functions in NPPs. This has implications on the safety of NPPs in the event of reactor over-pressurization shock, or earthquakes, and, with the increasing age of NPPs, as radiation induced degradation will increase over a multi-decade service-life.

Therefore, this work elucidates how irradiation alters the atomic structures of minerals that commonly constitute aggregates in concrete. Focus is placed on contrasting how irradiation may or may not influence the chemical reactivity of a mineral with aqueous solutions, quantified in terms of its dissolution rate, in relation to chemical composition. The outcomes have significant implications on specifying radiation resistant aggregates for use in NPP concretes, and for assessing the risk-profiles of which concretes and hence nuclear power plants may be possibly more sensitive, to radiation-induced damage, than others.

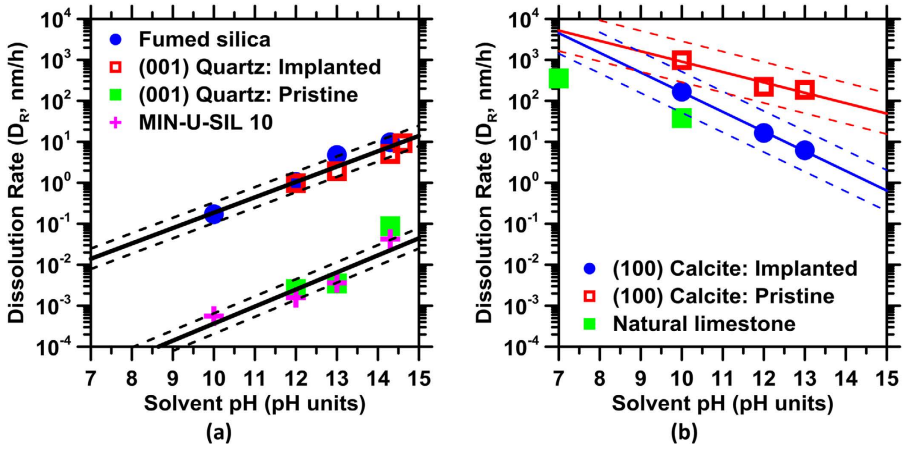

Figure 1. The dissolution rate (T = 25° ± 3 °C, p = 1 bar) as a function of solution pH for: (**a**) SiO_2 based solids and (**b**) $CaCO_3$ based solids. In the case of SiO_2 based solids, the dissolution rate increases with pH, while the opposite is true for $CaCO_3$ based solids. It is noted that, while quartz shows slight, if any, sensitivity to surface orientation, calcite dissolution appears more sensitive to surface orientation, and potentially solid composition (i.e., impurities present in the natural limestone). The thick solid lines show trends in dissolution rates while the thin dashed lines show the corresponding uncertainty bounds. The trend lines are fitted to an equation of the form: $D_R = A \cdot \exp(\pm B \cdot \mathrm{pH})$, where A and B are numerical constants. The highest uncertainty in the measured dissolution rates is on the order of ±0.5 log units.

Results and Discussion

Figure 1 shows the dissolution rates of α-quartz and calcite, before and following their irradiation. Also shown are the dissolution rates of pulverized quartz, fumed silica, and of natural limestone samples for comparison. It is noted that the dissolution rate of α-quartz significantly elevates after irradiation to full amorphization; attaining near equivalence to the dissolution rate of fumed (glassy) silica for the same solution compositions. This enhancement in the dissolution rate by around 3 orders of magnitude indicates that the chemical stability of α-quartz is very significantly compromised following irradiation. Calcite, on the other hand, shows a slight decrease in its dissolution rate following irradiation – even when the measurement uncertainty is accounted for (see Fig. 2b). These results, which comprise the first direct experimental evidence of differing irradiation-induced reactivity alterations, highlight a specificity to structure and composition – where quartz exhibits enhancements in aqueous reactivity, while calcite shows little if any change in reactivity following irradiation.

It should also be noted that, while minerals would show differences in their chemical reactivity (in aqueous solution) as a function of surface orientation and surface energy, this effect is more pronounced in the case of calcite than quartz. For example, the pulverized quartz (MIN-U-SIL 10), in spite of presenting a multiplicity of surface orientations, shows a dissolution rate similar to the (001)-quartz single crystal. On the other hand, the natural limestone shows more substantial differences (±0.5 log units, see Fig. 1b) in its dissolution rate, as a compared to the (100)-calcite surface. While this behavior may indeed be influenced by differences in the nature of surface defects, or elemental impurities present in the calcite samples – it is within range of experimental uncertainty, which is higher for calcite, than for quartz dissolution rates.

Near equivalence in the dissolution rates of amorphous silica, and α-quartz following irradiation suggests that the latter has been disordered under radiation exposure – a consequence which explains elevations of its dissolution rate. Dissolution has been explained within the context of crystal growth theory, focusing on the free-energy difference between the dissolving solid, and the solution in contact[40,41]. As such, it has been shown that dissolution occurs preferentially, and originates from high-energy sites on surfaces (structural defects and impurities), favoring the formation of etch pits (shown below). While this explanation is consistent for crystal dissolution, for compounds such as amorphous silica, the lack of atomic periodicity/structural disorder only implicates the role of (ionic) impurities in altering dissolution rates. Impurities, when present, are thought to disrupt/weaken intermolecular bonds, destabilizing a solid, either crystalline (quartz) or amorphous (silica). Such weakening ensures that a smaller driving force is sufficient to overcome the free energy barrier; thereby making both quartz and silica more susceptible to dissolution – but, only when impurities may be present. While this view is reasonable, it does not explain, or parametrize differences in the dissolution rates of compositionally analogous, and phase pure solids – e.g., quartz and amorphous silica, when they dissolve in similar solutions.

To assess structural alterations induced by irradiation, cross-sectional TEM and SAED patterns were acquired and are shown in Fig. 2. The sharp diffraction maxima noted in the SAED pattern past the end-of-range regions (i.e., of Ar^+ implantation) of quartz (Fig. 2a(II)) are not observed in SAED patterns of the corresponding ion-irradiated regions (Fig. 2a(I)). Rather, a diffuse band is noted, which is indicative of complete amorphization. This amorphous region extends ≈550 nm into the sample, in agreement with the depth of the damage zone predicted by SRIM (≈550 nm, see Fig. S1). On the other hand, no changes in crystallinity are noted in calcite after irradiation – that is, SAED patterns of implanted (Fig. 2b(IV)) and pristine regions (Fig. 2b(III)) are similar and

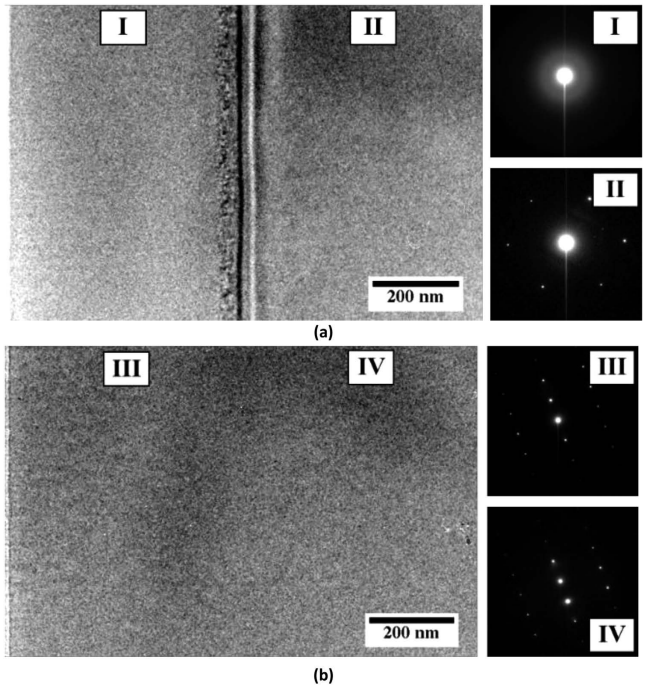

Figure 2. Cross-sectional TEM images and corresponding selected area electron diffraction (SAED) patterns from the ion implanted regions (I,III) and past ion end-of-range (II,IV) for: (**a**) α-quartz single crystal and (**b**) calcite single crystal. (**a**-**I**) shows the amorphization of α-quartz, while (**b**-**III**) shows the lack of amorphization in calcite. Ion implantation was carried out at an energy of 400 keV using Ar^+-ions for a total fluence of 1.0×10^{14} Ar^+/cm^2 at room temperature. The free-sample surface is located towards the left extremity of the image(s).

both present sharp diffraction maxima. Thus, while quartz attains a *metamict* state following ion-implantation, calcite remains resistant to radiation damage for the same implantation dose.

Such composition linked structural differences were also suggested in[13], on the susceptibility of different minerals to irradiation. Evidence for such behavior is also noted in vibrational (FTIR) spectra acquired on irradiated samples which shows a shift toward lower wavenumbers and an intensity decrease of the asymmetric stretching modes (777, 1170 cm^{-1}) of quartz and of the CO_3^{2-} bending/stretching modes of calcite (712, 874 and 1350 cm^{-1}). Such alterations in FTIR patterns have been attributed to structural modifications caused by irradiation including: changes in the average Si-O-Si inter-tetrahedral angle and Si-O-Si bonds in quartz[42,43], and the distortion and breakage of carbonate groups in calcite[44]. Collectively, these results support the idea that, while calcite is slightly influenced by irradiation, quartz undergoes severe damage, resulting in disorder and lack of longer-range (>10 Å) periodicity.

Similar results of irradiation damage induced in calcite and quartz have also been found in natural thorium/uranium containing deposits, e.g., in: calcite crystals surrounding urano-thorianite in Tranomaro granulitic skarns[45] and quartz found in the uranium-mineralized Athabasca Basin in Canada[46]. Seydoux-Guillaume *et al.* noted that calcite appears to be more resistant to irradiation damage than diopside (pyroxene, a silicate mineral), due to the type of interatomic forces in the former's structure[5]. This conclusion is in agreement with data presented herein. Radiation damage of quartz was investigated by Botis *et al.* using cathodoluminescence (CL) and electron paramagnetic resonance (EPR). Their results highlight the formation of oxygen vacancy centers, silicon vacancy hole centers and peroxy centers[6]. But, in a recent study[47], Wang *et al.* showed that measurements of damage level based simply on point defect analyses provoke only a partial view of the damage evolved. Based on these latter results, the identification of oxygen vacancy centers following radiation damage suggests that substantial modification and amorphization has already been induced in the Si-O atomic network.

Original molecular dynamics simulations[48] show that, in agreement with the TEM-SAED analysis, that quartz is near completely disordered by radiation, while calcite is far less affected. It should be noted that the qualifier "disordered" is used in lieu of amorphized, as the resultant glassy-SiO_2 structure formed following irradiation though non-periodic, is not equivalent to amorphous silica (Figs 2 and S2). Calcite shows substantially more resistance to radiation induced alterations. For example, for an incident energy of 600 eV no change in its structural, or physical parameters is produced. At higher incident energies, on the order of 1000 eV, calcite experiences alterations in the form of distortions and rotations of its CO_3^{2-} groups with respect to the Ca-atom positions. These distortions and rotations of the CO_3^{2-} groups, however, alter the atomic packing of the calcite structure – as a result of which calcite expands, resulting in a reduction in density. This expansion, which increases with the radiation dosage, achieves a limiting value, when the density of irradiated calcite stabilizes to a value of ≈90% of the pristine phase (see Fig. 3a). While this magnitude of expansion is larger than that estimated by Wong[49]

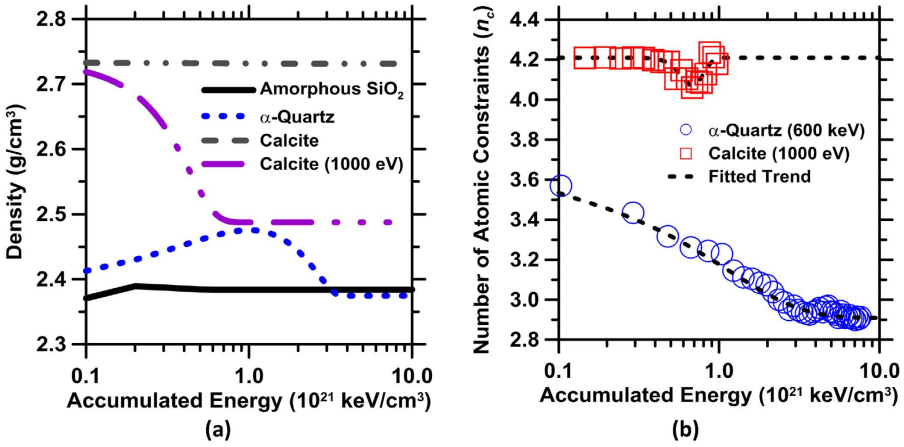

Figure 3. (**a**) The density evolution of pure minerals as a function of accumulated radiation dosage. The density of quartz is somewhat underestimated due to the choice of interatomic potential used in the MD-simulations[50] and (**b**) The evolution of n_c, in α-quartz and calcite as a function of accumulated radiation dosage. Calcite when exposed to 600 eV incident radiation remains unaffected. However, a higher incident energy of 1000 eV is noted to induce changes in density. Density changes are provoked by rotations and distortions of the CO_3^{2-} groups with respect to the Ca-atom positions, post-irradiation. Unless stated otherwise, an incident energy of 600 eV is simulated.

following high neutron fluence exposure, given the limited data available, this difference cannot be marked to an inconsistency of the simulation scheme.

Due to the nature of interatomic potentials selected in the calculations, i.e., chosen to capture lattice dynamics accurately for disordered silica, but somewhat less so for α-quartz, the density of pristine quartz and of amorphous silica is underestimated. This underestimation is on the order of 7.5% for both the silicate solids, i.e., $\rho \approx 2.42\,g/cm^3$ (calculated) and $\rho \approx 2.62\,g/cm^3$ (measured) for α-quartz, and $\rho \approx 2.37\,g/cm^3$ (calculated) and $\rho \approx 2.2\,g/cm^3$ (measured) for disordered silica. Given that the terminal density of quartz following irradiation matches that of disordered silica, quartz would undergo a reduction in density, or conversely an increase in its molar volume of around 15%. This extent of volumetric expansion (swelling) is in excellent agreement with the analyses of Field *et al.* who estimated that α-quartz would swell around 14% upon its complete disordering[13]. Amorphous silica, on the other hand, shows slight, if any changes in its density[28]; around 1% across all radiation dosages (Fig. 4a). It should be noted, that irradiation induces significant changes in the inter-tetrahedral (Si-O-Si) bond angles (a decrease of around 7% is noted) in agreement with FTIR observations – but not the bond length, in irradiated quartz with respect to pristine quartz. As a result, a floppy, glassy disordered silica phase forms.

Structural disordering is not seen in calcite as, in general, as compared to the Si-O bond ($E_b = 440\,kJ/mole$, where E_b is the bond energy) in quartz, the Ca-O bond ($E_b = 134\,kJ/mole$) in calcite is weaker, and less directional in 3D (i.e., the Ca-O-Ca bond angles show a broader distribution than Si-O-Si ones, see[50,51]) – as a result, under radiation induced excitations – the Ca-O bond is free to reorganize, and show near complete recovery of initial (pristine) bond parameters once the radiation flux has ceased. It is postulated that this "differing behavior" is a function of the dominantly ionic character of the bonds in calcite, and the covalent character of quartz, an idea that was previously suggested by Wong[49]. This suggests that radiation perturbs the weaker angular bonds, rather than stronger radial constraints: the former which, in calcite, cannot be perturbed any further. This explains why ionically bonded solids may indeed be more resistant to radiation fluxes, than their covalent counterparts.

To comprehensively elucidate the influences of radiation on disordering the number of atomic topological constraints is computed. In solids, atoms are constrained by radial bond-stretching (BS) and angular bond-bending (BB) interactions, which act to maintain bond lengths and angles fixed around their average values. Analogous to Maxwell's stability analysis of a mechanical truss[52], the rigidity of a solid can be determined by enumerating the total number of constraints per atom (n_c, unitless), and by then comparing n_c to the number of degrees of freedom per atom (i.e., three in 3D). As such, atomic networks can be classified as being flexible, i.e., hypostatic, ($n_c < 3$)[53], showing internal low-energy modes of deformation, stressed-rigid ($n_c > 3$), i.e., being locked or hyperstatic, or being isostatic (i.e., statically determinate with $n_c = 3$). As a point of note, the hardness of such atomic structures, in order of their instability scales from: flexible, to isostatic to stressed rigid networks in ascending order, i.e., from least hard to most hard[54,55].

It is noted that quartz and calcite, in the pristine state both show a stressed-rigid type character. However, following irradiation, while quartz transitions to a flexible state (i.e., $n_c \approx 2.9$), calcite remains stressed-rigid (i.e., $n_c \approx 4.2$, Fig. 3b). Interestingly, when the dissolution rates of these solids are cast as a function of the number of atomic constraints for a given (fixed) solution pH – a significant trend results as shown in Fig. 4(a). Specifically, in the case of SiO_2-based solids, the dissolution rate is noted to smoothly, and linearly increase with reducing n_c – spanning from pristine to irradiated quartz, and from pulverized to fumed silica respectively. On the other hand, calcite, which shows no change in n_c, independent of radiation exposure, correspondingly shows little, if any change in its dissolution rate. The slight reduction that manifests in calcite dissolution rates, for irradiated calcite,

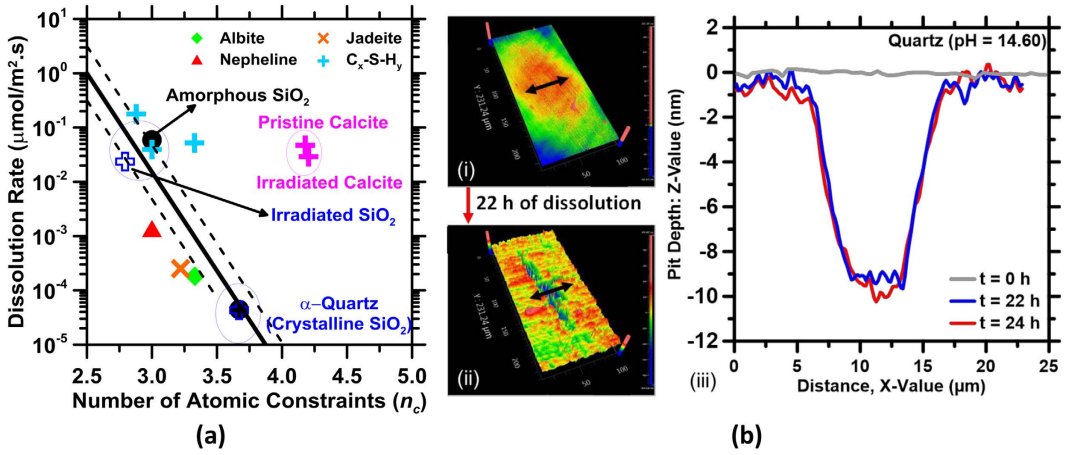

Figure 4. (**a**) A dissolution sensitivity diagram, which shows the dissolution rates of minerals and selected glasses as function of n_c at pH 13 (0.15 M NaOH); a concrete relevant pH (T = 25° ± 3 °C, p = 1 bar). Dissolution sensitivities of *more covalently bonded silicate minerals* increase with a decreasing number of atomic constraints (n_c). Decreasing n_c often denotes an increase in atomic disorder, e.g., as induced by irradiation. *More ionically bonded minerals* such as calcite show little if any change in n_c and dissolution rates following irradiation (Fig. 1b). Rate data for glasses compositionally analogous to albite, jadeite, and nepheline was sourced from the literature[50] while all other rate data was measured using VSI. The thick dashed lines show the trends in dissolution rates while the thin solid lines show relevant uncertainty bounds. The trend line is fitted to an equation of the form: $D_R = A \cdot \exp(B \cdot n_c)$, where A and B are numerical constants. The highest uncertainty in the measured dissolution rate(s) is on the order of ±0.5 log units. (**b**) 3D VSI images of a (100)-surface of irradiated quartz: (i) prior to its dissolution, and (ii) after 22 hours of dissolution at pH 14.6. The cross section profile (ii) indicates the change in the morphology caused due to etch pit opening on the surface.

is likely due to: (a) rapid dissolution of the surface exposed to solution such that distortions of CO_3^{2-} groups, may render their removal easier, or (b) may be related to observations of a slight increase in calcite hardness, and hence stability following irradiation[29,56]. If the former mechanism is operative, facilitated surface dissolution (i.e., an increase in the CO_3^{2-} abundance in the solution, in proximity to the dissolving surface) would lower the driving force for calcite dissolution, an effect which would slightly reduce its dissolution rate (see Fig. 1b).

It should be noted that while Fig. 4(a) shows dissolution rate correlations only for pH 13 (0.15 M NaOH), the conclusions remains unchanged for other solution pH's – an indication of the genericity of the approach – so long as the solution composition remains consistent. This diagram which indicates *the dissolution sensitivity of compositionally similar solids*, in which a specific network feature (in this case SiO_4 tetrahedra) controls chemical instability, captures the dissolution rate dependence on n_c that is displayed by glasses compositionally analogous to albite, jadeite and nepheline[56], and the calcium silicate hydrates (i.e., C_x-S-H_y, where C = CaO, S = SiO_2, and H = H_2O, and x and y are coefficients, where $1.2 \leq$ Ca/Si ≤ 1.8, molar units), a family of disordered compounds, which comprise the primary binding and strength provisioning components of hydrated cementitious solids. These trends indicate that in regimes of high undersaturations with respect to the solute (dissolving solid), wherein defects are proposed to nucleate homogenously, the kinetics of the dissolution process can be characterized by n_c, a fundamental indicator of the chemical instability of a solid in a solution – as a function of its atomic organization and network structure – more rigorously than other parameters, such as "the degree of crystallinity".

Summary and Implications on concrete durability in nuclear power plants

The outcomes of this work clarify that radiation exposure, especially in the form of heavy ions, and analogously neutrons, alters the structural, physical, and chemical properties of minerals such as calcite and quartz. While the end-effects are structural (at an atomic scale), physical and chemical in the case of quartz, they only influence the physical properties (e.g., density) of calcite. This differing behavior is correlated with the dominantly ionic nature of calcite and the covalent bonding environment in quartz, the latter of which is less resistant to radiation damage. Mineral dissolution rates are shown to be strongly correlated with the number of constraints per atom (n_c), which describes the rigidity of a network of atoms. This offers, for the first time, a quantitative means of linking the state of atomic ordering of a given mineral to its chemical reactivity (i.e., dissolution rate). The research therefore demonstrates a basis by which chemical composition-structure-property relations can be elucidated, for pristine minerals, and for minerals which have been exposed to heat, pressure or radiation, and have thus experienced irreversible alterations of their atomic structures.

The outcomes suggest different potential routes to structural concrete damage when carbonate and silicate mineral aggregates may be exposed to radiation, e.g., when proximate to the reactor pressure vessel, in NPP environments. First, calcite on account of its expansion (i.e., its reduction in density, Fig. 3a) is expected to induce physical damage in the concrete. Such damage will result in microcracking within the binding cement paste matrix in relation to the level of (neutron) radiation exposure. However, following exposure to a threshold dosage, no further damage should evolve. Therefore, it is important to understand the implications of internal damage

(microcracking) on the mechanical properties of concrete – so that its structural implications can be ascertained, and potential remediation measures implemented. Second, quartz due to its swelling, and increasing chemical instability following irradiation, is expected to expand, causing microcracking of the cement paste matrix, and eventually dissolve in the caustic cementitious pore fluid. Since any atomic disordering is expected to be progressive, quartz is expected to dissolve incrementally faster – until a metamict state is achieved, and dissolution proceeds at a limiting-rate, i.e., of glassy silica (Fig. 4a). This is problematic as the continuing dissolution of silica, so long as water, and alkali ions are available will result in the formation of an expansive alkali-silica gel, i.e., ASR. Cessation of ASR will occur only when the internal relative humidity in the concrete is lowered (RH $<$ 80%), or when the alkalis or siliceous aggregate are consumed. This is expected to need long time scales, i.e., on the order of decades, in which time the amount of damage induced would be very substantial, and detrimental to concrete microstructure, and mechanical properties.

Both types of damage, physical and chemical are problematic as they are expected to show a gradient from the inner wall of the reactor pressure vessel (i.e., the inner surface of the reactor cavity concrete), to the outer surface of the concrete. Such gradients in expansion, i.e. strain, will result in the development of tensile hoop stresses in the reactor cavity concrete exacerbating the effects of radiation-induced damage. On a closing note, while this work has elucidated critical, and thus far unknown aspects of radiation induced alterations in minerals, significant aspects, remain worthy of evaluation: e.g., a wider range of minerals, and rocks, time dependence effects, radiation dose and energy dependence, and mechanical integrity of the affected cementitious elements. These are topics which require detailed study so that the long-term effects of radiation damage to concrete, and on NPP operations, safety and on license renewals can be rigorously and comprehensively evaluated.

Materials and Methods

Materials and ion-irradiations. Synthetic single crystals of α-quartz and calcite with dimensions 10 mm $\times$ 10 mm $\times$ 1 mm (l $\times$ w $\times$ h) were sourced from MTI Corporation[57]. The calcite crystals are (100)-oriented, whereas the quartz crystals are sectioned perpendicular to their optical axis (i.e., corresponding to the crystallographic *c*-axis), and are thus (001)-oriented. The quartz and calcite single-crystals were ion-beam irradiated at room temperature at the Michigan Ion Beam Laboratory (MIBL[58]) using an implantation energy of 400 keV with Ar^{+}-ions to a total fluence of 1.0×10^{14} ions/cm^2. No signs of blistering or significant sputtering were observed post-irradiation. The damage dose (dpa), the range and the concentrations of implanted ions were determined using SRIM using the quantification scheme proposed in[59]. In addition to the single crystals, an untreated fumed silica (Cabosil HS-5), a size graded, pulverized α-quartz (MIN-U-SIL 10) and a natural limestone were also analyzed to assess their aqueous dissolution rates, so as to establish comparisons to the oriented single crystal surfaces.

Dissolution analysis using vertical scanning interferometry. The dissolution rates of pristine (i.e., non-implanted) and irradiated (i.e., implanted) calcite and quartz samples were measured using vertical scanning interferometry (VSI) at room temperature (25 $\pm$ 3 °C). The solutions used in these studies included: reagent grade buffer solution (pH 7, 10) and NaOH solutions prepared using deionized (DI) water: 0.015 M NaOH: pH 12, 0.15 M NaOH: pH 13, 2 M NaOH: pH 14.3, 4 M NaOH: pH 14.6. The single crystal samples were fixed onto the surface of a glass slide using an inert adhesive to facilitate handling. In the case of *flat* samples, the topographical profile of the sample mapped prior to solution contact was used as the reference plane with respect to which surface dissolution (retreat) was tracked. Powder samples were embedded in a thin-film of inert adhesive applied on the surface of a glass slide. The surface of the non-reactive adhesive once again served as the reference plane with respect to which particle dissolution was mapped[60].

To induce solid dissolution, a small quantity of solution (i.e., 50-to-75 μL) is applied to the sample surface using a micropipette to obtain a liquid-to-solid ratio (*l/s*, mass basis) between 50,000-to-75,000, to approximate the dilute limit. This *l/s* is appropriate to minimize the effects of solution saturation, with ions, during dissolution and limit phase precipitation, if any. After allowing for a pre-determined contact time ranging between 15-to-60 minutes (i.e., depending on the mineral dissolution rates), with reapplication of the solution if needed, the solution was removed using a compressed air stream. All measurements were carried out at ambient pCO_2. It should be noted that, in the manner implemented, the same solution, of a fixed composition repetitively contacts the mineral surface. As such, no evolutions in solution composition are permitted, and dissolution occurs at very high undersaturations with respect to the dissolving solid. As such, the dissolution rates quantified are relevant to initially fixed, essentially non-evolving solution compositions. The solution pH is the primary variable that influences the undersaturation.

A Zygo NV 9200 vertical scanning interferometer fitted with a 50$\times$ Mirau objective (N.A. = 0.55) was used in the analysis. The objective used yields a lateral spatial resolution around 500 nm. The interferometer used has a resolution of $\approx$0.1 nm in the vertical, i.e., *z*-direction. The analysis scheme was organized as follows: first an image of the dry sample surface, i.e., prior to solution contact was acquired. This constituted the "time-zero" (t_0) image, and dissolution was tracked using this image, and its topographical profile (i.e., of the crystal surface, or of the particles when they are embedded in adhesive) as the reference. Following solution contact, other images were periodically acquired after the removal of the solution. These images and their topographical profiles, which were altered by dissolution, were compared to the reference image, and the change in height (Δh, nm: negative in the case of dissolution which produces surface retreat) per unit time (Δt, hours), reveals the solid's dissolution rate. Each image comprises a total scanning area of 433.81 μm $\times$ 433.81 μm in stitched mode using a 3 $\times$ 3 grid, and a back-scan length of 145 μm. The total time required for capture of the full image field is on the order of 390 seconds. It should be noted that the height reduction was mapped at up to 80 discrete points on the planar single crystal, or on particle surfaces. This statistical mapping was carried out to account for the effects of surface roughness which may differ as a function of x-y (spatial) position, and may influence dissolution rates, and to

ensure that the dissolution rate that were quantified account for material inhomogeneities, if any may be present. The resulting dissolution rate (D_R, nm/h) is written as: $D_R = (\Delta h/\Delta t)$, where h is the surface height (nm) for a given profile, and $\Delta h = h_{(i)} - h_{(i+1)}$ is the change in height between the successive steps measured over a dissolution period, Δt (hours). It should be noted that division of D_R by the molar volume (V_M, m^3/mole) of a compound reveals the dissolution rate in units of μmol/m^2/s. All measurements were repeated 3 times.

Transmission electron microscopy. Cross-sectional lift-outs were prepared from pristine and irradiated quartz and calcite samples using a FEI Quanta 200i DualBeam focused ion beam (FIB). Low-angle, low-energy milling was carried out following the primary thinning to obtain electron transparent sections, while minimizing any damage that may be induced by the ion-beam. The electron transparent samples were then analyzed using a Philips CM200 transmission electron microscope (TEM) at an accelerating voltage of 200 kV. Selected area electron diffraction (SAED) patterns were acquired on both pristine and irradiated regions to determine the degree, if any, of disordering in the irradiated regions. Due care was taken to minimize the electron dose to the imaged areas to reduce damage imparted by the imaging electron beam.

Molecular dynamics simulations. Molecular dynamics simulations were carried out on calcite and quartz structures using LAMMPS[61] at 300 K to study the influences of radiation damage on atomic structures[47]. The simulated system consists of a supercell of pristine quartz or calcite containing between 4500 and 21000 atoms, depending on the incident irradiation energy. To simulate ballistic collisions induced by irradiation, a randomly selected atom is accelerated with a given kinetic energy (similar to an incident energy) to mimic energy transfer between radiation and an atom. The acceleration initiates a cascade of collisions between atoms, causing damage to the crystal structure. This process is repeated until the desired dosage is achieved. Quartz and calcite are simulated using the inter-atomic potentials of [62] and [63] respectively, which have been shown to suitably reproduce crystalline and amorphous structures of these two minerals[47,63–68]. In order to provide a realistic prediction of high-energy events, which cause atoms to temporarily come unusually close to each other, the Ziegler, Biersack and Littmark (ZBL) potentials are used at short inter-atomic separations (<1 Å)[69]. Since such a small inter-atomic separation is not observed during typical conditions, i.e., close to equilibrium, the ZBL potentials only take effect during the collision cascade, while the rest of the relaxation dynamics remain unaffected. After the radiation damage simulation is completed, a series of atomic configurations are extracted at different dosage levels for detailed structural analyses. Special focus is placed on quantifying the type and nature of damage, including amorphization, and evaluating structural rigidity[70,71] by analysis of atomic trajectories. The rigidity analysis consists of an enumeration of the number of intact and broken radial and angular bond constraints at 300 K[72,73]. A bond constraint is considered to be broken if the relative variation in the bond distance (or bond angle) is sufficiently large, i.e., exceeding 7%[50], which indicates the absence of an underlying restoring force that would maintain the bond length (and angle) fixed around its average value. It should be noted that the constraints enumeration procedure does not significantly depend on the choice of this threshold, similar to the Lindemann criterion[50].

References

1. Neville, A. In *Properties of concrete* 1–844 (John Wiley and Sons Inc, 1963).
2. Mehta, P. K. & Monteiro, P. J. In *Concrete: microstructure, properties, and materials* 3–653 (McGraw-Hill New York, 2006).
3. Naus, D. In *Primer on Durability of Nuclear Power Plant Reinforced Concrete Structures - A Review of Pertinent Factors*. Technical Report NUREG/CR-6927 - ORNL/TM-2006/529, Oak Ridge National Laboratory - U.S. Nuclear Regulatory Commission (2007).
4. Graves, H., Le Pape, Y., Naus, D., Rashid, J., Saouma, A., Sheikh, A. & Wall., J. In *Expanded material degradation assessment (EMDA)*, Vol. 4: Aging of concrete. Technical Report NUREG/CR-7153, ORNL/TM-2011/545. U.S. Nuclear Regulatory Commission (2013).
5. Clark, R. In *Radiation damage to concrete.* Technical Report HW-56195. General Electric. Hanford Laboratories, Richland, WA (1958).
6. Hilsdorf, H. K., Kropp, J. & Koch, H. J. The effects of nuclear radiation on the mechanical properties of concrete. *ACI Spec. Publ.* **55,** 223–251 (1978).
7. Naus, D. In *Concrete Component Aging and its Significance Relative to Life Extension of Nuclear Power Plant*. Technical Report NUREG/CR-6927 - ORNL/TM-2006/5298, Oak Ridge National Laboratory - U.S. Nuclear Regulatory Commission (1986).
8. Ichikawa, T. & Koizumi, H. Possibility of radiation-induced degradation of concrete by alkali-silica reaction of aggregates. *J. Nucl. Sci. Technol.* **39,** 880–884 (2002).
9. Fillmore, D. L. In *Literature Review of the Effects of Radiation and Temperature on the Aging of Concrete*. Technical Report INEL/EXT-04-02319. Idaho National Engineering and Environmental Laboratory (2004).
10. Ichikawa, T. & Kimura, T. Effect of Nuclear Radiation on Alkali-Silica Reaction of Concrete. *J. Nucl. Sci. Technol.* **44,** 1281–1284 (2007).
11. Fujiwara, K., Ito, M., Sasanuma, H., Tanaka, K., Hirotani, K., Onizawa, K., Suzuki, M. & Amezawa, H. In Experimental Study of the Effect of Radiation Exposure to Concrete, *Proceedings of the 20th International Conference on Structural Mechanics in Reactor Technology*, SMiRT 20 - Division I (2009).
12. Kontani, O., Sawada, S., Maruyama, I., Takizawa, M. & Sato, O. Evaluation of Irradiation Effects on Concrete Structure: Gamma-Ray Irradiation Tests on Cement Paste. *ASME 2013 Power Conference (American Society of Mechanical Engineers)*, 1–8 (2013).
13. Field, K. G., Remec, I. & Le Pape, Y. Radiation effects in concrete for nuclear power plants - Part I: Quantification of radiation exposure and radiation effects. *Nucl. Eng. Des.* **282,** 126–143 (2015).
14. Le Pape, Y., Field, K. G. & Remec, I. Radiation effects in concrete for nuclear power plants. Part II: Perspective from micromechanical modelling. *Nucl. Eng. Des.* **282,** 144–157 (2015).
15. Streckeisen, A. Classification and nomenclature of plutonic rocks recommendations of the IUGS subcommission on the systematics of Igneous Rocks". *Geologische Rundschau* **63(2),** 773–786 (1974).
16. Douillard, L. & Durand, J. P. Amorphization of α-quartz under irradiation. *J. Phys. III France* **6,** 1677–1687 (1996).
17. Douillard, L. & Durand, J. P. Swift heavy ion amorphisation of quartz - a comparative study of the particle amorphization mechanism of quartz. *Nucl. Instr. and Meth. in Phys. Res. B* **107,** 212–217 (1996).
18. Ewing, R. C., Meldrum, A., Wang, L. & Wang, S. Radiation-Induced Amorphization. *Rev. Mineral. Geochem.* **39(1),** 319–361 (2000).
19. Kinchin, G. H. & Pease, R. S. The displacement of atoms in solids by radiation. *Rep. Prog. Phys.* **18,** 1–51 (1955).
20. Okamoto, P. R., Lam, N. Q. & Rehn, L. E. Physics of crystal-to-glass transformations. *Solid State Phys.* **52,** 2–133 (1999).
21. Ewing, R. C. The metamict state: 1993—the centennial. *Nucl. Instr. Meth.* **B91,** 22–29 (1994).

22. Ewing, R. C., Chakomakos, B. C., Lumpkin, G. R., Murakami, T., Greegor, R. B. & Lytle, F. W. Metamict minerals: natural analogues for radiation damage effects in ceramic nuclear waste forms. *Nucl. Instr. Meth.* **B32,** 487–497 (1988).
23. Bylov, V., Denisov, A., Dubrovskii, V., Korenevskii, V., Krivokoneva, G. & Muzalevskii, L. Effect of Irradiation Temperature on the Radiation Expansion of Quartz. *Atomnaya Energiya* **51,** 593–595 (1981).
24. Gray, B. In *The effects of reactor radiation on cement and concrete.* Proceedings of an Information Exchange Meeting on 'Results of Concrete Irradiation Programmes'. EUR 4751 f-e (1971).
25. Kelly, B., Brocklehurst, J., Mottershead, D. & McNearney, S. *The Effects of Reactor Radiation on Concrete.* Proceedings of the Second Information Meeting on Pre Stress Concrete and Reactor Pressure Vessels and their Thermal Isolation. EUR-4531, 237–265 (1969).
26. Elleuch, L., Dubois, F. & Rappeneau, J. Effects of Neutron Radiation on Special Concretes and Their Components. *Special Publication of The American Concrete Institute* **43,** 1071–1108 (1972).
27. Dubrovskii, V., Ibragimov, S., Kulakovskii, M. Y., Ladygin, A. Y. & Pergamenshchik, B. Radiation Damage in Ordinary Concrete. *Atomnaya Énergiya* **23,** 310–316 (1967).
28. Primak, W. Fast-neutron-induced changes in quartz and vitreous silica. *Phys. Rev.* **110,** 1240 (1958).
29. Raju, K. S. Radiation effects in calcite. *Pramāṇa* **8(3),** 266–275 (1977).
30. Rao, E. V. & Murthy, M. R. Ion beam modifications of defect sub-structure of calcite cleavages. *Bull. Mater. Sci.* **31,** 139–142 (2008).
31. Hauser, O. & Schenk, M. Veränderungen der Kristallstruktur einiger Oxyde, Karbonate und Titanate durch Neutronenbestrahlung. *Phys. Status Solidi B* **6,** 83–88 (1964).
32. Luthra, J. X-ray studies on pile-irradiated calcite. *Indian J. Pure Ap. Phy.* **7,** 444–445 (1969).
33. Ewing, R. C. & Haaker, R. F. The metamict state: Implications for radiation damage in crystalline waste forms. *Nuclear Chem. Waste Management* **1,** 51–57 (1980).
34. Ewing, R. C., Weber, W. J. & Clinard, F. W., Jr. Radiation effects in nuclear waste forms. *Progress Nucl. Energy* **29,** 63–127 (1995).
35. Eby, R. K., Ewing, R. C. & Birtcher, R. C. The amorphization of complex silicates by ion-beam irradiation. *J. Mater. Res.* **7,** 3080–3102 (1992).
36. Ewing, R. C., Meldrum, A., Wang, L. M., Weber, W. J. & Corrales, L. R. Radiation damage in zircon. In *Zircon*, Vol. 53 (eds Hanchar, J. M. & Hoskin, P. W. O.) 387–425, Reviews in Mineralogy and Geochemistry, Mineralogical Society of America (2003).
37. Wittels, M. Structural behavior of neutron irradiated quartz. *Philos. Mag.* **2,** 1445–1461 (1957).
38. Zubov, V. & Ivanov, A. Expansion of quartz caused by irradiation with fast neutrons. *Sov.* Phys. *Crystallogr.* **11,** 372–374 (1966).
39. Seeberger, J. & Hilsdorf, H. Einfluss von radioactiver Strahlung auf die Festogkeit and Struktur von beton. *Technical Report NR2005*. Institut für Massivbau and Baustofftechnologie, Universität Karlsruhe (1982).
40. Dove, P. M., Han, N. & De Yoreo, J. J. Mechanisms of classical crystal growth theory explain quartz and silicate dissolution behavior. *Proc. Natl. Acad. Sci*. USA **102(43),** 15357–15362 (2005).
41. Dove, P. M., Han, N., Wallace, A. F. & De Yoreo, J. J. Kinetics of amorphous silica dissolution and the paradox of the silica polymorphs. *Proc. Natl. Acad. Sci.* **105(29),** 9903–9908 (2008).
42. Mazzoldi, P., Carnera, A., Caccavale, F. & Favaro, M. L. N and Ar ion-implantation effects in SiO_2 films on Si single-crystal substrates. *J. Appl. Phys.* **70,** 3528–3536 (1991).
43. Battaglin, G., Boscolo-Boscoletto, A., Caccavale, F., De Marchi, G., Mazzoldi, P. & Arnold, G-W. Etching effects in ion Implanted SiO_2. In *Modifications Induced by Irradiation in Glasses*. Elsevier Science Publishers BV, Amsterdam, 91–96 (1992).
44. Nagabhushana, H., Prashantha, S. C., Nagabhushana, B. M., Lakshminarasappa, B. N. & Singh, F. Damage creation in swift heavy ion-irradiated calcite single crystals: Raman and Infrared study. *Spectrochim Acta A Mol. Biomol. Spectrosc.* **71,** 1070–1073 (2008).
45. Seydoux-Guillaume, A. M., Montel, J. M., Wirth, R. & Moine, B. Radiation damage in diopside and calcite crystals from uranothorianite inclusions. *Chem. Geol.* **261,** 318–332 (2009).
46. Botis, S. *Electron-paramagnetic-resonance spectroscopy study of radiation-damage-induced cathodoluminescence in quartz, Athabasca Basin*. Thesis, University of Saskatchewan (2005).
47. Wang, B., Yu, Y., Pignatelli, I., Sant, G. & Bauchy, M. Nature of radiation-induced defects in quartz. *J. Chem. Phys.* **143,** 024505 (2015).
48. Campañá, C., Müser, M. H., Tse, J. S., Herzbach, D. & Schöffel, P. Irreversibility of the pressure-induced phase transition of quartz and the relation between three hypothetical post-quartz phases. *Phys. Rev. B* **70,** 224101 (2004).
49. Wong, C. Neutron radiation damage in some birefringent crystals. *Phys. Lett. A* **50,** 346 (1974).
50. Bauchy, M., Abdolhosseini Qomi, M. J., Bichara, C., Ulm, F.-J. & Pellenq, R. J. M. Nanoscale Structure of Cement: Viewpoint of Rigidity Theory. *J. Phys. Chem. C* **118,** 12485–12493 (2014).
51. Bauchy, M. Structural, vibrational, and thermal properties of densified silicates: Insights from molecular dynamics. *J. Chem. Phys.* **137,** 044510 (2012).
52. Maxwell, J. C. L. On the calculation of the equilibrium and stiffness of frames. *Philos. Mag.* **27,** 294–299 (1864).
53. Cai, Y. & Thorpe, M. F. Floppy modes in network glasses. *Phys. Rev. B* **40,** 10535–10542 (1989).
54. Bauchy, M., Qomi, M. J. A., Bichara, C., Ulm, F.-J. & Pellenq, R. J. M. Rigidity Transition in Materials: Hardness is Driven by Weak Atomic Constraints. *Phys. Rev. Lett.* **114,** 125502 (2015).
55. Smedskjaer, M. M., Mauro, J. C. & Yue, Y. Prediction of Glass Hardness Using Temperature-Dependent Constraint Theory. *Phys. Rev. Lett.* **105,** 115503 (2010).
56. Hamilton, J. P., Brantley, S. L., Pantano, C. G., Criscenti, L. J. & Kubicki, J. D. Dissolution of nepheline, jadeite and albite glasses: toward better models for aluminosilicate dissolution. *Geochim. Cosmochim. Acta* **65,** 3683–3702 (2001).
57. MTI Corporation. *Company Webpage*, http://www.mtixtl.com (2015).
58. Rotberg, V. H., Toader, O. & Was, G. S. A. High Intensity Radiation Effects Facility in: Applications of Accelerators in Research and Industry, edited by J. L. Duggan and I. L. Morgan, *AIP Conf. Proc*. **578**, 687–691 (2001).
59. Stoller, R. E., Toloczko, M. B., Was, G. S., Certain, A. G., Dwaraknath, S. & Garner, F. A. On the use of SRIM for computing radiation damage exposure. *Nucl. Instrum. Methods Phys. Res. Sect. B* **310,** 75–80 (2013).
60. Kumar, A., Reed, J. & Sant, G. Vertical Scanning Interferometry: A New Method to Measure the Dissolution Dynamics of Cementitious Minerals. *Jour. Amer. Cer. Soc.* **96(9),** 2766–2778 (2013).
61. Plimpton, S. Fast parallel algorithms for short-range molecular dynamics. *J. Comput. Phys.* **117,** 1–19 (1995).
62. van Beest, B. W. H., Kramer, G. J. & van Santen, R. A. Force fields for silicas and aluminophosphates based on ab initio calculations. *Phys. Rev. Lett.* **64(16),** 1955–1958 (1990).
63. Vuilleumier, R., Seitsonen, A., Sator, N. & Guillot, B. Structure, equation of state and transport properties of molten calcium carbonate ($CaCO_3$) by atomistic simulations. *Geochim. Cosmochim. Acta* **141,** 547–566 (2014).
64. Phillips, C. L., Magyar, R. J. & Crozier, P. S. A two-temperature model of radiation damage in α-quartz. *J. Chem. Phys.* **133(14),** 144711–144721 (2010).
65. Wang, B., Yu, Y., Lee, Y. J. & Bauchy, M. Intrinsic nano-ductility of glasses: the critical role of composition. *Glass Sci.* **2,** 11 (2015).
66. Yuan, F. & Huang, L. Brittle to Ductile Transition in Densified Silica Glass. *Scientific Reports* **4** (2014).
67. Sifré, D., Hashim, L. & Gaillard, F. Effects of temperature, pressure and chemical compositions on the electrical conductivity of carbonated melts and its relationship with viscosity. *Chem. Geol.* (2014).
68. Vuilleumier, R., Seitsonen, A. P., Sator, N. & Guillot, B. Carbon dioxide in silicate melts at upper mantle conditions: Insights from atomistic simulations. *Chem. Geol.* (2015).
69. Ziegler, J. F. & Biersack, J. P. In *Treatise on Heavy-Ion Science* (ed. Bromley, D. A.) 93–129 (Springer US, 1985).

70. Mauro, J. C. Topological constraint theory of glass. *Am. Ceram. Soc. Bull.* **90,** 31–37 (2011).
71. Phillips, J. C. Topology of covalent non-crystalline solids I: Short-range order in chalcogenide alloys. *J. Non-Cryst. Solids* **34,** 153–181 (1979).
72. Bauchy, M. & Micoulaut, M. Atomic scale foundation of temperature-dependent bonding constraints in network glasses and liquids. *J. Non-Cryst. Solids* **357,** 2530–2537 (2011).
73. Bauchy, M., Micoulaut, M., Celino, M., Le Roux, S., Boero, M. & Massobrio, C. Angular rigidity in tetrahedral network glasses with changing composition. *Phys. Rev. B* **84,** 054201 (2011).

Acknowledgements

The authors acknowledge financial support for this research provided by: The Oak Ridge National Laboratory operated for the U.S. Department of Energy by UT-Battelle (LDRD Award Number: 4000132990), National Science Foundation (CMMI: 1066583 and 1235269), Federal Highway Administration (DTFH61-13-H-00011) and the University of California, Los Angeles (UCLA). The contents of this paper reflect the views and opinions of the authors, who are responsible for the accuracy of data presented herein. This research was conducted in: Laboratory for the Chemistry of Construction Materials (LC^2), the Laboratory for the Physics of AmoRphous and Inorganic Solids (PARISlab), and the Molecular Instrumentation Center (MIC) at UCLA, the Michigan Ion Beam Laboratory (MIBL) and the Low Activation Materials Development and Analysis (LAMDA) facility of Oak Ridge National Laboratory (ORNL). Support for KGF was provided by the ORNL Alvin M. Weinberg Fellowship. The authors gratefully acknowledge the support that has made these laboratories and their operations possible. This manuscript has been co-authored by UT-Battelle, LLC under Contract: DE-AC05-00OR22725 with the U.S. Department of Energy. The United States Government retains and the publisher, by accepting the article for publication, acknowledges that the United States Government retains a non-exclusive, paid-up, irrevocable, world-wide license to publish or reproduce the published form of this manuscript, or allow others to do so, for United States Government purposes. The Department of Energy will provide public access to these results of federally sponsored research in accordance with the DOE Public Access Plan (http://energy.gov/downloads/doe-public-access-plan). The authors acknowledge Prof. Jacob Israelachvili (UCSB) for stimulating and insightful discussions on the dissolution behaviors and mechanisms of silicates.

Author Contributions

G.S. and Y.P. conceptualized the work. G.S. and A.K. designed the experiments. I.P. and A.K. performed the dissolution measurements. K.F. performed the TEM experiments and acquired SAED patterns. M.B., B.W. and Y.Y. performed the molecular simulations and the rigidity analysis. M.B., G.S. and Y.P. wrote the manuscript. All authors contributed to discussion of the results, provided inputs on the manuscript, and approved the final version.

Additional Information

Supplementary information accompanies this paper at http://www.nature.com/srep

Competing financial interests: The authors declare no competing financial interests.

How to cite this article: Pignatelli, I. *et al.* Direct Experimental Evidence for Differing Reactivity Alterations of Minerals following Irradiation: The Case of Calcite and Quartz. *Sci. Rep.* **6**, 20155; doi: 10.1038/srep20155 (2016).

Available online at www.sciencedirect.com

ScienceDirect

Geochimica et Cosmochimica Acta 209 (2017) 106–122

Geochimica et Cosmochimica Acta

www.elsevier.com/locate/gca

Mineralogical, crystallographic and redox features of the earliest stages of fluid alteration in CM chondrites

Isabella Pignatelli [a,*], Yves Marrocchi [a], Enrico Mugnaioli [b,c], Franck Bourdelle [d], Matthieu Gounelle [e,f]

[a] CRPG, UMR 7358, CNRS – Université de Lorraine, 54500 Vandoeuvre-lès-Nancy, France
[b] Dipartimento di Scienze Fisiche, della Terre e dell'Ambiente, Università degli Studi di Siena, Via Laterino 8, 53100 Siena, Italy
[c] Center for Nanotechnology Innovation@NEST, Istituto Italiano di Tecnologia, Piazza San Silvestro 12, 56127 Pisa, Italy
[d] LGCgE, Université de Lille 1, SN 5, 59655 Villeneuve d'Ascq, France
[e] IMPMC, MNHN, UPMC, UMR CNRS 7590, 61 rue Buffon, 75005 Paris, France
[f] Institut Universitaire de France, Maison des Universités, 103 bd. Saint-Michel, 75005 Paris, France

Received 28 October 2016; accepted in revised form 11 April 2017; Available online 19 April 2017

Abstract

The CM chondrites represent the largest group of hydrated meteorites and span a wide range of conditions, from less altered (i.e., CM2) down to heavily altered (i.e., CM1). The Paris chondrite is considered the least altered CM and thus enables the earliest stages of aqueous alteration processes to be deciphered. Here, we report results from a nanoscale study of tochilinite/cronstedtite intergrowths (TCIs) in Paris—TCIs being the emblematic secondary mineral assemblages of CM chondrites, formed from the alteration of Fe-Ni metal beads (type-I TCIs) and anhydrous silicates (type-II TCIs). We combined high-resolution transmission electron microscopy, scanning transmission X-ray microscopy and electron diffraction tomography to characterize the crystal structure, crystal chemistry and redox state of TCIs. The data obtained are useful to reconstruct the alteration conditions of Paris and to compare them with those of other meteorites. Our results show that tochilinite in Paris is characterized by a high hydroxide layer content ($n = 2.1$–2.2) regardless of the silicate precursors. When examined alongside other CMs, it appears that the hydroxide layer and iron contents of tochilinites correlate with the degree of alteration experienced by the chondrites. The $Fe^{3+}/\Sigma Fe$ ratios of TCIs are high: 8–15% in tochilinite, 33–60% in cronstedtite and 70–80% in hydroxides. These observations suggest that alteration of CM chondrites took place under oxidizing conditions that could have been induced by significant H_2 release during serpentinization. Similar results were recently reported in CR chondrites (Le Guillou et al., 2015), suggesting that the process (es) controlling the redox state of the secondary mineral assemblages were quite similar in the CM and CR parent bodies despite the different alteration conditions.

According to our mineralogical and crystallographic survey, the formation of TCIs in Paris occurred at temperatures lower than 100 °C, under neutral, slightly alkaline conditions that favored the formation of both tochilinite and cronstedtite. During the course of alteration, the reduction in sulfur activity and/or the decrease of temperature prevented tochilinite crystallization and favoured the formation of cronstedtite and iron hydroxides. We suggest that iron hydroxides probably formed as ferrihydrite and then progressively converted to goethite between 50° and 80 °C, a temperature range that is also favorable for cronstedtite formation. The presence of cronstedtite plays a key role in the reconstruction

* Corresponding author.
E-mail address: isabella.pignatelli@univ-lorraine.fr (I. Pignatelli).

http://dx.doi.org/10.1016/j.gca.2017.04.017

of the alteration history, demonstrating that the alteration of Paris took place by way of serpentinization processes similar to those described on the Earth.

Keywords: Fluid alteration; CM chondrites; Secondary minerals; Pseudomorphism; Cronstedtite; Tochilinite

1. INTRODUCTION

Chondrites are leftover solids from the evolution of the solar protoplanetary disk 4.56 Gyr ago. They are partially composed of high temperature components (refractory inclusions, chondrules and Fe-Ni metal beads) formed by different nebular and/or planetary processes (Meibom et al., 2000; Krot et al., 2005; Marrocchi and Libourel, 2013; Scott and Krot, 2014; Marrocchi et al., 2016). Chondrules are silicate spherules that represent the most abundant high-temperature constituents of chondrites (Hewins et al., 2005). The different chondrite components are all surrounded by a volatile-rich fine-grained matrix material, which fills the interstices between them and thus represents the cement of chondrites (Scott and Krot, 2014; Le Guillou et al., 2014). The modal abundance of matrix is highly variable among carbonaceous chondrites, ranging from less than 5% in CB/CH chondrites to more than 95% in CI chondrites (Scott and Krot, 2014). The characterization of chondritic matrices has been a long-standing issue in meteorite studies due to the sub-micrometer size and the complexity of their mineral assemblages as well as the presence of organic matter (Brearley, 2006; Le Guillou et al., 2014; Elmaleh et al., 2015). However, understanding the nature of matrix material is of primary importance as it may hold invaluable information on the processes at the origin of dust in the protoplanetary disk (Le Guillou et al., 2015; Leroux et al., 2015). In addition, the potential chondrule/matrix complementarity (Palme et al., 2015) highlights the importance of deciphering the nature of primitive chondritic matrices in terms of understanding (i) the conditions of chondrule formation (Hezel and Palme, 2010) and (ii) the transport of dust in the accretion disk (Anders, 1964). The matrix materials also experienced variable degrees of aqueous and/or thermal alteration, which affected their texture, mineralogy, as well as chemical and isotopic properties (Brearley, 2006). Even though it is widely acknowledged that chondrites underwent such secondary modifications, the physico-chemical conditions under which they took place, the timing and duration of the alteration processes are still only partially understood. The difficulty to quantify the conditions of secondary processes experienced by chondrites is related to many factors: (i) direct samples of alteration fluids are extremely rare and difficult to analyze (Zolensky et al., 1999), (ii) the setting(s) of alteration remains controversial (Metzler et al., 1992; Krot et al., 2006), (iii) secondary minerals form complex, fine-grained mixtures leading to analytical problems for their characterization and (iv) the stability field of chondritic secondary minerals are largely under-constrained because of their scarcity on Earth (Brearley, 2006). This can result in contradictory interpretations regarding the origins of secondary minerals and this gap in our understanding severely restricts interpretation of meteorite data, data that would help us to better understand the hydrothermal processes in the early solar system.

Regarding the aqueous alteration processes, CM chondrites are of primary importance because they record highly variable extents of hydrothermal alteration (Zolensky et al., 1997; Rubin et al., 2007; Hewins et al., 2014) though sharing common bulk chemical and isotopic compositions. CM matrix phyllosilicates point toward oxidizing alteration conditions as attested by their high $Fe^{3+}/\Sigma Fe$ (i.e., 50–70%) determined by electron energy loss spectroscopy (EELS; Zega et al., 2003) and scanning transmission X-ray microscopy (STXM-XANES; Elmaleh et al., 2015). However, the Fe valence of CM chondrite matrices has only been determined at the bulk scale (Beck et al., 2012) or in CMs characterized by moderate to heavy alteration (i.e., Murray, Murchison and Cold Bokkeveld; Zega et al., 2003; Vollmer et al., 2014; Elmaleh et al., 2015). The recent characterizations of Paris, a weakly altered CM chondrite (Bourot-Denise et al., 2010; Hewins et al., 2014; Marrocchi et al., 2014; Rubin, 2015; Vacher et al., 2016; Verdier-Paoletti et al., 2017), offer an interesting opportunity to better understand the earliest stages of CM alteration. Paris is a complex breccia characterized by the presence of fresh, metal-rich zones in contact with moderately altered, metal-poor zones (Hewins et al., 2014; Marrocchi et al., 2014; Vacher et al., 2016). Transmission electron microscope (TEM) observations of Paris have revealed that the least altered matrix sample is composed of amorphous silicate grains similar to those observed in CR chondrites (Le Guillou et al., 2015; Leroux et al., 2015). However, the occurrence of tochilinite-cronstedite intergrowths (hereafter TCIs) with euhedral shapes that are characteristic of silicates (Pignatelli et al., 2016) shows that pseudomorphic alteration affected Paris. Tochilinite is a mineral with incommensurate structure based on two layers: (i) a mackinawite-type $Fe_{1-x}S$ sulfide layer and (ii) a brucite- or amakinite-type hydroxide layer, depending on the composition. Its ideal formula is $2(Fe_{1-x}S)\cdot n(Fe, Mg, Al, Ca)(OH)_2$ with $1.58 < n < 1.85$ (Zolensky and Mackinnon, 1986) and $0.08 < x < 0.28$ (Gubaidulina et al., 2007), where n and x correspond to the hydroxide layer content and the vacancies of the sulfide layer, respectively. Cronstedtite is a T-O phyllosilicate with a general formula $(Fe^{2+}_{3-x}Fe^{3+}_{x})(Si_{2-x}Fe^{3+}_{x})O_5(OH)_4$ with $0 < x < 0.8$ in terrestrial crystals (Pignatelli et al., 2013, 2015 and references therein). TCIs are dispersed throughout the Paris matrix, regardless of its alteration degree, and correspond to the alteration of Fe-Ni metal beads (type-I TCIs) or silicates (type-II TCIs). Type-I TCIs are composed of tochilinite/cronstedtite intergrowths whereas type-II TCIs

are characterized by a complex compositional zoning, comprising three different Fe-bearing secondary minerals: tochilinite, cronstedtite and Fe-hydroxides (Pignatelli et al., 2016).

Tochilinite and cronstedtite are two complex, layered minerals that can help to better understand the alteration conditions of Paris, as well as of other CMs. However, the stability fields of these minerals are limited to few experimental and thermodynamic data. Tochilinite is thought to form under extremely reducing condition, high fS_2 and fH_2 (Zolensky and Mackinnon, 1986; Browning and Bourcier, 1996). Laboratory syntheses show that tochilinite can form in alkaline medium ($7.8 < pH < 11.5$) and at temperatures ranging from 80 to 320 °C, but it stability field is strongly affected by the Mg-Fe substitutions (Kozerenko et al., 1996, 2001). In comparison to tochilinite, cronstedtite requires less-reducing, neutral-alkaline conditions ($7 < pH < 8$) and temperatures lower than 100 °C (Schulte and Shock, 2004; McAlister and Kettler, 2008; Zolotov, 2014; Pignatelli et al., 2013, 2014a). The occurrence of tochilinite-cronstedtite intergrowths within CMs is fundamental because it implies that they formed under a narrow range of conditions, which are still poorly characterized.

In order to better constrain the formation conditions of the secondary mineralogical assemblages (tochilinite, cronstedtite and hydroxides), as well as the redox state of iron, we present a nanoscale study of TCIs in the Paris CM chondrite conducted using TEM, STXM-XANES and electron diffraction tomography (EDT). This accurate mineralogical characterization of Paris has allowed us to determine the variations in physico-chemical and redox conditions that occurred during the earliest stages of CM alteration.

2. MATERIAL AND METHODS

Detailed observations of a section of the Paris chondrite (#2010-1 – Hewins et al., 2014; Pignatelli et al., 2016) were performed at CRPG with a JEOL JSM-6510 Scanning Electron Microscope (SEM) equipped with a tungsten filament and an energy dispersive X-ray (EDX) Genesis detector, using a 3 nA primary beam accelerated at 15 kV. Based on these observations, we selected three TCIs for FIB extraction: (i) a euhedral type-II TCI with pyroxene precursor (Fig. 1A), (ii) an anhedral type-II TCI with forsterite remnant in the center (Fig. 1C) and (iii) a type-I TCI surrounding a kamacite bead (Fig. 1E). The ultra-thin foils were prepared using FEI strata DualBeam 235 at the Institute d'Electronique, de Microélectronique et de Nanotechnologie (Lille, France). We used a lift-out procedure described by Heaney et al. (2001). The foils have a thickness of around 100 nm and variable sizes of ~20 × 5 µm, ~20 × 6 µm and ~14 × 4 µm, respectively (Fig. 1B, D and F)

High-resolution TEM images (HRTEM), selected area electron diffraction (SAED) patterns, and energy dispersive X-ray (EDX) spectra were acquired at Siena University using a JEOL 2010 microscope operated at 200 kV and equipped with LaB_6 gun and UHR pole pieces able to achieve a point-to-point resolution of 0.19 nm. This microscope was also used to collect 3D electron diffraction data by combining electron diffraction tomography (EDT) (Kolb et al., 2007, 2008; Mugnaioli, 2015) and precession electron diffraction (PED) (Vincent and Midgley, 1994; Mugnaioli et al., 2009). HRTEM and SAED data were acquired using an Olympus Tengra CCD camera (2 k × 2 k × 14 bit). TEM-EDX analyses were carried out using an Oxford ISIS spectrometer with a probe diameter of ~100 nm, a counting time of 60 s, a dead time lower than 15%, and K_{AB} factors calibrated on standards. Sequential SAED diffraction patterns were collected in a tilt range of up to −40/+40° with a step of 1°, using an area selector of 10 µm, equivalent to a beam size on the sample of about 100 nm. ADT3D software and in-house Matlab routines were used for the data processing, including three-dimensional reciprocal space reconstruction, cell parameter determination and intensity integration. The main advantages of this technique for characterizing nanometric crystals, such as those in meteorites, are detailed in Pignatelli et al. (2014b).

X-ray adsorption near-edge structure spectroscopy (XANES) was used to obtain iron L-edge data at the Pollux beamline (Raabe et al., 2008) at the Swiss Light Source (Paul Scherrer Institute – SLS, Switzerland). During data collection, the SLS synchrotron storage ring was operated at 2.4 GeV and 400 mA current in a top-up mode. XANES spectroscopy was carried out with a scanning transmission X-ray microscope (STXM), which allows the spectrum on each pixel of a "sample image" to be collected and enables the variation in the $Fe^{3+}/\Sigma Fe$ ratio to be evaluated with an uncertainty of around 10%. Spectra and stacks were obtained over the 690–730 eV energy range (Fe $L_{2,3}$-edge), using circularly polarized light and a 1 ms dwell time per pixel and energy point. Data were processed using aXis2000 software (Hitchcock, 2012). The procedure for the $Fe^{3+}/\Sigma Fe$ ratio determination is detailed in Bourdelle et al. (2013).

3. RESULTS

3.1. Type-I TCIs

The type-I TCI comprised a kamacite core composed of lamellae with a slightly different Ni content ($\Delta_{Ni} \sim 2$ at.%), surrounded by an alteration rim composed of tochilinite/cronstedtite intergrowths (Fig. 1E). These alteration phases are nanocrystalline or amorphous, as revealed by the presence of diffuse rings in the SAED pattern, and correspond to matrix-like materials that encompass iron-rich, needle-like crystals (Fig. 2A and B) and sub-spherical Cr-bearing phases (Fig. 2C). These iron-rich minerals have a $Fe^{3+}/\Sigma Fe$ ratio of 30% and their SAED patterns show the superimposition of several lattices with d_{hkl} values of ~4.3, 3.1, 2.6, 2.1, 1.6, and 1.5 Å. The Cr-bearing phases contain variable concentrations of Cr and S, ranging from 12.83 to 25.40 at.% and 25.17 to 39.57 at.%, respectively; they are also iron rich and contain significant amounts of oxygen (Table 1). The primitive cell of Cr-bearing phase, computed from EDT data after excluding diffraction spots originating from surrounding

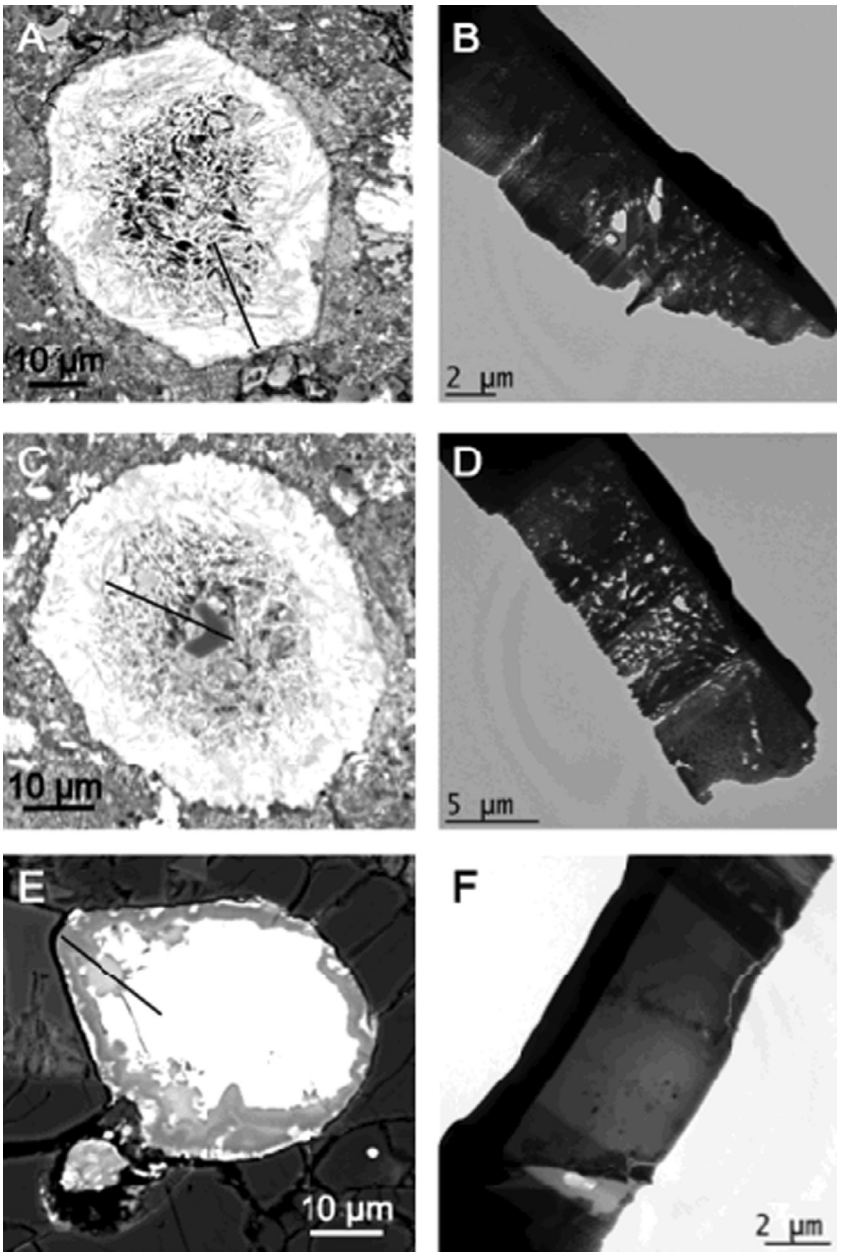

Fig. 1. SEM back-scattered electron images of (A) a type-II TCI with the shape of euhedral pyroxene, (C) an anhedral type-II TCI with forsterite remnant in the center, (E) a type-I TCIs surrounding a Fe-Ni metal bead. Black lines indicate where the FIB foils are extracted. (B, D and F) TEM images of FIB foils extracted from the TCIs shown in images A, C, and F, respectively.

individua, has the following parameters: $a = 13.7$ Å, $b = 7.3$ Å, $c = 7.0$ Å, $\alpha = 120.4°$, $\beta = 76.7°$ and $\gamma = 74.4°$.

The outer edge of the alteration rim is characterized by the presence of Ni- and Fe-bearing crystals (Fig. 2D) disordered pentlandite composed of multiple domains and well-crystallized schreibersite. Pentlandite was identified using the electron diffraction patterns, showing a diffraction maximum at ~1.8 Å, whereas EDT analysis allowed the schreibersite crystals to be characterized according to the cell parameters $a = b = 9$ Å, $c = 4.4$ Å, $\alpha = \beta = \gamma = 90°$ and the space group $I\bar{4}$ (Fig. 3).

3.2. Type-II TCIs

Both types of type-II TCIs present mineralogical zonation of three different Fe-bearing secondary minerals: tochilinite, cronstedtite and hydroxides (Pignatelli et al., 2016). The TEM and HRTEM images show that anhedral and lath crystals of tochilinite (Fig. 4A) are located in the outer zone of the TCIs and that tochilinite is often associated with cronstedtite at micrometer scale (Fig. 5C and D). Because of the complex intergrowths, we only took into account the analyses with the lowest Si

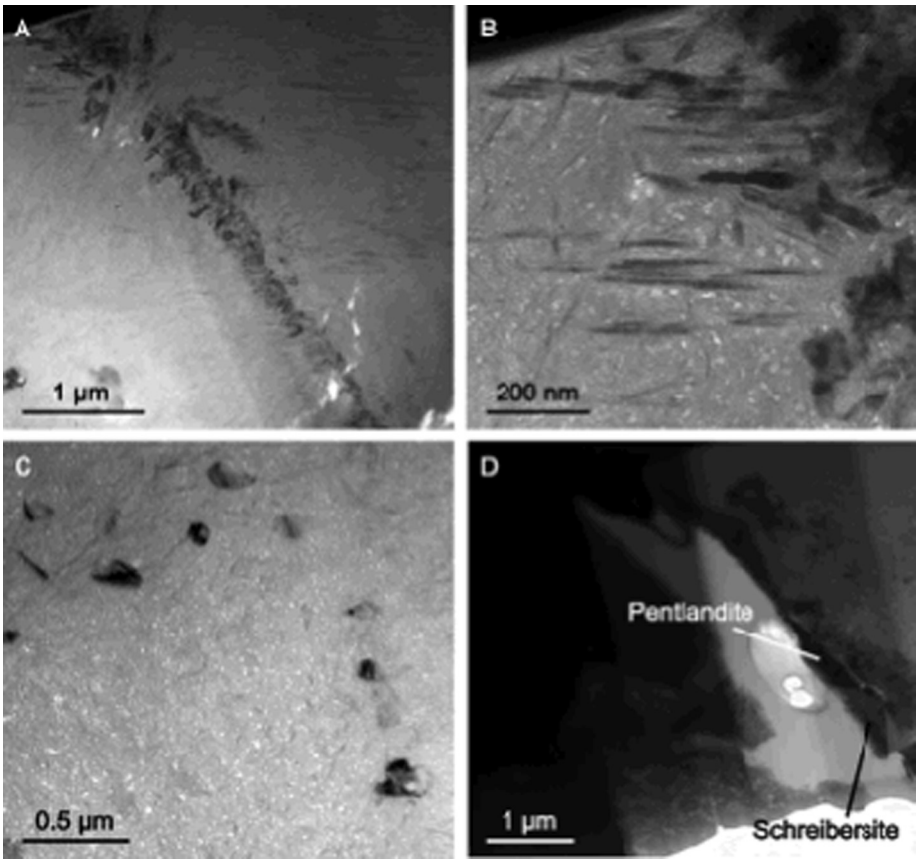

Fig. 2. (A, B) Area of type-I TCI containing iron-rich, needle-like minerals. (C) Sub-spherical minerals with S, Cr, Fe and O. (D) Pentlandite and schreibersite crystals on the outer edge of the alteration rim (right part). In the left part of the image, there is a portion of the matrix surrounding the type-I TCI.

Table 1
TEM-EDX data of Cr-bearing phases (at.%) in type-I TCI.

	O	Mg	Al	Si	P	S	Cr	Fe	Ni	Total
	31.23	0.25	0.11	1.90	1.93	33.26	17.25	13.42	0.62	99.97
	30.48	0.15	0.14	1.45	1.32	34.36	19.50	12.29	0.31	100.00
	29.28	0.19	0.11	2.40	1.15	32.98	23.10	10.61	0.18	100.00
	24.08	0.14	0.14	2.12	1.35	39.57	25.40	6.94	0.25	99.99
	32.93	0.25	0.20	2.31	1.03	31.34	21.79	9.85	0.30	100.00
	41.70	0.74	0.30	2.55	0.93	25.17	12.83	14.77	1.02	100.01
	34.63	0.23	0.16	2.73	0.87	30.00	16.79	14.00	0.60	100.01
	25.11	0.21	0.18	2.42	1.15	36.69	20.01	13.57	0.57	99.61
	39.55	0.67	0	3.91	0	28.50	14.69	11.65	1.03	100.00
Average	32.11	0.31	0.15	2.42	1.08	32.43	19.04	11.90	0.54	
σ	5.91	0.23	0.08	0.67	0.51	4.32	4.06	2.46	0.32	

contents (Si < 2.5 at.%, Table 2) as corresponding to tochilinite. Tochilinite crystals have similar chemical compositions in both type-II TCIs and negligible amounts of P, Cr, Co and Ca (<0.6 at.%; Table 2); Ni is not detected. The average tochilinite formulae, calculated by neglecting Si and all elements of less than 1 at.%, correspond to:

$$2(Fe_{0.88}S) \cdot 2.1(Fe_{0.88}Mg_{0.12})(OH)_2 \quad \text{[forsterite precursor]} \tag{1}$$

$$2(Fe_{0.87}S) \cdot 2.2(Fe_{0.89}Mg_{0.11})(OH)_2 \quad \text{[pyroxene precursor]} \tag{2}$$

The TEM-EDX and STXM-XANES data indicate that the tochilinite crystals are characterized by high Fe/Mg ratios, in the range 8.8–33.1 (Table 2), and yield mostly Fe^{2+} with $Fe^{3+}/\Sigma Fe \leq 15\%$ (Fig. 6). The HRTEM images show that the tochilinite generally has an interplanar distances d_{001} of ~19 Å (Fig. 5C and D), but sometimes of ~11 Å (Fig. 5B).

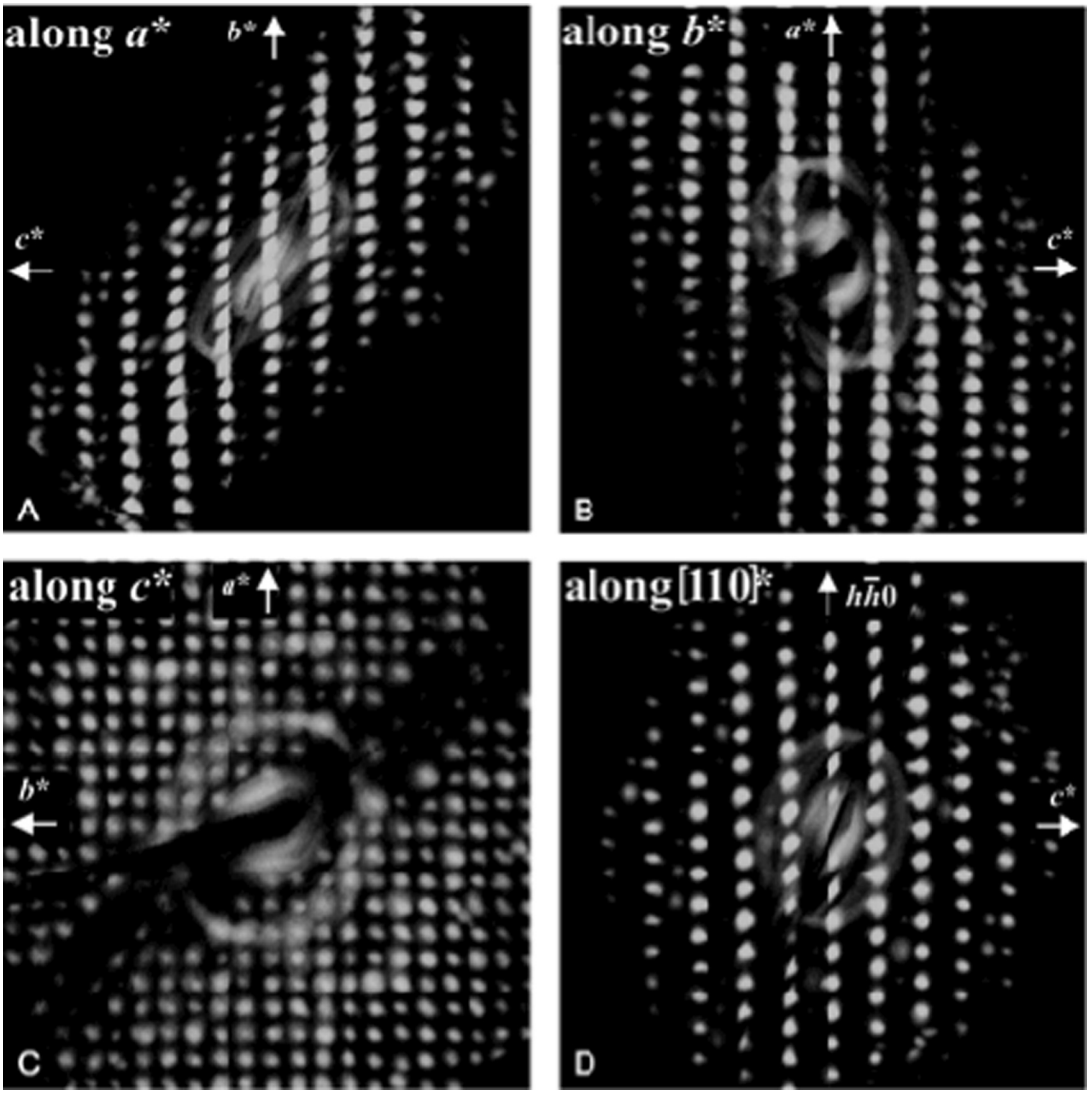

Fig. 3. Projections of the 3D reconstructed diffraction volume from EDT data of schreibersite: (A) projection along a^*; (B) projection along b^*; (C) projection along c^*; (D) projection along $[110]^*$.

Anhedral and euhedral crystals of cronstedtite (Fig. 4B and C) have compositions close to those reported for terrestrial and synthetic cronstedtite (Pignatelli et al., 2013). The cronstedtites have Al and Mg contents in the range 0.42–2.25 at.% and 1.27–8.09 at.%, respectively (Fig. 7; Table 3), indicating that iron can be replaced in both tetrahedral and octahedral sites, as was shown in previous studies (Frondel, 1962; Geiger et al., 1983; Hybler et al., 2002). The crystals with the highest Mg contents (Fig. 7) are all located near to either the forsterite remnant or to the edges of the pyroxene precursor. STXM-XANES data show that the averaged $Fe^{3+}/\Sigma Fe$ ratio in cronstedtite crystals formed from a pyroxene precursor is ~36.5% whereas crystals formed by forsterite alteration have higher $Fe^{3+}/\Sigma Fe$ ratio, ranging from 38% to 75% (Fig. 6). Given that the Paris cronstedtite crystals are very close to Fe^{3+}-rich hydroxides and that Fe^{3+} ranges from 15% to 57% in terrestrial cronstedtite (Zega et al., 2003 and references therein), we neglected Fe^{3+} values higher than 60%. Consequently, the average Fe^{3+} content of crystals formed from forsterite is 48%. The mean cronstedtite formulae, calculated on the basis of seven oxygens and determined by combining the STXM-XANES and TEM-EDX data, are

$$(Fe^{2+}_{1.56}Fe^{3+}_{0.87}Mg_{0.50})_{\Sigma=2.93}(Si_{1.27}Fe^{3+}_{0.57}Al_{0.15})_{\Sigma=1.99}O_5(OH)_4 \quad \text{[forsterite precursor]} \quad (3)$$

$$(Fe^{2+}_{2.01}Fe^{3+}_{0.61}Mg_{0.43})_{\Sigma=3.04}(Si_{1.31}Fe^{3+}_{0.55}Al_{0.14})_{\Sigma=2.00}O_5(OH)_4 \quad \text{[pyroxene precursor]} \quad (4)$$

Cronstedtite crystals are characterized by a variable degree of stacking disorder, however the ADT data show that the most common polytype is 1*T*, though the 3*T* polytype is also observed. The common occurrence of 1*T* cronstedtite is in agreement with the findings reported in studies of other CMs (Müller et al., 1979; Zega and Buseck, 2003). It should be noted that our results represent the first identification and characterization of cronstedtite *sensu stricto* in CM2 chondrites, whereas previous studies reported solid

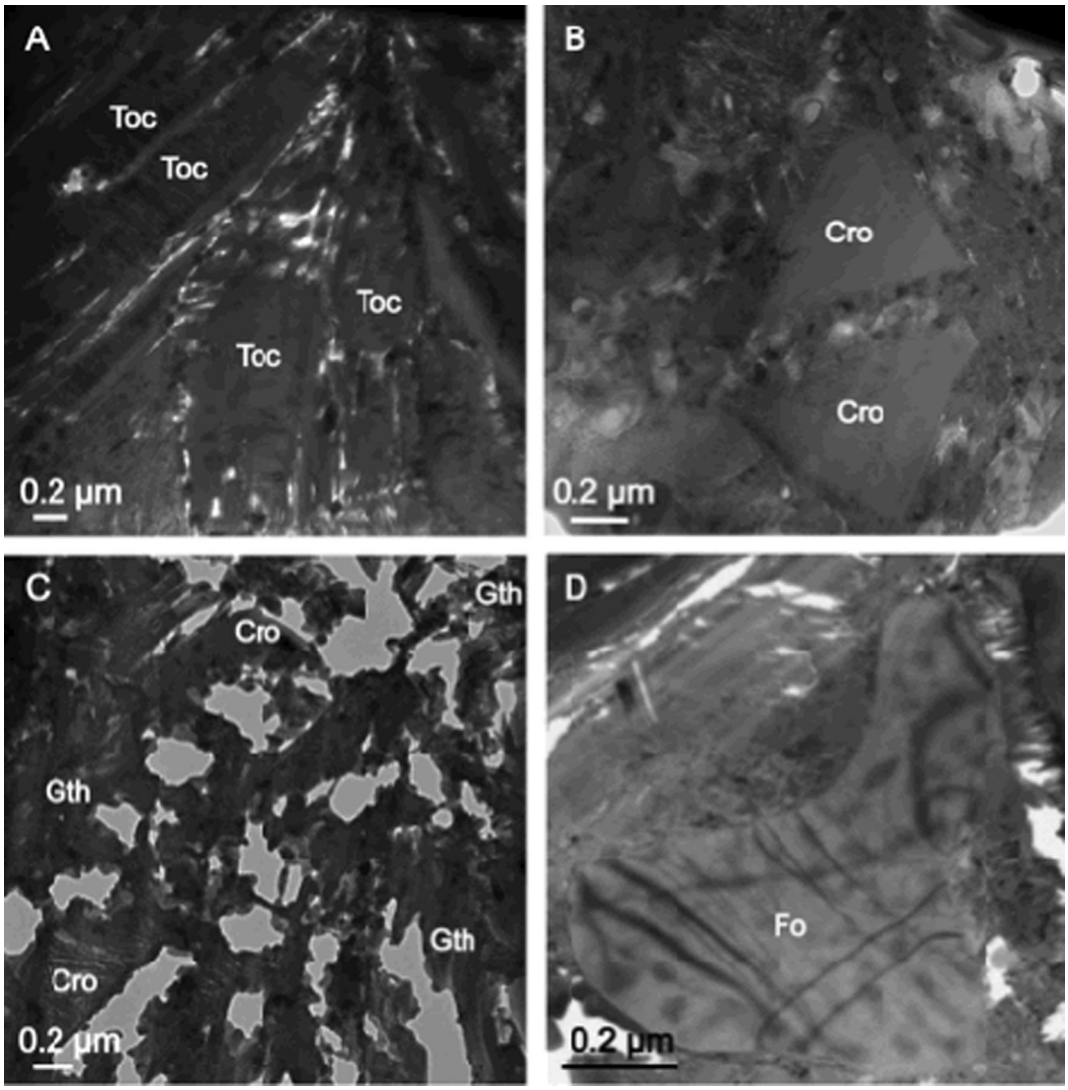

Fig. 4. (A) Lath crystals of tochilinite (Toc). (B) Euhedral cronstedtite (Cro) crystals. (C) Porous area of TCI characterized by the occurrence of goethite (Gth) and cronstedtite. (D) Forsterite (Fo) remnant.

solutions between chrysotile and cronstedtite (Velbel, 2014).

Iron-rich minerals were observed in both type-II TCIs, in particular in more porous areas where they occur with small cronstedtite crystals (Fig. 4C). They are characterized by an average Fe/O ratio of ~0.5 and low Mg and Al contents (<3 and 1.5 at.%, respectively). On the basis of the STXM-XANES data (Fig. 6), which indicate a high amount of Fe^{3+} (70–80%), these minerals are likely iron hydroxides. The EDT data indicate that iron hydroxides have cell parameters $a = 4.6$ Å, $b = 9.9$ Å, $c = 3.0$ Å, $\alpha = \beta = \gamma = 90°$, and space group *Pbnm* corresponding to goethite.

It worth nothing that TEM analysis of type-II TCIs indicated that the forsterite remnant (Figs. 1C and 4D) is characterized by a mottled pattern suggesting the presence of subgrains, i.e. areas with slightly different crystallographic orientations. Dislocations (black lines on Fig. 4D), generally associated to subgrains, are also observed. The interfaces between forsterite and secondary minerals are sharp, without sawtooth texture, suggesting that the replacement process occurred by dissolution-precipitation, rather than solid-state diffusion (Putnis et al., 2007). However, the absence of the sawtooth texture could be due also to the orientation of forsterite cross-section (Lee and Lindgren, 2016).

4. DISCUSSION

4.1. Extent of hydrothermal alteration recorded in tochilinite

Tochilinite in Paris is characterized by a higher hydroxide layer content compared to the ideal formula ($n = 2.1$–2.2), regardless of the silicate precursors (Eq. (1) and (2)). However, other examples of tochilinite with $n > 1.85$ have previously been reported: (i) synthetic crystals ($n = 1.92$; Kakos et al., 1994), (ii) terrestrial tochilinites from Pennsylvania ($n = 1.97$; Jambor, 1976) and Czechoslovakia

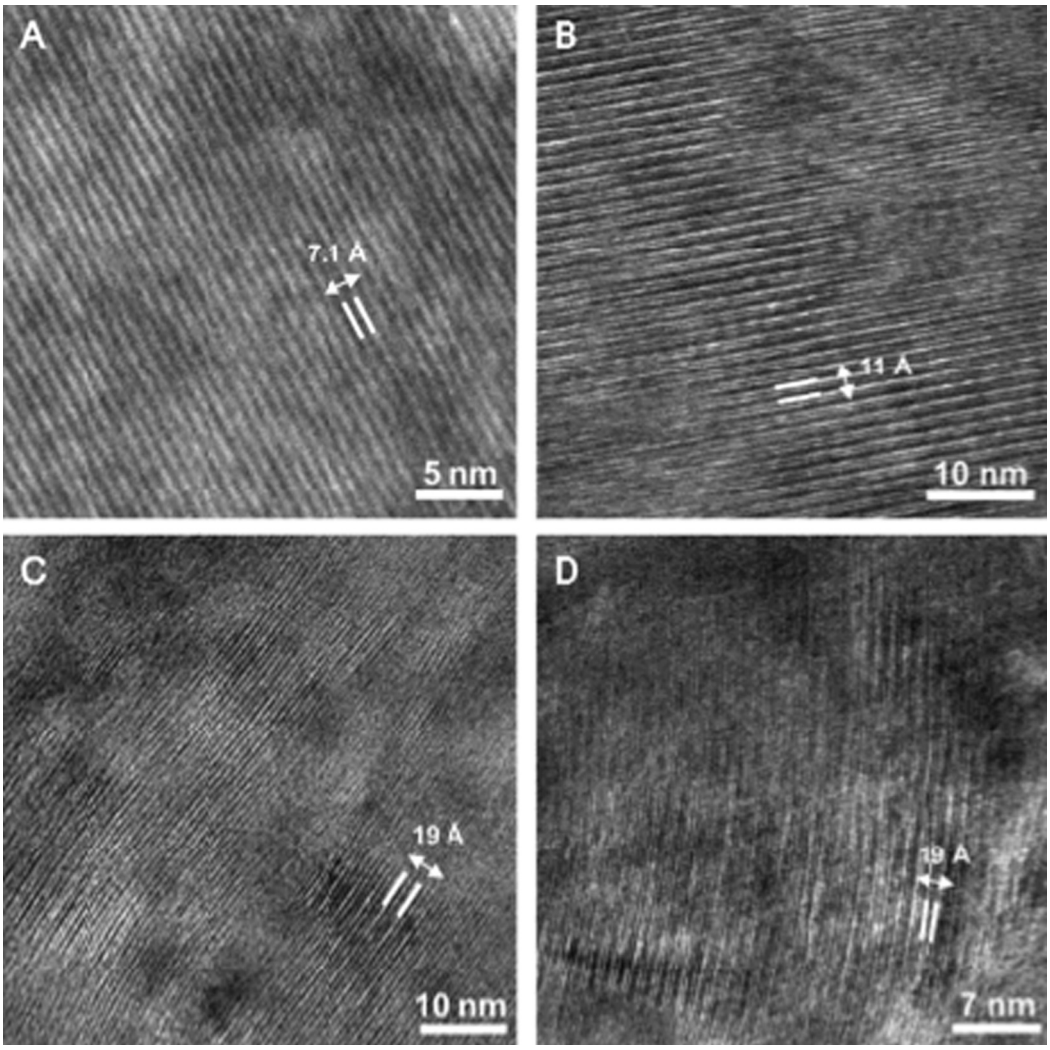

Fig. 5. (A) HRTEM images of well-ordered cronstedtite lamellae with typical interplanar distances of 7.1 Å. (B) Tochilinite lamella consisting of packs of three alternating layers with different contrast, interplanar distance of ~11 Å. (C, D) Tochilinite/cronstedite intergrowths; tochilinite has interplanar distance of ~19 Å. In the bottom left corner of image D, a slight change in the orientation of tochilinite fibers has resulted in a wave that produces a band contrast in HRTEM images.

($n = 7.3$; Johan, 1990), and (iii) extraterrestrial tochilinite within the Murchison and Nogoya CM chondrites ($n = 1.90$ and 1.95, respectively; Palmer and Lauretta, 2011). The high hydroxide layer content of Paris tochilinites is supported by their high Fe/Mg ratios (Table 2), indicating that the brucite layer has been replaced by an amakinite layer with an ideal formula of $Fe(OH)_2$ (Zolensky, 1984). This is confirmed by the interplanar distance d_{001} of ~19 Å measured in several tochilinite crystals, which reflects the greater thickness of the amakinite layer compare to brucite layer. Nevertheless, we also found an interplanar distance of $d_{001} \sim 11$ Å, consistent with the presence of a brucite layer probably caused by a local Mg enrichment (Organova et al., 1973). Tochilinite crystals in Paris are enriched in iron compared to tochilinite in other CM chondrites (Fig. 8A). In addition, it appears that the iron content of tochilinite crystals is a direct proxy of the degree of alteration experienced by a given CM chondrite (Fig. 8A). Paris tochilinite also contains the lowest concentrations of Mg (Table 2), supporting previous studies that suggest an enrichment of Mg in secondary minerals during the course of alteration (Tomeoka and Buseck, 1985; Browning et al., 1996; Hanowski and Brearley, 2001; Palmer and Lauretta, 2011; Leroux et al., 2015; Pignatelli et al., 2016). It is worth noting that the hydroxide layer content (n) of tochilinite crystals also correlates with the degree of alteration of CM chondrites (Fig. 8B). Taken together, these observations demonstrate that tochilinite can be used to estimate the extent of alteration experienced by CM chondrites.

4.2. Physico-chemical and redox conditions of CM alteration recorded in TCIs

Type-II TCIs result from the pseudomorphism of anhydrous silicates (Pignatelli et al., 2016) – a peculiar process in which the alteration reaction proceeds from the surface of the parent mineral toward the center (Putnis et al., 2015) and is controlled by the fluid composition

Table 2
TEM-EDX data of tochilinite in type-II TCIs (at.%). Bld = below the detection limit.

TCI precursor	O	Mg	Al	Si	S	Fe	Fe/Mg	Total
Olivine	43.5	1.0	bdl	bdl	20.0	35.3	33.0	99.80
	43.3	2.5	0.3	0.2	19.1	33.8	13.3	99.20
	43.5	2.7	0.6	2.4	17.2	33.2	11.9	99.60
	42.6	2.0	0.3	1.8	19.0	33.9	16.2	99.60
	43.9	1.8	0.3	1.7	19.1	32.8	17.5	99.60
	43.6	2.3	0.6	1.8	19.6	31.2	13.5	99.60
Average	43.4	2.1	0.0	1.3	19.0	33.4	15.84	
σ	0.4	0.6	0.2	1.0	1.0	1.3		
Pyroxene	36.7	2.0	0.6	0.3	20.9	38.6	19.2	99.10
	38.6	2.0	bdl	0.1	19.9	38.7	18.8	99.30
	42.8	1.7	0.4	1.0	18.3	35.5	20.4	99.70
	44.9	3.5	1.1	1.2	17.8	31.3	8.7	99.80
	39.1	2.1	0.6	0.7	20.1	37.1	17.5	99.70
	39.9	2.3	0.6	0.7	19.9	36.4	15.3	99.80
	40.7	2.3	0.5	0.6	20.3	35.3	14.9	99.70
	41.6	1.6	0.2	0.9	19.4	36.0	21.8	99.70
	40.9	2.9	0.5	0.8	19.5	35.2	12.1	99.80
	41.8	2.1	0.5	1.0	18.7	35.7	16.3	99.80
	46.9	3.1	1.1	0.9	18.5	29.3	9.2	99.80
	45.1	3.0	0.8	1.0	19.1	30.7	10.1	99.70
	41.3	2.8	0.8	1.2	19.8	34.1	12.1	100.00
	49.5	2.2	0.8	1.2	17.4	28.7	12.6	99.8
	41.2	2.1	0.7	1.0	20.4	33.9	15.9	99.3
	44.3	2.1	0.8	1.0	18.3	33.2	15.4	99.7
	40.5	2.5	0.9	0.9	21.5	33.1	12.9	99.4
Average	42.1	2.3	0.6	0.9	19.4	34.3	14.4	
σ	3.1	0.5	0.5	0.3	1.1	2.9		

(Hanowski and Brearley, 2001), and by the structural features of primary minerals (Lee and Lindgren, 2016). Consequently, the mineralogical and chemical zoning observed within type-II TCIs can be used to decipher the evolution of the physico-chemical and redox conditions during the course of the alteration of Paris. In addition, even though type-I and type-II TCIs present differences in the morphology and degree of crystallinity of the main alteration products, they present near identical chemical compositions that suggest similar alteration conditions. Moreover, the fact that secondary minerals replacing olivine and pyroxene present similar compositions is also observed in ALH 81002 meteorite and is interpreted as being more strongly dependent on the fluid composition than on the composition of primary minerals (Hanowski and Brearley, 2001; Velbel et al., 2012). Similar observations are reported for other CM meteorites by Velbel et al. (2015) who described this peculiar behavior as "*intrameteorite homogeneity*" resulting from the compositionally uniformity of the alterating fluid on scales much larger than individual TCIs or chondrules.

Iron-rich tochilinite are observed in both types of TCIs and is only found in association with cronstedtite in the outer zone of type-II TCIs. The limited spatial distribution of tochilinite within TCIs implies that (i) the alteration conditions quickly changed, preventing its formation, and/or that (ii) the source of sulfur was limited (Pignatelli et al., 2016). Tochilinite is described as a mineral that is stable under high fS_2 and low fO_2 conditions (Zolensky and Mackinnon, 1986). Interestingly, its stability field can be modified when Fe substitutes for Mg; its upper temperature limit decreasing to 130 °C and its pH stability range extending from 7.8 to 11.5 (Gooding and Zolensky, 1987; Kozerenko et al., 1996, 2001). However, the occurrence of tochilinite/cronstedtite intergrowths indicates that both phases likely formed at temperatures below 100 °C because cronstedtite crystals become unstable above this temperature (Schulte and Shock, 2004; McAlister and Kettler, 2008; Pignatelli et al., 2013; Zolotov, 2014). This estimate is consistent with the formation temperature of serpentines inferred from the oxygen isotopic compositions of matrix phyllosilicates and CM water (i.e., 75 °C; Verdier-Paoletti et al., 2017) and the H isotopic compositions of insoluble organic material (i.e. <200 °C; Alexander et al., 2010). In addition, the pH range in which cronstedtite can form is rather limited to neutral, slightly alkaline conditions (i.e., pH ~ 7–8; Pignatelli et al., 2013). This implies that the early stages of alteration took place under a restricted stability range common to both tochilinite and cronstedtite. It should be noted that formation of TCIs can be favored by elevate concentrations of Fe^{2+} in solution, which can stabilize cronstedtite at fH_2 close to those required for tochilinite formation (Zolotov, 2014).

The hydroxide layers content (n) that can be accommodated by tochilinite crystals is directly related to the alteration conditions, with high n forming under high fO_2 and low fS_2 (Johan, 1990). This suggests that the Paris tochilinite with $n = 2.1$–2.2, formed under higher fO_2 and lower fS_2 than the tochilinite crystals in Murchison and Nogoya, which are characterized by lower hydroxide contents (i.e., $n = 1.90$ and 1.95, respectively; Palmer and Lauretta,

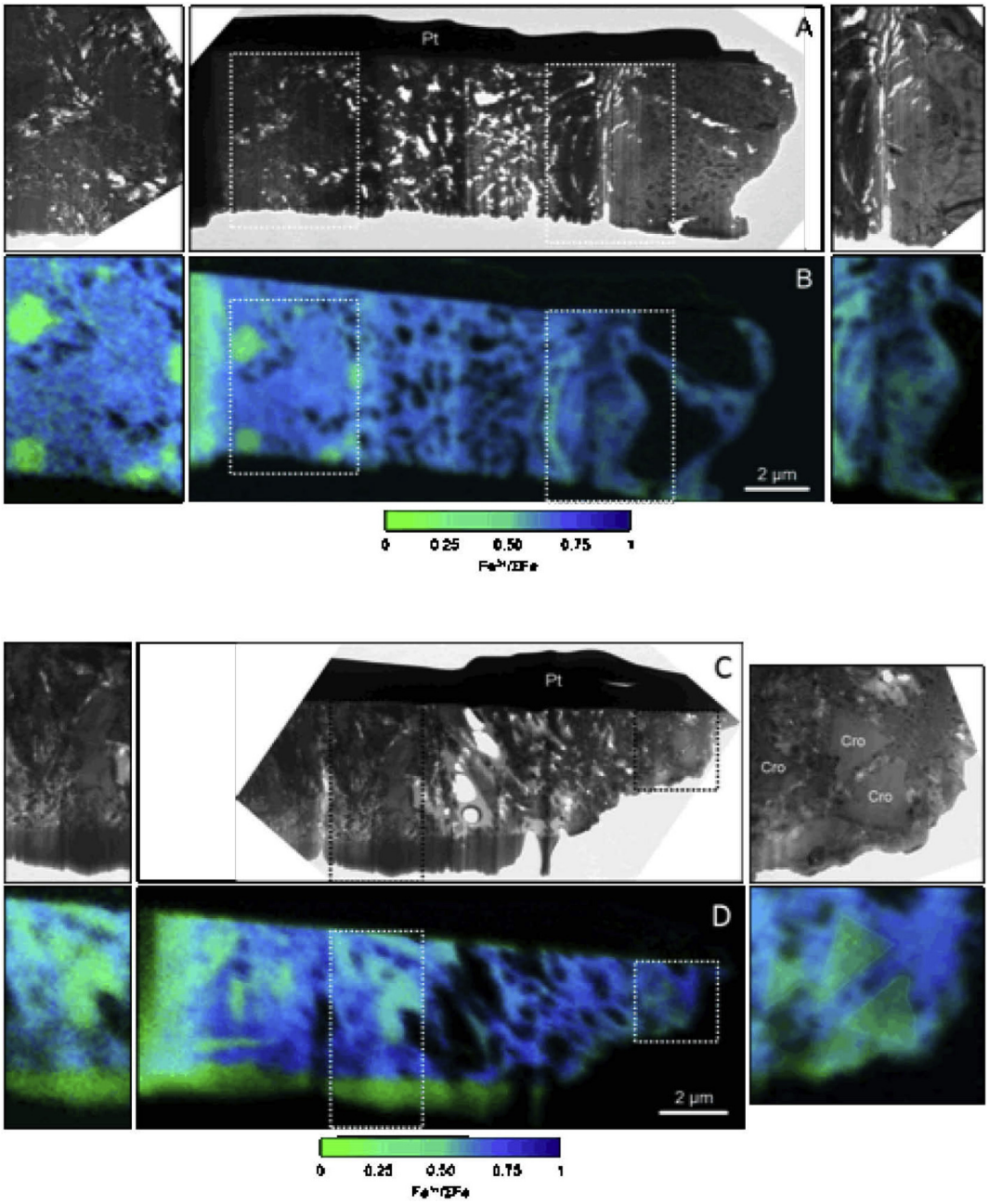

Fig. 6. FIB foils of (A) an anhedral type-II TCI with forsterite remnant in the center and (C) a euhedral type-II TCI with pyroxene precursor. (B) and (D) are the quantitative Fe redox nanomaps of these FIB foils, calculated from STXM-XANES Fe L_3-edge data. On both sides of each FIB foils there are the magnification of two zones with cronstedtite (Cro) and tochilinite (Toc) crystals.

2011). This is confirmed by the presence of low but significant amounts of Fe^{3+} (i.e., ≤15%; Fig. 6) in the structure of tochilinite crystals, although the presence of ferric iron can be partially due to the intergrowth with cronstedtite. However, Fe^{3+} could be incorporated in the hydroxide layer of tochilinite for balancing the net negative charge resulting from the vacancies in sulfide layer (Makovicky and Hyde, 1981; Mackinnon and Zolensky, 1984). Three lines of evidence support this possibility:

(i) Al^{3+} (another trivalent cation) has been identified in several terrestrial and extraterrestrial tochilinite crystals (Zolensky and Mackinnon, 1986; Jambor, 1976; Johan, 1990; Kakos et al., 1994; Palmer and Lauretta, 2011).

(ii) If the Fe^{3+} in tochilinite were linked to the presence of nearby cronstedtite, then the $Fe^{3+}/\Sigma Fe$ should be significantly lower than 15%. For example, if we consider the average tochilinite composition with

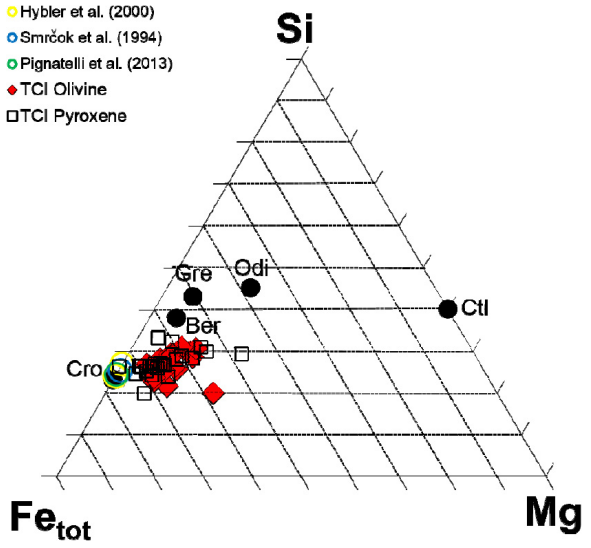

Fig. 7. Compositions (at.%) of cronstedtite crystals in Paris meteorite plotted in a Si-Mg-Fe_{tot} ternary diagram (diamonds). Compositions of terrestrial and synthetic crystal of cronstedtite (Cro) are represented by colored circles (Smrčok et al., 1994; Hybler et al., 2000; Pignatelli et al., 2013). By comparison, other T-O phyllosilicates are rappresented by black circles. Gre: grenalite (Guggenheim et al., 1982); Odi: odinite (Bailey, 1988); Ber: berthierine (Brindley, 1982); Ctl: chrysotile. (For interpretation of the references to colour in this figure legend, the reader is referred to the web version of this article.)

Si = 0.89 at.% (Table 2) and an ideal Si to Fe^{3+} ratio of 0.75 for cronstedtite (i.e., $x = 0.8$ in the ideal formula $(Fe^{2+}_{3-x}Fe^{3+}_{x})(Si_{2-x}Fe^{3+}_{x})O_5(OH)_4$, where 0.8 is the maximum value for terrestrial cronstedtites reported in literature), then $Fe^{3+}/\Sigma Fe$ in tochilinite should be ~1.19%, much lower than STXM-XANES quantifications.

(iii) No other Fe^{3+}-bearing mineral has been detected in TEM investigations of tochilinite.

The presence of ferric iron in Paris tochilinite is surprising because thermodynamic calculations suggest that this phase formed under very reduced conditions (Browning and Bourcier, 1996). However, our STXM-XANES data imply formation under more oxidized conditions than previously thought and require further investigation to decipher the formation conditions of this mineral.

Considering the redox conditions, Paris' cronstedtites are characterized by the lowest Fe^{3+} content with respect to serpentines of CM chondrites with higher degrees of alteration (Fig. 9). At first sight, it appears that the oxidation state of CM chondrites increases with the extent of alteration (Fig. 9), the opposite of the trend reported in CR chondrites (Le Guillou et al., 2015). However, this possible trend is questionable, as (i) redox heterogeneities are also observed within any given CM chondrite and (ii) different techniques involving different scales of characterization were used to determine the $Fe^{3+}/\Sigma Fe$ ratios of the CM chondrites (i.e., XANES at the iron L-edge and EELS; Zega et al., 2003, 2006; Beck et al., 2012; Elmaleh et al., 2015).

Table 3
TEM-EDX data of cronstedtite (at.%) in type-II TCIs.

TCI precursor	O	Mg	Al	Si	Fe	Total
Olivine	62.75	8.09	0.42	7.37	21.38	100.01
	62.95	4.29	0.75	7.85	24.15	99.99
	63.92	4.19	2.25	10.08	19.56	100.00
	65.50	2.02	0.49	8.99	23.00	100.00
	65.92	3.90	0.89	8.52	20.75	99.98
	66.36	3.57	1.24	8.46	20.37	100.00
	66.07	4.41	1.30	9.36	18.86	100.00
	64.39	4.43	2.04	10.28	18.86	100.00
	65.22	2.43	0.95	9.53	21.87	100.00
	66.15	1.67	0.75	8.90	22.53	100.00
	67.40	2.98	1.08	7.95	20.59	100.00
	68.67	2.64	0.96	8.89	18.84	100.00
	66.78	2.99	0.81	9.49	19.93	100.00
	66.68	3.01	0.96	9.43	19.92	100.00
	64.47	3.50	1.21	10.59	20.23	100.00
	64.24	3.00	1.08	7.91	23.77	100.00
	68.78	2.48	0.97	7.16	20.61	100.00
Average	65.66	3.51	1.07	8.87	20.90	
σ	1.75	1.45	0.47	1.00	1.66	
Pyroxene	62.91	1.48	0.75	8.90	25.96	100.00
	63.74	2.71	0.64	8.59	24.32	100.00
	65.57	3.62	0.72	9.41	20.69	100.01
	66.53	3.73	0.81	9.39	19.54	100.00
	65.27	4.61	1.35	9.41	19.36	100.00
	66.55	2.97	0.96	8.59	20.94	100.01
	65.25	2.66	0.84	8.73	22.50	99.98
	66.36	2.05	0.76	8.60	22.23	100.00
	66.19	2.00	0.84	8.26	22.71	100.00
	64.27	2.93	1.12	9.27	22.41	100.00
	64.88	2.69	1.13	9.19	22.11	100.00
	65.05	2.25	1.07	8.94	22.69	100.00
	64.53	1.51	1.00	9.14	24.23	100.00
	66.52	1.27	0.99	8.56	22.66	100.00
	65.12	2.32	1.25	9.04	22.27	100.00
	64.52	7.88	1.65	9.88	16.05	99.98
	67.35	5.05	0.83	9.49	17.27	99.98
	62.25	3.04	0.92	7.30	26.50	99.99
	68.03	2.39	0.73	10.04	18.81	100.01
	69.65	1.27	0.96	9.61	18.21	99.70
	63.75	0	0.76	9.28	26.21	100.00
	68.23	4.34	1.33	9.38	16.72	100.00
Average	65.55	3.00	0.98	9.23	22.21	
σ	1.78	1.74	0.25	1.05	4.21	

In porous areas of type-II TCIs, cronstedtite coexists with goethite, whose presence might be considered controversial because it commonly forms during terrestrial weathering (Bland et al., 2006). However, our data support an extraterrestrial origin because goethite is found in the central zone of type-II TCIs, a zone that would be protected from terrestrial weathering. In addition, in type-I TCIs, goethite is surrounded by tochilinite and cronstedtite (Fig. 2A and B), minerals that are extremely rare on Earth. Hence, we suggest that the goethite formed from a ferrihydrite precursor after the oxidation of Fe^{2+} in solution and hydrolysis of Fe^{3+}. Ferrihydrite has been reported in Paris (Leroux et al., 2015) and is one of the first minerals formed under oxic aqueous conditions (Cudennec and Lecerf, 2006). Because ferrihydrite is metastable, it gradually

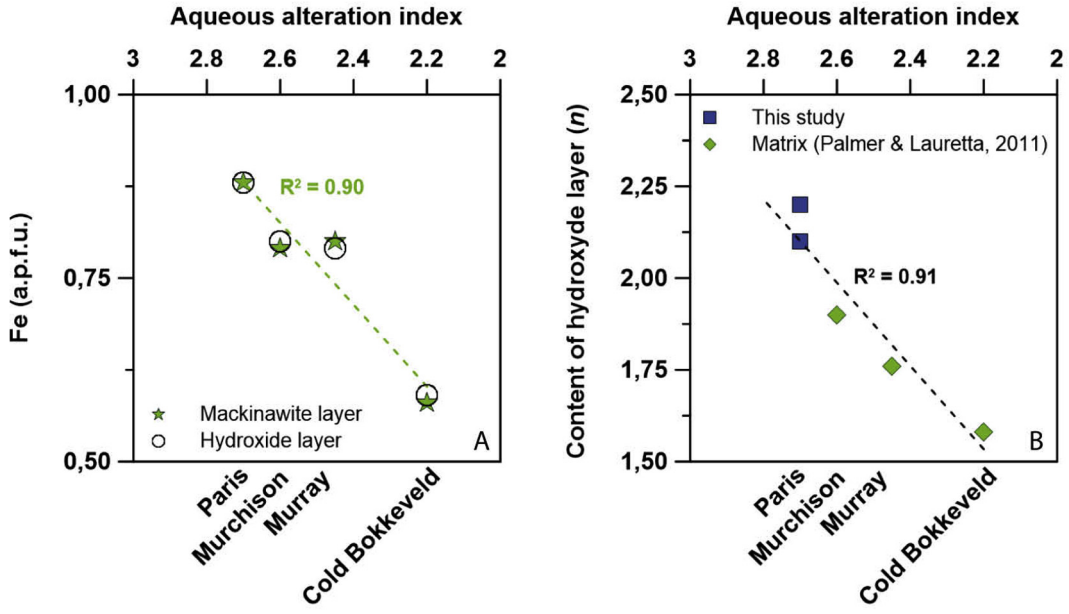

Fig. 8. (A) Fe content (a.p.f.u.) of tochilinite in TCIs in Paris compared to tochilinite in the matrix of Murchison, Murray, and Cold Bokkeveld (Palmer and Lauretta, 2011). (B) Hydroxide layer content (*n*) of meteoritic tochilinite (square = this study; diamond = Palmer and Lauretta, 2011).

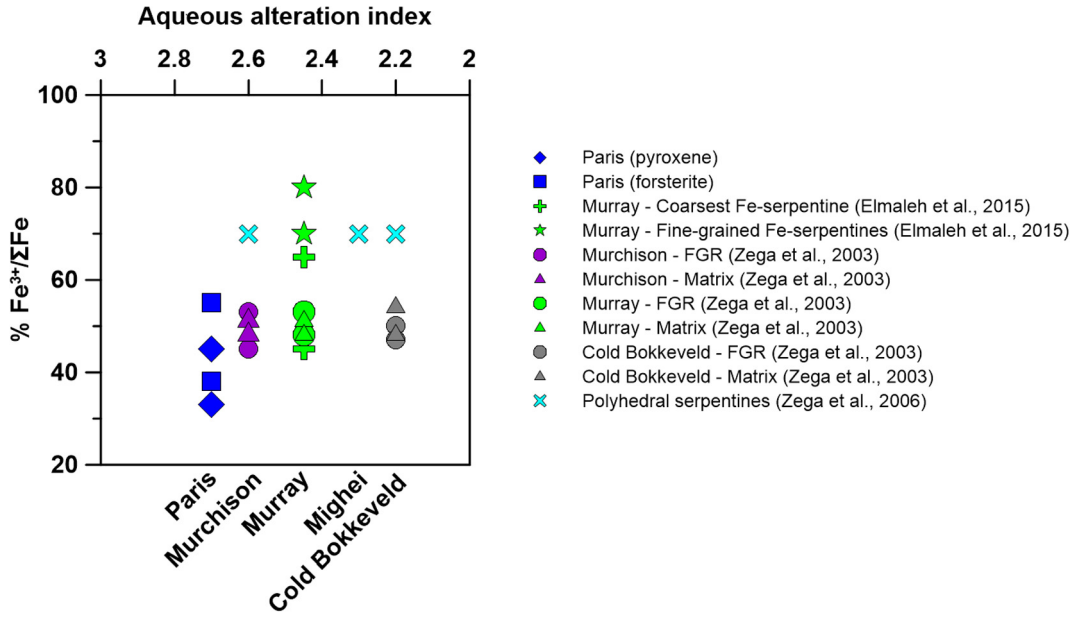

Fig. 9. Maximum and minimum $Fe^{3+}/\Sigma Fe$ values for: cronstedtite from TCIs in Paris (this study); cronstedtite and polyhedral serpentines from matrix and fine-grained rims (FGR) in Murchison, Murray, Cold Bokkeveld (Zega et al., 2003, 2006); and Fe-rich serpentine from altered CAI of Murray (Elmaleh et al., 2015).

converts to more crystalline and stable Fe^{3+}-bearing oxides and hydroxides (Das et al., 2011). This conversion is temperature- and pH-dependent and can occur by way of dissolution/precipitation mechanism or solid-state transformation (Cudennec and Lecerf, 2006; Liu et al., 2007; Das et al., 2011). Under neutral conditions, ferrihydrite converts to goethite under a narrow range of temperatures (i.e., 50–80 °C) that are compatible with the favorable conditions for cronstedtite crystallization. Both thermodynamic models and experimental results indicated that the maximum production of cronstedtite occurs at 70 °C (Pignatelli et al., 2013, 2014a; Zolotov, 2014). The ferrihydrite-goethite conversion can be enhanced by Fe^{2+} adsorption at the surface of ferrihydrite (Liu et al., 2007). Such a process could have

played a significant role in Paris as attested by (i) the occurrence of cronstedtite with goethite and (ii) the Fe^{2+} present in iron hydroxides (i.e., 20–30% according to STXM-XANES data; Fig. 6). Thermodynamic calculations indicate that the coexistence of ferrihydrite and cronstedtite increases the stability field of the latter in terms of fH_2 and $SiO_{2(aq)}$ activity (Zolotov, 2014). Interestingly, our observations show that the sizes of cronstedtite crystals increase from the outer edge of type-II TCIs toward the center, from layers in tochilinite/cronstedtite intergrowths giving way to micrometer euhedral crystals (Fig. 4B). This indicates that the conditions needed to crystallize cronstedtite becomes more favorable as the alteration proceeds, likely due to the decrease in temperature, which would favor the formation of 1*T* polytypes of cronstedtite as observed in Paris.

4.3. Alteration stages of Paris chondrite

On the basis of features of type-II TCIs, at least three stages of aqueous alteration can be distinguished for the Paris meteorite (Pignatelli et al., 2016). The first stage of alteration is characterized by the formation of tochilinite trough the interaction of olivine and pyroxene with a S-rich fluid ($T < 100$ °C; pH < 11.5). The second stage is marked by a change in fluid composition, which is enriched in Si and depleted in S, favoring the precipitation of cronstedtite ($50 < T < 80$ °C; pH = 7–8). The incorporation of silicon in this mineral reduces the Si concentration in the fluid, and iron hydroxides can form in the last alteration stage. However, the evolution of the fluid compositions occurs gradually, as indicated by tochilinite-cronstedtite intergrowths and the occurrence of hydroxides associated with cronstedtite.

Two steps of alteration have been identified for Murchison, the least altered CM chondrites after Paris (Lee and Lindgren, 2016). Although the nature of secondary minerals in Murchison reflects the fluctuations in fluid chemistry, it also appeared that the nature of the precursors played a significant role in establishing the alteration features. Murchison forsterite is first altered in cronstedtite (containing layers of tochilinite) and then in Mg-Fe serpentines, whereas clinoenstatite is replaced by tochilinite-rich veins and later by submicrometer-sized crystals of polyhedral serpentines (Lee and Lindgren, 2016). The higher degree of alteration experienced by Murchison might explain why the secondary minerals are richer in Mg than those observed in Paris, as well as why iron hydroxides are not formed.

4.4. Serpentinization and H_2 release

The presence of cronstedtite crystals indicates that serpentinization of anhydrous minerals, such as olivine and pyroxene, occurred in the Paris chondrite. During serpentinization reactions, oxidation of Fe^{2+} to Fe^{3+} is accompanied by the reduction of hydrogen in the water and the subsequent release of H_2 (Marcaillou et al., 2011). Iron oxidation and partition in secondary minerals is affected by the serpentinization conditions, such as the temperature, water/rock ratio, activity of Si, and the nature of precursor phases (Klein et al., 2009, 2013; Marcaillou, 2011). Serpentinization of olivine in terrestrial environments (Neubeck et al., 2014) leads to the formation of magnetite with serpentine according to the following reaction:

$$\text{olivine} + H_2O \rightarrow \text{serpentine} + \text{brucite} + \text{magnetite} + H_2 \quad (5)$$

The absence of magnetite in the alteration products of the Paris chondrite is consistent with recent observations of CR chondrites (Le Guillou et al., 2015). This might be linked to the lower temperature of the alteration experienced by chondrites compared to terrestrial settings (Seyfried et al., 2007; Klein et al., 2009). The composition of the alteration fluids could have also inhibited the formation of magnetite. For instance, olivine serpentinization by carbonate-rich fluids induces an alternative route for Fe oxidation and H_2 release without production of magnetite (Neubeck et al., 2014). In addition, kinetic factors might also have played a role, with the fast oxidation of Fe^{2+} inducing a high Fe^{3+} content that would favor the formation of Fe^{3+}-bearing secondary minerals, such as ferrihydrite or goethite, instead of magnetite.

During the serpentinization of dunite, the $Fe^{3+}/\Sigma Fe$ is mainly controlled by the water/rock ratio (defined hereafter as *w: r*), an increase from 1 to 100 in this ratio leading to an increase from 30% to 75% in the $Fe^{3+}/\Sigma Fe$. The estimated $Fe^{3+}/\Sigma Fe$ ratio of the Paris cronstedtite, in the range 33–60%, thus suggests a moderate to high *w: r* ratio (i.e., 50–100). A high *w: r* ratio has similarly been proposed on the basis of high $Fe^{3+}/\Sigma Fe$ ratios (i.e., 50–70%) of hydrated amorphous silicates in CR chondrites (Le Guillou et al., 2015). However, such elevated ratios appear unlikely, as it would induce fluid circulation and mass transfer that are rarely observed in CM and CR chondrites (Brearley, 2006). In addition, thermodynamic calculations (Zolotov, 2014, 2015) point toward significantly lower values with *w: r* ratio < 1. Similar results are inferred from O-isotope mass balance for CM and CR (Clayton and Mayeda, 1999; Brearley, 2006). Such discrepancies could result from local fluid enrichments within geochemical microenvironments, independent on the *w: r* ratios in the system (Zolotov, 2014). Another possibility might be linked to the loss of H_2 that would generate more oxidizing conditions (Le Guillou et al., 2015). It worth mentioning that more oxidizing conditions can also result from the production of O_2 and H_2O_2 through radiolysis of water (Zolotov, 2013). The reaction between H_2O_2 and Fe^{2+} will produce very reactive (and strong oxidant) hydroxyl radicals by way of Fenton's reaction, which could explain why the insoluble organic matter is oxidized in chondrites' matrix (Cody and Alexander, 2005).

The H_2 release can be estimated for the least altered CM chondrite Paris using the $Fe^{3+}/\Sigma Fe$ quantification obtained with STXM-XANES (Eq. (6) and (7)). Based on experimental geochemical kinetics, textural observations and mineral modal-abundance in CM chondrites, it has been proposed that replacement of olivine by serpentine follow the reaction 5olivine → 2serpentine (Velbel, 2014). Consequently, the reaction for olivine in Paris could be written as follows (modified after Pignatelli et al., 2016):

$$2.5(Mg_{1.85}Fe_{0.15})SiO_4[\text{Forsterite}] + 2.625Fe^{2+}_{(aq)} + 2.72H_2O + 0.15Al^{3+}_{(aq)} \rightarrow (Fe^{2+}{}_{1.56}Fe^{3+}{}_{0.87}Mg_{0.50})(Si_{1.27}Fe^{3+}{}_{0.57}Al_{0.15})O_5(OH)_4 \times [\text{Cronstedtite}] + 3.495Mg^{2+}_{(aq)} + 1.23SiO_{2(aq)} + 0.63MgO_{(aq)} + 0.72H_2 \quad (6)$$

According to the STXM-XANES data, the isovolumetric reaction describing the serpentine formation from pyroxene in Paris could be written as (modified after Pignatelli et al., 2016):

$$1.8(Mg_{1.8}Fe_{0.2})SiO_2O_6[\text{pyroxene}] + 2.81Fe^{2+}_{(aq)} + 2.58H_2O + 0.14Al^{3+}_{(aq)} \rightarrow (Fe^{2+}{}_{2.01}Fe^{3+}{}_{0.61}Mg_{0.43})(Si_{1.31}Fe^{3+}{}_{0.55}Al_{0.14})O_5(OH)_4 \times [\text{Cronstedtite}] + 2.81Mg^{2+}_{(aq)} + 1.10Si^{4+}_{(aq)} + 2.19SiO_{2(aq)} + 0.58H_2 \quad (7)$$

The higher amount of H_2 production in Eq. (6) is related to the higher Fe^{3+} in cronstedtite crystals formed from olivine. This could be due to the faster dissolution of olivines relative to pyroxenes (Seyfried et al., 2007), which would release more Fe^{2+} that would rapidly oxidize into Fe^{3+} and would favor Fe^{3+} incorporation in cronstedtite. Moreover, the dissolution rate of forsterite in Paris is likely affected (increased) by the presence of subgrains and dislocations visible on TEM images (Fig. 4). That is not always the case for CM chondrite, for instance in Murchison the serpentinization of forsterite seems not to be controlled or influenced by defects (Lee and Lindgren, 2016).

Eqs. (6) and (7) also indicated that serpentinization in Paris requires iron mobility as well as the decrease of the Mg and Si, in agreement with the observations reported by Velbel et al. (2015) for a more altered CM chondrite (QUE 93005) and terrestrial pseudomorphism of pyroxene (Velbel and Barker, 2008). The iron source could be linked to the alteration of Fe-Ni metal beads, iron sulfides and Fe-rich amorphous silicates dispersed throughout the matrix (Leroux et al., 2015; Velbel et al., 2015; Pignatelli et al., 2016). Mg and Si released in solution could be taken up by surrounding phases including the matrix (Velbel et al., 2015) or be removed by the fluid itself (Pignatelli et al., 2016).

Considering the very low Al content of Paris cronstedtite, it does not require significant Al mobility but it can be provided *in situ* by the dissolution of pyroxene or amorphous silicates, the latter representing the main constituent of the unaltered CM matrices (Le Guillou et al., 2015; Leroux et al., 2015). This is supported by the fact that: (i) Paris present enstatite with Al $\leq$ 0.35 at.% and diopside with Al $\leq$ 4.88 at.% and (ii) the alteration of Paris amorphous silicate grains produces serpentines with higher Al content than cronstedtite (Leroux et al., 2015).

The role played by the amorphous silicates in the alteration of carbonaceous chondrites cannot be neglected because they (i) are systematically mixed with nanometer-sized phyllosilicates, and (ii) show systematic oxidation with $Fe^{3+}/\Sigma Fe$ in the range 50–70% (Brearley and Le Guillou, 2015; Le Guillou et al., 2015). Our study reveals that CM secondary minerals that formed from the alteration of Fe-Ni metal beads or pseudomorphism of anhydrous silicates are also systematically enriched in Fe^{3+}. Taken together, this demonstrates that both CR and CM chondrites experienced early hydration and oxidation after the accretion of their respective parent bodies. This is also confirmed by the studies concerning the organic compounds present in the matrix of chondrites whose chemical variations are consistent with oxidation during aqueous alteration at low temperature (Cody and Alexander, 2005; Alexander et al., 2010; Herd et al., 2011). It follows that the process(es) controlling the redox state of secondary mineral assemblages are similar in CM and CR parent bodies, despite the different alteration conditions. Our results confirm that H_2 release during serpentinization is a plausible mechanism for explaining the oxidized nature of secondary mineral assemblages observed in altered chondrites.

5. CONCLUSION

This study has provided a detailed nanoscale description of secondary minerals of TCIs in the Paris chondrite, the least altered CM chondrite known so far. Thanks to a combination of several techniques (TEM, STXM-XANES and EDT), we were able to carry out a rapid screening of the nanocrystalline phases and determine their redox state. The main results can be summarized as follows:

1. Type-II TCIs that formed from the pseudomorphism of anhydrous silicates (i.e., olivine and pyroxene) present complex compositional zoning composed of three different Fe-bearing phases, from the outside inwards: tochilinite, cronstedtite and goethite.
2. Cronstedtite *sensu stricto* is identified and well characterized for the first time in a CM2 chondrite, while the others generally contain solid solutions of the serpentine-group minerals.
3. Though the presence of goethite might be controversial, EDT data clearly confirm the presence of this mineral at the center of type-II TCIs. In addition, goethite is surrounded by tochilinite and cronstedtite, minerals that are extremely rare on Earth. The formation of goethite is formed from a ferrihydrite precursor after the oxidation of Fe^{2+} in solution and hydrolysis of Fe^{3+}.
4. The tochilinite in Paris is characterized by high hydroxide layer content ($n = 2.1$–2.2) regardless of the silicate precursors. When combined with data from other CMs, it appears that the iron and hydroxide layer contents of tochilinites are direct proxies for the degree of alteration experienced by these chondrites.
5. The $Fe^{3+}/\Sigma Fe$ ratios of TCIs are high, with values of $\leq$15% in tochilinite, 35–60% in cronstedtite and 70–80% in hydroxides. These observations suggest that the alteration of CM chondrites took place under oxidizing conditions that could have been induced by (i) local fluid enrichment relative to the whole rock and/or (ii) by significant H_2 release during serpentinization processes.
6. We suggest that the formation of tochilinite and cronstedtite intergrowths occurred at a temperature lower than 100 °C, in a narrow pH range of 7–8 and under a high

water/rock ratio. A decrease of the sulfur activity could have prevented the formation of tochilinite and allowed the coexistence of cronstedtite and ferrihydrite, whose conversion into more stable goethite was favored by the availability of Fe^{2+} Both ferrihydrite-goethite conversion and cronstedtite formation are likely promoted by a temperature decrease during the course of alteration, in the range of 50–80 °C.

7. Our results suggest that the process(es) controlling the redox state of secondary mineral assemblages are quite similar in CM and CR parent bodies, despite the different alteration conditions.

ACKNOWLEDGMENTS

This work was funded by l'Agence Nationale de la Recherche through grant ANR-14-CE33-0002-01 SAPINS (PI Yves Marrocchi). We acknowledge Italian project FIRB2013 – Exploring the Nanoworld. We are grateful to the Paul Scherrer Institute Swiss Light Source, and especially to Benjamin Watts (PolLux beamline). We thanked Michael Velbel and two anonymous reviewers for constructive comments and Associate Editor Alexander Krot for careful editing. This is CRPG contribution #2501 and SAPINS contribution #09.

REFERENCES

Alexander C. M. O. D., Newsome S. D., Fogel M. L., Nittler L. R., Busemann H. and Cody G. D. (2010) Deuterium enrichments in chondritic macromolecular material – implications for the origin and evolution of organics, water and asteroids. *Geochim. Cosmochim. Acta* **74**, 4417–4437.

Anders E. (1964) Origin, age, and composition of meteorites. *Space Sci. Rev.* **3**, 583–714.

Bailey S. W. (1988) Odinite, a new dioctahedral-trioctahedral Fe^{3+}-rich 1:1 clay mineral. *Clay Mineral.* **23**, 237–247.

Beck P., De Andrade V., Orthous-Daunay F.-R., Veronesi G., Cotte M., Quirico E. and Schmitt B. (2012) The redox state of iron in the matrix of CI, CM and metamorphosed CM chondrites by XANES spectroscopy. *Geochim. Cosmochim. Acta* **99**, 305–316.

Bland P. A., Zolensky M. E., Benedix G. K. and Sephton M. A. (2006) Weathering of chondritic meteorites. In *Meteorites and the Early Solar System II*, pp. 853–867. Available at: <http://adsabs.harvard.edu/abs/2006mess.book..853B>.

Bourdelle F., Benzerara K., Beyssac O., Cosmidis J., Neuville D. R., Brown G. E. and Paineau E. (2013) Quantification of the ferric/ferrous iron ratio in silicates by scanning transmission X-ray microscopy at the Fe $L_{2,3}$ edges. *Contrib. Mineral. Petrol.* **166**, 423–434.

Bourot-Denise M., Zanda B., Marrocchi Y., Greenwood R. C., Pont S., Hewins R. H., Franchi I. A. and Cornen G. (2010) Paris: the slightly altered, slightly metamorphosed CM that bridges the gap between CMs and COs. *Lunar Planet. Sci.* **XLI**. Abstract No. 1683.

Brearley A. J. (2006) The action of water. In *Meteorites and the Early Solar System II*, pp. 584–624. Available at: <http://adsabs.harvard.edu/abs/2006mess.book..584B>.

Brearley A. J. and Le Guillou C. (2015) More evidence of the importance of amorphous silicates in CM carbonaceous chondrites: new observations from a fine-grained rim in the CM2 chondrite, TIL 91722. In *78th Annual Meeting of the Meteoritical Society*, p. 5192.

Brindley G. W. (1982) Chemical compositions of berthierines – a review. *Clays Clay Miner.* **30**, 153–155.

Browning L. B., McSween H. Y. and Zolensky M. E. (1996) Correlated alteration effects in CM carbonaceous chondrites. *Geochim. Cosmochim. Acta* **60**, 2621–2633.

Browning L. B. and Bourcier W. L. (1996) Tochilinite: A sensitive indicator of alteration conditions on the CM asteroidal parent body. In *44th Lunar and Planetary Science Conference*, pp. 171–172.

Clayton R. N. and Mayeda T. K. (1999) Oxygen isotope studies of carbonaceous chondrites. *Geochim. Cosmochim. Acta* **63**, 2089–2104.

Cody G. D. and Alexander C. M. O. D. (2005) NMR studies of chemical structural variation of insoluble organic matter from different carbonaceous chondrite groups. *Geochim. Cosmochim. Acta* **69**, 1085–1097.

Cudennec Y. and Lecerf A. (2006) The transformation of ferrihydrite into goethite or hematite, revisited. *J. Solid State Chem.* **179**, 716–722.

Das S., Hendry M. J. and Essilfie-Dughan J. (2011) Transformation of two-line ferrihydrite to goethite and hematite as a function of pH and temperature. *Environ. Sci. Technol.* **45**, 268–275.

Elmaleh A., Bourdelle F., Caste F., Benzerara K., Leroux H. and Devouard B. (2015) Formation and transformations of Fe-rich serpentines by asteroidal aqueous alteration processes: a nanoscale study of the Murray chondrite. *Geochim. Cosmochim. Acta* **158**, 162–178.

Frondel C. (1962) Polytypism in cronstedtite. *Am. Miner.* **47**, 781–783.

Geiger C. A., Henry D. L., Bailey S. W. and Maj J. J. (1983) Crystal structure of cronstedtite-$2H_2$. *Clays Clay Miner.* **31**, 97–108.

Gooding J. L. and Zolensky M. E. (1987) Thermal stability of tochilinite. In *Lunar and Planetary Science Conference*, XVIII, pp. 343–344. Lunar and Planetary Science Conference.

Gubaidulina T. V., Chistyakova N. I. and Rusakov V. S. (2007) Mössbauer study of layered iron hydroxysulfides: tochilinite and valleriite. *Bull. Russ. Acad. Sci. Phys.* **71**, 1269–1272.

Guggenheim S., Bailey S. W., Eggleton R. A. and Wilkes P. (1982) Structural aspects of greenalite and related minerals. *Can. Mineral.* **20**, 1–18.

Hanowski N. P. and Brearley A. J. (2001) Aqueous alteration of chondrules in the CM carbonaceous chondrite, Allan Hills 81002: implications for parent body alteration. *Geochim. Cosmochim. Acta* **65**, 495–518.

Heaney P. J., Vicenzi E. P., Giannuzzi L. A. and Livi J. T. (2001) Focused ion beam milling: a method of site-specific sample extraction for microanalysis of earth and planetary materials. *Am. Miner.* **86**, 1094–1099.

Herd C. D. K., Blinova A., Simkus D. N., Huang Y., Tazoro R., Alexander C. M. O. D., Gyngard F., Nittler L. R., Cody G. D., Fogel M. L., Kebukawa Y., Kilcoyne L. D., Hilts R. W., Slater G. F., Glavin D. P., Dworkin J. P., Callahan M. P., Elsila J. E., De Gregorio B. T. and Stroud R. M. (2011) Origin and evolution of prebiotic organic matter as inferred from the Tagish Lake Meteorite. *Science* **332**, 1304–1307.

Hewins R. H., Bourot-Denise M., Zanda B., Leroux H., Barrat J.-A., Humayun M., Göpel C., Greenwood R. C., Franchi I. A., Pont S., Lorand J.-P., Cournède C., Gattacceca J., Rochette P., Kuga M., Marrocchi Y. and Marty B. (2014) The Paris meteorite, the least altered CM chondrite so far. *Geochim. Cosmochim. Acta* **124**, 190–222.

Hewins R. H., Connolly H. C., Lofgren, Jr., G. E. and Libourel G. (2005) Experimental constraints on chondrule formation. In *Chondrites and the Protoplanetary Disk*, p. 286. Available at: <http://adsabs.harvard.edu/abs/2005ASPC..341..286H>.

Hezel D. C. and Palme H. (2010) The chemical relationship between chondrules and matrix and the chondrule matrix complementarity. *Earth Planet. Sci. Lett.* **294**, 85–93.

Hitchcock A. P. (2012) *AXis 2000 Analysis of X-ray Images and Spectra*. McMaster University, Hamilton, ON, Canada.

Hybler J., Petříček V., Ďurovič S. and Smrčok Ľ. (2000) Refinement of the crystal structure of cronstedtite-1*T*. *Clays Clay Miner.* **48**, 331–338.

Hybler J., Petříček V., Fábry J. and Durovič S. (2002) Refinement of the crystal structure of cronstedtite-2H_2. *Clays Clay Miner.* **50**, 601–613.

Jambor J. L. (1976) New occurrence of the hybrid sulphide tochilinite. *Bull. Geol. Surv. Can.* **65**, 65–69, Paper 76–1B.

Johan Z. (1990) Chromian valleriite and associated minerals from the Ransko mafic-ultramafic complex, Czechoslovakia. *Neues Jahrb. Mineral. Monatsh.* **6**, 269–279.

Kakos G. A., Turney T. W. and Williams T. B. (1994) Synthesis and structure of tochilinite: a layered metal hydroxide/sulfide composite. *J. Solid State Chem.* **108**, 102–111.

Klein F., Bach W., Jöns N., McCollom T., Moskowitz B. and Berquó T. (2009) Iron partitioning and hydrogen generation during serpentinization of abyssal peridotites from 15°N on the Mid-Atlantic Ridge. *Geochim. Cosmochim. Acta* **73**, 6868–6893.

Klein F., Bach W. and McCollom T. M. (2013) Compositional controls on hydrogen generation during serpentinization of ultramafic rocks. *Lithos* **178**, 55–69.

Kolb U., Gorelik T. and Otten M. T. (2008) Towards automated diffraction tomography. Part II-Cell parameter determination. *Ultramicroscopy* **108**, 763–772.

Kolb U., Gorelik T., Kübel C., Otten M. T. and Hubert D. (2007) Towards automated diffraction tomography: Part I-Data acquisition. *Ultramicroscopy* **107**, 507–513.

Kozerenko S. V., Fadeev V. V., Organova N. I., Chstyakova N. I., Kolpakova N. N. and Senin V. G. (2001) Synthesis, formation conditions and crystallochemistry of tochilinites – iron, magnesium and sodium hydroxide-sulfides. *Exp. Geosci.* **10**, 57–58.

Kozerenko S. V., Organova N. J., Fadeev V. V., Magazina L. O., Kolpakova N. N. and Kopneva L. A. (1996) Tochilinite produced in laboratory. In *Lunar and Planetary Science Conference*, XXVII, pp. 695–696. Lunar and Planetary Science Conference.

Krot A. N., Hutcheon I. D., Brearley A. J., Pravdivtseva O. V., Petaev M. I. and Hohenberg C. M. (2006) Timescales and setting for alteration of chondritic meteorites. In *Meteorites and Early Solar System* (eds. D. S. Lauretta and H. Y. McSween). Arizona University Press, pp. 525–553.

Krot A. N., Hutcheon I. D., Yurimoto H., Cuzzi J. N., McKeegan K. D., Scott E. R. D., Libourel G., Chaussidon M., Aléon J. and Petaev M. I. (2005) Evolution of oxygen isotopic composition in the inner solar nebula. *Astrophys. J.* **622**, 1333.

Le Guillou C., Bernard S., Brearley A. J. and Remusat L. (2014) Evolution of organic matter in Orgueil, Murchison and Renazzo during parent body aqueous alteration: In situ investigations. *Geochim. Cosmochim. Acta* **131**, 368–392.

Le Guillou C., Changela H. G. and Brearley A. J. (2015) Widespread oxidized and hydrated amorphous silicates in CR chondrites matrices: Implications for alteration conditions and H_2 degassing of asteroids. *Earth Planet. Sci. Lett.* **420**, 162–173.

Lee M. R. and Lindgren P. (2016) Aqueous alteration of chondrules from the Murchison CM carbonaceous chondrite: Replacement, pore filling, and the genesis of polyhedral serpentine. *Meteorit. Planet. Sci.* **51**, 1003–1021.

Leroux H., Cuvillier P., Zanda B. and Hewins R. H. (2015) GEMS-like material in the matrix of the Paris meteorite and the early stages of alteration of CM chondrites. *Geochim. Cosmochim. Acta* **170**, 247–265.

Liu H., Li P., Zhu M., Wei Y. and Sun Y. (2007) Fe(II)-induced transformation from ferrihydrite to lepidocrocite and goethite. *J. Solid State Chem.* **180**, 2121–2128.

Mackinnon I. D. R. and Zolensky M. E. (1984) Proposed structures for poorly characterized phases in C2M carbonaceous chondrite meteorites. *Nature* **309**, 240–242.

Makovicky E. and Hyde B. G. (1981) Non-commensurate (misfit) layer structures. In *Inorganic Chemistry Structure and Bonding*. Springer, Berlin, Heidelberg, pp. 101–170. Available at: <http://link.springer.com/chapter/10.1007/3-540-10655-3_3>.

Marcaillou C. (2011) *Serpentinisation et production d'hydrogène en context de dorsale lente: approche expérimentale et numérique* (Ph.D. thesis). Université de Grenoble.

Marcaillou C., Muñoz M., Vidal O., Parra T. and Harfouche M. (2011) Mineralogical evidence for H2 degassing during serpentinization at 300 °C/300 bar. *Earth Planet. Sci. Lett.* **303**, 281–290.

Marrocchi Y. and Libourel G. (2013) Sulfur and sulfides in chondrules. *Geochim. Cosmochim. Acta* **119**, 117–136.

Marrocchi Y., Chaussidon M., Piani L. and Libourel G. (2016) Early scattering of the solar protoplanetary disk recorded in meteoritic chondrules. *Sci. Adv.* **2**, e1601001.

Marrocchi Y., Gounelle M., Blanchard I., Caste F. and Kearsley A. T. (2014) The Paris CM chondrite: secondary minerals and asteroidal processing. *Meteorit. Planet. Sci.* **49**, 1232–1249.

McAlister J. A. and Kettler R. M. (2008) Metastable equilibria among dicarboxylic acids and the oxidation state during aqueous alteration on the CM2 chondrite parent body. *Geochim. Cosmochim. Acta* **72**, 233–241.

Meibom A., Desch S. J., Krot A. N., Cuzzi J. N., Petaev M. I., Wilson L. and Keil K. (2000) Large-scale thermal events in the solar nebula: evidence from Fe, Ni metal grains in primitive meteorites. *Science* **288**, 839–841.

Metzler K., Bischoff A. and Stoeffler D. (1992) Accretionary dust mantles in CM chondrites – evidence for solar nebula processes. *Geochim. Cosmochim. Acta* **56**, 2873–2897.

Mugnaioli E. (2015) Single nano crystal analysis using automated electron diffraction tomography. *Rendiconti Lincei* **26**, 211–223.

Mugnaioli E., Gorelik T. and Kolb U. (2009) "Ab initio" structure solution from electron diffraction data obtained by a combination of automated diffraction tomography and precession technique. *Ultramicroscopy* **109**, 758–765.

Müller W. F., Kurat G. and Kracher A. (1979) Chemical and crystallographic study of cronstedtite in the matrix of the Cochabamba (CM2) carbonaceous chondrite. *Tschermaks Mineral. Petrogr. Mitteilungen* **26**, 293–304.

Neubeck A., Duc N. T., Hellevang H., Oze C., Bastviken D., Bacsik Z. and Holm N. G. (2014) Olivine alteration and H_2 production in carbonate-rich, low temperature aqueous environments. *Planet. Space Sci.* **96**, 51–61.

Organova N. I., Drits V. A. and Dmitrik A. L. (1973) Structural study of tochilinite. Part I. The isometric variety. *Sov. Phys. – Crystallogr.* **17**, 667–671.

Palmer E. E. and Lauretta D. S. (2011) Aqueous alteration of kamacite in CM chondrites. *Meteorit. Planet. Sci.* **46**, 1587–1607.

Palme H., Hezel D. C. and Ebel D. S. (2015) The origin of chondrules: constraints from matrix composition and matrix-chonsrule complementarity. *Earth Planet. Sci. Lett.* **411**, 11–19.

Pignatelli I., Marrocchi Y., Vacher L. G., Delon R. and Gounelle M. (2016) Multiple precursors of secondary mineralogical

assemblages in CM chondrites. *Meteorit. Planet. Sci.* **51**, 785–805.

Pignatelli I., Mugnaioli E., Hybler J., Mosser-Ruck R., Cathelineau M. and Michau N. (2013) A multi-technique characterization of cronstedtite synthesized by iron-clay interaction in a step-by-step cooling procedure. *Clays Clay Miner.* **61**, 277–289.

Pignatelli I., Bourdelle F., Bartier D., Mosser-Ruck R., Truche L., Mugnaioli E. and Michau N. (2014a) Iron-clay interactions: detailed study of the mineralogical transformation of claystone with emphasis on the formation of iron-rich T-O phyllosilicates in a step-by-step cooling experiment from 90 °C to 40 °C. *Chem. Geol.* **387**, 1–11.

Pignatelli I., Mugnaioli E., Mosser-Ruck R., Barres O., Kolb U. and Michau N. (2014b) A multi-technique, micrometer- to atomic-scale description of a synthetic analogue of chukanovite, $Fe_2(CO_3)(OH)_2$. *Eur. J. Mineral.* **26**, 221–229.

Pignatelli I., Vacher L. G. and Marrocchi Y. (2015) Comment on "Hydrothermal preparation of analogous matrix minerals of CM carbonaceous chondrites from metal alloy particles" by Peng Y. and Jing Y. [Earth Planet. Sci. Lett. 408 (2014) 252–262]. *Earth Planet. Sci. Lett.* **428**, 304–306.

Putnis A., Geisler T., Schmid-Beurmann P., Stephan T. and Giampaolo C. (2007) An experimental study of the replacement of leucite by analcime. *Am. Miner.* **92**, 19–26.

Putnis C. V., Tsukamoto K. and Nishimura Y. (2015) Letter. Direct observations of pseudomorphism: compositional and textural evolution at a fluid- solid interface. *Am. Miner.* **90**, 1909–1912.

Raabe J., Tzvetkov G., Flechsig U., Böge M., Jaggi A., Sarafimov B., Vernooij M. G. C., Huthwelker T., Ade H., Kilcoyne D., Tyliszczak T., Fink R. H. and Quitmann C. (2008) PolLux: A new facility for soft x-ray spectromicroscopy at the Swiss Light Source. *Rev. Sci. Instrum.* **79**, 113704.

Rubin A. E. (2015) An American on Paris: extent of aqueous alteration of a CM chondrite and the petrography of its refractory and amoeboid olivine inclusions. *Meteorit. Planet. Sci.* **50**, 1595–1612.

Rubin A. E., Trigo-Rodríguez J. M., Huber H. and Wasson J. T. (2007) Progressive aqueous alteration of CM carbonaceous chondrites. *Geochim. Cosmochim. Acta* **71**, 2361–2382.

Schulte M. and Shock E. (2004) Coupled organic synthesis and mineral alteration on meteorite parent bodies. *Meteorit. Planet. Sci.* **39**, 1577–1590.

Scott E. R. D. and Krot A. N. (2014) Chondrites and their components. In *Meteorites and Cosmochemical Processes*, pp. 65–137.

Seyfried, Jr., W. E., Foustoukos D. I. and Fu Q. (2007) Redox evolution and mass transfer during serpentinization: An experimental and theoretical study at 200 °C, 500 bar with implications for ultramafic-hosted hydrothermal systems at Mid-Ocean Ridges. *Geochim. Cosmochim. Acta* **71**, 3872–3886.

Smrčok L., Durovic S., Petricek V. and Weiss Z. (1994) Refinement of the crystal structure of cronstedtite-3T. *Clays Clay Miner.* **42**, 544–551.

Tomeoka K. and Buseck P. R. (1985) Indicators of aqueous alteration in CM carbonaceous chondrites: microtextures of a layered mineral containing Fe, S, O and Ni. *Geochim. Cosmochim. Acta* **49**, 2149–2163.

Vacher L. G., Marrocchi Y., Verdier-Paoletti M. J., Villeneuve J. and Gounelle M. (2016) Inward radial mixing of interstellar water ices in the solar protoplanetary disk. *Astrophys. J. Lett.* **827**, L1.

Velbel M. A. (2014) Stoichiometric reactions describing serpentinization of anhydrous primary silicates: a critical appraisal, with application to aqueous alteration of chondrule silicates in CM carbonaceous chondrites. *Clays Clay Miner.* **62**, 126–136.

Velbel M. A. and Barker W. W. (2008) Pyroxene weatherinf to smectite: conventional and low-voltage cryo-fiel emission scanning electron microscopy, Koua Bocca ultramafic complex, Ivory Coast. *Clays Clay Miner.* **56**, 111–126.

Velbel M. A., Tonui E. K. and Zolensky M. E. (2012) Replacement of olivine by serpentine in the carbonaceous chondrite Nogoya (CM2). *Geochim. Cosmochim. Acta* **87**, 117–135.

Velbel M. A., Tonui E. K. and Zolensky M. E. (2015) Replacement of olivine by serpentine in the Queen Alexandra Range 93005 carbonaceous chondrite (CM2): reactant-product compositional relations, and isovolumetric constraints on reaction stoichiometry and elemental mobility during aqueous alteration. *Geochim. Cosmochim. Acta* **148**, 402–425.

Verdier-Paoletti M., Marrocchi Y., AVice G., Roskosz M., Gureko A. and Gounelle M. (2017) Oxygen isotope constraints on the alteration temperatures of CM chondrites. *Earth Planet. Sci. Lett.* **458**, 273–281.

Vincent R. and Midgley P. A. (1994) Double conical beam-rocking system for measurement of integrated electron diffraction intensities. *Ultramicroscopy* **53**, 271–282.

Vollmer C., Barth M., Le Guillou C., Leitner J., Ramasse Q., Horstmann M. and Bischoff A. (2014) The onset of aqueous alteration in CM chondrites – FIB-TEM-ultraSTEM-STXM investigations of the pristine chondrite Maribo. In *45th Lunar and Planetary Sci. Conference. Abstr. # 1354*.

Zega T. J. and Buseck P. R. (2003) Fine-grained-rim mineralogy of the Cold Bokkeveld CM chondrite. *Geochim. Cosmochim. Acta* **67**, 1711–1721.

Zega T. J., Garvie L. A. J. and Buseck P. R. (2003) Nanometer-scale measurements of iron oxidation states of cronstedtite from primitive meteorites. *Am. Miner.* **88**, 1169–1172.

Zega T. J., Garvie L. A. J., Dódony I., Friedrich H., Stroud R. M. and Buseck P. R. (2006) Polyhedral serpentine grains in CM chondrites. *Meteorit. Planet. Sci.* **41**, 681–688.

Zolensky M. E. (1984) Hydrothermal alteration of CM carbonaceous chondrites; implications of the identification of tochilinite as one type of meteoritic PCP. In *47th Annual Meeting of the Meteoritical Society*, p. 19. Available at: <http://adsabs.harvard.edu/abs/1984LPICo.537E..19Z>.

Zolensky M. E. and Mackinnon I. D. R. (1986) Microstructures of cylindrical tochilinites. *Am. Miner.* **71**, 1201–1209.

Zolensky M. E., Bodnar R. J., Gibson E. K. J., Niyquist L. E., Resse Y., Shih C. Y. and Wiesman H. (1999) Asteroidal water within fluid inclusion-bearing halite in an H5 chondrite, Monahans. *Science* **285**, 1377–1379.

Zolensky M. E., Mittlefehldt D. W., Lipschutz M. E., Wang M.-S., Clayton R. N., Mayeda T. K., Grady M. M., Pillinger C. and David B. (1997) CM chondrites exhibit the complete petrologic range from type 2 to 1. *Geochim. Cosmochim. Acta* **61**, 5099–5115.

Zolotov M. Y. (2013) Strong oxidant are needed to form sulfates in CM chondrites. In *76th Annual Meteoritical Society Meeting. Abstr. # 5334*.

Zolotov M. Y. (2014) Formation of brucite and cronstedtite-bearing mineral assemblages on Ceres. *Icarus* **228**, 13–26.

Zolotov M. Y. (2015) Microchemical environments of aqueous alteration in CR chondrites: chemical equilibrium models. In *45th Lunar and Planetary Science Conference. Abstr. # 1470*.

Associate editor: Alexander N. Krot

The Texture and Chemical Composition of Trapiche Ruby from Khoan Thong, Luc Yen Mining District, Northern Vietnam

Isabella Pignatelli, Gaston Giuliani, Christophe Morlot and Pham Van Long

ABSTRACT: The trapiche texture and chemical composition of two rubies from the Khoan Thong placer in northern Vietnam were examined by X-ray computed tomography, scanning electron microscopy and electron microprobe analysis. Their texture is similar to that of some Burmese trapiche rubies, with inclusion-rich sector boundaries intersecting at a small central point and a significant concentration of elongated tube-like voids in growth sectors. The most common inclusions are anorthite and margarite; the latter formed by destabilisation of both ruby and anorthite during retrograde metamorphism. The chemical composition of the samples plots in the field of Vietnamese alluvial and primary marble-hosted deposits, although differences in Fe_2O_3, TiO_2 and Cr_2O_3 contents may distinguish trapiche rubies from various mining areas in Vietnam. Their composition differs from that of Burmese trapiche rubies by a higher Fe_2O_3/TiO_2 ratio and a lower Cr_2O_3 content. Vietnamese trapiche rubies formed in the same geological environment as non-trapiche ones, under metamorphic conditions prevailing for the Himalayan orogenesis. In this geological context, localised fluid pressure variations and hydraulic fracturing caused changes in the driving force of crystallisation, favouring the development of the trapiche texture.

The Journal of Gemmology, **36**(8), 2019, pp. 726–746, http://doi.org/10.15506/JoG.2019.36.8.726

The term *trapiche* was introduced by McKague (1964) to refer to an unusual texture in some Colombian emeralds, which resembles the spokes of a milling wheel that is used to process sugar cane. In the 1990s, trapiche rubies with a similar texture appeared on the gem market from Mong Hsu in Myanmar (Schmetzer *et al.* 1996, 1999; Sunagawa *et al.* 1999). Then, in the 2000s, trapiche tourmalines were reported from Zambia (Hainschwang *et al.* 2007; Schmetzer *et al.* 2011). Recently, a fluid inclusion study of samples from Mong Hsu confirmed that both non-trapiche and trapiche rubies formed from the same parental CO_2-H_2S-rich fluid (Giuliani *et al.* 2018).

In the present article, we describe in detail (and for the first time) trapiche rubies from northern Vietnam (e.g. Figure 1). We examine two samples from the Khoan Thong placer in the Luc Yen mining district of northern Vietnam, and discuss their formation conditions, texture acquisition and growth, as well as their chemical composition, through mineralogical and petrographic studies, X-ray computed tomography and electron probe micro-analysis. The results give a complete overview of the relationships among the three components of the trapiche texture (core, growth sectors and sector boundaries) in Vietnamese rubies, which we compare to those from other localities.

Figure 1: The trapiche texture of this ruby (15 × 15 × 27 mm) is representative of the material from the Luc Yen District of Vietnam described in this article. Photo by Shang-i (Edward) Liu.

TRAPICHE TEXTURE IN RUBY

Trapiche texture is formed of growth sectors separated by more or less sharp boundaries containing abundant mineral and fluid inclusions (Win 2005; Schmetzer *et al.* 2011). These boundaries surround a central portion, generally called the 'core', and extend from its edges to the rim of the crystal. Some trapiche samples lack a distinct core, and the boundaries intersect at a central point. The trapiche texture is best seen in slices cut perpendicular to the *c*-axis, and the presence and size of the core portion depend on the slice's position within the host crystal (Pignatelli *et al.* 2015; see Figure 2).

In the literature, the terminology used to indicate the main components of the trapiche pattern varies with the mineral and the authors (Figure 3). There is consensus only for the 'core'. The growth sectors have been called 'arms' in trapiche emeralds (Nassau & Jackson 1970), and 'ruby sectors' or 'growth sectors' in trapiche rubies (Schmetzer *et al.* 1996, 1999; Sunagawa *et al.* 1999). 'Growth sectors' is also used for trapiche tourmaline (Schmetzer *et al.* 2011). More complex is the nomenclature for the boundaries between the gemmy portions: 'two-phase regions' or 'dendrites' have been used for emeralds (Nassau & Jackson 1970; Pignatelli *et al.* 2015), 'arms' for rubies (Schmetzer *et al.* 1996, 1999; Sunagawa *et al.* 1999) and 'sector boundaries' for tourmalines (Schmetzer *et al.* 2011). To avoid further confusion, in this article we use the terms *core, growth sectors* and *sector boundaries*, consistent with Schmetzer *et al.* (2011).

Trapiche texture in ruby was described for the first time by K. Schmetzer and his co-authors (Schmetzer *et al.* 1996, 1999; Sunagawa *et al.* 1999). According to their data, this texture is characterised by six yellowish or white sector boundaries separating six growth sectors. In some ruby samples the sector boundaries intersect at a central point (a core being absent), giving rise to triangular growth sectors (Figure 2c). In others, a hexagonal core is present, and the growth sectors have a trapezoidal shape (Figure 2b).

The core can appear red, black and, when similar to the sector boundaries, yellowish to white. Zoning in Cr and variable contents of other chromophores such as Ti and V have been reported in different trapiche ruby samples,

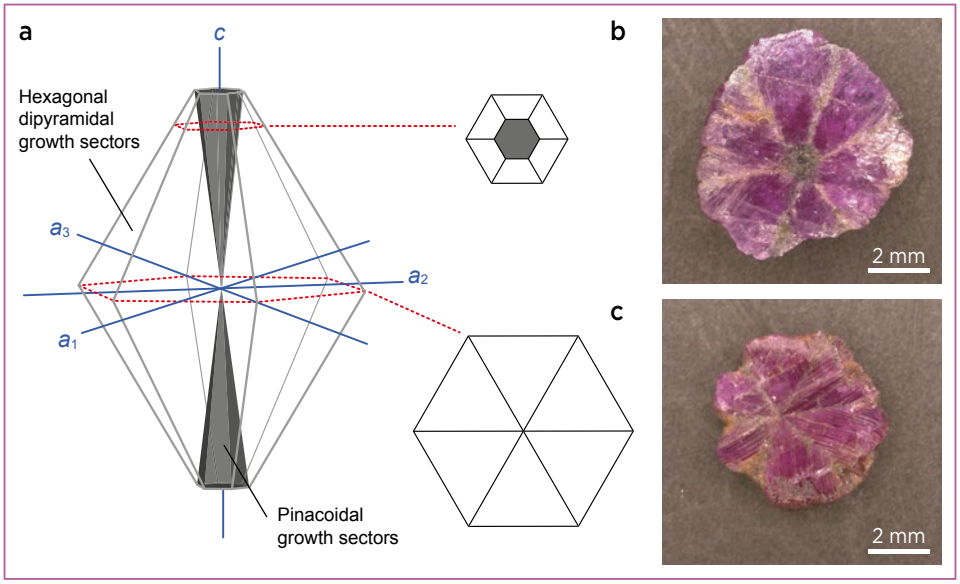

Figure 2: (**a**) Variations in the size of the trapiche core, which corresponds to the pinacoidal growth sectors, can be seen in the areas shown in grey. These sectors have a tapered shape, so the core size varies depending on where a section is cut perpendicular to the *c*-axis. The core is largest near the ends of the crystal (**b**) and decreases towards the centre, where the sector boundaries intersect (**c**). Both slices shown here are from Mong Hsu in Myanmar. Photos by I. Pignatelli and G. Giuliani.

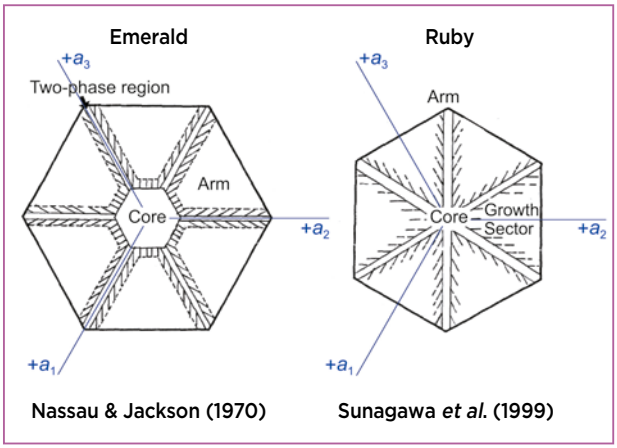

Figure 3: The trapiche texture as seen in sections perpendicular to the *c*-axis is illustrated here for emerald (left) and ruby (right). The *a*-axes are labelled in both drawings, as well as the differing descriptive terminology used in the literature. In the present article, the *arms* referred to by Sunagawa *et al.* (1999) are called *sector boundaries*. Modified from Sunagawa *et al.* (1999).

but also within the same sample (Schmetzer *et al.* 1999; Garnier *et al.* 2002a, b). This explains why the core can be red (Cr>Ti) or bluish to black (Ti>Cr; Peretti *et al.* 1996). The yellowish-to-white colour of both the core and sector boundaries has been attributed to the presence of calcite, dolomite, corundum and K-Al-Fe-Ti silicate inclusions, as well as Fe-rich secondary minerals formed during the weathering process (Schmetzer *et al.* 1999).

Other solid inclusions have also been found within the sector boundaries, including siderite, chlorite, adularia, sillimanite, rutile, titanite, graphite, baryte, mica, amphibole, zircon, diaspore and pyrite (Garnier *et al.* 2002a, b). Tube-like voids filled by solids (i.e. calcite or dolomite), liquid and gas have also been described (Schmetzer *et al.* 1996; Giuliani *et al.* 2018). They originate from the core or sector boundaries and extend into the growth sectors, running perpendicular to the sectors with an inclination of 5° relative to the {0001} faces of the ruby. In some samples, the tube-like voids in the core can also be oriented parallel to the *c*-axis.

Between the tube-like voids and/or their extensions into the sector boundaries, single-phase (liquid), two-phase (liquid + gas) or three-phase (liquid + gas + solid) inclusions have been found (Garnier *et al.* 2002a, b). These inclusions correspond to the trapping of two immiscible fluids during ruby formation: a carbonic fluid in the CO_2-H_2S-COS-S_8-AlO(OH) system and molten salts (Giuliani *et al.* 2015a, 2018).

Trapiche rubies have not been studied *in situ* in their primary deposits; instead, they are typically acquired in Thai and Burmese gem markets. Based on information given by the suppliers, they originated from the Mong Hsu mines in Myanmar, but some of them might have come from Vietnam (Schmetzer *et al.* 1996). Although the geology of Mong Hsu is not well known because of security issues, Hlaing (1991) reported that the trapiche rubies are apparently hosted by marbles similar to those in the Mogok Stone Tract. This was supported by Garnier *et al.* (2002a, b), who underlined that trapiche and non-trapiche rubies from Mong Hsu have similar mineralogical and chemical features because they formed in the same geological environment.

GEOLOGICAL SETTING OF VIETNAMESE TRAPICHE RUBIES

In northern Vietnam, the main ruby and red spinel deposits are located in marble associated with large-scale shear zones that were active during the Tertiary (Leloup *et al.* 1995; Garnier 2003; Garnier *et al.* 2008; see Figure 4). The Red River shear zone is formed by the Day Nui Con Voi metamorphic belt and the Lo Gam tectonic zone (Garnier 2003; Pham *et al.* 2004, 2013, 2018). The Lo Gam zone contains the ruby and spinel deposits, and consists of metasedimentary sequences (i.e. marble units and intercalated gneisses and schists) of Cambrian depositional age, which are situated between two main left-lateral faults in an area about 10–15 km wide within the Red River shear zone, together with granitoid intrusions of Triassic age (Garnier 2003).

Geothermobarometry of the Day Nui Con Voi metamorphic belt revealed that peak metamorphism took place under amphibolite-facies pressure-temperature (P-T) conditions of about 4.5 ± 1.5 kbar and 710 ± 70°C (Leloup and Kienast 1993; Leloup *et al.* 2001), while Nam *et al.* (1998) estimated 6.5 ± 1.5 kbar and about 690 ± 30°C. Gem ruby formed under conditions of about 620–650°C and 2.6–2.9 kbar during a retrograde P-T metamorphic path, mainly by the destabilisation of muscovite or spinel (Garnier *et al.* 2008). The metamorphic fluid system was rich in CO_2 released from the devolatilisation of carbonates, and also contained fluorine, chlorine and boron, as well as salts and sulphates (NaCl, KCl and $CaSO_4$). Evaporites are the key to explaining the formation of these ruby deposits. Molten salts mobilised *in situ* aluminium and metal transition elements contained within phengites hosted by the marbles, leading to the crystallisation of ruby (Giuliani *et al.* 2003, 2018).

Primary ruby occurs as disseminated crystals within marble—associated with phlogopite, dravite, margarite, pyrite, rutile, spinel, pargasite-edenite and graphite

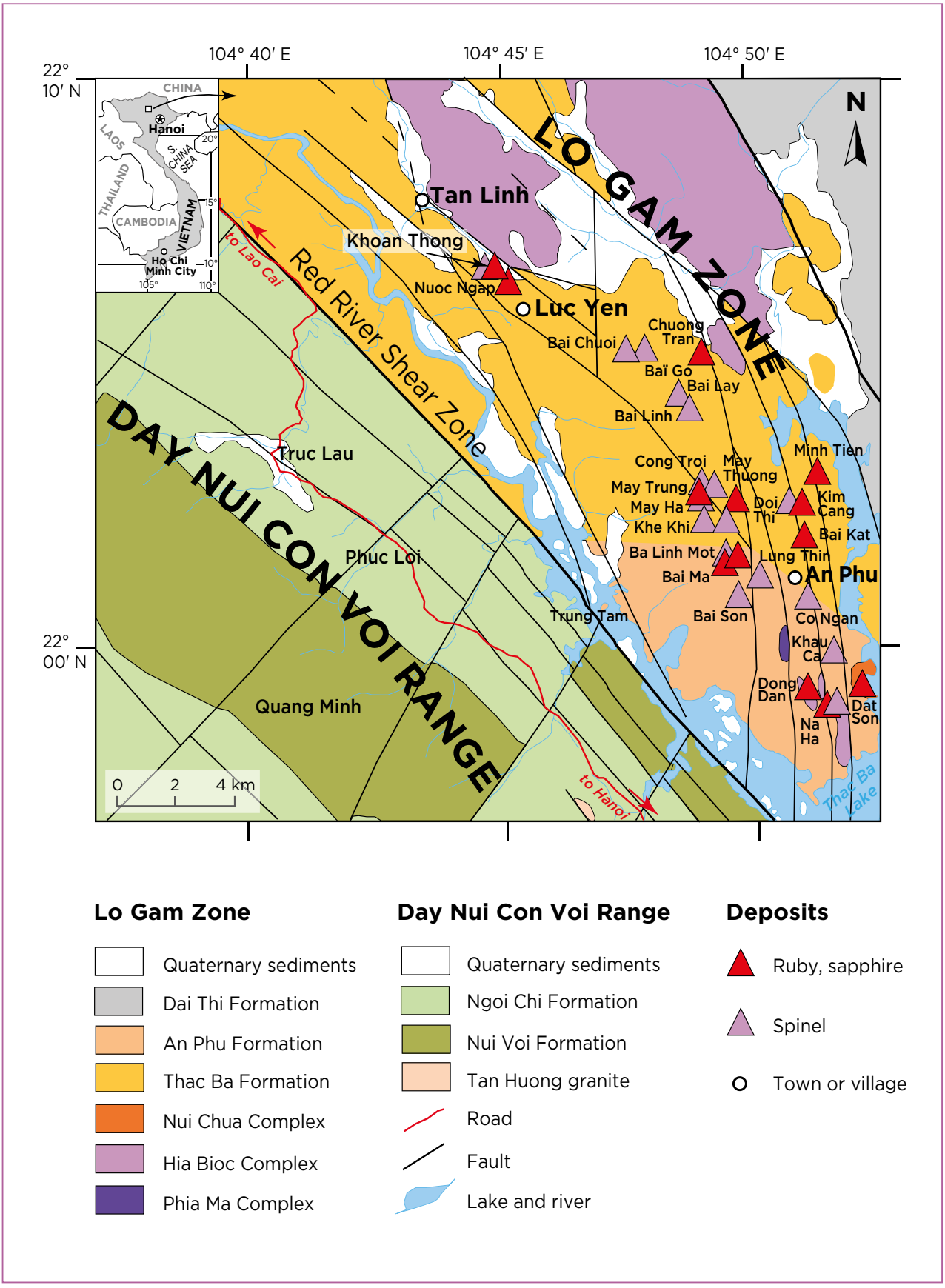

Figure 4: This geological map of the Luc Yen area in northern Vietnam (modified from Garnier 2003) shows the main ruby and red spinel deposits located in marbles associated with large-scale shear zones. The samples studied for this report originated from the Khoan Thong placer north-west of Luc Yen.

(Garnier *et al.* 2008)—in the Luc Yen mining district, which includes the Khoan Thong placer. Ruby also occurs within veinlets and fissures—which crosscut the marbles and are filled by calcite, dravite, pyrite, margarite and phlogopite—at the An Phu, Bai Da Lan and Minh Tien mines.

Placer deposits formed by the concentration of gem-bearing gravels and sands in karst and alluvial fans throughout the Luc Yen mining district. The gem-producing valleys are typically small (i.e. 2–3 km^2). Blue and fancy-colour sapphires, spinel, tourmaline, pargasite, humite and garnet are recovered together with ruby (including rare trapiche ruby). These placers furnish a variety of gem-quality materials to the Luc Yen market, which has been open daily since 1987.

MATERIALS AND METHODS

Seven trapiche rubies were collected by one of the authors (Pham Van Long) in the Luc Yen mining district, from placers related to ruby-bearing marble (i.e. the Cong Troi, May Trung and Khoan Thong mining areas; Figure 4). The crystals were alluvially transported and most of them were transformed into rounded grains. Two of the best-preserved but fractured crystals (samples T1 and T2) found in the Khoan Thong placer were analysed for the present study.

The two samples were analysed by X-ray computed tomography (CT), a non-destructive technique that has previously been used to obtain high-resolution three-dimensional (3D) details of various gem materials, including trapiche emeralds (Karampelas *et al.* 2010; Giuliani *et al.* 2015b; Morlot *et al.* 2016; Pignatelli *et al.* 2017; Richard *et al.* 2019). This technique provides information on the size, distribution and shape of solid inclusions, as well as the geometry and volume of fluid inclusions, and can quantify the volume of porosity. CT scans of the two trapiche rubies were collected with a Phoenix Nanotom S instrument, using resolutions of 6 and 3 µm/voxel and nanofocus X-ray tube tensions of 90 and 110 kV, respectively, for samples T1 and T2. The tomography produces files with voxel (3D pixel) resolutions between 30 and 0.6 µm as a function of sample size. Virtual cross-sections were digitally extracted from the volume of the samples to observe textural details (e.g. porosity) and to visualise the distribution of inclusions with different densities. The volume of porosity and inclusions was calculated using VGStudio and Avizo 9.5 software.

Both samples were sliced perpendicular to the crystallographic *c*-axis, embedded in resin and polished for

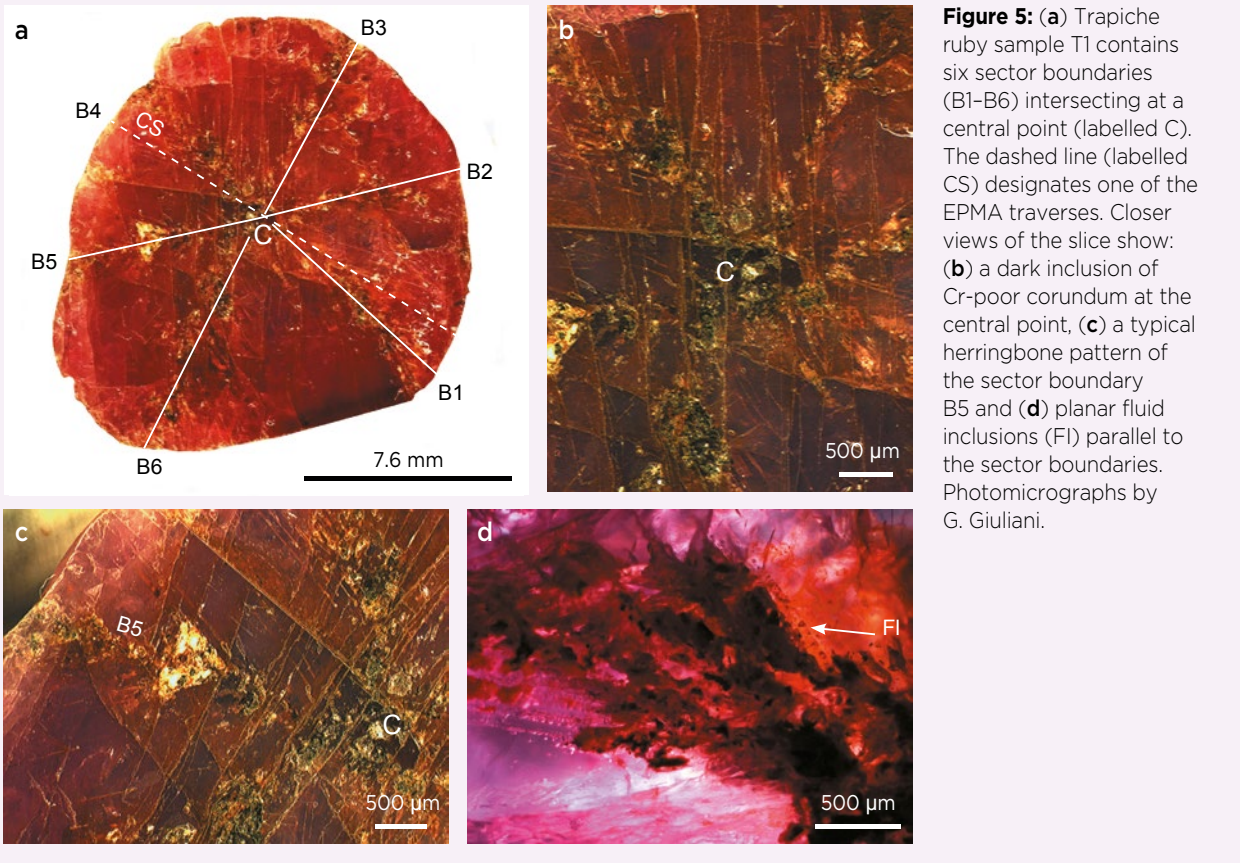

Figure 5: (**a**) Trapiche ruby sample T1 contains six sector boundaries (B1–B6) intersecting at a central point (labelled C). The dashed line (labelled CS) designates one of the EPMA traverses. Closer views of the slice show: (**b**) a dark inclusion of Cr-poor corundum at the central point, (**c**) a typical herringbone pattern of the sector boundary B5 and (**d**) planar fluid inclusions (FI) parallel to the sector boundaries. Photomicrographs by G. Giuliani.

further analysis (Figures 5a and 6a). At the CRPG-CNRS laboratory, they were studied with a JEOL JSM-6510 scanning electron microscope (SEM) equipped with a Genesis energy-dispersive X-ray (EDX) detector, using a 3 nA primary beam accelerated at 15 kV. Backscattered electron (BSE) images and EDX spectra were recorded to analyse the trapiche texture and identify the solid inclusions.

Eighty-seven point analyses of the inclusions and host rubies were performed by electron probe micro-analysis (EPMA) at the Service Commun de Microscopie Electronique et Microanalyse (GeoResources laboratory) with a fully automated Cameca SX100 instrument. The samples were analysed using: an accelerating voltage of 15 kV, a beam current of 12 nA and a raster length of 0.03 µm (focused beam on a surface of 1 µm^2) for Al; and an accelerating voltage of 25 kV, a beam current of 100 nA and a raster length of 0.03 µm for Mg, Ti, V, Cr, Fe and Ga. The collection times were 10 s for Al and 120 s for the other elements. The microprobe was calibrated using mineral and synthetic standards: olivine for Mg, corundum for Al, titanite for Ti, V-SX9 metal for V, chromite for Cr, hematite for Fe and AsGa for Ga. Special care was taken with regard to possible interferences between the chromophores Cr and V: Cr($K\beta_1$) and V($K\alpha_1$) lines were measured using a pentaerythritol (PET) analysing crystal with positive and negative background offsets of 600, large enough to have no interference, respectively, with the V($K\alpha_1$) and Ti($K\beta_1$) lines. The limits of detection were (in ppmw) 48 for Mg, 65 for Ti, 125 for Fe, 154 for Ga, 87 for V and 54 for Cr.

RESULTS

Texture Description

The abraded surfaces of the two trapiche rubies indicate that the crystals had been alluvially transported. They were rounded and fractured, such that little of their original euhedral habit was still recognisable.

Below we describe the features of the trapiche texture in the two Vietnamese samples from the core to the sector boundaries and, finally, the growth sectors.

Core: The trapiche texture in both samples was characterised by sector boundaries that intersected at a central point and the absence of a well-developed hexagonal core. In sample T1, this intersection was underlined by a small inclusion of Cr-poor corundum (Figure 7), which corresponds to the darker area labelled 'C' in Figures 5b and 5c.

Sector Boundaries: The sector boundaries in trapiche rubies develop from the core towards the rim of the crystals and follow <1$\bar{1}$0> directions, whereas they are parallel to

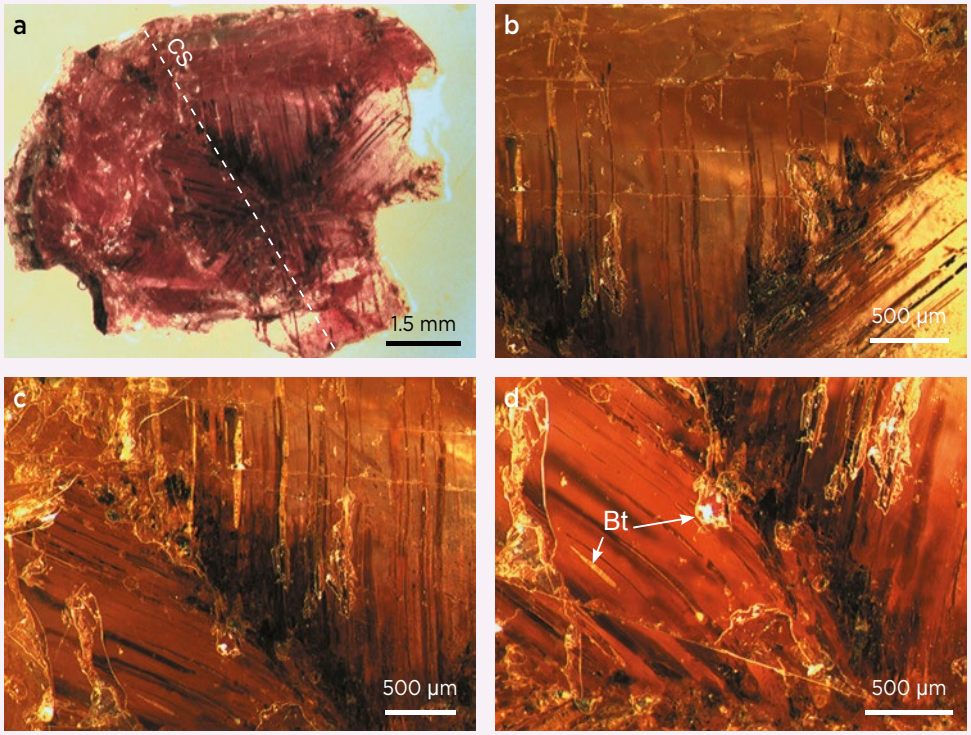

Figure 6: (**a**) Trapiche ruby sample T2 exhibits sector boundaries extending from a central point towards the rim of the crystal. The dashed line (labelled CS) designates one of the EPMA traverses. Closer views of the slice show: (**b**, **c**) tube-like inclusions extending from the sector boundaries into the growth sectors and (**d**) biotite (Bt) inclusions near the sector boundaries. Photomicrographs by G. Giuliani.

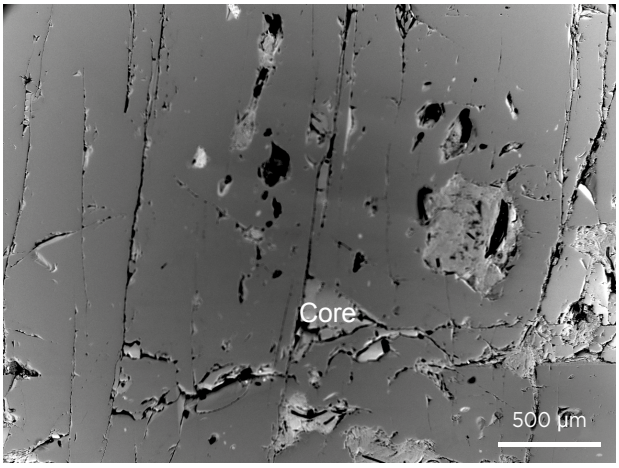

Figure 7: This BSE image of the core of trapiche ruby sample T1 shows an inclusion of Cr-poor corundum (appearing lighter grey) corresponding to the darker-coloured area seen in Figures 5b and 5c.

<100> directions (i.e. *a*-axes) in trapiche emeralds (Figure 3). Their brown colour is due to inclusions of iron oxides/hydroxides (Figures 8d, 8e, 9b and 9d) formed during a late weathering process that affected the trapiche rubies. SEM observations indicate that weathering was favoured by the high porosity of the sector boundaries, which is visible in the CT images (e.g. Figure 10). As calculated from the CT images, the porosity corresponds to a sample volume of 0.6% for T1 (total sample volume 1,720 mm³) and 0.4% for T2 (total volume 267 mm³).

Syngenetic solids were concentrated along the sector boundaries (see Table I); only a few of them were found in the adjacent growth sectors (Figures 11 and 12). There was no correlation between the position and size of inclusions in the rubies, as shown by Figure 12; large and small inclusions were mixed together. The volume occupied by all inclusions, as calculated from CT images, was 0.160 mm³ for sample T1 and 0.246 mm³ for T2 (i.e. about 0.1% and 0.9%).

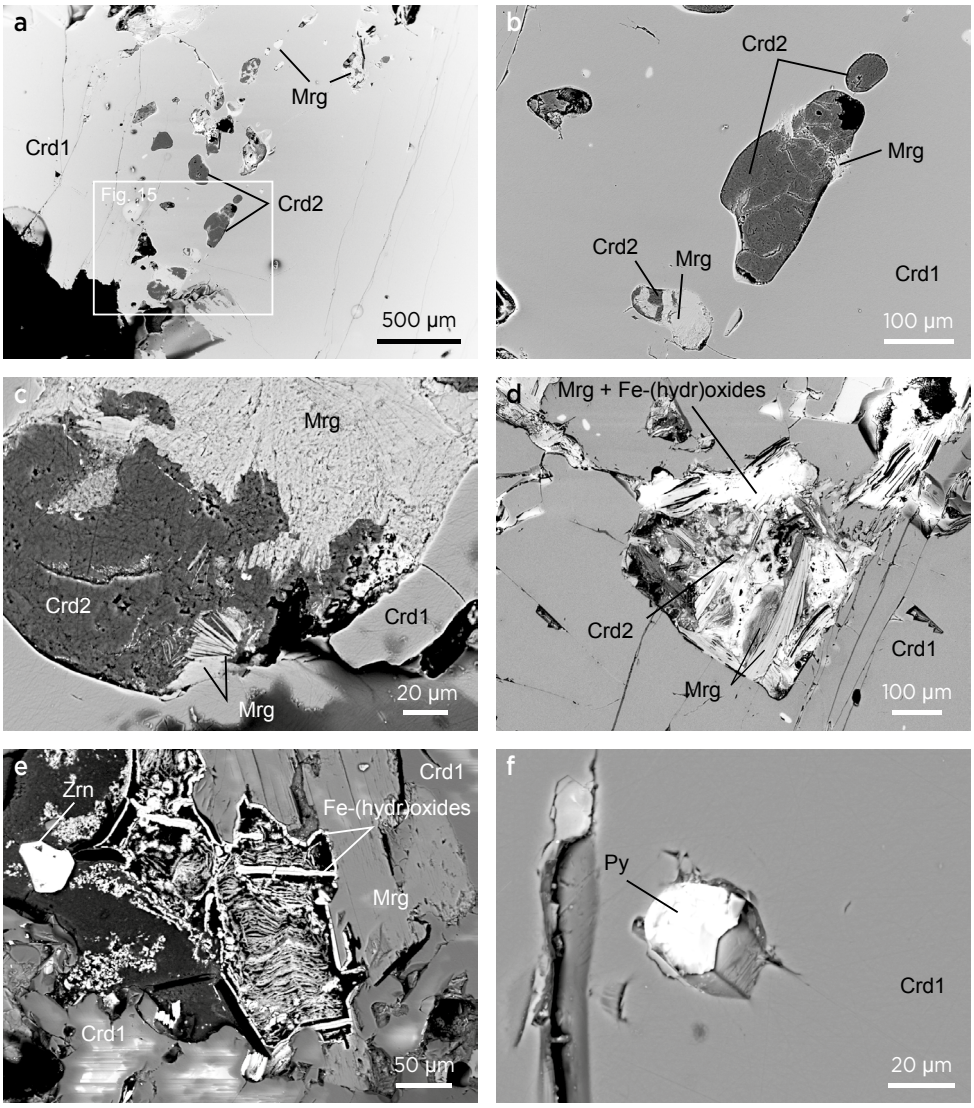

Figure 8: BSE images illustrate the nature of the various solids trapped in trapiche ruby sample T1. (**a**) Inclusions of corundum (Crd2) and margarite (Mrg) are present in the sector boundaries within the ruby (Crd1). The white rectangle corresponds to the location of Figure 15. (**b**) A closer view shows margarite partially replacing a corundum inclusion. (**c**) Margarite is present in the sector boundaries either as porous masses or as flakes developed on corundum inclusions. (**d**) Flakes of margarite are also associated with late Fe-(hydr)oxides in the sector boundaries. Remnants of corundum inclusions are also present. (**e**) Fe-(hydr)oxides are common in the sector boundaries, here associated with margarite and a zircon (Zrn) inclusion. (**f**) A pyrite (Py) inclusion is trapped within a growth sector in the trapiche ruby.

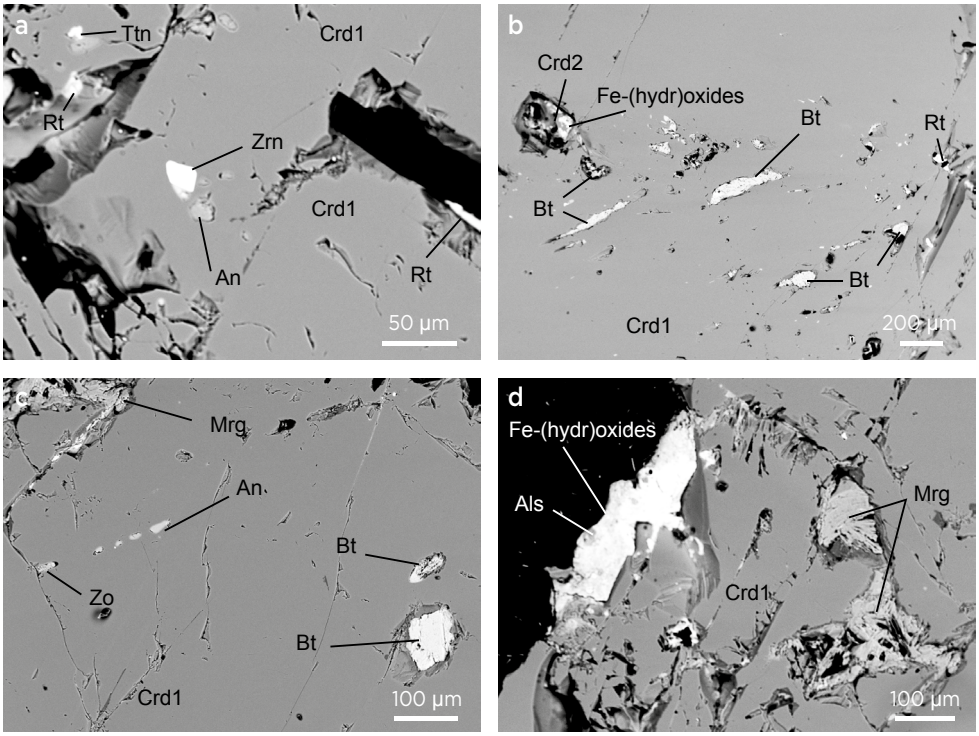

Figure 9: BSE images of sample T2 show a variety of solid inclusions in the sector boundaries of the trapiche ruby, including: (**a**) titanite (Ttn), zircon, anorthite (An) and rutile (Rt); (**b**) biotite (Bt) and corundum (Crd2); (**c**) anorthite, biotite, margarite and zoisite; and (**d**) flakes of margarite associated with Fe-(hydr)oxides and Al-silicates (Als).

The chemical compositions by EPMA of the various solids in samples T1 and T2 are reported in Table II. In sample T1, the most important syngenetic inclusions were anorthite (CaO = 20 wt.%), corundum, margarite, Al-silicates (Al_2SiO_5) and titanite; other minor phases are pyrite, calcite, zircon and rutile. Margarite was present in the sector boundaries either as porous masses (Figure 8c) or as flakes (Figure 8d) developed on corundum inclusions (Crd2—Figure 8b). In sample T2, the main inclusions were biotite and margarite, which were present along with anorthite, corundum, muscovite, rutile, titanite, zircon and zoisite. The biotite had an Fe/Mg ratio of about 1 with a composition between phlogopite and annite. The chemical composition of corundum inclusions (Crd2) is described below.

We found no supported-matrix material from the

Figure 10: This CT image shows the high porosity (here coloured blue) of trapiche ruby sample T1. The porosity corresponds to 0.6% of the sample's volume and is concentrated along the sector boundaries.

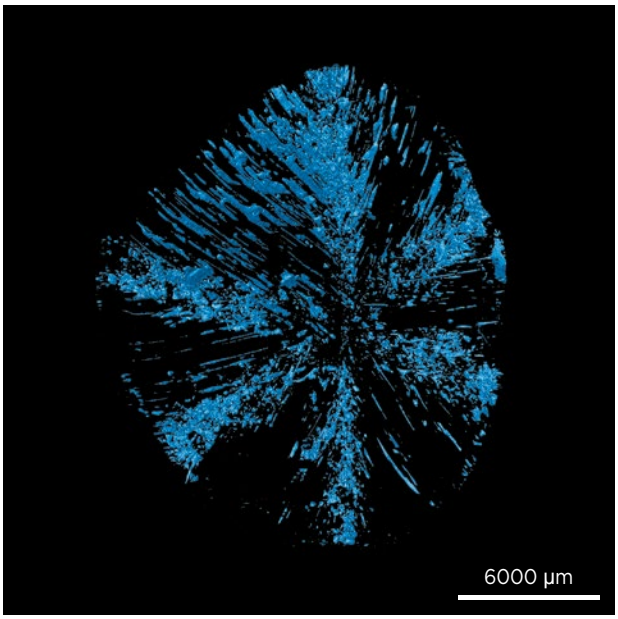

Table I: Solid inclusions observed in trapiche ruby samples T1 and T2.*

Mineral	Sample T1			Sample T2
	Sector boundary B1	Sector boundary B3	Sector boundary B5	
Anorthite	XX	XX	XX	XX
Biotite				XX
Calcite	X		X	
Corundum	XX	X	X	X
Margarite	XXX	XXX	XXX	XX
Muscovite				X
Oxides/ hydroxides of Fe (±Ti±Mn)	XXX	XXX	XXX	XXX
Pyrite	X			
Rutile	X	X		X
Al-silicates	X	X	X	X
Titanite	X	X	X	X
Zircon	X	X		X
Zoisite				X

* Symbols: XXX = main, XX = important and X = occasional phase. All are syngenetic except for the oxides/hydroxides, which are epigenetic (i.e. due to weathering).

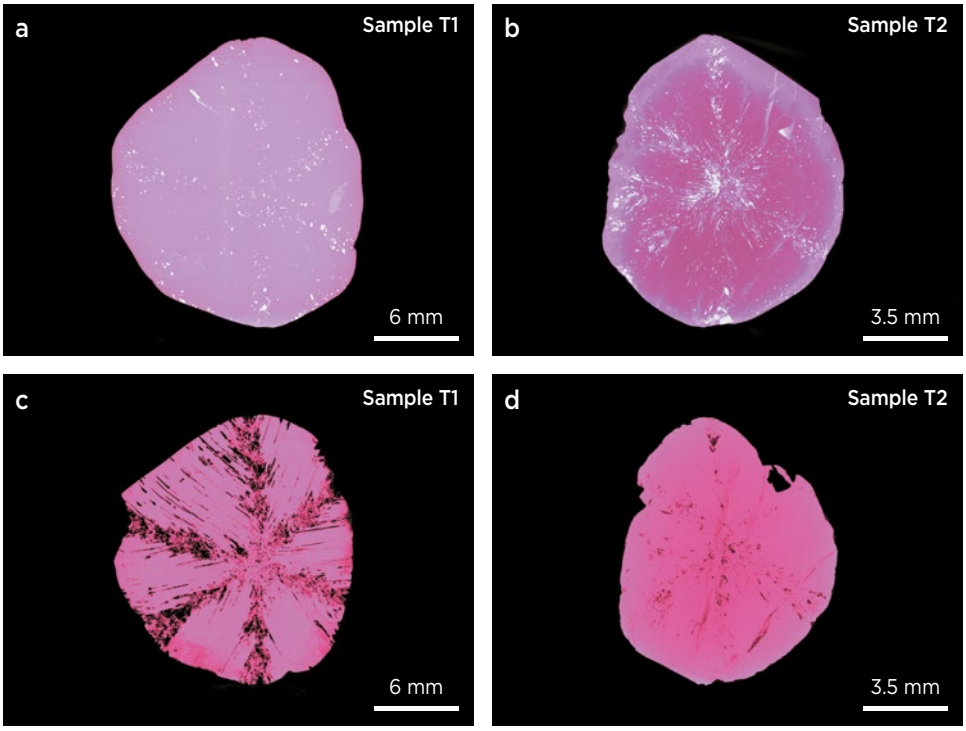

Figure 11: CT images show solid inclusions (white) and fluid inclusions (black) in trapiche ruby samples T1 and T2. (**a**) Solid inclusions in T1 are concentrated along the sector boundaries. (**b**) Tube-like inclusions in T2 are filled by solid phases. (**c**) Tube-like inclusions without solid phases developed in T1 perpendicular to the crystal's faces. (**d**) Fluid inclusions in sample T2 follow the sector boundaries.

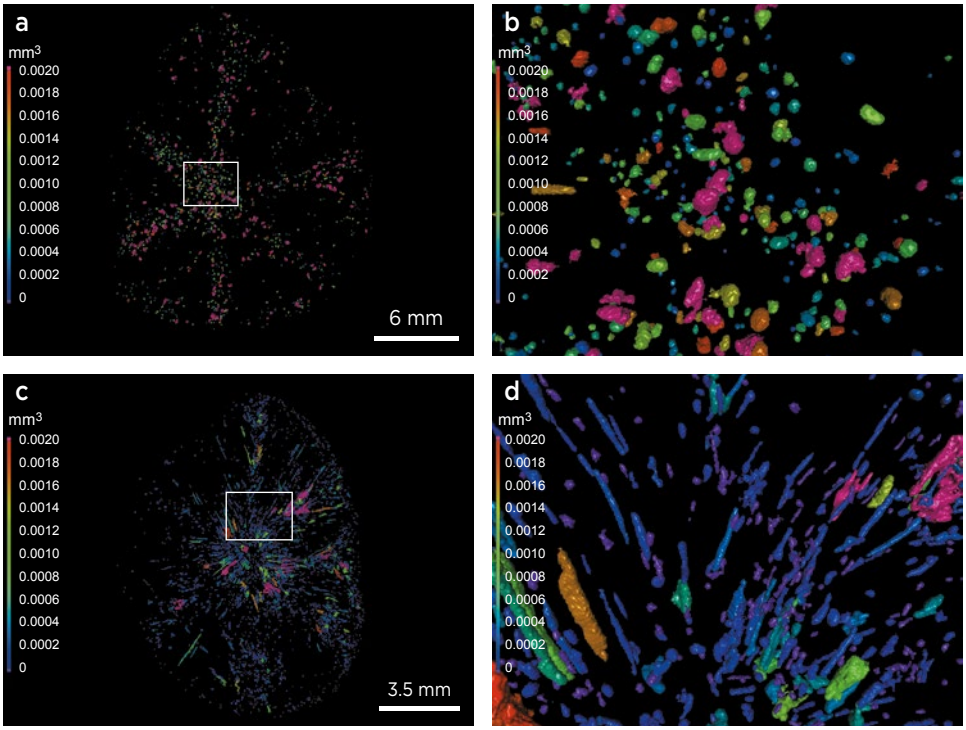

Figure 12: CT images show the spatial distribution of solid inclusions in trapiche ruby samples T1 (**a**, **b**) and T2 (**c**, **d**). The colour of each inclusion corresponds to its volume. Blue-coloured inclusions have the smallest volume and those in pink have the largest volume. The other colours represent intermediate volumes, as indicated by the coloured bar on the left side of each image.

marble host rocks incorporated along the sector boundaries of either sample. The absence of host-rock matrix from these Vietnamese rubies, as also noted previously for trapiche rubies from Mong Hsu (Schmetzer *et al.* 1996), is an important difference from the texture described for Colombian trapiche emeralds (Pignatelli *et al.* 2015).

Growth Sectors: The six growth sectors separated by the sector boundaries were sometimes fractured (e.g. sample T2; see Figure 6). The sectors could not be indexed due to the lack of a well-preserved crystal habit on the water-worn crystals, although they were most likely bounded originally by hexagonal dipyramidal faces.

Table II: Chemical composition by EPMA of solid inclusions in trapiche ruby samples T1 and T2.[a]

Oxides (wt.%)	Anorthite	Titanite	Margarite	Biotite	Muscovite	Zoisite	Corundum (Crd1)[b]	Corundum (Crd2)[b]
	T1-B1-37	T2-28	T1-B1-45	T2-13	T2-3	T2-42	T1-CS	T1-B1
Na_2O	0.90	nd	0.86	0.39	0.18	nd	na	na
MgO	nd	nd	0.38	12.15	0.45	nd	0.005	nd
Al_2O_3	36.61	4.08	52.52	23.71	36.98	33.89	99.64	99.95
SiO_2	42.23	31.81	30.30	33.51	48.25	36.92	na	na
K_2O	nd	nd	nd	10.48	10.18	nd	na	na
CaO	20.25	30.40	12.66	nd	nd	27.94	na	na
TiO_2	nd	33.96	0.03	1.61	0.01	nd	0.040	0.040
V_2O_3	nd	na	na	na	na	na	0.015	nd
Cr_2O_3	na	na	na	na	na	na	0.183	0.110
Ga_2O_3	na	na	na	nd	na	na	0.016	nd
MnO	nd	nd	nd	0.08	nd	nd	na	na
FeO	nd	nd	0.25	14.24	1.45	nd	0.160	0.160
Total	99.99	100.25	97.00	96.17	97.50	98.75	100.06	100.26

[a] Abbreviations: na = not analysed; nd = not detected.
[b] Crd1: Average values for growth sector corundum within the traverse T1-CS (22 points; see Figure 5a). Crd2: Average values for corundum inclusions within a sector boundary of T1 (five points; see Figure 15).

Elongated tube-like voids extended from the sector boundaries into the growth sectors (Figures 6b, 6c and 11d), perpendicular to the crystal faces. The tube-like voids were similar to those observed in trapiche emeralds from Colombia (Touray & Poirot 1968; Pignatelli *et al.* 2015), in trapiche rubies from Myanmar (Schmetzer *et al.* 1996; Sunagawa *et al.* 1999) and in trapiche tourmalines from Zambia (Schmetzer *et al.* 2011). CT images clearly showed that the tube-like voids in sample T2 were often filled by solid phases (Figures 11b, 12c and 12d), while those in T1 were more often fluid-filled (Figure 11c). However, closer analysis of the tomographic contrast (Figure 13) proved that the tube-like voids in sample T2 contained at least two phases: a solid and a less-dense phase (i.e. a liquid and/or a vapour). Viewed with the microscope, isolated primary fluid inclusions occurred along tube-like voids in the sector boundaries and also rarely formed cavities in the growth sectors. They were 15–50 µm wide, and sometimes showed a 'necking-down' phenomenon. At room temperature, the liquid phase occupied 30–90% of the cavity's volume and the remainder was composed of vapour. However, some of these inclusions consisted of a single phase (liquid), while others were multi-phase (liquid + vapour + solid).

Chemical Analysis of Trapiche Rubies

Three cross-sectional traverses of sample T1 and one of sample T2 were analysed by EPMA to evaluate chemical variations in the core, sector boundaries and growth sectors. Two traverses of sample T1 ran along sector

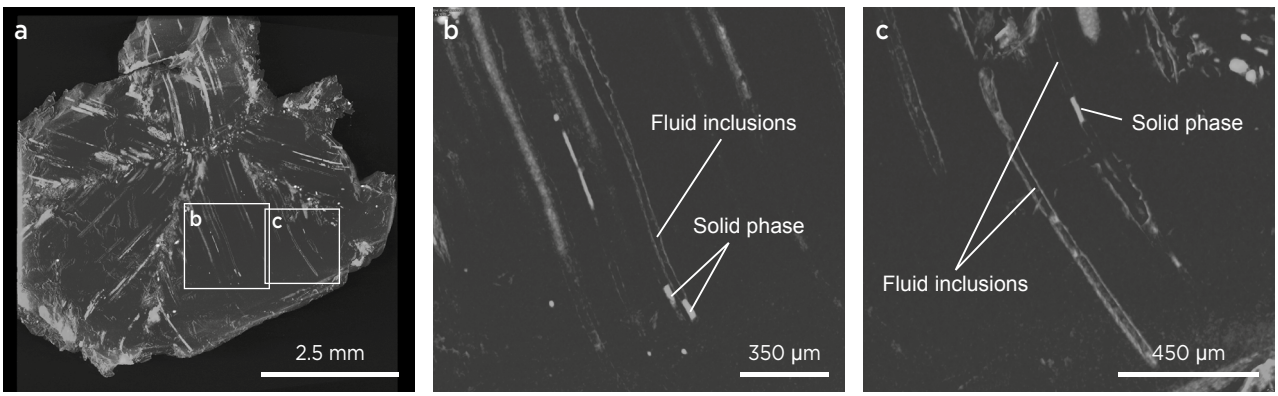

Figure 13: CT contrast images of trapiche ruby sample T2 show tube-like voids that locally contain solid phases (white) or a less-dense phase corresponding to fluid inclusions (dark grey).

boundaries from the rim to the centre (T1-B1 and T1-B3), and the third crossed the sample from rim to rim, passing through its centre (T1-CS; see Figure 5a and Tables III–V). For sample T2, one traverse was analysed between two opposite rims (CS; see Figure 6a and Table VI).

Overall, rubies T1 and T2 had some differences in chemical composition (see Tables V and VI). The Ti concentrations were lower in T2, with TiO_2 contents of 80–1,030 ppmw (vs. 40–1,470 ppmw in T1). The contents of Mg and Ga were more or less the same, with values of 20–70 ppmw for MgO and 70–240 ppmw for Ga_2O_3. Sample T1 had higher concentrations of Fe_2O_3 (1,243–1,698 ppmw) and Cr_2O_3 (1,100–3,340 ppmw). By comparison, sample T2 contained 88–1,500 ppmw Fe_2O_3 and 650–2,190 ppmw Cr_2O_3. Vanadium was much less abundant, and therefore was not the main chromophore; V_2O_3 comprised 80–210 ppmw in T1 and 60–150 ppmw in T2.

The distribution of the various chemical elements in the corundum (Crd1) along sector boundary T1-B1 is recorded in Table III and illustrated in Figure 14. The contents of Fe and V were constant, but those of Cr and Ti behaved differently. Cr_2O_3 decreased from the trapiche ruby rim (point 1—0.39 wt.%) towards the core (point 26—0.11 wt.%). This difference in Cr was not evident in

Table III: Chemical composition (wt.%) by EPMA of corundum in trapiche ruby sample T1, along sector boundary B1 shown in Figures 5a and 14, and as inclusions shown in Figure 15.*

Analysis Point	MgO	Al_2O_3	TiO_2	V_2O_3	Cr_2O_3	Fe_2O_3	Ga_2O_3	Total
Corundum (Crd1) in the Growth Sector and Near the Core								
T1-B1-1	0.007	100.00	0.009	0.011	0.388	0.137	0.018	100.57
T1-B1-2	0.005	98.02	0.009	0.012	0.366	0.139	0.014	99.57
T1-B1-3	0.008	99.41	0.029	0.012	0.326	0.130	0.017	99.93
T1-B1-4	0.002	98.67	0.011	0.016	0.325	0.146	0.019	99.19
T1-B1-5	0.005	99.02	0.015	0.012	0.333	0.139	0.014	99.54
T1-B1-6	0.003	99.78	0.009	0.011	0.312	0.164	0.018	100.30
T1-B1-7	0.006	99.86	0.040	0.017	0.268	0.153	0.017	100.36
T1-B1-8	0.007	98.93	0.048	0.018	0.270	0.100	0.016	99.39
T1-B1-9	0.005	99.65	0.050	0.015	0.268	0.153	0.017	100.16
T1-B1-10	0.002	98.07	0.034	0.014	0.258	0.147	0.021	98.55
T1-B1-11	0.002	98.07	0.034	0.014	0.258	0.147	0.021	98.55
T1-B1-12	0.004	99.20	0.015	0.011	0.222	0.149	0.020	99.62
T1-B1-13	0.010	99.22	0.057	0.019	0.232	0.147	0.020	99.70
T1-B1-14	0.005	99.42	0.054	0.017	0.214	0.148	0.015	99.87
T1-B1-15	0.006	99.00	0.027	0.016	0.210	0.147	0.019	99.42
T1-B1-16	0.006	99.67	0.034	0.014	0.214	0.152	0.028	100.12
T1-B1-17	0.007	99.84	0.050	0.017	0.184	0.157	0.016	100.27
T1-B1-18	0.005	99.08	0.063	0.017	0.199	0.155	0.016	99.54
T1-B1-19	0.004	99.76	0.020	0.016	0.168	0.155	0.020	100.14
T1-B1-20	0.009	99.53	0.024	0.015	0.163	0.160	0.017	99.92
T1-B1-21	0.002	99.60	0.023	0.014	0.141	0.150	0.017	99.95
T1-B1-22	0.004	99.49	0.062	0.017	0.155	0.164	0.015	99.91
T1-B1-23	0.006	99.85	0.050	0.018	0.120	0.155	0.017	100.21
T1-B1-24	0.004	99.95	0.055	0.016	0.124	0.161	0.017	100.33
T1-B1-25	0.005	99.57	0.069	0.018	0.122	0.160	0.016	99.96
T1-B1-26	0.008	99.85	0.020	0.018	0.109	0.184	0.011	100.20
Corundum Inclusions (Crd2) in the Sector Boundary								
1	0.002	99.50	0.020	nd*	0.100	0.200	nd	99.82
2	0.001	99.20	0.060	nd	0.090	0.100	nd	99.45
3	0.001	98.75	0.030	nd	0.150	0.150	nd	99.08
4	0.002	99.80	0.040	nd	0.110	0.160	nd	100.11
5	0.001	98.90	0.040	nd	0.010	0.170	nd	99.12

* Abbreviation: nd = not detected.

Table IV: Chemical composition (wt.%) by EPMA of corundum in sample T1 along sector boundary B3 shown in Figure 5a.

Analysis Point	MgO	Al_2O_3	TiO_2	V_2O_3	Cr_2O_3	Fe_2O_3	Ga_2O_3	Total
T1-B3-1	0.003	99.25	0.010	0.015	0.230	0.152	0.021	99.68
T1-B3-2	0.004	99.25	0.031	0.013	0.240	0.167	0.016	99.72
T1-B3-3	0.001	99.75	0.018	0.016	0.239	0.168	0.020	100.21
T1-B3-4	0.003	99.76	0.009	0.014	0.252	0.160	0.014	100.21
T1-B3-5	0.003	99.52	0.020	0.014	0.226	0.142	0.017	99.94
T1-B3-6	0.003	99.78	0.027	0.016	0.211	0.157	0.014	100.21
T1-B3-7	0.006	99.27	0.058	0.019	0.217	0.157	0.017	99.75
T1-B3-8	0.004	99.01	0.060	0.018	0.199	0.178	0.015	99.49
T1-B3-9	0.004	99.67	0.036	0.016	0.160	0.161	0.016	100.06
T1-B3-10	0.006	99.75	0.050	0.015	0.180	0.157	0.014	100.17
T1-B3-11	0.009	99.85	0.035	0.020	0.166	0.191	0.014	100.28
T1-B3-12	0.007	99.46	0.066	0.025	0.303	0.192	0.014	100.07
T1-B3-13	0.007	99.85	0.060	0.018	0.178	0.168	0.017	100.30
T1-B3-14	0.005	99.26	0.061	0.018	0.154	0.159	0.014	99.67
T1-B3-15	0.004	99.80	0.054	0.018	0.164	0.153	0.017	100.21
T1-B3-16	0.004	99.76	0.066	0.018	0.167	0.171	0.018	100.20

Table V: Chemical composition (wt.%) by EPMA of corundum in sample T1 along cross-section CS shown in Figure 5a.

Analysis Point	MgO	Al_2O_3	TiO_2	V_2O_3	Cr_2O_3	Fe_2O_3	Ga_2O_3	Total
T1-CS-1	0.007	99.82	0.009	0.009	0.334	0.128	0.017	100.33
T1-CS-2	0.003	99.40	0.013	0.016	0.262	0.145	0.019	99.86
T1-CS-3	0.004	99.40	0.037	0.016	0.244	0.158	0.018	99.88
T1-CS-4	0.004	99.68	0.086	0.016	0.207	0.147	0.018	100.16
T1-CS-5	0.004	99.69	0.042	0.015	0.193	0.157	0.016	100.11
T1-CS-6	0.003	99.61	0.021	0.014	0.114	0.141	0.014	99.92
T1-CS-7	0.003	99.51	0.037	0.014	0.149	0.149	0.008	99.87
T1-CS-8	0.007	99.62	0.058	0.018	0.143	0.158	0.021	100.02
T1-CS-9	0.005	99.31	0.147	0.021	0.159	0.169	0.024	99.84
T1-CS-10	0.003	99.53	0.051	0.019	0.150	0.170	0.012	99.93
T1-CS-11	0.004	99.83	0.004	0.012	0.110	0.152	0.012	100.12
T1-CS-12	0.007	99.55	0.072	0.016	0.139	0.162	0.015	99.96
T1-CS-13	0.005	99.49	0.065	0.019	0.136	0.159	0.015	99.89
T1-CS-14	0.005	99.76	0.035	0.017	0.143	0.154	0.016	100.13
T1-CS-15	0.007	99.84	0.038	0.017	0.163	0.161	0.011	100.24
T1-CS-16	0.007	99.87	0.016	0.013	0.111	0.143	0.018	100.18
T1-CS-17	0.007	99.05	0.021	0.013	0.176	0.145	0.016	99.43
T1-CS-18	0.006	99.85	0.020	0.014	0.209	0.151	0.021	100.27
T1-CS-19	0.003	99.97	0.013	0.016	0.205	0.134	0.018	100.36
T1-CS-20	0.006	99.66	0.015	0.014	0.210	0.153	0.018	100.08
T1-CS-21	0.001	99.97	0.009	0.017	0.206	0.131	0.013	100.35
T1-CS-22	0.004	99.74	0.009	0.008	0.253	0.124	0.012	100.15

Table VI: Chemical composition (wt.%) by EPMA of sample T2 along a traverse between opposite rims shown in Figure 6a.

Analysis Point	MgO	Al_2O_3	TiO_2	V_2O_3	Cr_2O_3	Fe_2O_3	Ga_2O_3	Total
T2-1	0.003	99.36	0.091	0.014	0.196	0.107	0.012	99.78
T2-2	0.007	99.63	0.054	0.015	0.190	0.109	0.014	100.01
T2-3	0.002	99.74	0.064	0.012	0.187	0.100	0.013	100.12
T2-4	0.004	99.74	0.076	0.012	0.184	0.143	0.009	100.17
T2-5	0.003	99.89	0.053	0.011	0.065	0.092	0.016	100.13
T2-6	0.007	99.92	0.036	0.010	0.070	0.090	0.009	100.14
T2-7	0.002	99.19	0.086	0.013	0.207	0.150	0.016	99.66
T2-8	0.002	99.23	0.052	0.012	0.155	0.099	0.013	99.56
T2-9	0.003	99.41	0.065	0.012	0.130	0.095	0.012	99.73
T2-10	0.003	99.65	0.058	0.011	0.111	0.092	0.020	99.95
T2-11	0.002	99.75	0.008	0.006	0.067	0.090	0.013	99.94
T2-12	0.005	99.33	0.060	0.012	0.144	0.104	0.017	99.67
T2-13	0.005	99.60	0.011	0.011	0.128	0.088	0.017	99.86
T2-14	0.005	99.47	0.038	0.009	0.147	0.098	0.015	99.78
T2-15	0.002	99.71	0.046	0.011	0.125	0.099	0.016	100.01
T2-16	0.005	99.98	0.059	0.010	0.160	0.097	0.014	100.32
T2-17	0.003	99.77	0.039	0.011	0.128	0.097	0.018	100.06
T2-18	0.005	99.05	0.103	0.014	0.120	0.104	0.015	99.41
T2-19	0.005	99.86	0.064	0.011	0.219	0.098	0.007	100.26

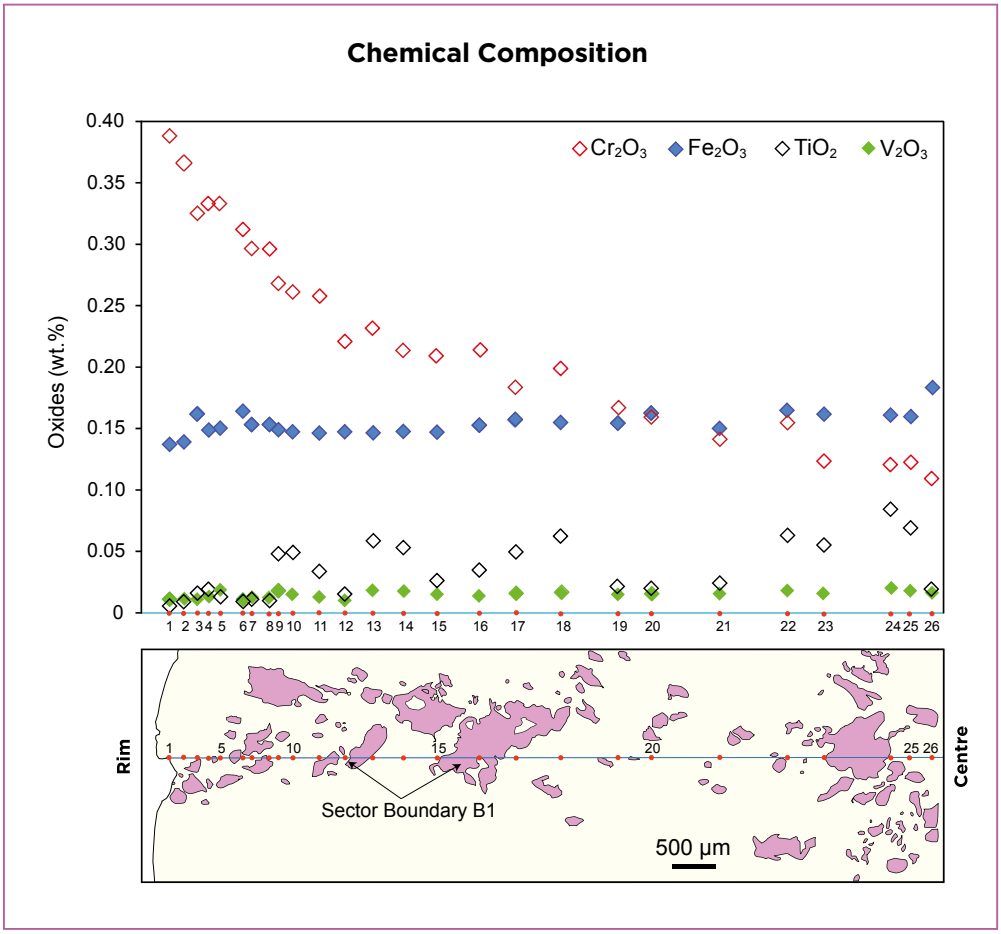

Figure 14: This graph shows variations in Cr_2O_3, Fe_2O_3, TiO_2 and V_2O_3 contents along sector boundary B1 in trapiche ruby sample T1 (see Figure 5a and Table III). The solid inclusions in this sector boundary are shown as pink in the corresponding map below the graph. The red dots in the map correspond to the EPMA point analyses of the corundum (Crd1). The Cr_2O_3 content decreases progressively from the rim towards the centre of the trapiche ruby, from 0.39 to 0.11 wt.%.

the colouration of the sample, but the regular decrease in Cr_2O_3 from the rim (point 1—0.39 wt.%) to point 11 (0.26 wt.%) indicates no sharp chemical discontinuity between the rim and the interior of the crystal. The greater Cr_2O_3 of the rim (points 1–5) corresponded to the outer 1.9 mm of the entire cross-section of the crystal (9.75 mm). The TiO_2 content increased irregularly from the rim to a maximum of 0.07 wt.% near the centre of the crystal. At the centre, the data showed the lowest Cr (and rather low Ti) but the highest Fe of the entire traverse.

The corundum inclusions (Crd2) analysed within the sector boundary (see Figure 15 and Table III) had a very different composition (average Cr_2O_3 = 0.11 wt.%; no detectable Ga_2O_3) compared to corundum Crd1 (average Cr_2O_3 = 0.18 wt.% and maximum = 0.39 wt.%; average Ga_2O_3 = 0.16 wt.%). The average Cr_2O_3 content of the corundum inclusions was similar to the lowest Cr content measured near the centre of sample T1 (see Table III, analysis point T1-B1-26).

The chemical concentrations were plotted in the correlation diagram of Cr_2O_3/Ga_2O_3 versus Fe_2O_3/TiO_2 proposed by Sutherland *et al.* (2003) and applied by Pham *et al.* (2004) to Vietnamese rubies from the Luc Yen and An Phu areas (Figure 16). Overall, the present data plot within the fields of (1) primary non-trapiche ruby-bearing marble deposits and (2) alluvial trapiche rubies from marble-hosted deposits at Luc Yen and An Phu of Pham *et al.* (2004). The chemical compositions of the alluvial trapiche rubies from various localities in Vietnam are presented in Appendix Table A-I.

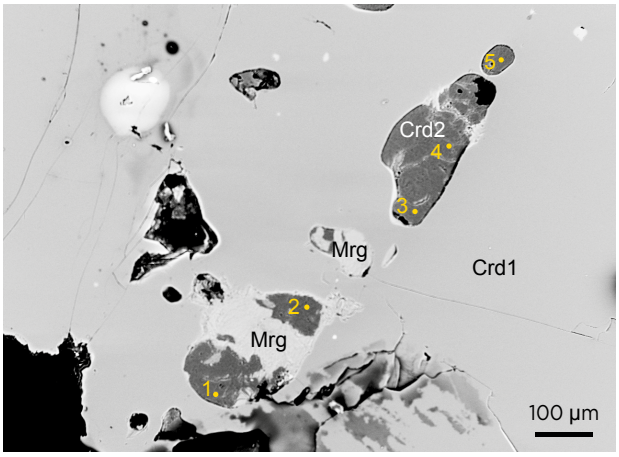

Figure 15: This BSE image (corresponding to the white rectangle in Figure 8a) shows the location of five EPMA analyses of the corundum inclusions (Crd2) in sector boundary B1 of the trapiche ruby (Crd1) sample T1.

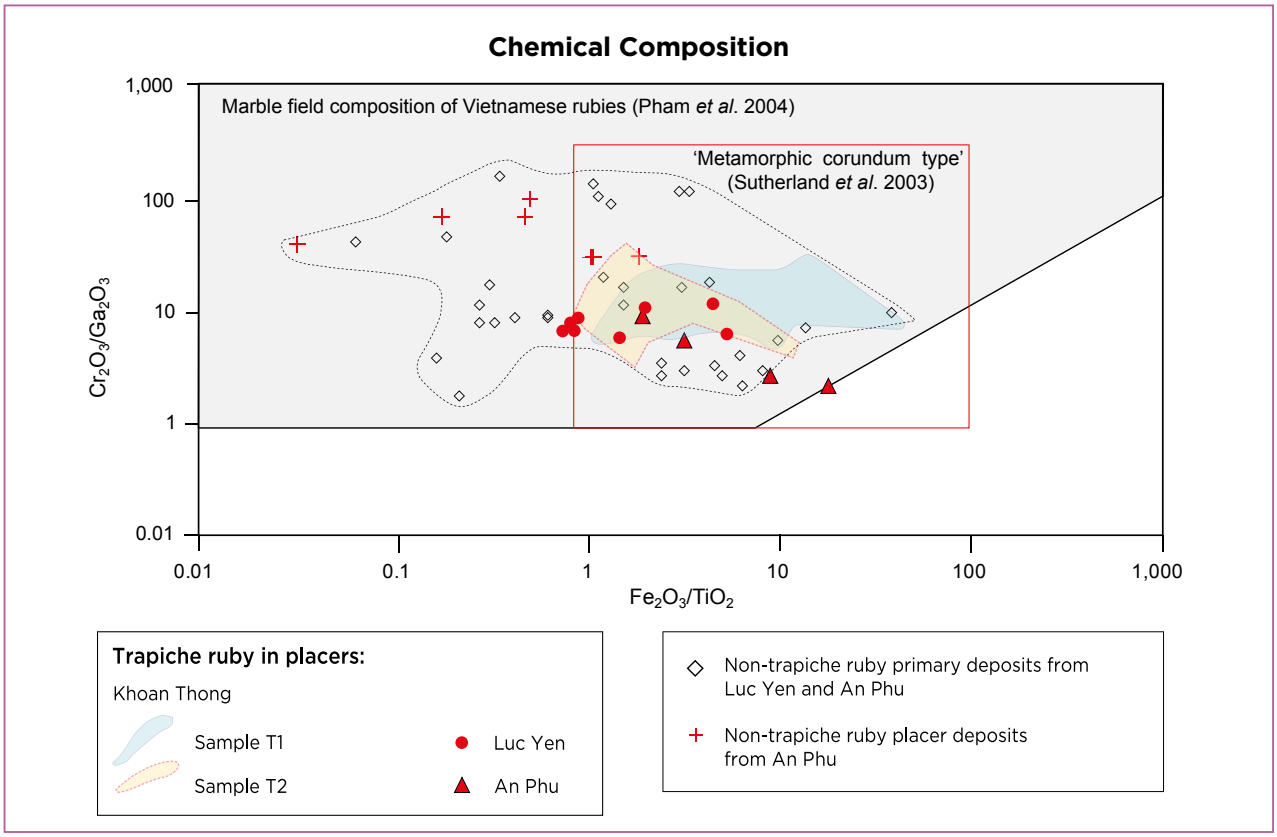

Figure 16: Chemical data for the two trapiche ruby samples (87 point analyses) from Khoan Thong plot within the marble composition field of Vietnamese rubies, as shown in this diagram of Cr_2O_3/Ga_2O_3 versus Fe_2O_3/TiO_2. Shown for comparison are data for trapiche and non-trapiche rubies from different primary and secondary deposits in Vietnam (Pham *et al.* 2004).

DISCUSSION

The solid inclusions observed in the two trapiche rubies from the Khoan Thong placer are dominated by the association anorthite-corundum-margarite. Calcite was found in small amounts and dolomite was absent. The association between coexisting anorthite and margarite with corundum has been documented for Asian ruby-bearing marble deposits (Garnier 2003; Garnier *et al.* 2008). These petrographic relations have shown that ruby and anorthite could form by destabilisation of margarite during prograde metamorphism such as described for the Jegdalek (Afghanistan) and An Phu (Vietnam) deposits (Garnier 2003). Inversely, margarite formed in the presence of water during retrograde metamorphism (Garnier 2003), following reaction 1 (Figure 17):

margarite ↔ anorthite + corundum + water (1)

$CaAl_2(Si_2Al_2)O_{10}(OH)_2 \leftrightarrow CaAl_2Si_2O_8 + Al_2O_3 + H_2O$

Margarite formation at the expense of corundum and anorthite was observed in both samples T1 and T2 (e.g. Figure 8). This retrograde transformation occurred at temperatures between 450 and 500°C (Garnier *et al.* 2008; see Figure 17).

The other chemical reactions involved in the formation of ruby in marbles (Garnier *et al.* 2008) are due to:

- the destabilisation of muscovite, as described at Jegdalek (Afghanistan) and at the Bai Da Lan deposits in the Luc Yen mining area (Garnier 2003):

muscovite ↔ K-feldspar + corundum + water (2)

$KAl_2(Si_3Al)O_{10}(OH)_2 \leftrightarrow KAlSi_3O_8 + Al_2O_3 + H_2O$

- the destabilisation of sapphirine, as evidenced at the deposit in Hunza (Pakistan):

sapphirine + 4 water ↔ 2 spinel + 6 corundum + Mg-chlorite (3)

$Mg_7Al_{18}Si_3O_{40} + 4H_2O \leftrightarrow 2MgAl_2O_4 + 6Al_2O_3 + Mg_5Al(Si_3Al)O_{10}(OH)_8$

- the destabilisation of paragonite, as evidenced at the Hunza and Nangimali (Pakistan) deposits:

paragonite ↔ albite + corundum + water (4)

$NaAl_2(Si_3Al)O_{10}(OH)_2 \leftrightarrow NaAlSi_3O_8 + Al_2O_3 + H_2O$

- the destabilisation of spinel in contact with calcite during retrograde metamorphism (Figure 17), which is the most common reaction, as evidenced at Jegdalek, Hunza and Luc Yen (Garnier *et al.* 2008):

spinel + calcite + CO_2 ↔ corundum + dolomite (5)

$MgAl_2O_4 + CaCO_3 + CO_2 \leftrightarrow Al_2O_3 + CaMg(CO_3)_2$

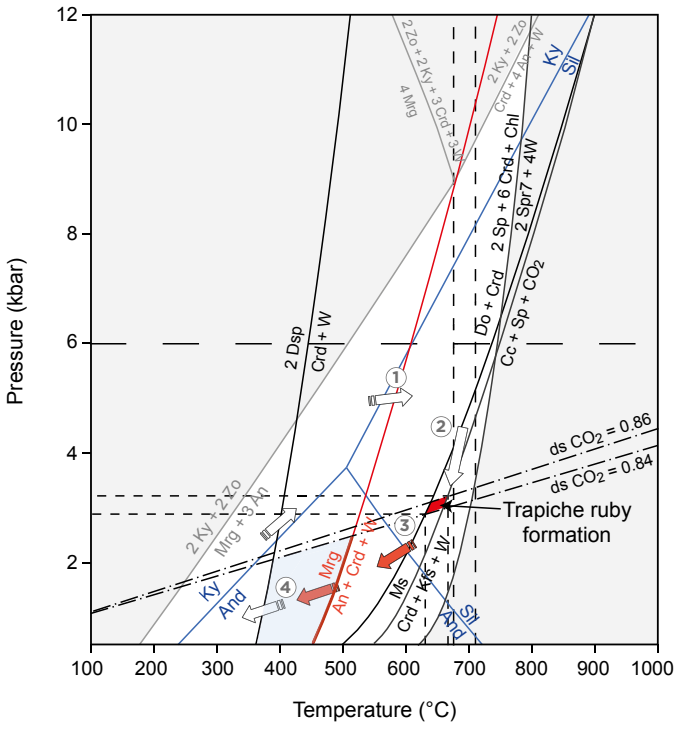

Figure 17: This pressure-temperature diagram shows the conditions of stability for mineral associations in ruby-bearing marbles from Luc Yen (modified from Garnier *et al.* 2008). White arrows 1 and 2 represent different possibilities for forming corundum during prograde metamorphism. The red arrows represent the formation of corundum during retrograde metamorphism (3) and then the transformation of corundum to margarite (4). Abbreviations: An = anorthite, And = andalusite, Cc = calcite, Clin = clinochlore, Crd = corundum, Do = dolomite, Dsp = diaspore, Ksp = K-feldspar, Ky = kyanite, Mrg = margarite, Mu = muscovite, Sil = sillimanite, Spr = sapphirine, Sp = spinel, W = water and Zo = zoisite.

The rubies that form from reaction 5 commonly have calcite and dolomite inclusions trapped either in growth sectors (Peretti *et al.* 1995; Giuliani *et al.* 2018) or in tube-like voids in trapiche rubies (Schmetzer *et al.* 1996, 1999; Giuliani *et al.* 2018). The very low amount of carbonates in trapiche rubies from Khoan Thong cannot exclude their formation in marble. Although the anorthite-corundum-margarite metamorphic assemblage is uncommon for the marble-type deposits, it was already described for the An Phu ruby-bearing marble deposit located south of Khoan Thong (Garnier 2003).

The mineral inclusion assemblage in the Khoan Thong trapiche rubies (Table VII) is completed by micas (biotite and muscovite, in addition to margarite mentioned above), Al-silicates (Al_2SiO_5), anorthite, calcite, pyrite, rutile, titanite, zoisite and zircon, as well as secondary oxide/hydroxides of Fe (±Ti±Mn).

The chemical composition of the trapiche rubies from Khoan Thong plots within the field of Vietnamese marble-hosted rubies (Figure 16). When the data are plotted in a diagram of Fe_2O_3/TiO_2 versus Cr_2O_3 (Figure 18), the Khoan Thong rubies show a similar Fe_2O_3/TiO_2 ratio but somewhat higher Cr_2O_3 contents compared to analyses of trapiche rubies from the An Phu, Luc Yen and Yen Bai mining areas (Pham *et al.* 2004). The diagram also shows that trapiche rubies from northern Vietnam can be distinguished from those of Quy Chau in central Vietnam (Pham *et al.* 2004) and Mong Hsu in Myanmar (Garnier *et al.* 2002a, b). This is due to the higher TiO_2 (up to 0.38 wt.%) and lower Fe_2O_3 (less than 0.01 wt.%) contents of Quy Chau and Mong Hsu rubies.

Table VII: Solid inclusions identified in Khoan Thong samples T1 and T2, compared to those recorded in trapiche rubies from Mong Hsu.

Solid inclusions	Mong Hsu (Myanmar)			Khoan Thong (Vietnam)
	Schmetzer *et al.* (1996, 1999)	Sunagawa *et al.* (1999)	Garnier *et al.* (2002a, b)	This work
Calcite	X	X	X	X
Dolomite	X	X	X	
Silicates (K-Al-Fe±Ti)	X	X	X	X
Corundum		X	X	X
Muscovite				X
Biotite				X
Chlorite			X	
Andularia			X	
Rutile			X	X
Titanite			X	X
Graphite			X	
Baryte			X	
Pyrite			X	X
Mica			X	
Amphibole			X	
Zircon			X	X
Al-hydroxide			X	
Oxides/ hydroxides of Fe (±Ti±Mn)			X	X
Siderite			X	
Bastnaesite			X	
Anorthite				X
Margarite				X
Zoisite				X

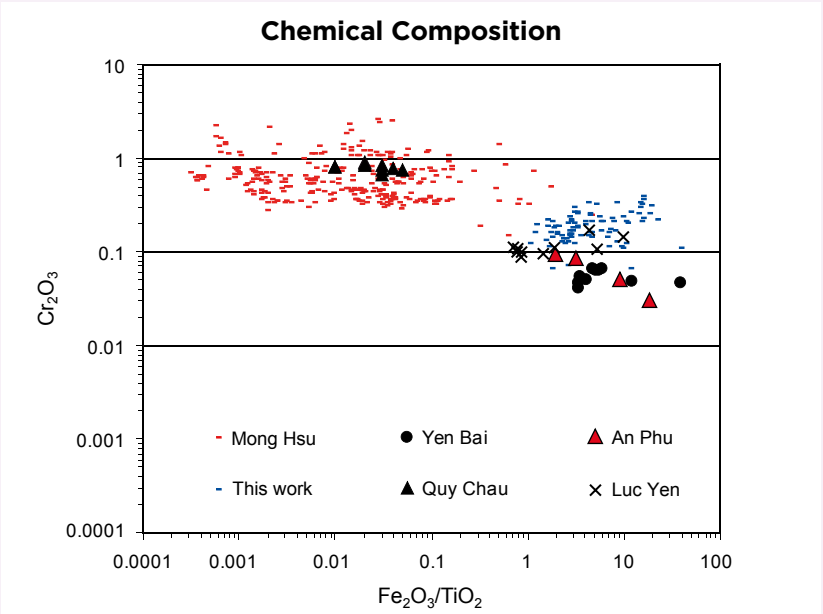

Figure 18: A plot of Cr_2O_3 versus Fe_2O_3/TiO_2 for the trapiche rubies from Khoan Thong analysed in this study is compared to data for trapiche rubies from Mong Hsu (Myanmar; Garnier *et al.* 2002b) and various Vietnamese deposits (Pham *et al.* 2004). Stones from Quy Chau (central Vietnam) and Mong Hsu have overlapping compositions, while those from northern Vietnam contain less Cr_2O_3 and have a greater ratio of Fe_2O_3/TiO_2.

According to the genetic model proposed for marble-hosted ruby deposits in Central and South East Asia by Garnier *et al.* (2008), the Vietnamese rubies formed during Tertiary regional metamorphism and are spatially related to major tectonic structures formed during the Himalayan orogenesis. The sediments of the Paleo-Tethys basin were metamorphosed in the amphibolite facies, transforming carbonates into marbles. The Al, Cr and V necessary for the formation of ruby were mobilised from micas, clay minerals and/or organic matter present in the sedimentary photoliths. Rubies formed during the beginning of the retrograde metamorphic path at 620–670°C and 2.6–3.3 kbar (Garnier 2003). The trapiche rubies formed from the same parental fluids as non-trapiche rubies in the same metamorphic zones within the Luc Yen and An Phu mining areas (Giuliani *et al.* 2015a, 2018). Moreover, the transformation of ruby and anorthite to margarite occurred at lower temperature and pressure conditions (450–500°C and <2 kbar) during retrograde metamorphism.

It is worth noting that the corundum inclusions in the sector boundaries have a similar composition as the small inclusion at the centre of sample T1 (Table III), suggesting that they formed at the same time and under the same conditions. This also means that the trapiche texture formed very quickly, such that the core did not have enough time to develop. According to the formation model proposed by Sunagawa *et al.* (1999), the core seems to be 'frozen' just after the nucleation stage (step 1 in Figure 19). Its development is hindered by the rapid formation of the sector boundaries which enveloped it (step 2). The growth sectors developed at a later stage (step 3), filling the interstices left between the sector boundaries. The rapid formation of the trapiche texture is proven by the elevated number of trapped inclusions and the formation of tube-like voids. When an inclusion is trapped, a channel can develop in the growth direction behind the inclusion, or in front of it if the inclusion moves along the growth direction. This formation mechanism was proposed for similar voids in trapiche tourmalines (Schmetzer *et al.* 2011). However, the fact that the tube-like voids are perpendicular to the faces of the ruby crystals suggests another possible mechanism of formation. They also could form by dissolution along bundles of dislocations after changes in driving-force conditions that occurred during the crystal growth (Scandale & Zarka 1982; Authier & Zarka 1994).

The three growth steps are governed by changes in driving-force conditions (Sunagawa *et al.* 1999). First, a small core can form under low driving-force conditions through layer-by-layer growth (step 1). After driving-force conditions increase, adhesive-type growth takes place, forming the sector boundaries, which constitute the 'skeleton' of the trapiche ruby (step 2). Finally, a decrease in the driving force lets the growth sectors and corresponding crystal faces develop through ordinary layer-by-layer growth (step 3). The morphological stability of the interface is dependent on the driving-force conditions (Sunagawa 2005). At the beginning, a

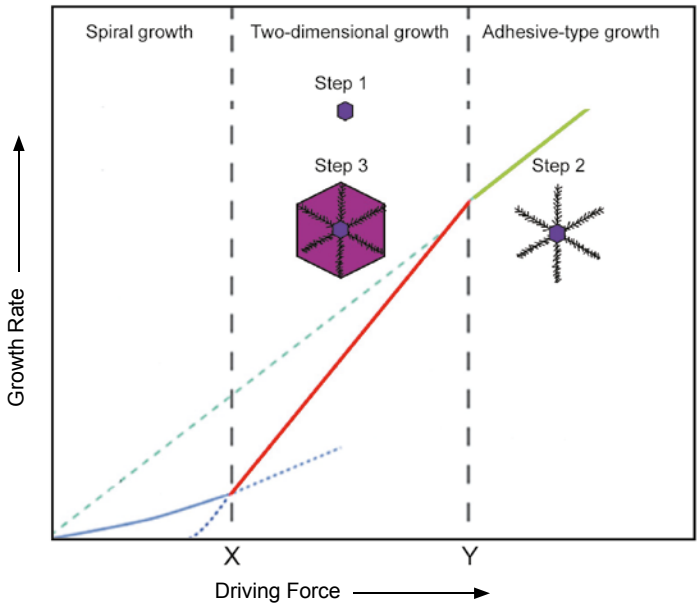

Figure 19: A diagram of growth rate versus driving force of crystallisation (modified from Sunagawa *et al.* 1999) shows the three development steps for trapiche texture in rubies from Khoan Thong. The positions marked by X and Y indicate changes in the predominant growth mechanism according to the driving force of crystallisation. The coloured lines represent growth rate versus driving force relations for spiral, two-dimensional and adhesive-type growth mechanisms. The dashed lines indicate where a particular growth mechanism is not stable.

core with smooth, flat interfaces forms, but when the driving force increases, the interface morphology loses its stability, resulting in one that is rough and dendritic. A further change in driving-force conditions will yield a euhedral ruby bounded by flat faces, with the dendritic 'skeleton' visible inside (Sunagawa 2005).

The changes in the driving-force conditions reflect variations in the growth medium (i.e. fluid composition, temperature and/or pressure). The fluid composition does not change during the rapid development of the trapiche texture, as witnessed by the fact that the corundum in the centre of the trapiche ruby has almost the same chemistry as the corundum inclusions (Crd2) in the sector boundaries. A variation of temperature was hypothesised by Garnier *et al.* (2002a) to explain the formation of Mong Hsu trapiche rubies. They suggested that the layer-by-layer growth became unstable when supercooling occurred and adhesive-type growth took over to form the sector boundaries. The chemical elements not included in the crystal structure of corundum (e.g. Ca and Mg) were pushed towards the sector boundaries and contributed to the formation of solid inclusions there. However, a rapid cooling is in disagreement with the rather stable thermal conditions of the regional metamorphism in Central and South East Asia (Giuliani *et al.* 2018).

A more plausible hypothesis involves variations in fluid pressure. The devolatilisation reactions of carbonate rocks during metamorphism produced a fluid overpressure until hydraulic fracturing occurred and, therefore, provoked an increase in the driving force. At this stage, the core and sector boundaries would have formed quickly and almost at the same time. The opening of fractures and cavities in the marbles led to a decrease of fluid pressure and, therefore, of the driving force (Giuliani *et al.* 2018). This allowed for the formation of the growth sectors that completed the trapiche texture.

CONCLUSIONS

The main conclusions of this study of two trapiche rubies from Khoan Thong can be summarised as follows:

(1) The expected hexagonal core is not well developed, and elongated tube-like voids extend from the sector boundaries into the growth sectors. The voids are filled by solid and fluid inclusions. The sector boundaries contain different syngenetic solid inclusions, in particular margarite that formed at the expense of ruby and anorthite during the retrograde metamorphic path.

Figure 20: This ruby from Tai Dinh near Minh Tien in northern Vietnam exhibits well-developed trapiche texture. Photo by Shang-i (Edward) Liu.

(2) Their chemical composition plots within the field of Vietnamese rubies hosted in marbles. Their Fe_2O_3/TiO_2 ratios (>1) are higher than those of trapiche rubies from Quy Chau (central Vietnam) and Mong Hsu (Myanmar), while their Cr_2O_3 contents are lower (<0.39 wt.%).

(3) The main mineral assemblage of inclusions in equilibrium—anorthite and ruby—has been described for several non-trapiche rubies hosted in marbles from Central and South East Asia, such as at An Phu, Vietnam. The very low amount of calcite and the absence of dolomite in the Khoan Thong trapiche rubies does not mean that these rubies could not have formed from the metamorphism of marble. It signifies that ruby did not form by the main metamorphic reaction involving the formation of corundum and dolomite through the destabilisation of spinel and calcite.

(4) A change of fluid pressure during formation was likely caused by local decompression and fracturing in the marbles. Such pressure variations enhance changes in driving-force conditions, leading to the formation of trapiche texture (e.g. Figure 20). The core forms first, followed by the sector boundaries and then the growth sectors, under high and low driving-force conditions, respectively.

REFERENCES

Authier, A. & Zarka, A. 1994. X-ray topographic study of the real structure of minerals. *In*: Marfunin, A.S. (ed) *Advanced Mineralogy Vol. 1—Composition, Structure, and Properties of Mineral Matter: Concepts, Results, and Problems*, Springer-Verlag, Berlin and Heidelberg, Germany, 221–233.

Garnier, V. 2003. *Les gisements de rubis associés aux marbres de l'Asie Centrale et du Sud-est: Génèse et caractérisation isotopique*. Ph.D. thesis, National Polytechnic Institute of Lorraine, Nancy, France, 390 pp.

Garnier, V., Ohnenstetter, D., Giuliani, G. & Schwarz, D. 2002a. Rubis trapiches de Mong Hsu, Myanmar. *Revue de Gemmologie A.F.G.*, No. 144, 5–12.

Garnier, V., Ohnenstetter, D., Giuliani, G., Blanc, P. & Schwarz, D. 2002b. Trace-element contents and cathodoluminescence of 'trapiche' rubies from Mong Hsu, Myanmar (Burma): Geological significance. *Mineralogy and Petrology*, **76**(3–4), 179–193, http://doi.org/10.1007/s007100200040.

Garnier, V., Giuliani, G., Ohnenstetter, D., Fallick, A.E., Dubessy, J., Banks, D., Vinh, H.Q., Lhomme, T., *et al.* 2008. Marble-hosted ruby deposits from Central and Southeast Asia: Towards a new genetic model. *Ore Geology Reviews*, **34**(1–2), 169–191, http://doi.org/10.1016/j.oregeorev.2008.03.003.

Giuliani, G., Dubessy, J., Banks, D., Hoàng, Q.V., Lhomme, T., Pironon, J., Garnier, V., Phan Trong, T., *et al.* 2003. CO_2–H_2S–COS–S_8–AlO(OH)-bearing fluid inclusions in ruby from marble-hosted deposits in Luc Yen area, North Vietnam. *Chemical Geology*, **194**(1–3), 167–185, http://doi.org/10.1016/s0009-2541(02)00276-0.

Giuliani, G., Dubessy, J., Banks, D.A., Lhomme, T. & Ohnenstetter, D. 2015a. Fluid inclusions in ruby from Asian marble deposits: Genetic implications. *European Journal of Mineralogy*, **27**(3), 393–404, http://doi.org/10.1127/ejm/2015/0027-2442.

Giuliani, G., Boiron, M.-C., Morlot, C., Raoul, J. & Chatagnier, P.-Y. 2015b. Gem News International: Demantoid garnet with giant fluid inclusions. *Gems & Gemology*, **51**(4), 446–448.

Giuliani, G., Dubessy, J., Pignatelli, I. & Schwarz, D. 2018. Fluid inclusions study of trapiche and non-trapiche rubies from the Mong Hsu deposit, Myanmar. *Canadian Mineralogist*, **56**(5), 691–703, http://doi.org/10.3749/canmin.1800013.

Hainschwang, T., Notari, F. & Anckar, B. 2007. Trapiche tourmaline from Zambia. *Gems & Gemology*, **43**(1), 36–46, http://doi.org/10.5741/gems.43.1.36.

Hlaing, T. 1991. A new Myanmar ruby deposit. *Australian Gemmologist*, **17**(2), 509–510.

Karampelas, S., Michel, J., Zheng-Cui, M., Schwarz, J.-O., Enzmann, F., Fritsch, E., Leu, L. & Krzemnicki, M.S. 2010. X-ray computed microtomography applied to pearls: Meth-odology, advantages, and limitations. *Gems & Gemology*, **46**(2), 122–127, http://doi.org/10.5741/gems.46.2.122.

Leloup, P.H. & Kienast, J.-R. 1993. High-temperature metamorphism in a major strike-slip shear zone: The Ailao Shan–Red River, People's Republic of China. *Earth and Planetary Science Letters*, **118**(1–4), 213–234, http://doi.org/10.1016/0012-821x(93)90169-a.

Leloup, P.H., Lacassin, R., Tapponnier, P., Schärer, U., Zhong, D., Liu, X., Zhang, L., Ji, S., *et al.* 1995. The Ailao Shan–Red River shear zone (Yunnan, China), Tertiary transform boundary of Indochina. *Tectonophysics*, **251**(1–4), 3–84, http://doi.org/10.1016/0040-1951(95)00070-4.

Leloup, P.H., Arnaud, N., Lacassin, R., Kienast, J.R., Harrison, T.M., Trong, T.T.P., Replumaz, A. & Tapponnier, P. 2001. New constraints on the structure, thermochronology, and timing of the Ailao Shan-Red River shear zone, SE Asia. *Journal of Geophysical Research: Solid Earth*, **106**(B4), 6683–6732, http://doi.org/10.1029/2000jb900322.

McKague, H.L. 1964. Trapiche emeralds from Colombia, Part I. *Gems & Gemology*, **11**(7), 210–223.

Morlot, C., Pignatelli, I., Giuliani, G., Sterpenich, J., Boiron, M.-C., Ohnenstetter, D., Andriamamonjy, A., Raoul, J., *et al.* 2016. La tomographie à rayons X et ses applications en gemmologie : exemples de l'émeraude trapiche et du grenat démantoïde. *Revue de Gemmologie A.F.G.*, No. 198, 13–18.

Nam, T.N., Toriumi, M. & Itaya, T. 1998. P–T–t paths and post-metamorphic exhumation of the Day Nui Con Voi shear zone in Vietnam. *Tectonophysics*, **290**(3–4), 299–318, http://doi.org/10.1016/s0040-1951(98)00054-7.

Nassau, K. & Jackson, K.A. 1970. Trapiche emeralds from Chivor and Muzo, Colombia. *American Mineralogist*, **55**(3–4), 416–427.

Peretti, A., Schmetzer, K., Bernhardt, H.-J. & Mouawad, F. 1995. Rubies from Mong Hsu. *Gems & Gemology*, **31**(1), 2–26, http://doi.org/10.5741/gems.31.1.2.

Peretti, A., Mullis, J. & Mouawad, F. 1996. The role of fluorine in the formation of colour zoning in rubies from Mong Hsu, Myanmar (Burma). *Journal of Gemmology*, **25**(1), 3–19, http://doi.org/10.15506/JoG.1996.25.1.3.

Pham, V.L., Hoàng, Q.V., Garnier, V., Giuliani, G. & Ohnenstetter, D. 2004. Marble-hosted ruby from Vietnam. *Canadian Gemmologist*, **25**(3), 83–95.

Pham, V.L., Pardieu, V. & Giuliani, G. 2013. Update on gemstone mining in Luc Yen, Vietnam. *Gems & Gemology*, **49**(4), 233–245, http://doi.org/10.5741/gems.49.4.233.

Pham, V.L., Giuliani, G., Fallick, A.E., Boyce, A.J. & Pardieu, V. 2018. Trace elements and oxygen isotopes of gem spinels in marble from the Luc Yen – An Phu areas, Yen Bai Province, North Vietnam. *Vietnam Journal of Earth Sciences*, **40**(2), 165–177, http://doi.org/10.15625/0866-7187/40/2/12241.

Pignatelli, I., Giuliani, G., Ohnenstetter, D., Agrosi, G., Mathieu, S., Morlot, C. & Branquet, Y. 2015. Colombian trapiche emeralds: Recent advances in understanding their formation. *Gems & Gemology*, **51**(3), 222–259, http://doi.org/10.5741/gems.51.3.222.

Pignatelli, I., Giuliani, G., Morlot, C., Rouer, O., Claiser, N., Chatagnier, P.-Y. & Goubert, D. 2017. Recent advances in understanding the similarities and differences of Colombian euclases. *Canadian Mineralogist*, **55**(4), 799–820, http://doi.org/10.3749/canmin.1700011.

Richard, A., Morlot, C., Créon, L., Beaudoin, N., Balitsky, V.S., Pentelei, S., Dyja-Person, V., Giuliani, G., *et al.* 2019. Advances in 3D imaging and volumetric reconstruction of fluid and melt inclusions by high resolution X-ray computed tomography. *Chemical Geology*, **508**, 3–14, http://doi.org/10.1016/j.chemgeo.2018.06.012.

Scandale, E. & Zarka, A. 1982. Sur l'origine des canaux dans les cristaux. *Journal of Applied Crystallography*, **15**(4), 417–422, http://doi.org/10.1107/s0021889882012291 (in French).

Schmetzer, K., Beili, Z., Yan, G., Bernhardt, H.-J. & Hänni, H.A. 1999. Element mapping of trapiche rubies. *Journal of Gemmology*, **26**(5), 289–301, http://doi.org/10.15506/JoG.1999.26.5.289.

Schmetzer, K., Bernhardt, H.-J. & Hainschwang, T. 2011. Chemical and growth zoning in trapiche tourmaline from Zambia — A re-evaluation. *Journal of Gemmology*, **32**(5), 151–173, http://doi.org/10.15506/JoG.2011.32.5.151.

Schwarz, D., Bernhardt, H.-J., Hänni, H.A. & Schmetzer, K. 1996. Trapiche rubies. *Gems & Gemology*, **32**(4), 242–250, http://doi.org/10.5741/gems.32.4.242.

Sunagawa, I. 2005. *Crystals: Growth, Morphology and Perfection*. Cambridge University Press, Cambridge, 295 pp.

Sunagawa, I., Bernhardt, H.-J. & Schmetzer, K. 1999. Texture formation and element partitioning in trapiche ruby. *Journal of Crystal Growth*, **206**(4), 322–330, http://doi.org/10.1016/s0022-0248(99)00331-0.

Sutherland, F.L., Coenraads, R.R., Schwarz, D., Raynor, L.R., Barron, B.J. & Webb, G.B. 2003. Al-rich diopside in alluvial ruby and corundum-bearing xenoliths, Australian and SE Asian basalt fields. *Mineralogical Magazine*, **67**(4), 717–732, http://doi.org/10.1180/0026461036740129.

Touray, J.C. & Poirot, J.P. 1968. Observations sur les inclusions fluides primaires de l'émeraude et leurs relations avec les inclusions solides. *Comptes Rendus de l'Académie des Sciences, Paris*, **266**, Série D, 305–308.

Win, K.K. 2005. Trapiche of Myanmar. *Australian Gemmologist*, **22**(6), 269–270.

The Authors

Dr Isabella Pignatelli
Université de Lorraine, GeoResources UMR 7359 CNRS-UL, BP 70239, 54506 Vandœuvre-lès-Nancy cedex, France
Email: isabella.pignatelli@univ-lorraine.fr

Dr Gaston Giuliani
Université Paul Sabatier, GET/IRD, UMR CNRS-IRD-CNES 5563, 14 avenue Edouard Belin, 31400 Toulouse, France

and

Université de Lorraine, CRPG UMR 7358 CNRS-UL, 15 rue Notre-Dame-des-Pauvres, BP 20, 54501 Vandœuvre-lès-Nancy cedex, France

Christophe Morlot
Université de Lorraine, GeoResources UMR 7359 CNRS-UL, BP 70239, 54506 Vandœuvre-lès-Nancy cedex, France

Dr Pham Van Long
Institute for Gems and Gold Research of Vinagems, 15 Ngoc Hoi, Hoang Liet, Hoang Mai, Hanoi, Vietnam

Acknowledgements

The authors thank Dr Olivier Rouer of the Service Commun de Microscopie Électronique et de Microanalyses laboratory at the University of Lorraine for the EPMA analyses. Corrections and suggestions from three anonymous reviewers helped improve the final version of the manuscript. We also thank Dr Shang-i (Edward) Liu for the photographs in Figures 1 and 20.

APPENDIX

Table A-1: Chemical composition (wt.%) by EPMA of alluvial trapiche rubies from the An Phu, Luc Yen, Yen Bai and Quy Chau mining areas in Vietnam (Pham *et al.* 2004; G. Giuliani unpublished data).

Analysis	MgO	Al_2O_3	TiO_2	V_2O_3	Cr_2O_3	Fe_2O_3	Ga_2O_3	Total
An Phu (Northern Vietnam)								
AP1	nd	98.73	0.080	0.005	0.080	0.255	0.014	99.16
AP2	nd	98.60	0.127	0.006	0.092	0.246	0.009	99.08
AP3	nd	98.75	0.015	0.006	0.029	0.279	0.013	99.09
AP4	nd	99.19	0.023	0.006	0.048	0.297	0.018	99.58
Luc Yen (Northern Vietnam)								
LY1	0.001	99.36	0.196	0.004	0.087	0.173	0.010	99.83
LY2	0.001	99.70	0.216	0.007	0.103	0.174	0.015	100.22
LY3	0.001	99.67	0.228	0.005	0.098	0.178	0.014	100.19
LY4	0.001	99.85	0.275	0.006	0.107	0.200	0.016	100.45
LY5	nd	99.81	0.123	0.004	0.095	0.179	0.015	100.23
LY6	nd	100.06	0.089	0.008	0.107	0.172	0.010	100.45
LY7	0.001	99.73	0.208	0.003	0.096	0.178	0.016	100.23
LY8	nd	99.77	0.031	0.006	0.103	0.166	0.015	100.09
LY9	nd	99.72	0.016	0.006	0.142	0.162	0.013	100.06
LY10	0.001	99.46	0.038	0.015	0.166	0.164	0.015	99.86
Yen Bai (Northern Vietnam)								
YB1	nd	100.88	0.086	0.005	0.044	0.288	0.007	101.31
YB2	0.002	100.04	0.073	0.005	0.047	0.288	0.008	100.46
YB3	nd	100.21	0.093	0.005	0.047	0.319	0.007	100.68
YB4	nd	100.58	0.066	0.003	0.051	0.267	0.004	100.97
YB5	nd	100.38	0.020	0.002	0.049	0.239	0.008	100.70
YB6	0.002	99.89	0.067	0.004	0.054	0.233	0.007	100.26
YB7	nd	98.55	0.051	0.002	0.066	0.308	0.010	98.99
YB8	nd	98.81	0.060	0.003	0.066	0.283	0.010	99.23
YB9	nd	99.94	0.048	0.004	0.063	0.263	0.009	100.33
YB10	nd	98.86	0.050	0.001	0.064	0.259	0.008	99.24
Quy Chau (Central Vietnam)								
QC1	0.001	98.65	0.380	0.029	0.897	0.008	0.011	99.99
QC2	0.011	98.23	0.340	0.028	0.838	0.006	0.012	99.47
QC3	0.012	98.99	0.340	0.032	0.915	0.004	0.011	100.30
QC4	0.007	98.51	0.290	0.029	0.749	0.010	0.005	99.61
QC5	0.003	99.03	0.180	0.031	0.768	0.007	0.013	100.03
QC6	0.004	99.37	0.120	0.037	0.764	0.005	0.012	100.31
QC7	0.009	98.30	0.300	0.047	0.869	0.007	0.010	99.54
QC8	0.009	99.16	0.250	0.040	0.832	0.007	0.009	100.31
QC9	0.011	98.76	0.320	0.045	0.818	0.005	0.010	99.98
QC10	0.006	99.12	0.260	0.048	0.670	0.009	0.009	100.12

Clays and Clay Minerals, Vol. 68, No. 4:394–412, 2020

THE EFFECT OF THE STARTING MINERALOGICAL MIXTURE ON THE NATURE OF Fe-SERPENTINES OBTAINED DURING HYDROTHERMAL SYNTHESIS AT 90°C

Isabella Pignatelli[1]*, Régine Mosser-Ruck[1], Enrico Mugnaioli[2], Jérôme Sterpenich[1], and Mauro Gemmi[2]

[1]Georessources UMR 7359 CNRS-UL, Université de Lorraine, BP 70239, 54506 Vandœuvre-lès-Nancy, Cedex, France
[2]Center for Nanotechnology Innovation@NEST, Istituto Italiano di Tecnologia, Piazza San Silvestro 12, 56127 Pisa, Italy

Abstract—The formation conditions and stability fields of Fe-serpentines are still poorly understood in both terrestrial (natural or anthropic) and extraterrestrial environments. Knowledge of the effects of physical-chemical parameters on compositional and structural features of Fe-serpentines is lacking, and only a few thermodynamic parameters of these minerals are available in the literature. To fill these gaps, the synthesis of these minerals, while controlling all the physicochemical experimental parameters, was undertaken. Two hydrothermal syntheses were carried out at 90°C to investigate the effect of two different starting mineralogical mixtures on the nature of Fe-serpentines. The run products were identified by several analytical techniques (powder X-ray diffraction, transmission, and scanning electron microscopy). Berthierine crystals were synthesized from a starting mixture of kaolinite and metal iron. The berthierines synthesized show different morphologies and iron contents (~3–38 at.%). From a starting mineralogical mixture composed of quartz and metal iron, cronstedtite crystallizes. Most of the crystals are 1*M* polytypes. Magnetite is always associated with both berthierine and cronstedtite. Lepidocrocite was observed only in the experiment with kaolinite. These experimental results demonstrated that Fe enrichment in serpentines depends on the silicate precursor (kaolinite or quartz) of the starting mixture. The results are also in agreement with the geochemical equilibrium predicted by thermodynamic modeling, i.e. the formation of berthierine and cronstedtite in association with magnetite at the expense of metal iron and silicates.

Keywords—Berthierine · Cronstedtite · Fe-serpentines · Hydrothermal synthesis

INTRODUCTION

Berthierine, cronstedtite, greenalite, and odinite are Fe-bearing serpentines, phyllosilicate minerals which consist of a tetrahedral and an octahedral sheet (T–O or 1:1 layer). Their general formula is $M_3T_2O_5(OH)_4$, where T are the tetrahedral sites generally occupied by Si^{4+} and Al^{3+} and *M* are divalent or trivalent cations in octahedral coordination, such as Fe^{3+}, Fe^{2+}, Al^{3+}, Mg^{2+}. The octahedral sheet contains three *M* sites but the presence of cations with different oxidation states or valences implies an intermediate occupancy between di- and trioctahedral for most of them.

Cronstedtite $(Fe^{2+}_{3-x}\,Fe^{3+}_{x})(Si_{2-x}\,Fe^{3+}_{x})O_5(OH)_4$ is an exception because: (1) there are no vacant sites in the octahedral sheet; and (2) it contains tetrahedrally coordinated Fe^{3+} (Bailey 1969; Geiger et al. 1983; Smrčok et al. 1994; Hybler et al. 2000, 2002; Kogure et al. 2002). The same features are shown by a rare Fe-bearing serpentine, guidottiite, the Mn-analogue of cronstedtite with the formula $(Mn_{1.86}Fe^{3+}_{0.61}Mg_{0.54})(Si_{1.36}Fe^{3+}_{0.64})O_5(OH)_4$ (Wahle et al. 2010).

Fe-serpentines form during fluid–rock interactions in both extraterrestrial and terrestrial environments. In the terrestrial one, these minerals can be formed in natural and anthropic contexts. On Earth, greenalite $(Fe^{2+}_{a}Fe^{3+}_{b}Mg_{c}\square_{d})_{\Sigma=3}Si_2O_5(OH)_4$ ($a > b$ and $(a + b) > (c + d)$; Guggenheim et al. 1982) occurs in metamorphosed Archean banded-iron formations at $T < 450$°C (Gole 1980a, 1980b), where it may have precipitated under anoxic, ferruginous, marine conditions (Tosca et al. 2016). Odinite $(R^{3+}_{a}R^{2+}_{b}\square_{c})_{\Sigma=3}(Si_{2-x}\,Al_x)O_5(OH)_4$ (with $a > b$, R^{3+} and R^{2+} dominantly Fe and Mg, respectively) is believed to form at 25°C in marine waters at the sediment–water interface (Bailey 1988). It occurs in shallow marine shelfs and reef lagoonal areas in tropical latitudes where it is associated with biogenic carbonate and fluviatile systems. This mineral is not found in sediments older than Recent due to its alterability to chlorite (Bailey 1988). Berthierine $(R^{2+}_{a}R^{3+}_{b}\square_{c})_{\Sigma=3}(Si_{2-x}\,Al_x)O_5(OH)_4$ (Brindley 1982) is found in marine and brackish oolitic ironstone formations (Hornibrook and Longstaffe 1996). It can form by the diagenetic transformation of kaolinite under slightly alkaline conditions at $T < 160$°C (Iijima and Matsumoto 1982; Bhattacharyya 1983). Berthierine can also form by hydrothermal and diagenetic processes in a marine sedimentary exhalative environment where it is associated with siderite, organic matter, and magnetite (Rivas-Sanchez et al. 2006). Cronstedtite is observed in low-*T* hydrothermal veins associated with pyrite, quartz, carbonates (siderite, calcite), and sphalerite (Frondel 1962; López-García et al. 1992; Hybler et al. 2016, 2017).

Fe-serpentines are found also on other bodies of the Solar System. Berthierine crystals have been found in the Nakhla Martian meteorite as an alteration product of melt inclusion glasses within olivine phenocrysts (Lee and Chatzitheodoris 2016). These crystals are Al depleted and Fe enriched in comparison to terrestrial berthierine due to an interstratification with another Fe-serpentine, likely greenalite. A serpentine containing only ferric iron and with composition similar to that

* E-mail address of corresponding author: isabella.pignatelli@univ-lorraine.fr
DOI: 10.1007/s42860-020-00080-y

of odinite occurred in the mesostasis fractures of Martian meteorite, Lafayette (Hicks et al. 2014). A complex mixture of Fe-phyllosilicates is also found within veins and mesostasis of this Martian meteorite, and TEM data are consistent with a mixture of a Fe-smectite with Fe-serpentines having a berthierine-type composition (Changela and Bridges 2011). Visible and near-infrared spectroscopic data suggested the occurrence of: (1) cronstedtite and greenalite in some dark regions of Mars (Calvin 1998); (2) cronstedtite on the dwarf planet Ceres (Zolotov 2014); and (3) berthierine in CI and CM meteorites such as Orgueil, Murchison, and Murray (Calvin and King 1997). Other analytical techniques (electron probe microanalysis - EPMA, scanning and transmission electron microscopy – SEM/TEM) confirmed the presence of Fe-serpentine, in particular cronstedtite and greenalite, in both the fine-rims and the matrices of CM meteorites where they are mixed with Mg-serpentines (Barber 1981; Browning et al. 1996; Lauretta et al. 2000; Elmaleh et al. 2012, 2015). Cronstedtite crystals also occur in pseudomorphs after olivine and pyroxene of a CM meteorite known as Paris (Pignatelli et al. 2016, 2017, 2018).

In the anthropic context, thermodynamic modeling and experimental data predicted the formation of Fe-serpentines during iron–clay interactions simulating the conditions of radioactive-waste disposal facilities in multi-barrier systems (e.g. Wilson et al. 2006; Mosser-Ruck et al. 2010; de Combarieu et al. 2011; Pignatelli et al. 2014, etc.). Although many studies have been carried out during the last 20 years, the formation of Fe-serpentines is still under investigation because it could modify the chemical, physical, and mechanical properties of clay barriers with time (Bildstein et al. 2006).

Whatever the environment, the formation conditions and the stability fields of Fe-serpentines are poorly understood, although it is important that they be reconstructed so that the fluid–rock interactions and the chemical environments during the evolution of Earth and other bodies of the Solar System are better understood better (Zolensky and Keller 1999). In particular, there is a lack of knowledge about the effects of physical-chemical parameters (temperature, fluid composition, water/solid ratio, etc.) on compositional and structural features of Fe-serpentines, above all on cation substitutions. This knowledge is fundamental for comparing terrestrial and extraterrestrial Fe-serpentines in order to check if their similarities are simply fortuitous, or, on the contrary, they can give important information about analogous processes in both environments (Zolensky 1984).

The main objectives of this study were (1) to synthesize Fe-serpentines using a new procedure (two different silicate precursors, rather than gels, in a chloride solution at 90°C); (2) to investigate the effect of the two different starting mineralogical mixtures on the nature of Fe-serpentines; and (3) to compare the experimental run products with geochemical equilibria calculated by thermodynamic modeling.

MATERIALS AND METHODS

Batch experiments were carried out using Parr® non/stirred pressure vessels (Parr Instrument Company, Moline, Illinois, USA) made of Teflon® (capacity of 23 mL) at a temperature of 90°C. The samples were labeled K90 and Q90 because the starting mineralogical mixtures were made, respectively, of kaolinite (1 g) or Fontainebleau sandstone (1 g), each mixed with 500 mg of metal iron powder to give a mass ratio of 0.5. A commercial kaolinite supplied by Sigma-Aldrich Co. (Darmstadt, Germany; Catalog #K7375; Ø 0.1–0.4 μm) and Fontainebleau sandstone were used. Minerals rather than gels were used as starting materials to better simulate the fluid–rock interactions occurring in natural and anthropic environments, as well as to favor the formation of well crystalline serpentines. The Fontainebleau sandstone was chosen because it is composed almost entirely of quartz, with traces of clay minerals (kaolinite, illite, smectite), feldspars, calcite, siderite, and chalcedony (SiO_2 = 99.5% – Kreutzer et al. 2017; Saadi et al. 2017). Powdered metal iron with a purity of 99.9% and mean grain size of 40 μm was provided by Sigma Aldrich. The starting mixtures were prepared in a glove box under inert argon atmosphere and added to a chlorine solution with $pH_{25°C}$ = 6.4 (NaCl 22 mmol L^{-1} + $CaCl_2$ 2.9 mmol L^{-1}) in agreement with previous studies on Fe-serpentine formation (Guillaume et al. 2003; Mosser-Ruck et al. 2010; Pignatelli et al. 2013; Rivard et al. 2013a; Bourdelle et al. 2014, 2017). A solution having the same composition was used because the dissolution of silicates is enhanced by the presence of alkaline or alkaline earth cations (e.g. Dove and Crerar 1990; Dove and Elston 1992; Dove et al. 2005). Silicate dissolution releases Si in solution, thus favoring the formation of Fe-serpentines. Both solution/kaolinite and solution/sandstone ratios were fixed at 10.

After 75 days, the vessels were opened in a glove box and prepared for analysis. The pH of the run solutions was measured, after cooling at room temperature, using a combination of a silver/sulfide electrode and 0.025 μm filtration. The accuracy of the pH measurement is 0.1. The electrode was calibrated using reference buffer solutions with pH 4, 7, and 10 certified by the Physikalisch-Technische Bundesanstalt (PTB, Germany) and the National Institute of Standards and Technology (NIST, USA). The run solutions were diluted ten times in 2 vol.% HNO_3 and analyzed at SARM laboratory (Université de Lorraine, France) by inductively coupled plasma optical emission spectroscopy (ICP-OES) with a Thermo Scientific iCAP 6500 spectrometer (Thermo Scientific, Waltham, Massachusetts, USA) to determine the concentrations of Si, Fe, and Al.

Powder X-ray diffraction (PXRD) was used to analyze the bulk run products (dried under an argon flux in the glove box) in order to identify the newly formed minerals. X-ray patterns were collected at LIEC laboratory (Université de Lorraine, France) at room temperature with a D8 Bruker diffractometer (Bruker, Billerica, Massachusetts, USA) using CoKα radiation (λ = 1.7902 Å), 35 kV accelerating voltage and 45 mA beam current. The analytical conditions of data collection were: scan step of 0.035°2θ, exposure time of 3 s, $2\theta_{min}$ = 3° to $2\theta_{max}$ = 74°. Scanning electron microscopy was used to obtain secondary electron (SE) and backscattered electron (BSE) images of run products, as well as energy dispersive X-ray (EDX) spectra. Both images and spectra were recorded at SCMEM laboratory

(Université de Lorraine, France) using a Hitachi S-4800 (Hitachi, Tokyo, Japan) cold field emission gun with an accelerating voltage of 15 kV and a beam current of 10 nA.

Transmission electron microscopy (TEM) was used to analyze the <2 μm fraction of run products. A drop of this fraction was dispersed in ethanol under ultrasonication (Fisherbrand™ S-Series Ultrasonic Cleaner, Thermo Fisher Scientific, Waltham, Massachusetts, USA) for a period of 3 min and then evaporated on a carbon film of a 200 mesh copper grid. The EDX spectra and three-dimensional electron diffraction (3D ED; Kolb et al. 2011; Mugnaioli and Gemmi 2018; Gemmi et al. 2019) were performed at the Center for Nanotechnology Innovation@NEST (Pisa, Italy) using a Zeiss Libra TEM (Zeiss, Jena, Germany) operating at 120 kV and equipped with a LaB_6 source and a Bruker EDS detector XFlash6T-60. The EDX data were collected using a probe diameter of ~100 nm and a counting time of 60–120 s. K_{AB} factors were determined without standards using the thin-specimen approximation of Cliff and Lorimer (1975).

3D ED acquisitions were done in STEM mode after defocusing the beam in order to have pseudo-parallel illumination of the sample. A beam diameter of ~150 nm was obtained by inserting a 5 μm C2 condenser aperture. An extremely mild illumination was adopted in order to avoid any alteration or amorphization of the sample during the 3D ED experiments. 3D ED was performed with a processing beam obtained by a Nanomegas Digistar P1000 device (Nanomegas, Brussels, Belgium). The precession semi-angle was kept at 1°. Independent data sets were recorded for each phase, with acquisition tilt ranges of ±40° and tilt step of 1°. Camera length was kept at 180 mm, with an actual resolution in reciprocal space of 0.75 Å. Conventional ED and 3D ED data were recorded using an ASI Timepix detector (Amsterdam Scientific Instruments, Amsterdam, The Netherlands), which was able to record the arrival of single electrons and deliver a pattern that is virtually background-free. These data were analyzed using *ADT3D* (Kolb et al. 2011) and in-house developed *MATLAB* routines.

Thermodynamic modeling was carried out using *PHREEQC* code (Parkhurst and Appelo 1999) in conjunction with the Thermoddem database of the BRGM institute (*Thermoddem V1.10* Code version 1.07_2.06, 2014). In that database, the cronstedtite formula is $Fe^{2+}{}_3(SiAl)O_5(OH)_4$, however, and it does not correspond to the correct one $(Fe^{2+}{}_{3-x}Fe^{3+}{}_x)(Si_{2-x}Fe^{3+}{}_x)O_5(OH)_4$ with $0 < x < 0.8$ (Geiger et al. 1983; Smrčok et al. 1994; Hybler et al. 2000, 2002; Kogure et al. 2002). Because of its Al content and the absence of iron in the tetrahedral sites, as well as the presence of only Fe^{2+}, the composition and thermodynamic data of cronstedtite reported by Wolery and Jove-Colon (2004) was used as previously by Zolotov (2014).

RESULTS

Kaolinite + Fe^0 Experiment (K90)

After heating at 90°C, the PXRD pattern underlined the slight decrease in reflection intensities for both kaolinite and metal iron in comparison to the starting sample (Fig. 1a), as well as the appearance of new reflections, corresponding to magnetite (35.1, 41.3, and 67.3°2θ, i.e. d_{hkl} 2.97, 2.53, and 1.62 Å) and lepidocrocite (16.4 and 31.5°2θ, i.e. d_{hkl} 6.28 and 3.30 Å). A more detailed analysis of the run product PXRD pattern showed other changes for the main kaolinite reflections: the reflection at 14.2°2θ (7.25 Å) shifted slightly toward higher angles and became broader, whereas that at 28.7°2θ (3.61 Å) showed a shoulder at 29.1°2θ (3.56 Å). These changes can be attributed to a loss of crystallinity, a partial dissolution of kaolinite, and the presence of new T–O phyllosilicates.

This was confirmed by the appearance of a small reflection at 38.3°2θ (2.72 Å) and by the decompositions of two regions on PXRD patterns performed using *DECOMPXR* software (Lanson 1997). This software allows for the subtraction of background and the decomposition of superimposed reflections into elementary ones with Gaussian and Lorentzian shapes (Lanson and Besson 1992; Lanson 1997). In the 13–15°2θ region of the PXRD pattern of the starting sample, the decomposition did not need more than one reflection at 14.2°2θ (7.25 Å), i.e. that of kaolinite, to obtain the best fit. At 90°C, the decomposition underlined the presence of two reflections: that of kaolinite at 14.2°2θ (7.25 Å) and a weaker one at 14.3°2θ (7.19 Å) corresponding to newly formed T–O phyllosilicates (Fig. 2).

Observations by SEM and semi-quantitative SEM-EDX analysis showed that T–O phyllosilicates were characterized by several morphologies and they differed from kaolinite in the presence of both Al and Fe (Fig. 3). Fe, Al, and Si contents were measured by TEM-EDX and plotted in a ternary diagram (Fig. 4). Newly formed T–O particles showed various Fe contents varying from ~3 to 38 atomic %. Particles enriched in Fe (~60–80 at. %) were also observed. The distribution field of all analyzed particles fell between the poles of kaolinite and berthierine, although the most Fe-enriched particles were closer to the cronstedtite pole. The linear trend representing the particles' composition was very close to the ideal one corresponding to the evolution of kaolinite toward cronstedtite, i.e. the most Fe-rich T–O phyllosilicate (Fig. 4).

Fontainebleau Sandstone + Fe^0 Experiment (Q90)

The PXRD pattern of run products showed the formation of Fe-bearing minerals, i.e. magnetite and T–O phyllosilicates (reflections at 14.5 and 29.1°2θ, i.e. d_{hkl} 7.13 and 3.55 Å – Fig. 1b). The crystals of newly formed T–O phyllosilicates were characterized by a pyramidal morphology with triangular or pseudo-hexagonal cross-sections. The latter were bigger and less abundant on SEM images (Fig. 5a,b). Few conical crystals were observed (Fig. 5d). These crystals contain only Si, Fe, and O (Fig. 5c). Their morphology is similar to that of natural terrestrial and extraterrestrial cronstedtite crystals (Hybler et al. 2000; Kogure et al. 2002; Pignatelli et al. 2018), and those synthetised by Pignatelli et al. (2013, 2014) from an experiment simulating the interaction of a claystone with iron between 90°C and 40°C.

The TEM-EDX data plotted in Fig. 6 were used to calculate the structural formula of cronstedtite pyramidal crystals, on the basis of 5 cations and adjusting the Fe^{3+}/Fe^{2+} ratio to obtain electroneutrality. The average formula is:

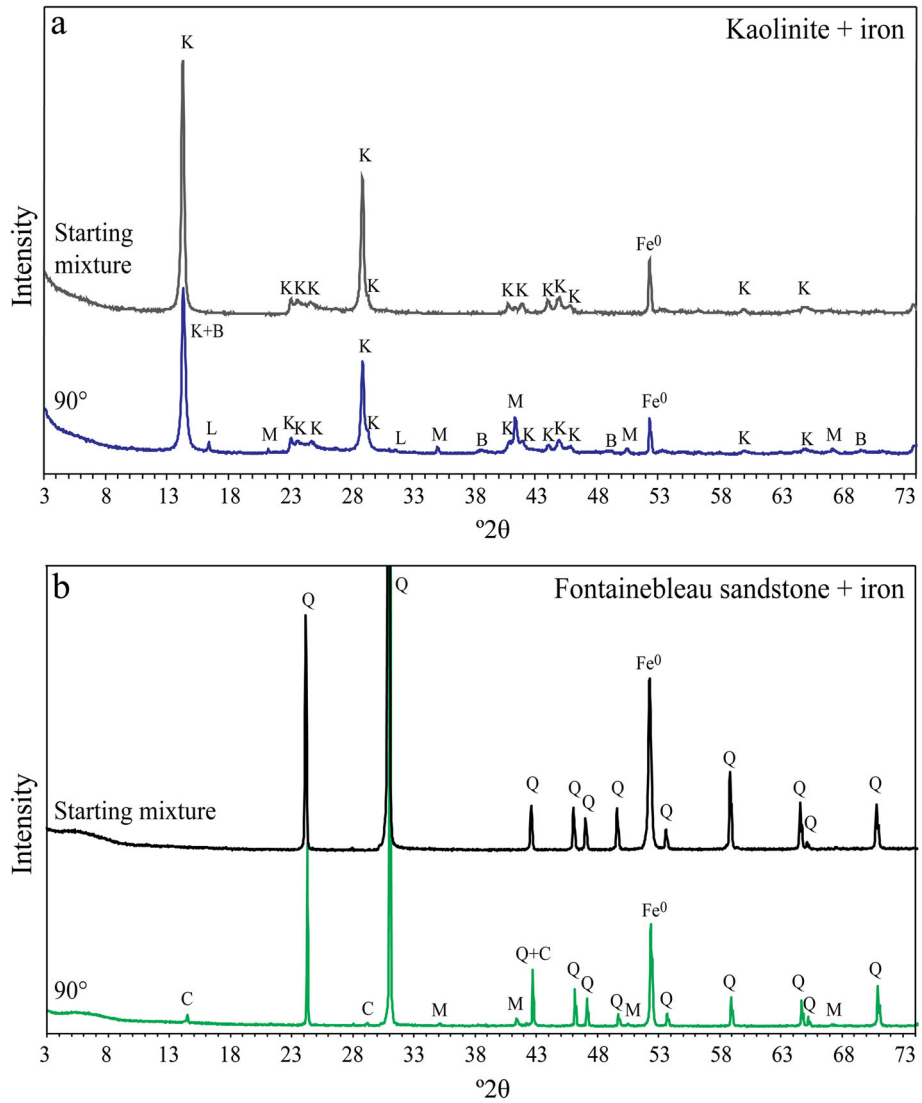

Fig. 1. a PXRD patterns of kaolin-iron starting mixture with a mass ratio kaolinite/iron of 0.5 (gray line) and run product at 90°C (blue line). **b** PXRD patterns of Fontainebleau sandstone-iron starting mixture with a mass ratio sandstone/iron of 0.5 (black line) and run product at 90°C (green line). K = kaolinite, M = magnetite, L = lepidocrocite, B = berthierine, Q = quartz, C = cronstedtite, Fe^0 = metal iron

$$\left(Fe^{2+}{}_{2.3}Fe^{3+}{}_{0.7}\right)\left(Si_{1.3}Fe^{3+}{}_{0.7}\right)O_5(OH)_4$$

The SAED patterns of cronstedtite crystals showed that some of them were characterized by streaking along the c^* axis typical of the stacking disorder in the polytypical sequence (Fig. 7d). Among the most ordered ones, 3D ED measurements enabled the identification of a 1*M* polytype by comparing 2D sections of the reconstructed 3D reciprocal space (Fig. 7) with the identification diagram for cronstedtite polytypes available in the literature (Smrčok and Weiss 1993; Ďurovič 1997; Hybler et al. 2008, 2018). In fact, the spot distribution along the [11*l*]* row on the $(hhl_{hex})^*$ plane suggested that the polytype belongs to Bailey's group A (Bailey 1969), whereas the spot distribution on the $(h0l_{hex})^*$ and $(h0l_{hex})^*$ planes corresponded to those of group I and II on the identification diagram. Moreover, 3D ED data indicated that the polytype is monoclinic with a *C*-centered cell and parameters a = 5.4(1) Å, and b = 9.3(2) Å, c = 7.4(1) Å, and β = 104.9(5)°, in agreement with the space group *Cm* of 1*M* polytype (Steadman and Nuttall 1964; Hybler 2014).

The SEM and TEM images also showed the presence of foil-like particles (Figs 8 and 9). These particles were nanocrystalline or amorphous as revealed by the presence of diffuse rings with few sharp diffraction spots in the SAED

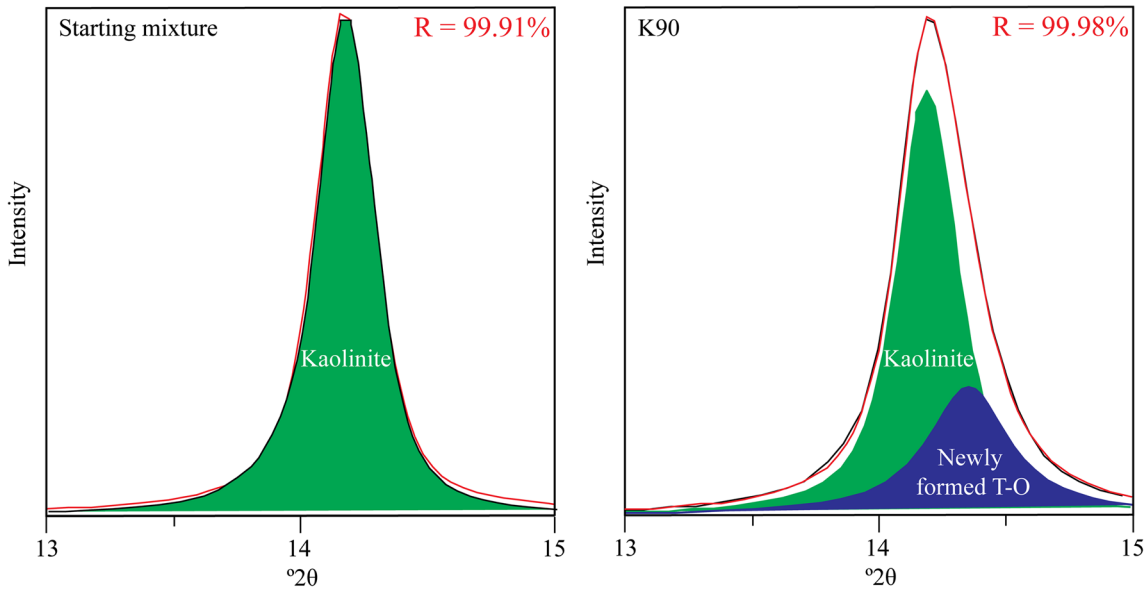

Fig. 2. Decomposition of PXRD patterns in the range 13–15°2θ for the starting mixture and run product of K90 experiment. Black line = experimental pattern, red line = fitting

patterns. Their indexation gave d_{hkl} values of ~4.8–4.5, 2.7, 2.5, and 1.5 Å and an angle of ~60° between the directions [100]* and [010]* (Fig. 9c, d, and e). These data are compatible with those of T–O phyllosilicates.

The compositions of foil-like particles were characterized by greater Si contents than those of cronstedtite crystals, which varied from ~34 to 38 at.% (Fig. 8). Their compositions were intermediate between those of cronstedtite and greenalite (Fig. 6). The average structural formula of these particles can be written as:

$$\left(Fe^{2+}_{2.8}Fe^{3+}_{0.2}\right)\left(Si_{1.8}Fe^{3+}_{0.2}\right)O_5(OH)_4$$

From the compositional point of view, these particles can be considered as being cronstedtite because they do not contain enough Si to fill the tetrahedral sites and consequently a small amount of Fe^{3+} is hypothesized to be present.

Run Solution Analysis

Very small amounts of Fe, Al, and Si were measured in the run solutions (<2 mg/L for K90 and <9 ml/L for Q90 – Table 1) and this suggests that almost all were incorporated into the structures of newly formed Fe serpentines (berthierine and cronstedtite) and also in iron (oxyhydr)oxides.

The presence of Al in the solution of experiment Q90 is likely due to the dissolution of trace minerals present in the Fontainebleau sandstone, such as clay minerals and feldspars (Kreutzer et al. 2017; Saadi et al. 2017).

Both the K90 and Q90 run solutions were supersaturated with respect to iron (oxyhydr)oxides other than magnetite and lepidocrocite (such as ferrihydrite, goethite, green rusts), but they were not detected analytically. However, the nucleation of metastable, poorly crystalline nanometric phases, for example ferrihydrite, during the experiment and/or the autoclave cooling cannot be excluded. According to the literature, when iron oxidizes in the presence of water, ferrihydrite is formed at first and it can transform to more thermodynamically stable hematite or goethite (Cudennec and Lecerf 2006; Liu et al. 2007). Although the run solutions were filtered before analysis, nanoparticles of ferrihydrite could pass through the filter and be present in the solutions, explaining why such amounts of iron were detected.

Thermodynamic Simulations

Thermodynamic tests were performed using *PHREEQC* software to simulate the following experimental observations: (1) kaolinite transformation into berthierine and more Fe-rich serpentines, such as greenalite or cronstedtite, associated with magnetite and lepidocrocite in experiment K90; (2) cronstedtite and magnetite formation in experiment Q90. The composition of the initial solution was simulated by adding Ca, Na, and Cl in the amounts described in the section "Materials and Methods", pH and pe were free to evolve, whereas the gas volume was fixed at 13 mL (taking into account the volume occupied by the solids and the solution in the autoclave).

A first simulation test at 90°C for both K90 and Q90 experiments consisted of reacting minerals with the aqueous solution to determine T–O phyllosilicates and iron (oxyhydr)oxides for which the solution presents a positive saturation index and are thus able to precipitate under the experimental conditions.

For experiment K90, they are greenalite, Fe^{2+}-berthierine, Fe^{3+}-berthierine, cronstedtite, magnetite, and lepidocrocite. The

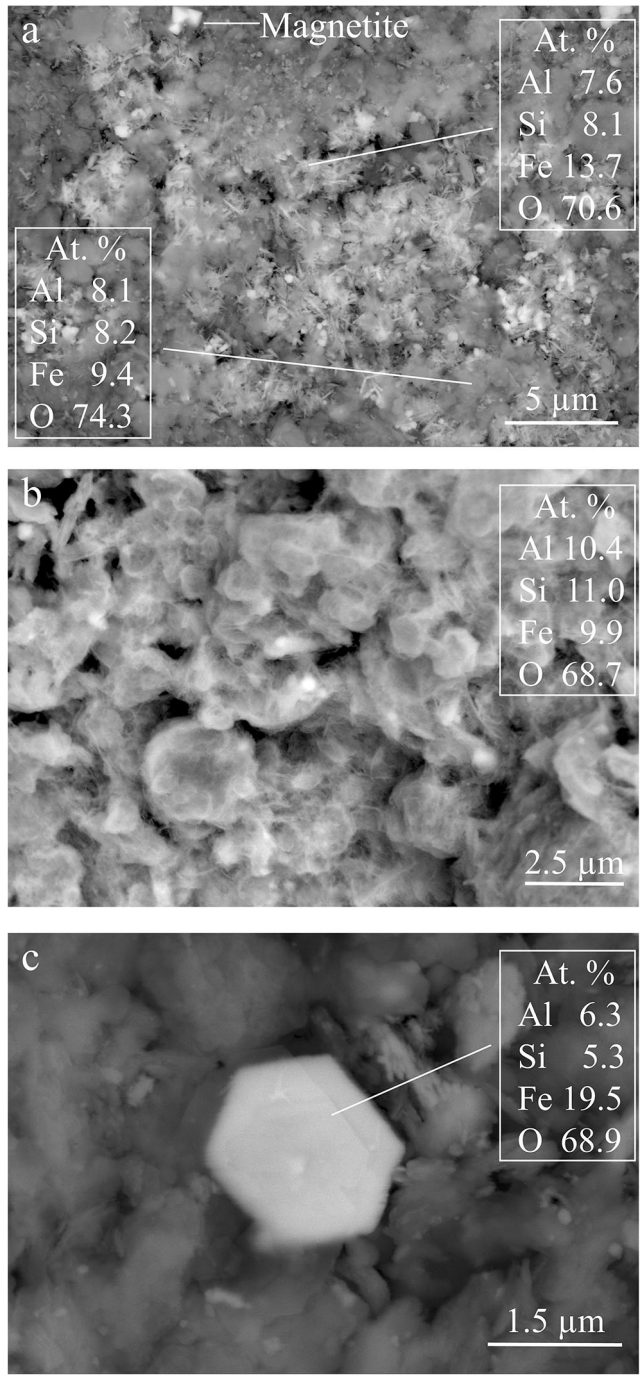

Fig. 3. BSE-SEM images and EDX data of run products in experiment K90. **a** Magnetite crystals mixed with newly formed T–O phyllosilicates. Other morphologies of T–O phyllosilicates characterized by **b** small and **c** large iron contents, respectively

solution is also over-saturated with respect to hematite and ferrihydrite, but they were not observed in the run products and thus were ignored in the first modeling. In the second simulation test, these minerals were able to precipitate. The results showed that kaolinite is partially dissolved (0.0024 moles), in agreement with the experimental results (Fig. 1a), and the final $pH_{90°C}$ was 7.02. Magnetite and lepidocrocite did not crystallize, nor did Fe^{3+}-berthierine. Although equilibrium is achieved in the model when all iron has been consumed, iron was still present in the run product at the end of the experiment (Fig. 1a). The modeling allowed for Fe^{2+}-berthierine and greenalite precipitation rather than cronstedtite. The most Fe-rich T–O phyllosilicates analyzed

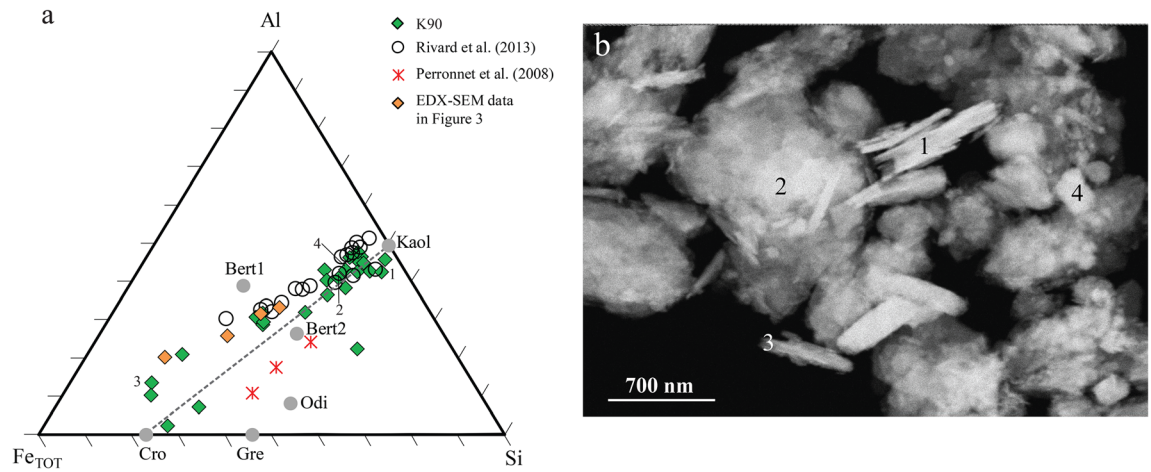

Fig. 4. **a** Al–Si–Fe_{tot} ternary diagrams of newly formed T–O phyllosilicates in the run product of kaolinite + Fe^0 experiment (K90). Their composition is compared with that of phyllosilicates synthesized by Rivard et al. (2013a) and Perronnet et al. (2008). The ideal trend (dashed gray line) indicating the compositional evolution from the dioctahedral pole of kaolinite toward the trioctahedral pole of cronstedtite is close to the experimental one. **b** STEM image of T–O phyllosilicates. Their TEM-EDX analyses indicated by numbers 1 to 4 are reported in the ternary diagram. Reference , indicated by gray circles, are: Kaol: kaolinite $Al_2Si_2O_5(OH)_4$; Gre: greenalite $(Fe^{2+}_{1.89}Fe^{3+}_{0.47}Mg_{0.32}\square_{0.31})Si_2O_5(OH)_4$ – Guggenheim et al. (1982); Bert1: berthierine $(Fe^{2+}_{1.49}Fe^{3+}_{0.22}Mg_{0.17}\square_{0.17})(Si_{1.15}Al_{0.85})O_5(OH)_4$; Bert2: berthierine $(Fe^{2+}_{1.01}Al_{0.82}Mg_{0.46}Fe^{3+}_{0.28}\square_{0.43})(Si_{1.74}Al_{0.26})O_5(OH)_4$ – Brindley (1982); Odi: odinite $(Fe^{3+}_{0.78}Mg_{0.77}Al_{0.56}Fe^{2+}_{0.28}Ti_{0.02}\ Mn_{0.01}\square_{0.58})(Si_{1.79}\ Al_{0.21})O_5(OH)_4$ – Bailey (1988); Cro: cronstedtite $(Fe^{2+}_{2.16}Fe^{3+}_{0.84})(Si_{1.16}\ Fe^{3+}_{0.84})O_5(OH)_4$ – Kogure et al. (2002)

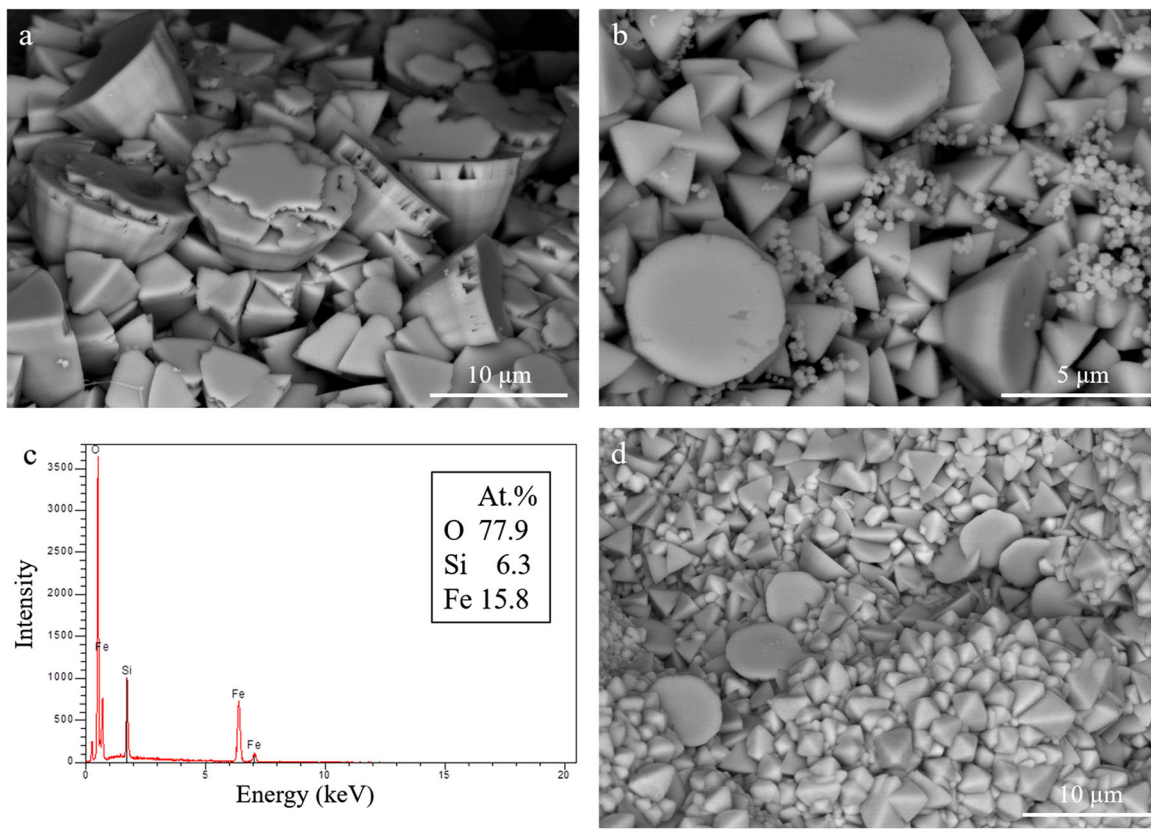

Fig. 5. **a**, **b** BSE-SEM images and **c** EDX data of cronstedtite in the experiment with Fontainebleau sandstone + Fe^0 at 90°C. They are characterized by a pyramidal morphology with triangular or pseudo-hexagonal cross sections. **d** BSE-SEM image of pyramidal and conical cronstedtites with magnetite crystals

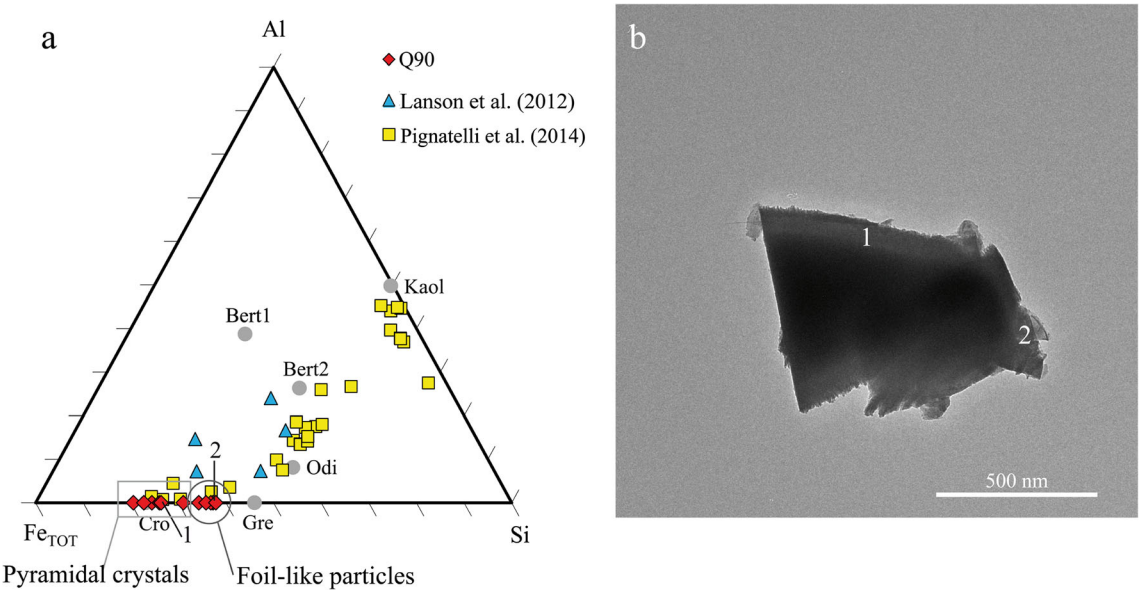

Fig. 6. a Al–Si–Fe_{tot} ternary diagram of newly formed T–O phyllosilicates in the run product of Fontainebleau sandstone + Fe^0 experiment (Q90). Reference are the same as in Fig. 4. **b** TEM image of cronstedtite observed in the Q90 run product

in the run product have compositions close to that of cronstedtite (Fig. 4). In a second run, greenalite was prevented from precipitating, implying the precipitation of cronstedtite together with Fe^{2+}-berthierine.

In order to understand why precipitation of magnetite and lepidocrocite were not predicted by the code, another simulation test was carried out by adding kaolinite gradually (10^{-4} moles/step for 39 steps) to mimic the reaction pathway. Lepidocrocite did not precipitate throughout the thermodynamic calculation. At the first step, iron is totally dissolved, magnetite, Fe^{2+}-berthierine, and cronstedtite form, and the pH reaches the value of 7.45. From the second step, the amount of cronstedtite increased slightly at the expense of magnetite, which dissolved completely when 0.0015 moles of kaolinite were dissolved ($pH_{90°C}$ = 7.25). At this point, the reaction ended because no source of iron was available form berthierine and cronstedtite (Fig. 10).

For experiment Q90, the list of minerals with a positive saturation index which may thus precipitate comprises of greenalite, cronstedtite, magnetite, lepidocrocite, ferrihydrite, and hematite. The last three were not observed in run products, thus they were ignored in further simulations. If both cronstedtite and greenalite are allowed to precipitate, cronstedtite never forms. Note (1) the greenalite formulae used in the database have the octahedral sites completely filled by Fe^{2+}, but greenalite can also contain Fe^{3+} (Guggenheim et al. 1982); (2) greenalite was not observed in the run product, whereas cronstedtite crystals were identified. For these reasons, greenalite was not allowed to precipitate in the subsequent simulation tests. The second simulation indicated that equilibrium was achieved when the amount of iron was completely consumed to form cronstedtite; the quartz was partially dissolved, but neither magnetite nor iron (oxyhydr)oxides were formed. Because cronstedtite was observed in association with magnetite in the run product, the hypothesis that the magnetite stability field decreases when the amount of Si in solution increases was tested. Thus, another simulation was carried out with a step-by-step addition of quartz (34 steps with increasing content of 0.0005 moles/step). The results indicated that both cronstedtite and magnetite formed and all of the iron was consumed in the first step. From the second step, the amount of cronstedtite increased at the expense of magnetite, which dissolved completely during the 5th step, i.e. when 0.0025 moles of quartz were added and consumed ($pH_{90°C}$ = 7.27 – Fig. 11a). At this point, the reaction was stopped. The addition of more quartz maked the solution in equilibrium with this mineral ([Si] = $8.97 \cdot 10^{-4}$ mol/kgw – Fig. 11b,c).

DISCUSSION

Kaolinite + Fe^0 Experiment (K90)

Fe-rich T–O phyllosilicates, magnetite, and lepidocrocite formed in the experiment with kaolinite and metal iron. Magnetite contains both Fe^{2+} and Fe^{3+}, whereas lepidocrocite contains only Fe^{3+} in its structure. Their formation indicates that iron oxidation occurred according to two reactions:

$$Fe^0 + 2H_2O \rightarrow Fe^{2+} + H_2 + 2OH^- \quad (1)$$

$$Fe^0 + 3H_2O \rightarrow Fe^{3+} + 3/2H_2 + 3OH^- \quad (2)$$

Both reactions produced OH^- and led to an increase in pH, favoring kaolinite dissolution. In fact, at temperatures closer to the experimental ones, the kaolinite dissolution rate was very low under near-neutral pH conditions (~$10^{-16.5}$ moles $cm^{-2}s^{-1}$ – rate based on Si release), but it will increase with pH (up to $10^{-14.4}$ moles $cm^{-2} \cdot s^{-1}$ at pH 12 – Carroll and Walther 1990).

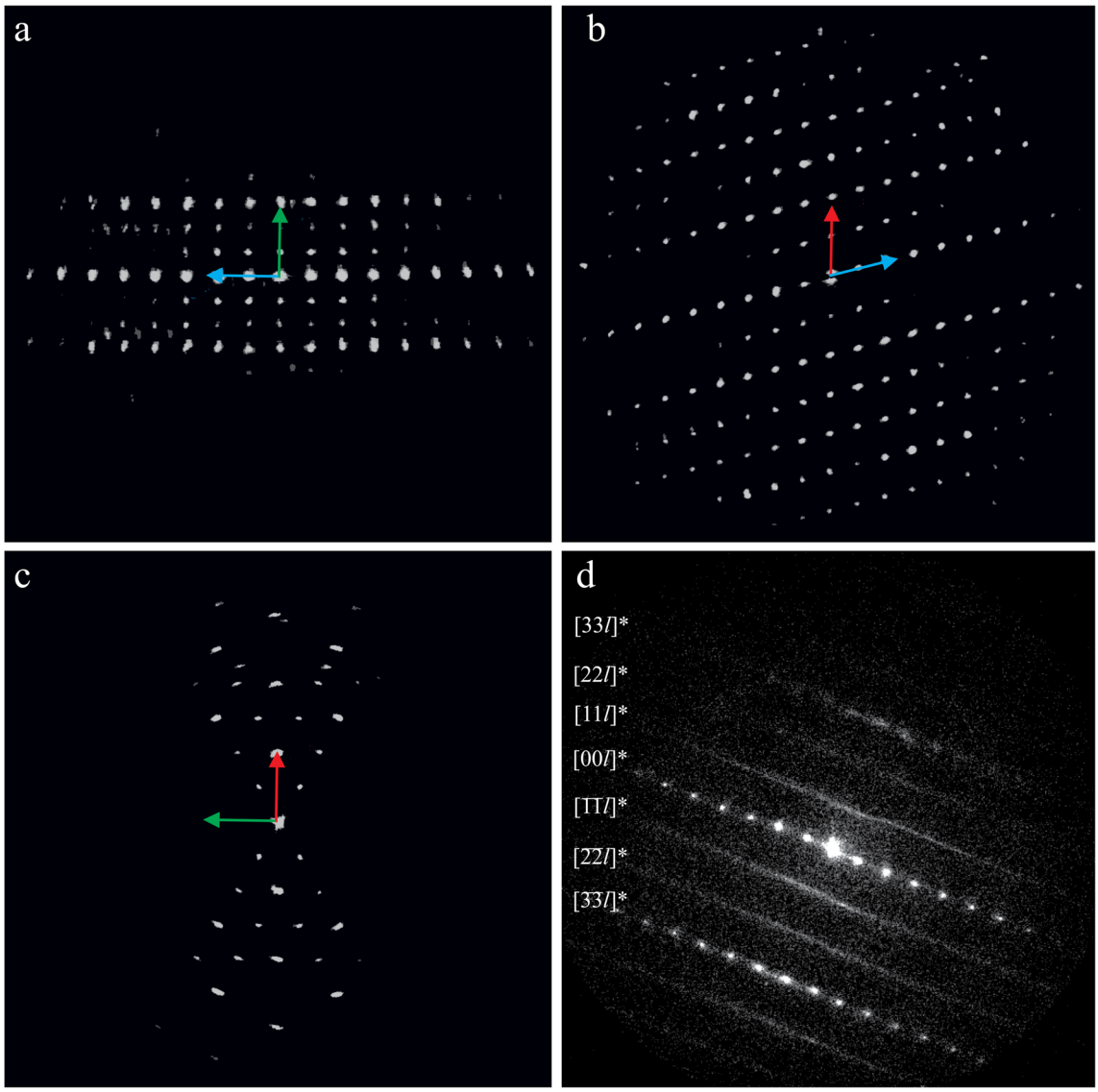

Fig. 7. Projection of 3D reconstructed diffraction volume from ED data of 1*M* cronstedtite polytype: **a** projection along *a**, **b** projection along *b**, **c** projection along *c**. **d** SAED pattern of (hhl_{hex})* plane for a disordered cronstedtite crystal. The projections of the main reciprocal axes are indicated: red vector: ***a****; green vector: ***b****; blue vector: ***c****

According to previous works on iron–clay interactions, the experimental conditions used here favored the formation of iron-rich T–O phyllosilicates, i.e. $T < 150°$ C, Fe/clays ≥ 0.33, Fe/liquid ≥ 10 (Perronnet et al. 2008; Mosser-Ruck et al. 2010; Rivard et al. 2013a). The composition of T–O phyllosilicates observed in the present work varied progressively from the kaolinite pole toward that of berthierine, although the most iron-rich phyllosilicates had a composition closer to that of cronstedtite (Fig. 4). This indicates both a progressive iron enrichment and a quasi-continuum evolution from a dioctahedral pole to a trioctahedral one.

The formation of Fe-bearing serpentines from kaolinite was reported in both natural environments and experimental syntheses. In nature, berthierine can form by interaction of kaolinite with a source of Fe, such as oolitic ironstones or Fe-bearing minerals such as siderite (Brindley 1951; Iijima and Matsumoto 1982; Bhattacharyya 1983). Under reducing conditions, the kaolinite transformation into greenalite is favored via cation substitutions in the octahedral sheet or a dissolution-recrystallization process (Giresse et al. 1988; Amouric et al. 1995).

In the laboratory, the hydrothermal synthesis of Fe-bearing serpentines from kaolinite showed the formation of berthierine-like minerals (Rivard et al. 2013a) or di-trioctahedral phases with composition between those of odinite and greenalite (Perronnet et al. 2008 – Fig. 4).

The composition of newly formed phyllosilicate particles with Fe < 40 at.% is similar to that reported by Rivard

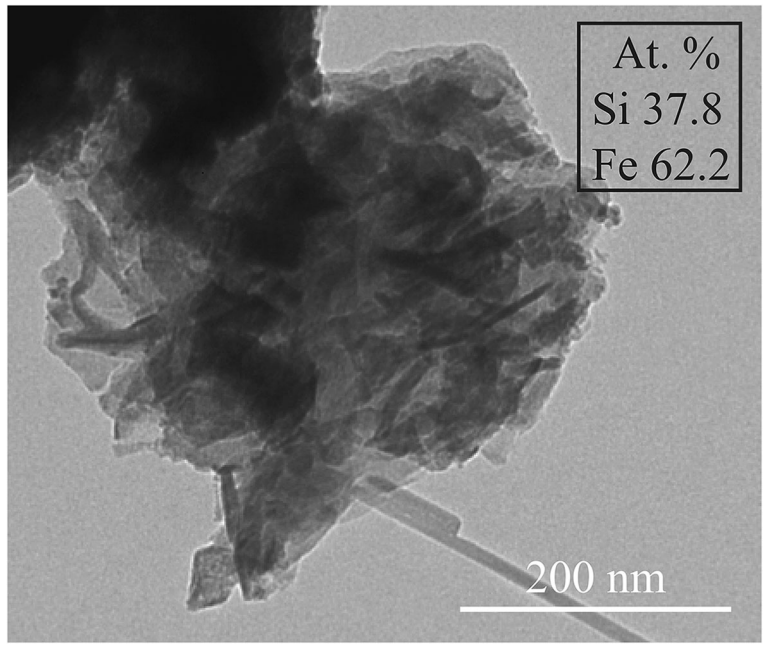

Fig. 8. TEM image of a Si-rich foil-like particle and its TEM-EDX data

et al. (2013a,b), but in the K90 experiment more Fe-rich particles also formed (Fig. 4). This difference was probably due probably to the experimental conditions. The temperature and the solution composition used by Rivard et al. (2013a,b) were the same as those used here, but they used a larger liquid/kaolinte ratio of 20 and a smaller Fe/

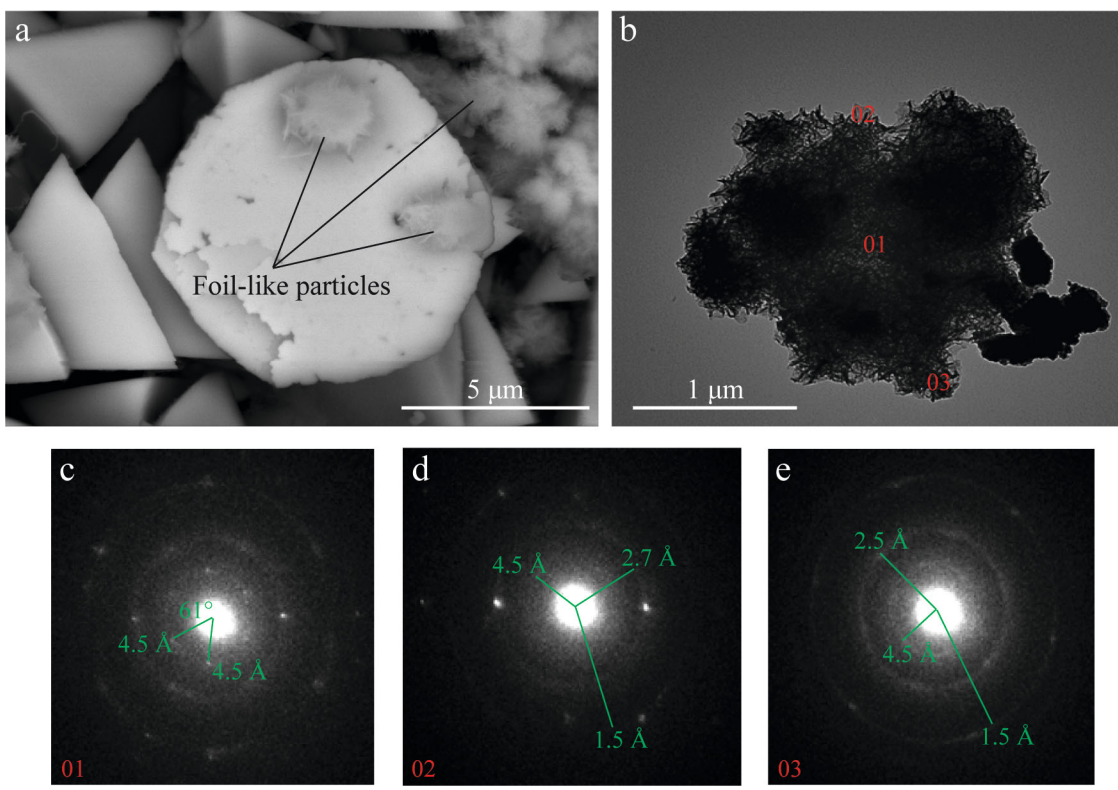

Fig. 9. a SEM image of foil-like particles on pyramidal crystals of cronstedtite. **b** TEM image of a foil-like particle. The latter is used to record SAED patterns in the zones 01, 02, and 03 (**c**, **d**, **e**)

kaolinite mass ratio of 0.33. In addition, their experiment was run three times with different durations (1, 3, and 9 months) whereas the K90 experiment lasted only 75 days. Rivard et al. (2013a) observed no significant differences in the reaction product compositions of 1, 3, and 9 month experiments, and the evolution of the particles followed the same trend (Rivard et al. 2013a). Thus, the presence of more Fe-rich particles in the K90 experiment is probably related to the larger Fe/kaolinite mass ratio of 0.5.

The comparison of the run products with those of Perronnet et al. (2008) is more complicated because those authors did not use kaolinite as the starting material, but the FoCa7 bentonite which is composed of mixed-layer kaolinite-smectite (80 wt.%), kaolinite (4 wt.%), and other accessory minerals. The experimental conditions were quite different: temperature of 80°C, duration of 45 days, bentonite/solution mass ratio of 1/16.7, and Fe/bentonite ratio ranging from 0 to 0.33. These experimental conditions may explain why their particles showed a different compositional evolution.

Two possible mechanisms, not mutually exclusive, have been proposed to explain the kaolinite destabilization and berthierine formation: (1) epitaxial growth and (2) transformation kaolinite-berthierine through an intermediate phase called "protoberthierine."

(1) According to Rivard et al. (2013a), the TEM-EDX analyses of newly formed T–O phyllosilicates were spread between those of kaolinite and berthierine because they were mixtures of these two minerals with variable relative amounts. These authors suggested that pristine kaolinite dissolved preferentially on the edges and moderately on the basal faces and released Al and Si. These elements and Fe (dissolution of iron metal) present in solution allowed for the precipitation of berthierine layers on the basal faces of kaolinite, which acted as support for an epitaxial growth (Rivard et al. 2013a).

(2) Bhattacharyya (1983) described the progressive transformation of dioctahedral kaolinite to trioctahedral berthierine via an intermediate step leading to the formation of a "protoberthierine" as shown by the following reactions:

$$\underset{\text{Kaolinite}}{Al_2Si_2O_5(OH)_4} + 1.5Fe^{2+} \rightarrow \underset{\text{Protoberthierine}}{\left(Fe^{2+}{}_{1.5}\ Al\right)_{\Sigma=2.5}\ Si_2O_5(OH)_4} + Al^{3+} \quad (3)$$

$$\underset{\text{Protoberthierine}}{\left(Fe^{2+}{}_{1.5}\ Al\right)_{\Sigma=2.5}\ Si_2O_5(OH)_4} + Fe^{3+} + 0.5Fe^{2+} \rightarrow \underset{\text{Berthierine}}{\left(Fe^{2+}{}_2\ Fe^{3+}\right)_{\Sigma=3}\ (Si\ Al)_2O_5(OH)_4} + Si^{4+} \quad (4)$$

According to Bhattacharyya (1983), the variable Fe contents in newly formed T–O phases could be explained by different "degrees of structural degradation in kaolinite": the most degraded kaolinite is the most susceptible to the intake of iron.

Based on the experimental results of the current study, it was not possible to make a choice between these two mechanisms to explain the formation of berthierine in the run product. Epitaxial growth could not be confirmed because the SAED patterns of newly formed T–O phyllosilicates showed a superposition of two or more lattices. Whether the superposition corresponds to several crystals of the same T–O mineral or of a berthierine and kaolinite mixture cannot be established. Both berthierine grown epitaxially on kaolinite and the existence of protoberthierine would result in similar TEM-EDX data. On the assumption that protoberthierine could form, the kaolinite–berthierine transformation in this experiment can be described as follows:

$$\underset{\text{Kaolinite}}{Al_2Si_2O_5(OH)_4} + 0.6Fe^{2+} \rightarrow \underset{\text{Protoberthierine}}{\left(Al_{1.6}Fe^{2+}{}_{0.6}\right)_{\Sigma=2.2}\ Si_2O_5(OH)_4} + 0.4Al^{3+} \quad (5)$$

$$\underset{\text{Protoberthierine}}{\left(Al_{1.6}Fe^{2+}{}_{0.6}\right)_{\Sigma=2.2}\ Si_2O_5(OH)_4} + 1.7Fe^{2+} + 0.5Fe^{3+} \rightarrow \underset{\text{Berthierine}}{\left(Fe^{2+}{}_{2.3}\ Fe^{3+}{}_{0.5}Al_{0.2}\right)_{\Sigma=3}\ (Si_{1.3}\ Al_{0.7})_{\Sigma=2}O_5(OH)_4} + 0.7Al^{3+} + 0.7Si^{4+} \quad (6)$$

where the protoberthierine formula corresponds to the average TEM-EDX data with Fe at.% < 20% (Fig. 4), because berthierines usually have larger iron contents as shown in Fig. 12. Natural berthierines also contain variable amounts of Mg, unlike those analyzed here, because no Mg-bearing phase was found in the starting material used in this study. The berthierine formula was thus calculated from the average of the data with Fe at.% > 20% (Fig. 4), following the method of Brindley (1982), based on three octahedral sites and a total valence of cations equal to +14. The abundance of estimated Fe^{2+} is in agreement with the composition of natural samples and indicated that berthierine formed under reducing conditions (Brindley 1982; Iijima and Matsumoto 1982; Giresse et al. 1988; Hornibrook and Longstaffe 1996; Rivas-Sanchez et al. 2006).

The results of thermodynamic simulations highlight the transformation of kaolinite in Fe^{2+}-berthierine and Fe-richer serpentines compositionally close to cronstedtite, in agreement with the experimental observations.

Magnetite is also predicted to form, but not lepidocrocite. Two explanations are possible: (1) the calculations do not take into account kinetic factors that may influence the reaction pathway and the nature of end-products; and (2) experimental data indicated that lepidocrocite crystallizes only if the Si/Fe ratio in solution is <0.05 (Schwertmann and Thalmann 1976). As the presence of Si in solution prevents the formation of this hydroxide, it should form before the formation of serpentines.

Knowing that lepidocrocite is an oxidation product of Fe^{2+} under neutral conditions (Liu et al. 2007), its formation during the cooling of the autoclave seems unlikely because the pH increases as the temperature decreases ($pH_{25°C}$ = 8.25). The simulations suggested that the equilibrium would be achieved when magnetite is dissolved, but in the run product it is still present. This means that at the end of the experiment, the system was probably not at equilibrium and a small Si content remained in the solution (Table 1, Fig. 10b).

Lepidocrocite can form in low chloride-containing solutions from a precursor, i.e. ferrihydrite or $Fe(OH)_2$ (Misawa et al. 1974; Schwertmann and Fechter 1994; Liu et al. 2007; de la Fuerte et al. 2016; Song et al. 2017). Ferrihydrite was not observed in the run product, but an unidentified Fe-bearing phase was found on the iron surface (Fig. 13). Based on the semi quantitative O/Fe ratio of ~4, this phase is thought not to be $Fe(OH)_2$ and could be a chloride green rust, which generally has an O/Fe ratio >2.5 (Refait et al. 1998). In this case, the lepidocrocite could have formed from a green rust which was an intermediate phase resulting from the easily oxidized $Fe(OH)_2$ (Refait and Génin 1997; Réguer et al. 2007).

Fontainebleau Sandstone + Fe^0 Experiment (Q90)

The iron oxidation reactions (1 and 2) release Fe^{2+} and Fe^{3+} into solution, favoring the formation of both magnetite and cronstedtite. The latter needs Si released by quartz dissolution to precipitate.

The formation of both magnetite and cronstedtite was also reported by Pignatelli et al. (2013, 2014) in a cooling experiment (90–40°C) simulating the interactions between iron and the Callovo-Oxfordian claystone of the Paris Basin. In addition to cronstedtite, greenalite and mixed-layered phases made of T–O–T and T–O phyllosilicates were also synthesized. These products had an intermediate composition between the starting clays and greenalite/cronstedtite (Fig. 6). This main difference could be due to claystone's complex mineralogical composition and the duration of experiments (6 months vs 75 days). In the experiment of Pignatelli et al. (2013, 2014), cronstedtite became unstable at $T \leq 50°C$ and rare relict crystals remained at 40°C. These authors proposed that cronstedtite formed by precipitation from a supersaturated solution.

Iron T–O phyllosilicates with compositions close to cronstedtite and odinite were synthesized by Lantenois et al. (2005) and analyzed by Lanson et al. (2012) in order to investigate the interactions between dioctahedral smectites and iron at 80°C for 45 days (Fig. 6). Their newly formed phyllosilicates were richer in Si and Al than the cronstedtite crystals of this study and those of Pignatelli et al. (2013, 2014), and they had variable amounts of vacancies in the octahedral sheet (0.25 to 0.75 – Lanson et al. 2012).

In natural environments, cronstedtite has been observed in low-temperature hydrothermal systems and in carbonaceous chondrites (Frondel 1962; López-García et al. 1992; Rubin et al. 2007; Hybler et al. 2016, 2017), but very little information is available about the formation conditions (starting mineralogical mixture, pH, temperature, etc.), preventing comparison with the Q90 experiment. The investigations of chondrites confirms that cronstedtite formation is due to the iron and silicon released by oxidation of kamacite and dissolution of silicates (Tomeoka and Buseck 1985; Zolensky and McSween 1988). Pignatelli et al. (2017) recently showed that in chondrites, cronstedtite can form by pseudomorphic replacement of olivines and pyroxenes, in association with Fe-tochilinite and goethite. Considering the stability field of Fe-tochilinite and the presence of tochilinite/cronstedtite intergrowths, it follows that cronstedtite in chondrites formed at $T < 30°C$ (Pignatelli et al. 2017). This is in agreement with thermodynamic simulations showing that the upper limit of cronstedtite stability is 100°C, whereas greenalite is stable up to 150°C (Schulte and Shock 2004; McAlister and Kettler 2008; Pignatelli et al. 2014).

From the structural point of view, sub-micrometric cronstedtite crystals investigated in this work by 3D ED belong to the 1*M* polytype or are characterized by a stacking disorder. Cronstedtite 1*M* polytype is quite rare in nature (Hybler et al. 2008), but 1*M* is commonly synthesized between 90 and 60°C. In this temperature range, other polytypes were obtained, such as $2M_1$ at 60–70°C and 3*A* at 80–90°C (Pignatelli et al. 2013; Hybler et al. 2018). The most abundant polytype in terrestrial and extraterrestrial samples is 1*T* (Müller et al. 1979; Zega and Buseck 2003; Hybler et al. 2008; Pignatelli et al. 2018), but this polytype seems difficult to reproduce in the laboratory; in fact, it was synthesized only once at 90°C in a mixed crystal with 1*M* (Hybler et al. 2018). Due to lack of knowledge, the differences in the polytypic sequence of synthetic and natural cronstedtite crystals cannot, currently, be explained.

Thermodynamic simulations give the reaction path describing the formation of cronstedtite and magnetite under the experimental conditions of the present study. The results indicate that iron is dissolved completely as well as magnetite, in disagreement with the experimental data where iron, magnetite, and cronstedtite coexist in the run product (Fig. 1b).

Table 1. Cation concentrations in run solutions measured by ICP-OES (given in both mg/L and mol/kgw to facilitate the comparison with thermodynamic simulation data). In the brackets, 1σ value was reported for each measurement

	$pH_{25°C}$	Al	Si	Fe	Units
K90	8.25	0.33 (0.10)	1.77 (0.18)	0.50 (0.10)	mg/L
		$1.2 \cdot 10^{-4}$	$6.3 \cdot 10^{-5}$	$8.9 \cdot 10^{-6}$	mol/kgw
Q90	7.38	0.16 (0.10)	6.15 (0.31)	8.46 (0.42)	mg/L
		$5.9 \cdot 10^{-6}$	$2.2 \cdot 10^{-4}$	$1.5 \cdot 10^{-4}$	mol/kgw

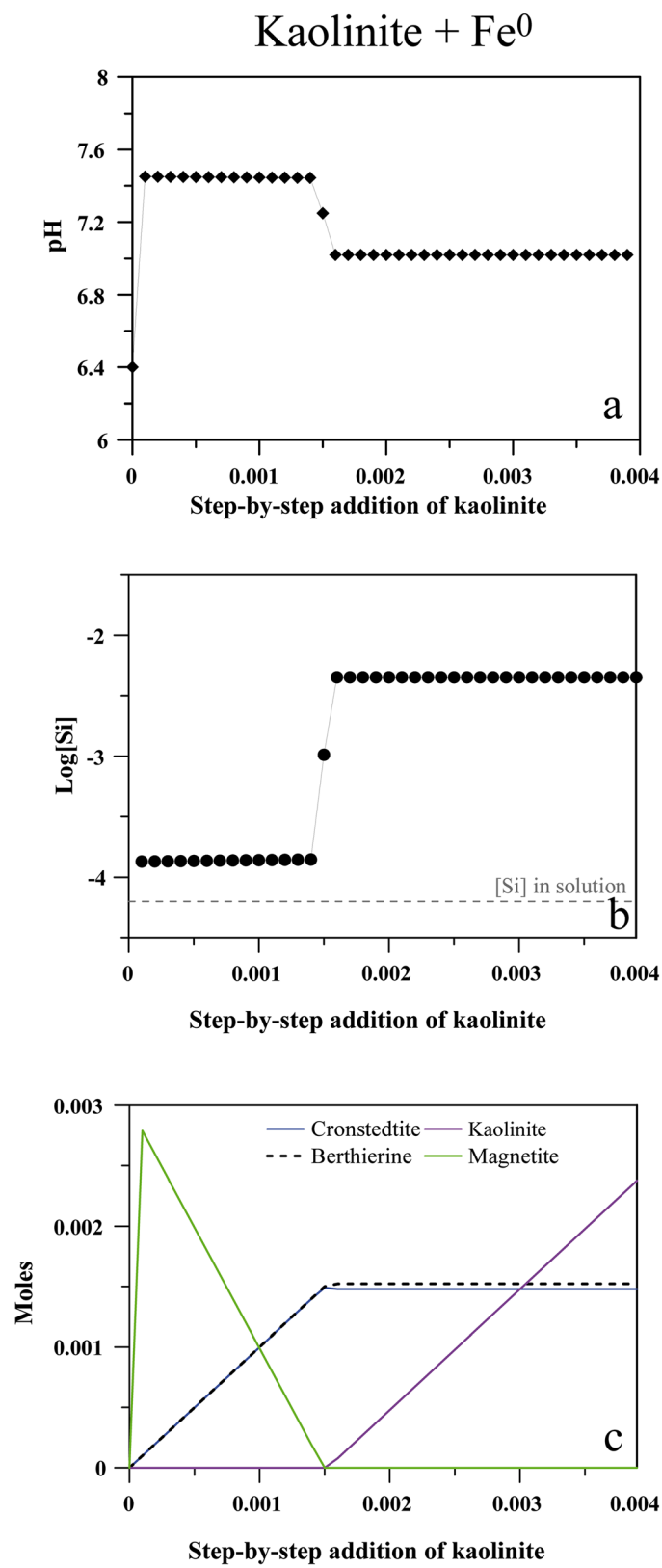

Fig. 10. Results of thermodynamic simulation for the experiment K90 obtained by a step-by-step addition of kaolinite (10^{-4} moles/step for 39 steps). **a** Evolution of pH, **b** Si concentration in solution, and **c** dissolution/precipitation of minerals. The dashed gray line indicates the Si content measured in the experimental solution

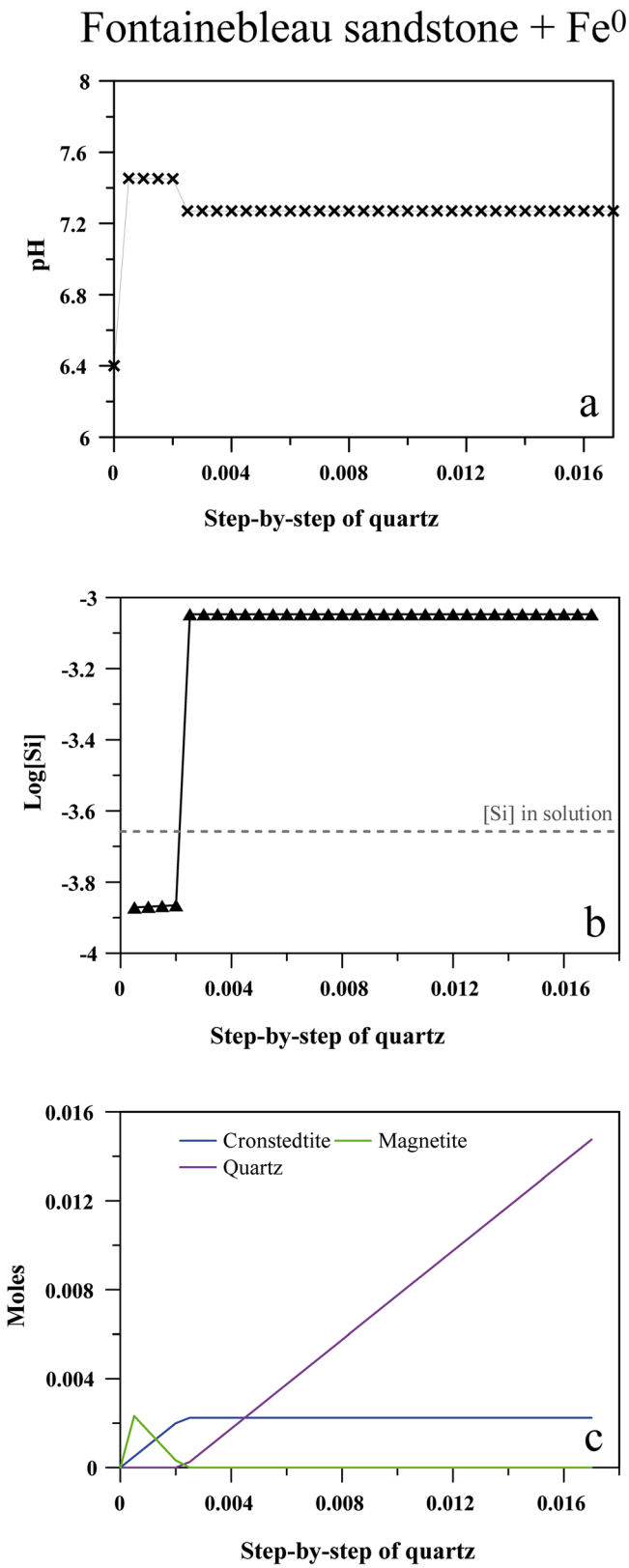

Fig. 11. Results of thermodynamic simulation for the experiment Q90 obtained by a step-by-step addition of quartz (0.0005 moles/step for 34 steps). **a** Evolution of pH, **b** Si concentration in solution, and **c** dissolution/precipitation of . The dashed gray line indicates the Si content measured in the experimental solution

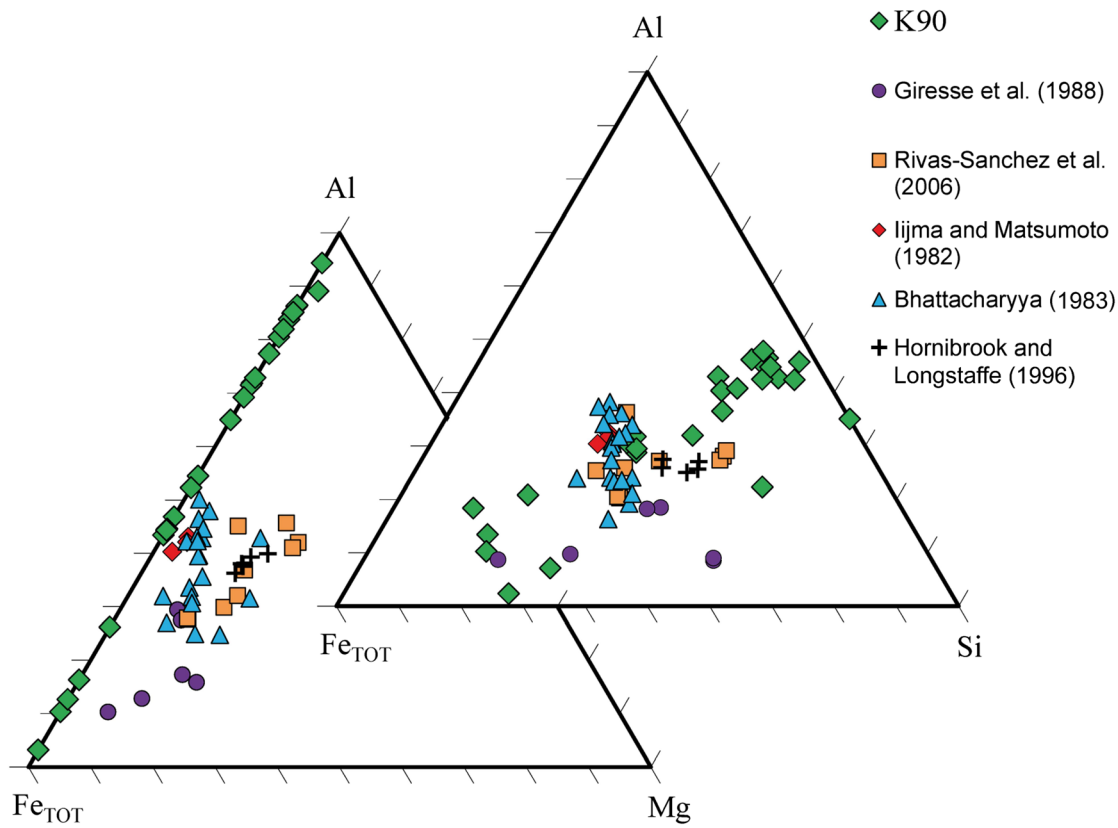

Fig. 12. Al–Si–Fe_{tot} and Al–Mg–Fe_{tot} ternary diagrams comparing the newly formed T–O phyllosilicates in experiment K90 and the compositions of natural berthierine crystals (Iijma and Matsumoto 1982; Giresse et al. 1988; Bhattacharyya 1983 and references therein; Hornibrook and Longstaffe 1996; Rivas-Sanchez et al. 2006)

Moreover, magnetite shows no sign of dissolution in SEM images. It follows that: (1) the reaction path probably did not come to the end in the Q90 experiment, probably because of short experimental duration (75 days), and/or the very slow dissolution rates of quartz and metal iron at 90°C under neutral pH ($1.57{\cdot}10^{-14}$ cm·s^{-1} and $9.12{\cdot}10^{-11}$ cm·s^{-1}, respectively (Van Lier et al. 1960; Schlegel et al. 2008); (2) modeling considers that all minerals dissolve and precipitate instantly when in reality they have different dissolution rates. Consequently, Fe would corrode much more quickly than quartz, and magnetite would then be the first mineral to form. After a further period of time, thanks to an increase in pH, quartz dissolution would provide silicon in solution, and the corrosion of the iron or a partial dissolution of the magnetite will release iron, favoring the precipitation of cronstedtite.

The experiment stopped probably at the third step of the simulation, where 0.0015 moles of quartz are dissolved and the $pH_{90°C}$ is 7.45 (Fig. 11a). At this step, the Si concentration released in solution is $1.36{\times}10^{-4}$ mol/kgw (Fig. 11b) which is very close to the concentration measured in the experimental solution ($2.2{\times}10^{-4}$ mol/kgw – Table 1). The difference of $0.84{\times}10^{-4}$ mol/kgw could be attributed to the dissolution of trace minerals present in the Fontainebleau sandstone, which is confirmed by the detection of Al in the run solution (Table 1).

CONCLUSIONS

For the first time, the effect of different starting mineralogical mixtures on the synthesis of Fe-bearing serpentines was shown. Two hydrothermal syntheses were carried out under the same conditions, with the exception of the Si source chosen, i.e. kaolinite and quartz (K90 and Q90 experiments, respectively). Although previous studies synthesized serpentines using gels or rocks (Dzene et al. 2018 and references therein), the aim of the current study was to underline the effects of composition and structure of the silicate precursors on newly formed serpentines. In addition, the Fe-serpentines synthesized here were well crystalline and have been characterized by several analytical techniques (XRD, SEM, TEM, and EDX).

The results have shown that different Fe-serpentines are formed in the K90 and Q90 experiments, i.e. berthierine from kaolinite and cronstedtite from quartz. Their growth mechanisms are also different; berthierine could form by epitaxial growth on kaolinite according to Rivard et al. (2013a), whereas cronstedtite forms probably by precipitation from a supersaturated solution (Pignatelli et al., 2013).

The formation of berthierine and cronstedtite in association with magnetite from their respective starting mineralogical mixtures was confirmed by the thermodynamic simulations.

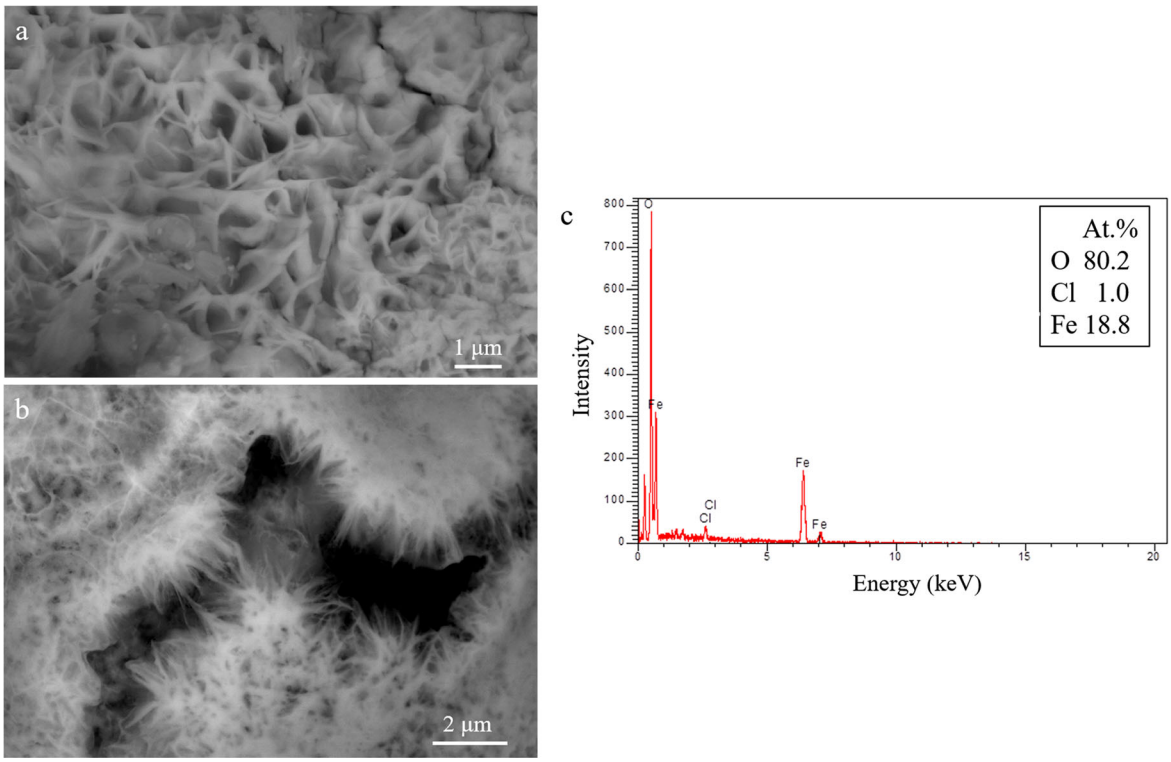

Fig. 13. **a**, **b** SEM images and **c** EDX spectrum of the Fe-bearing phase observed on the iron surface in experiment K90

The formation of these minerals needs Fe^{2+} and Fe^{3+} produced by previous oxidation of metal iron in the presence of water (see reactions 1 and 2). The oxidation produces H_2 and OH^-, leading to alkaline conditions and favoring the destabilization of kaolinite and quartz. The latter interact with Fe^{2+} and Fe^{3+} to form Fe-serpentines, according to:

$$Al_2Si_2O_5(OH)_4 + 3.3Fe^{2+} + 3.5Fe^{3+} + 10.7H_2O \rightarrow \quad (7)$$
$$\left(Fe^{2+}{}_{2.3}\ Fe^{3+}{}_{0.5}\ Al_{0.2}\right)_{\Sigma=3}\left(Si_{1.3}\ Al_{0.7}\right)_{\Sigma=2}O_5(OH)_4$$
$$+ 1.1Al(OH)_3 \ + 0.7SiO_2(aq) + 8.55H_2$$

$$3SiO_2 + +3.3Fe^{2+} + 3.4Fe^{3+} + 10.4H_2O \rightarrow \quad (8)$$
$$\left(Fe^{2+}{}_{2.3}\ Fe^{3+}{}_{0.7}\right)_{\Sigma=3}\left(Si_{1.3}\ Fe^{3+}{}_{0.7}\right)_{\Sigma=2}O_5(OH)_4 + 8.4H_2$$

Reactions 7 and 8 underline the importance of improving the current knowledge of Fe-serpentine formation due to the release of H_2, useful for several industrial purposes and sustainable energy (Ramachandran and Menon 1998; Edwards et al. 2007). In addition, H_2 generation is a key point to be investigated further with the aim of clarifying the possible relationship between Fe-serpentines and the origin of life (McCollom and Seewald 2013).

H_2 production during Fe-serpentine formation should be studied and quantified by performing more experiments using autoclaves equipped with *P-T* probes for in situ monitoring, as has been done for other minerals (e.g. Bourdelle et al. 2014, 2017). The new syntheses will also allow for (1) testing of the effect of other physical-chemical parameters (temperature, iron/silicate ratio, solution composition, etc.) on Fe-serpentines formation (2) a greater quantity of Fe-serpentines to be obtained in order to determine how their thermodynamic parameters vary as a function of their composition and polytypic sequence and, thus, improve the current geochemical databases. The shortcomings in our understanding of the thermodynamics of Fe-serpentines could be the source of inconsistencies between the experimental and thermodynamic results, and of inaccurate predictions for their formation and long-term stability (Seyfried et al. 2007; Pignatelli et al. 2014; Dzene et al. 2018). (3) It may also allow the determination of precipitation and dissolution rates of Fe-serpentines to improve the prediction of geochemical modeling.

ACKNOWLEDGMENTS

The authors thank Dr Iryna Andrusenko for helping in the acquisition and analysis of electron diffraction data. Authors Mauro Gemmi and Enrico Mugnaioli were supported by Regione Toscana through the FELIX project (Por CREO FESR 2014-2020 action). Prof. Fernando Nieto, two anonymous reviewers, and the Editor-in-Chief, Prof. Joseph W. Stucki, are also thanked for their corrections and suggestions which helped to improve the final version of the manuscript.

Compliance with ethical standards

Conflict of Interest

The authors declare that they have no conflict of interest.

Funding

Funding sources are as stated in the acknowledgments.

REFERENCES

Amouric, M., Parron, C., Casalini, L., & Giresse, P. (1995). A (1:1) 7-Å Fe phase and its transformation in recent sediments: an HRTEM and AEM study. *Clays and Clay Minerals, 43*, 446–454.

Bailey, S. W. (1969). Polytypism of trioctahedral 1:1 layer silicates. *Clays and Clay Minerals, 17*, 355–371.

Bailey, S. W. (1988). Odinite, a new dioctahedral-trioctahedral Fe^{3+}-rich 1:1 clay mineral. *Clay Minerals, 23*, 237–247.

Barber, D. J. (1981). Matrix phyllosilicates and associated minerals in C2M carbonaceous chondrites. *Geochimica et Cosmochimica Acta, 45*, 945–970.

Bhattacharyya, D. P. (1983). Origin of berthierine in ironstones. *Clays and Clay Minerals, 31*, 173–182.

Bildstein, O., Trotignon, L., Perronnet, M., & Jullien, M. (2006). Modelling iron–clay interactions in deep geological disposal conditions. *Physics and Chemistry of the Earth, 31*, 618–625.

Bourdelle, F., Truche, L., Pignatelli, I., Mosser-Ruck, R., Lorgeoux, C., Roszypal, C., & Michau, N. (2014). Iron–clay interactions under hydrothermal conditions: impact of specific surface area of metallic iron on reaction pathway. *Chemical Geology, 381*, 194–205.

Bourdelle, F., Mosser-Ruck, R., Truche, L., Lorgeoux, C., Pignatelli, I., & Michau, N. (2017). A new view on iron-claystone interactions under hydrothermal conditions (90°C) by monitoring in situ pH and H_2 generation. *Chemical Geology, 466*, 600–607.

Brindley, G. W. (1951). The crystal structures of some chamosite minerals. *Mineralogical Magazine, 29*, 502–525.

Brindley, G. W. (1982). Chemical compositions of berthierines – A review. *Clays and Clay Minerals, 30*, 153–155.

Browning, L. B., McSween Jr., H. Y., & Zolensky, M. E. (1996). Correlated alteration effects in CM carbonaceous chondrites. *Geochimica et Cosmochimica Acta, 60*, 2621–2633.

Calvin, W. M. (1998). Could Mars be dark and altered? *Geophysical Research Letters, 25*, 1597–1600.

Calvin, W. M., & King, T. V. V. (1997). Spectral characteristics of iron-bearing phyllosilicates: Comparison to Orgueil (CI1), and Murchison and Murray (CM2). *Meteoritics & Planetary Science, 32*, 693–701.

Carroll, S. A., & Walther, J. V. (1990). Kaolinite dissolution at 25°, 60°, and 80°C. *American Journal of Science, 290*, 797–810.

Changela, H. G., & Bridges, J. C. (2011). Alteration assemblages in the nakhlites: variation with depth on Mars. *Meteoritics & Planetary Science, 45*, 1847–1867.

Cliff, G., & Lorimer, G. W. (1975). The quantitative analysis of thin specimen. *Journal of Microscopy, 103*, 203–207.

Cudennec, Y., & Lecerf, A. (2006). The transformation of ferrihydrite into goethite or hematite, revisited. *Journal of Solid State Chemistry, 179*, 716–722.

de Combarieu, G., Schlegel, M. L., Neff, D., Foy, E., Vantelon, D., Barboux, P., & Gin, S. (2011). Glass-iron-clay interactions in a radioactive waste geological disposal: An integrated laboratory-scale experiment. *Applied Geochemistry, 26*, 65–79.

de la Fuerte, D., Díaz, I., Alcántara, J., Chico, B., Simancas, J., Llorente, I., García-Delgado, A., Jiménez, J. A., Adeva, P., & Morcillo, M. (2016). Corrosion mechanisms of mild stell in chloride-rich atmospheres. *Materials and Corrosion, 67*, 227–238.

Dove, P. M., & Crerar, D. A. (1990). Kinetics of quartz dissolution in electrolyte solutions using a hydrothermal mixed flow reactor. *Geochimica et Cosmochimica Acta, 54*, 955–969.

Dove, P., & Elston, S. F. (1992). Dissolution kinetics of quartz in sodium chloride solutions: analysis of existing data and a rate model for 25°C. *Geochimica et Cosmochimica Acta, 56*, 4147–4156.

Dove, P. M., Han, N., & De Yoreo, J. J. (2005). Mechanisms of classical crystal growth theory explain quartz and silicate dissolution behavior. *Proceedings of the National Academy of Sciences, 102*, 15357–15363.

Ďurovič, S. (1997). Cronstedtite-1*M* and co-existence of 1*M* and 3*T* polytypes. *Ceramics-Silikáty, 41*, 98–104.

Dzene, L., Brendlé, J., Limousy, L., Dutournié, P., Martin, C., & Michau, N. (2018). Synthesis of iron-rich tri-octahedral clay minerals: a review. *Applied Clay Science, 166*, 276–287.

Edwards, P. P., Kuznetsov, V. L., & David, W. I. F. (2007). Hydrogen energy. *Philosophical Transactions of the Royal Society, 365*, 1043–1056.

Elmaleh, A., Tarantino, S. C., Zema, M., Devouard, B., & Fialin, M. (2012). The low-temperature magnetic signature of Fe-rich serpentine in CM2 chondrites: comparison with terrestrial cronstedtite and evolution with the degree of alteration. *Geochemistry Geophysics Geosystems, 13*, Q05Z42. https://doi.org/10.1029/2011GC003964.

Elmaleh, A., Bourdelle, F., Caste, F., Benzerara, K., Leroux, H., & Devouard, B. (2015). Formation and transformations of Fe-rich serpentines by asteroidal aqueous. *Geochimica et Cosmochimica Acta, 158*, 162–178.

Frondel, C. (1962). Polytypism in cronstedtite. *American Mineralogist, 47*, 781–783.

Geiger, C. A., Henry, D. L., Bailey, S. W., & Maj, J. J. (1983). Crystal structure of cronstedtite-2H_2. *Clays and Clay Minerals, 31*, 97–108.

Gemmi, M., Mugnaioli, E., Gorelik, T. E., Kolb, U., Palatinus, L., Boullay, P., Hovmöller, S., & Abrahams, J. P. (2019). 3D Electron Diffraction: the nanocrystallography revolution. *ACS Central Science, 5*, 1315–1329.

Giresse, P., Wiewiora, A., & Lacka, B. (1988). Mineral phases and processes within green peloids from two recent deposits near the Congo river mouth. *Clay Minerals, 23*, 447–458.

Gole, M. L. (1980a). Low-temperature retrograde minerals in metamorphosed Archean banded iron-formations, Western Australia. *The Canadian Mineralogist, 18*, 205–214.

Gole, M. J. (1980b). Mineralogy and petrology of very-low metamorphic grade Archean banded iron-formations, Weld Range, Western Australia. *American Mineralogist, 65*, 8–25.

Guggenheim, S., Bailey, S. W., Eggleton, R. A., & Wilkes, P. (1982). Structural aspects of greenalite and related minerals. *The Canadian Mineralogist, 20*, 1–18.

Guillaume, D., Neaman, A., Cathelineau, M., Mosser-Ruck, R., Peiffert, C., Abdelmoula, M., Dubessy, J., Villiéras, F., Baronnet, A., & Michau, N. (2003). Experimental synthesis of chlorite from smectite at 300°C in the presence of metallic Fe. *Clay Minerals, 38*, 281–302.

Hicks, L. J., Bridges, J. C., & Gurman, S. J. (2014). Ferric saponite and serpentine in the nakhlite martian meteorites. *Geochimica et Cosmochimica Acta, 136*, 194–210.

Hornibrook, E. R. C., & Longstaffe, F. J. (1996). Berthierines from the Lower Cretaceous Clearwater formation, Alberta, Canada. *Clays and Clay Minerals, 44*, 1–21.

Hybler, J. (2014). Refinement of cronstedtite-1*M*. *Acta Crystallographica, B70*, 963–972.

Hybler, J., Petříček, V., Ďurovič, S., & Smrčok, L. (2000). Refinement of the crystal structure of cronstedtite-1*T*. *Clays and Clay Minerals, 48*, 331–338.

Hybler, J., Petříček, V., Fábry, J., & Ďurovič, S. (2002). Refinement of the crystal structure of cronstedtite-2*H*2. *Clays and Clay Minerals, 50*, 601–613.

Hybler, J., Ďurovič, S., & Kogure, T. (2008). Polytypism in cronstedtite. *Acta Crystallographica, A64*, 498–499.

Hybler, J., Sejkora, J., & Venclík, V. (2016). Polytypism of cronstedtite from Pohled, Czech Republic. *European Journal of Mineralogy, 28*, 765–775.

Hybler, J., Števko, M., & Sejkora, J. (2017). Polytypism of cronstedtite from Nižná Slaná, Slovakia. *European Journal of Mineralogy, 29*, 91–99.

Hybler, J., Klementová, M., Jarošová, M., Pignatelli, I., Mosser-Ruck, R., & Ďurovič, S. (2018). Polytype identification in trioctahedral 1:1 layer silicates. *Clays and Clay Minerals, 66*, 379–402.

Iijima, A., & Matsumoto, R. (1982). Berthierine and chamosite in coal measures of Japan. *Clays and Clay Minerals, 30*, 264–274.

Kogure, T., Hybler, J., & Yoshida, H. (2002). Coexistence of two polytypic groups in cronstedtite from Lostwithiel England. *Clays and Clay Minerals, 50*, 504–513.

Kolb, U., Mugnaioli, E., & Gorelik, T. E. (2011). Automated electron diffraction tomography – a new tool for nanocrystal structure analysis. *Crystal Research and Technology, 46*, 542–554.

Kreutzer, S., Friedrich, J., Sanderson, D., Adamiec, G., Chruśscińska, A., Fasoli, M., Martini, M., Polymeris, G. S., Burbidge, C. I., & Schmidt, C. (2017). Les sables de Fontainebleau: a natural quartz reference sample and its characterization. *Ancient TL, 35*, 21–31.

Lanson, B. (1997). Decomposition of experimental X-ray diffraction patterns (profile fitting): a convenient way to study clay minerals. *Clays and Clay Minerals, 45*, 132–146.

Lanson, B., & Besson, G. (1992). Characterisation of the end of smectite-to-illite transformation: decomposition of X-ray patterns. *Clays and Clay Minerals, 40*, 40–52.

Lanson, B., Van Lantenois, S., Aken, P. A., Bauer, A., & Plançon, A. (2012). Experimental investigation of smectite interaction with metal iron at 80°C: structural characterization of newly formed Fe-rich phyllosilicates. *American Mineralogist, 97*, 864–871.

Lantenois, S., Lanson, B., Muller, F., Bauer, A., Jullien, M., & Plançon, A. (2005). Experimental study of smectite interaction with metal Fe at low temperature: 1. Smectite destabilization. *Clays and Clay Minerals, 53*, 597–612.

Lauretta, D. S., Hua, X., & Buseck, P. R. (2000). Mineralogy of fine-grained rims in the ALH 81002 CM chondrite. *Geochimica et Cosmochimica Acta, 64*, 3263–3273.

Lee, M. R., & Chatzitheodoris, E. (2016). Replacement of glass in the Nakhla meteorite by berthierine: implications for understanding the origins of aluminum-rich phyllosilicates on Mars. *Meteoritics & Planetary Science, 51*, 1643–1653.

Liu, H., Li, P., Zhu, M., Wei, Y., & Sun, Y. (2007). Fe(II)-induced transformation from ferrihyfrite to lepidocrocite and goethite. *Journal of Solid State Chemistry, 180*, 2121–2128.

López-García, J. A., Manteca, J. I., Prieto, A. C., & Calvo, B. (1992). Primera aparicíon en España de cronstedtita. Caracterizacíon estructural. *Boletín de la Sociedad Española de Mineralogía, 15*, 21–25.

McAlister, J. A., & Kettler, R. M. (2008). Metastable equilibria among dicarboxylic acids and oxidation state during aqueous alteration on the CM2 chondrite parent body. *Geochimica et Cosmochimica Acta, 72*, 233–241.

McCollom, T. M., & Seewald, J. S. (2013). Serpentinites, hydrogen, and life. *Elements, 9*, 129–134.

Misawa, T., Hashimoto, K., & Shimodaira, S. (1974). The mechanism of formation of iron oxide and oxyhydroxides in aqueous solutions at room temperature. *Corrosion Science, 14*, 131–149.

Mosser-Ruck, R., Cathelineau, M., Guillaume, D., & Charpentier, D. (2010). Effects of temperature, pH, and iron/clay and liquid/clay ratios on experimental conversion of dioctahedral smectite to berthierine, chlorite, vermiculite, or saponite. *Clays and Clay Minerals, 58*, 280–291.

Mugnaioli, E., & Gemmi, M. (2018). Single-crystal analysis of nanodomains by electron diffraction tomography: mineralogy at the order-disorder borderline. *Zeitschrift für Kristallographie, 233*, 163–178.

Müller, W. F., Kurat, G., & Kracher, A. (1979). Chemical and crystallographic study of cronstedtite in the matrix of the Cochabamba (CM2) carbonaceous chondrite. *Tschermaks Mineralogische und Petrographische Mitteilungen, 26*, 293–304.

Parkhurst, D. & Appelo, C.A.J. (1999). *User's guide to PHREEQC (version 2) - a computer program for speciation, reaction-path, 1D-transport, and inverse geochemical calculations*. U.S. Geological Survey Water Resources Investigation Report 99, 99-4259. U.S. Geological Survey, Reston, Virginia, USA. 312 pp.

Perronnet, M., Jullien, M., Villiéras, F., Raynal, J., Bonnin, D., & Bruno, G. (2008). Evidence of a critical content in Fe(0) on FoCa7 bentonite reactivity at 80°C. *Applied Clay Science, 38*, 187–202.

Pignatelli, I., Mugnaioli, E., Hybler, J., Mosser-Ruck, R., Cathelineau, M., & Michau, N. (2013). A multi-technique characterization of cronstedtite synthesized by iron-clay interaction in a step-by-step cooling procedure. *Clays and Clay Minerals, 61*, 277–289.

Pignatelli, I., Bourdelle, F., Bartier, D., Mosser-Ruck, R., Truche, L., Mugnaioli, E., & Michau, N. (2014). Iron-clay interactions: detailed study of the mineralogical transformation of claystone with emphasis on the formation of iron-rich T-O phyllosilicates in a step-by-step cooling experiment from 90°C to 40°C. *Chemical Geology, 387*, 1–11.

Pignatelli, I., Marrocchi, Y., Vacher, L., Delon, R., & Gounelle, M. (2016). Multiple precursors of secondary mineralogical assemblages in CM chondrites. *Meteoritics & Planetary Science, 51*, 785–805.

Pignatelli, I., Marrocchi, Y., Mugnaioli, E., Bourdelle, F., & Gounelle, M. (2017). Mineralogical, crystallographic and redox features of the earliest stages of fluid alteration in CM chondrites. *Geochimica et Cosmochimica Acta, 209*, 106–122.

Pignatelli, I., Mugnaioli, E., & Marrocchi, Y. (2018). Cronstedtite polytypes in the Paris meteorite. *European Journal of Mineralogy, 30*, 349–354.

Ramachandran, R., & Menon, R. K. (1998). An overview of industrial uses of hydrogen. *International Journal of Hydrogen Energy, 23*, 593–598.

Refait, P., & Génin, J. M. R. (1997). The mechanisms of oxidation of ferrous hydroxychloride β-$Fe_2(OH)_3Cl$ in aqueous solution: the formation of akaganeite vs goethite. *Corrosion Science, 39*, 539–553.

Refait, P., Abdelmoula, M., & Génin, J. M. R. (1998). Mechanisms of formation and structure of green rust one in aqueous corrosion of iron in the presence of chloride ions. *Corrosion Science, 40*, 1547–1560.

Réguer, S., Dillmann, P., & Mirambet, F. (2007). Buried iron archeological artefacts: corrosion mechanisms related to the presence of Cl-containing phases. *Corrosion Science, 49*, 2726–2744.

Rivard, C., Pelletier, M., Michau, N., Razafitianamaharavo, A., Bihannic, I., Abdelmoula, M., Ghanbaja, J., & Villiéras, F. (2013a). Berthierine-like mineral formation and stability during the interaction of kaolinite with metallic iron at 90°C under anoxic and oxic conditions. *American Mineralogist, 98*, 163–180.

Rivard, C., Montargès-Pelletier, E., Vantelon, D., Pelletier, M., Karunakaran, C., Mochot, L. J., Villieras, F., & Michau, N. (2013b). Combination of multi-scale and multi-edge X-ray spectroscopy for investigating the products obtained from the interaction between kaolinite and metallic iron in anoxic conditions at 90°C. *Physics and Chemistry of Minerals, 40*, 115–132.

Rivas-Sanchez, M. L., Alva-Valdivia, L. M., Arenas-Alatorre, J., Urrutia-Fucugauchi, J., Ruiz-Sandoval, M., & Ramos-Molina, M. A. (2006). Berthierine and chamosite hydrothermal: genetic guides in the Peña Colorada magnetite-bearing ore deposit, Mexico. *Earth Planets and Space, 58*, 1389–1400.

Rubin, A. E., Trigo-Rodríguez, J. M., Huber, H., & Wasson, J. T. (2007). Progressive aqueous alteration of CM carbonaceous chondrites. *Geochimica et Cosmochimica Acta, 71*, 2361–2382.

Saadi, F. A., Wolf, K.-H., & Kruijsdijk, C. (2017). Characterization of Fontainebleau sandstone: quartz overgrowth and its impact on pore-throat framework. *Journal of Petroleum & Environmental Biotechnology, 8*, 1–12.

Schlegel, M. L., Bataillon, C., Benhamida, K., Blanc, C., Menut, D., & Lacour, J. L. (2008). Metal corrosion and argillite transformation at the water-saturated, high-temperature iron-clay interface: a microscopic-scale study. *Applied Geochemistry, 23*, 2619–2633.

Schulte, M., & Shock, E. (2004). Coupled organic synthesis and mineral alteration on the meteorite parent bodies. *Meteoritics & Planetary Science, 46*, 1577–1590.

Schwertmann, U., & Fechter, H. (1994). The formation of green rust and its transformation to lepidocrocite. *Clay Minerals, 29*, 87–92.

Schwertmann, U., & Thalmann, H. (1976). The influence of [Fe(II)], [Si], and pH on the formation of lepidocrocite and ferrihydrite

during oxidation of aqueous $FeCl_2$ solutions. *Clay Minerals, 11*, 189–200.

Seyfried Jr., W. E., Foustoukos, D. I., & Fu, Q. (2007). Redox evolution and mass transfer during serpentinization: An experimental and theoretical study at 200°C, 500 bar with implications for ultramafic-hosted hydrothermal systems at Mid-Ocean Ridges. *Geochimica et Cosmochimica Acta, 71*, 3872–3886.

Smrčok, L., & Weiss, Z. (1993). DIFK91: a program for the modelling of powder diffraction patterns on a PC. *Journal of Applied Crystallography, 26*, 140–141.

Smrčok, L., Ďurovič, S., Petříček, V., & Weiss, Z. (1994). Refinement of the crystal structure of cronstedtite-3*T*. *Clays and Clay Minerals, 42*, 544–551.

Song, Y., Jiang, G., Chen, Y., Zhao, P., & Tian, Y. (2017). Effects of chloride ions on corrosion of ductile iron and carbon steel in soil and environments. *Scientific Reports, 7*, 6865.

Steadman, R., & Nuttall, P. M. (1964). Further polymorphism in cronstedtite. *Acta Crystallographica, 17*, 404–406.

Tomeoka, K., & Buseck, P. R. (1985). Indicators of aqueous alteration in CM carbonaceous chondrites: Microtextures of a layered mineral containing Fe, S, O and Ni. *Geochimica et Cosmochimica Acta, 49*, 2149–2163.

Tosca, N. J., Guggenheim, S., & Pufahl, P. K. (2016). An authigenic origin for Precambrian greenalite: implications for iron formation and the chemistry of ancient seawater. *GSA Bulletin, 128*, 511–530.

Van Lier, J. A., De Bruyn, P. L., & Overbeek, J. T. G. (1960). The solubility of quartz. *The Journal of Physical Chemistry, 64*, 1675–1682.

Wahle, M. W., Bujnowski, T. J., Guggenheim, S., & Kogure, T. (2010). Guidottiite, the Mn-analogue of cronstedtite: a new serpentine-group mineral from South Africa. *Clays and Clay Minerals, 58*, 364–376.

Wilson, J., Cressey, G., Cressey, B., Cuadros, J., Ragnarsdottir, K. V., Savage, D., & Shibata, M. (2006). The effect of iron on montmorillonite stability. (II) Experimental investigation. *Geochimica et Cosmochimica Acta, 70*, 323–336.

Wolery, T.J. & Jove-Colon, C.F. (2004). Qualification of thermodynamic data for geochemical modeling of mineral–water interactions in dilute systems. Rep. ANL-WIS-GS-000003 REV 00, U.S. Dept. of Energy, Washington, DC.

Zega, T. J., & Buseck, P. R. (2003). Fine-grained-rim mineralogy of the Cold Bokkeveld CM chondrite. *Geochimica et Cosmochimica Acta, 67*, 1711–1721.

Zolensky, M.E. (1984). Hydrothermal alteration of CM carbonaceous chondrites; implications of the identification of tochilinite as one type of meteoritic PCP. In: *47th Annual Meeting of the Meteoritical Society*, p. 19.

Zolensky, M. & Keller, L.P. (1999). Clay Minerals. In Primitive Meteorites and Interplanetary Dust I. In *Program and Abstracts for Clay Minerals Society 28th Annual Meeting*, p. 184.

Zolensky M. & McSween H.Y. (1988). Aqueous alteration. Pp. 114–143 in: *Meteorites and the Early Solar System* (J.F. Kerridge and M.S. Matthews, editors). University of Arizona Press.

Zolotov, M. Y. (2014). Formation of brucite and cronstedtite bearing mineral assemblages on Ceres. *Icarus, 228*, 13–26.

(*Received 17 January 2020; revised 15 May 2020; AE: F. Javier Huertas***)**